A Report of Research

on the Topic

VIBRATION CONTROL IN TURBOMACHINERY
USING ACTIVE MAGNETIC JOURNAL BEARINGS

by:

Josiah D. Knight
Associate Professor

Department of Mechanical Engineering
and Materials Science
Duke University
Durham, NC 27706

submitted to:

ABSTRACT

The effective use of active magnetic bearings for vibration control in turbomachinery depends on an understanding of the forces available from a magnetic bearing actuator. The purpose of this project was to characterize the forces as functions shaft position.

Both numerical and experimental studies were done to determine the characteristics of the forces exerted on a stationary shaft by a magnetic bearing actuator. The numerical studies were based on finite element computations and included both linear and nonlinear magnetization functions.

Measurements of the force versus position of a nonrotating shaft were made using two separate measurement rigs, one based on strain guage measurement of forces, the other based on deflections of a calibrated beam.

The general trends of the measured principal forces agree with the predictions of the theory while the magnitudes of forces are somewhat smaller than those predicted. Other aspects of theory are not confirmed by the measurements. The measured forces in the normal direction are larger than those predicted by theory when the rotor has a normal eccentricity.

Over the ranges of position examined, the data indicate an approximately linear relationship between the normal eccentricity of the shaft and the ratio of normal to principal force. The constant of proportionality seems to be larger at lower currents, but for all cases examined its value is between 0.14 and 0.17. The nonlinear theory predicts the existence of normal forces, but has not predicted such a large constant of proportionality for the ratio.

The type of coupling illustrated by these measurements would not tend to cause whirl, because the coupling coefficients have the same sign, unlike the case of a fluid film bearing, where the normal stiffness coefficients often have opposite signs. They might, however, tend to cause other self-excited behavior. This possibility must be considered when designing magnetic bearings for flexible rotor applications, such as gas turbines and other turbomachinery.

In related work attached as an appendix, simulations of 2DOF systems subject to these force models show that significant nonlinear behavior can occur, including multiple coexisting solutions, bifurcations in response as the stabilities of the respective solutions change, and self-similarity in stability boundaries.

CONTENTS

CONTENTS, continued

1. INTRODUCTION

This report describes work done under Grant NAG 3-968 during the performance period October 1989 to 1 February 1992, in addition to further related work using knowledge gained during the work performed under this grant. The purpose of the research was to examine certain aspects of the potential of magnetic bearings for vibration control in turbomachinery. The principal thrusts of the research have been

1) Calculation of the two-dimensional forces exerted on a shaft by a typical magnetic actuator under open loop conditions.

2) Measurement of such forces using specially designed apparatus.

3) Simulation of dynamics of a simple rotor using the measured and calculated forces along with a control law.

The report consists of three principal sections, plus three appendices. Section 1 is an introduction and a brief review of pertinent literature at the time of the beginning of this work.

Section 2 describes the analytical and numerical modelling of the magnetic flux distribution in magnets of a magnetic actuator and the results of calculations of force between the actuator and the shaft. Section 3 describes two kinds of experiments conducted to determine the forces that are modelled in Section 2. Because comparisons between theory and experiment are made, it is sometimes necessary to refer in Section 2 to force measurements that will be described in more detail in Section 3. Similarly, Section 3 refers back to Section 2.

Appendix A is a listing of the computer program used for calculations using an air-gap method. Appendix B is a description of methods used in calculations of force including flux contained in metal parts.

Appendix C contains the text of a thesis submitted to Duke University by Thomas Walsh for the M.S. degree, which uses the results of measurements and calculations done under this grant in the simulation of a rotor-magnetic bearing system. This work was performed subsequent to the actual grant period, but is included because of the close relation to and dependence on the results obtained under this grant.

In addition to the sections describing technical findings, this report summarizes related activities, including papers and reports, personnel, equipment and progress of students.

1.1 Magnetic Suspension of Turbomachine Shafts

The introduction of practical magnetic supports for rotating shafts is a recent development. These devices have the potential of replacing fluid film bearings and rolling element bearings in some critical applications, and of acting as supplemental control actuators alongside these traditional bearings in order to limit vibration, noise and instability. Figure 1.1 shows the general concept of a rotating shaft suspended by a set of controlled magnetic actuators. In this report, the combination of an actuator, its sensors, controller and power amplifier is called a magnetic bearing.

In a magnetic bearing the shaft is supported by the force established between a set of electromagnets and the shaft due to the magnetic field. There is no direct contact between the shaft and any part of the bearing. This method of support has several advantages over traditional fluid film or rolling element bearings. Since no lubricant is needed, there is no sealing requirement to prevent either the lubricant or the working fluid from contaminating the other. Also, the lubricant supply system required for a traditional bearing is eliminated, and the frictional losses in the magnetic support are negligible compared to those in a fluid film bearing. Finally, since the magnetic bearing requires a feedback control system to maintain stability even in a nonrotating steady-state case, this feedback loop may be used to advantage in adjusting the dynamic characteristics of the rotor-bearing system to optimize the machine's vibration characteristics. The magnetic bearing could be designed so that it opposes the destabilizing effects of other parts of the system.

It is this last possibility that is the most exciting aspect of magnetic suspension. The ability to control better the dynamics of shafts and thus to reduce the danger and expense that result from high levels of vibration is the principal motivation for research in this field.

Magnetic bearings are rapidly gaining acceptance as replacements for traditional fluid film bearings in the design of turbomachinery. Applications include the small and sensitive, such as turbomolecular pumps and x-ray generation equipment, as well as the extremely precise, such as machine tool spindles. At the other extreme, applications include very large industrial machinery such as compressors, turbines and engines [1]. The motivations for these applications vary, but most are inspired by the possibility of precise control of the rotor through the magnetic bearing's active feedback loop. In the case of high precision machine tools there is an obvious need for precise control of tool position, and this control is made possible through the active magnetic bearing to a degree not possible by using other bearings, even the stiffest of rolling element bearings. This degree of control is possible even though the parameters of the bearing may not have been
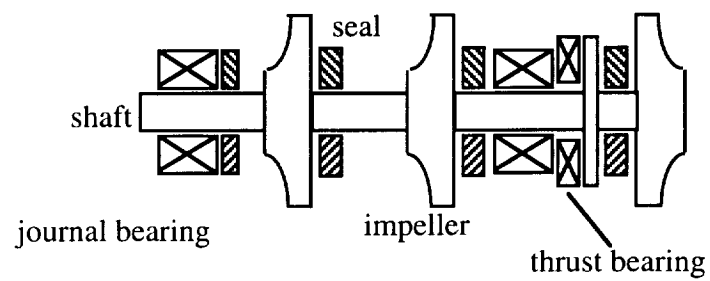
(a) A turbomachine schematic
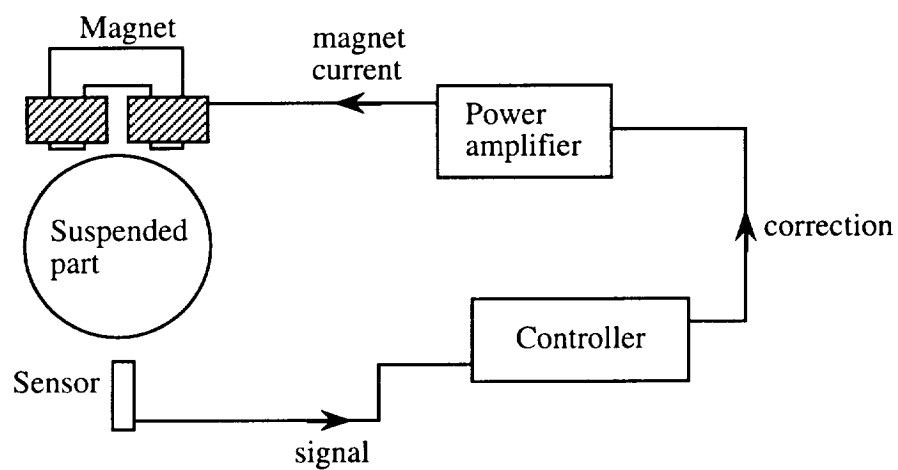
(b) Active levitation schematic, one dimension shown

Figure 1.1. The active magnetic bearing concept.

accurately assessed, because the active controller compensates for poorly known characteristics by the exercise of negative feedback. Thus, even though the system is not fully optimized, its performance may still far exceed that of passive bearings in terms of accuracy of positioning.

The need for precision force generation is less obvious but no less crucial in the case of large industrial machinery. In this case, the machines are so large and expensive, and down-time is so costly, that it is essential to minimize vibration problems. Many of these machines operate at speeds higher than one or two critical speeds, so vibration problems can be intense, and the nature of these problems becomes successively worse as performance demands are increased. The traditional approach toward minimizing vibration is to design passive fluid bearings by choosing clearances and length-to-diameter ratios to achieve the best possible effective stiffness and damping characteristics. Most of the damping in these large vibrational systems arises from the bearings, and in passive bearings there is always a trade off between damping and stiffness. In addition, most such bearings give rise not only to principal restoring forces, generally desirable, but also to forces that act normal to a perturbation direction. Depending on their signs, these forces can be stabilizing or destabilizing. It is the nature of fluid bearings that in most practical situations they are destabilizing. Thus the active magnetic bearing, which offers controllable forces that are in theory uncoupled, has a strong appeal to the manufacturers and users of such machinery.

1.1.1 Disadvantages

Magnetic bearings are not a panacea, however. There are significant drawbacks to their use: magnetic bearings in general are larger and heavier than equivalent fluid bearings, they require continuous control and an uninterrupted power supply and therefore need redundant controllers and backup power capability, plus emergency backup bearings for shut-down in case of complete failure of the active system. These disadvantages must be weighed against the positive factors of reduced power losses, elimination of lubricant supply system and controllability.

The disadvantages stemming from the size and weight factors may be minimized with better prediction of the forces available from actuators, and the effects of geometry on the available forces. Reliance on simplified theory for the forces available in an actuator has probably led to overdesign of the components, and to a reliance on controller robustness to compensate for inaccuracies in the force prediction. In practice the installation of a magnetic bearing system in a large turbomachine has been found to require

a lengthy process of tuning both on the test stand and later in the field for each individual machine

Better force prediction will allow optimization of the actuators themselves in an open loop sense, shortening the tuning process and freeing the designer of the controls to concentrate on higher orders of vibration control strategy To this end, the work described in this report is concentrated on developing reliable and efficient methods of predicting the forces exerted by magnets on a rotor. The work consists of both theoretical/numerical analysis and experimental measurements of forces.

1.1.2 Background

This section describes the background and state of technology in magnetic bearings largely as it existed at the start of this project. The following section contains limited references to developments that occurred as this work proceeded.

The concept of suspending a machine part by force of magnetic attraction was introduced as early as 1842 [2], and some early devices for magnetic support were attempted using permanent magnets and electromagnets, but practical application of the idea awaited relatively recent developments in control technology and power electronics.

Beams [3] in 1949 built a successful magnetic suspension device for a small diameter rotor (1/64 inch) in order to achieve high rotational speeds. The system used vacuum tubes for control and power amplification, and thus was limited to supporting only small masses.

The first application of fully active magnetic suspension was in the field of aerodynamic research where a system was developed to support models in wind tunnel tests [4]. This is a demanding application because the distances between the magnets and the model are large, but the forces required may be small.

More recently, with the development of solid state power electronics and advances in controls, more attention has been devoted to the possible applications of magnetic suspension to industrial and laboratory machinery where large forces may be involved. Nikolajsen, et. al. [5] reported on the use of an electromagnetic damping device for controlling vibration in a flexible transmission shaft. Schweitzer, et. al. [6] considered the application of magnetic bearings to vibration control of pumps and centrifuges, and discussed the merits of centralized versus decentralized control [7]. The use of magnetic bearings in a flexible rotor system was also considered [8].

A number of papers have been published beginning in the early 1980's on various aspects of the control of shaft vibration and suspension by magnetic forces.

Allaire, et. al. performed theoretical studies of the effects of using a feedback actuator on the unbalance response of a single mass rotor on rigid supports [9], and on flexible

supports [10]. The actuator was placed at the mass location and was represented by feedback with gains proportional to shaft displacement and shaft velocity. It was found that proportional feedback could be used to alter the critical speeds of the system over wide ranges, and that derivative feedback could be used to change the amplitudes of vibration. Combinations of proportional and derivative feedback significantly altered the system characteristics in terms of both critical speeds and amplitude of response.

An experimental test apparatus for applying feedback control to a multimass rotor at the bearing locations was constructed by Heinzmann [11]. The rig used actuators made from the moving voice coils of loudspeakers, and the force was applied directly through mechanical links attached to ball bearings on the shaft. Significant effects on the critical speeds of the system were achieved by feedback control.

Kelm [12] computed the linearized stiffness and damping coefficients for a four-magnet bearing, and measured the coefficients in an experimental bearing for a two-inch diameter shaft. Precise agreement between predicted and measured values was not achieved.

Connor and Tichy [13] have proposed an eddy current bearing that would generate repulsive rather that attractive forces by inducing currents in the rotor.

Chen and Darlow [14] tested a magnetic bearing constructed by modifying an induction motor stator and evaluated the effectiveness of two schemes for estimating velocity and acceleration in the feedback control loop.

Walowit, et. al. [15] and Albrecht et. al. [16] analyzed and tested a magnetic thrust bearing. Their analysis and experiment involved transverse misalignment of the plane surface gaps but no angular misalignment.

Keith, et al. [17] have examined several aspects of proportional-derivative control using a digital controller, and Maslen, et al. [18] consider some of the performance limitations of active bearings.

Papers contained in the proceedings of the first significant international gathering of researchers in the field of magnetic suspension of machine elements [19] address applications, control, identification of parameters and other aspects of magnetic bearings [20-22], as well as applications in space [23-24].

1.1.3 Developments During this Project

According to literature from magnetic bearing manufacturer S2M, as of 1991 a total of more than 440,000 hours of operation had been accumulated by machines equipped with the company's active magnetic bearings [25]. The 96 individual machines span a wide

range of sizes, from blowers in the 5 to 200 kW range up to industrial compressors in the 25,000 kW range.

Along with increased industrial application of magnetic bearings came significant new research. The proceedings of the Second International Symposium on Magnetic Bearings [26] contain 53 technical papers on various aspects of magnetic bearings, by authors from 12 countries.

These papers address several areas of application, including momentum wheels for energy storage [27, 28], electrospindles for boring, grinding and milling operations [29, 30, 31], as well as suspension of large industrial machine rotors such as those of boiler feed pumps [32], pipeline compressors [33], and nuclear circulating pumps [34].

There continued to be a growing interest in control aspects, with papers devoted to digital control [35, 36, 37] and amplifier design [38, 39]. Several philosophies of control were examined, including centralized vs. decentralized control [40], automatic balancing [41], and modal control [42, 43]. One method of approaching linearity in magnetic suspension systems is to apply large bias currents, upon which are superposed the control currents. Higuchi et al. [37], however, used a digital control scheme to effect a linearization of the magnetic bearing properties without using large bias fluxes.

Herzog and Bleuler [44] proposed the use of H^{∞} control to achieve required stiffness over wide bandwidth, and Fujita et al. [45], seeking a robust control design, implemented H^{∞} control using a commercial digital signal processor. Experiments indicated that the system was highly stable when subjected to step disturbances.

Ueyama and Fujimoto [46] physically measured the iron losses due to hysteresis and eddy currents by monitoring the coastdown of a rotor suspended in magnetic bearings, at different values of coil current, and propose an empirical equation to represent these losses.

Zhang et al. [47] describe a magnetic bearing application in which the rotor is a thin flexible shell, and discuss the advantages of individual magnet control versus control of opposing magnet pairs. They conclude that improved damping is possible using the individual magnet control. The authors speculate that the method will also be advantageous in suspending travelling metal sheets.

Stability of a suspended rotor was considered by Chen et al. [48], but as in previous such analyses, the representation of the magnetic forces is based on a linearized model.

Of particular interest in the context of the present project, Satoh et al. [49] examined a self-excited vibration of a suspended rotor in a flexible structure. The authors concluded that interactions between the mechanical structure and nonlinearity of the electromagnets led to a vibration with two frequency components.

A recent meeting devoted primarily to magnetic bearings was ROMAG'91, organized by the University of Virginia and held in Alexandria, VA in March 1991. In addition to considering applications in turbomachinery, some presentations also dealt with use of magnetic suspension in vibration isolation, particularly in applications related to space experimentation [50, 51], although one paper presented a digitally controlled magnetic suspension and vibration isolation system for optical tables [52].

With regard to magnetic bearings for turbomachinery, a number of applications were discussed, ranging from canned pumps to gas turbine engines [53] and rocket engine turbopumps [54].

Again, considerable emphasis was placed on control aspects, with papers devoted to the effects of sensor location [55], effects of amplifier design [56] and the general controllability of flexible rotors [57].

Subsequent meetings have explored a number of these aspects in greater detail. These include the Third International Symposium on Magnetic Bearings [58], and Mag '93 [59]. While the papers in these meetings address progressively more sophisticated control strategies, in much of the work presented, variations on a one-dimensional force model are used.

2. TECHNICAL FINDINGS: Analytical/Numerical Modeling

The objective of the modelling is to calculate the force exerted by the magnets on a journal in the case of steady currents through the coils. The techniques needed for this computation can also be applied to calculation of force in the dynamic case if the problem is assumed quasi-static in a magnetic sense. It is expected that this will be appropriate in most magnetic bearing applications, since the principal requirement for this assumption is that the frequencies of current and field variations do not approach radio frequencies. Some correction may be necessary to account for eddy current effects, which are neglected in the present work, if these methods are applied to the rotating shaft case.

The results of this section are also described in the Ph.D. thesis of Xia [60].

2.1 Fundamental Principle

The principle of force calculation is that the force component in a given direction is equal to the negative of the rate of energy change with respect to that coordinate, that is,

$$F_x = -\frac{\delta U}{\delta x} \tag{2.1.1a}$$

$$F_y = -\frac{\delta U}{\delta y} \tag{2.1.1b}$$

where the energy U is the energy associated with magnetic flux density contained in the magnetic circuit

$$U = \frac{1}{2} \int_V \vec{B} \; \vec{H} \, dV \tag{2.1.2}$$

where B is the magnetization and H is the magnetomotive force. If the linear approximation is made that $\vec{B} = \mu \vec{H}$, then this may be written.

$$U = \frac{1}{2\mu} \int_V B^2 \, dV \tag{2.1.3}$$

Development of the force model proceeded in two stages. The first method that was developed considered only the energy in and near the air gaps, approximating the metals as infinitely permeable. This method is referred to subsequently as the air gap method. It does account for nonuniform gap geometry as well as nonuniform distribution of flux within the gaps. The second method, referred to below as the full magnet method, includes the energy in the metal of the magnet and a portion of the rotor as well as that in the gaps and nearby air regions. Nonlinear magnetization functions can be considered as long as they are single-valued.

Both methods rely on two-dimensional finite element calculations of flux distributions. Computations are performed for one magnet at a time, and interactions of flux loops of individual magnets are neglected.

2.2 Air Gap Method

A computer program was written that calculates the force exerted on the journal by a magnet having a steady current in its coils. The force is found by calculating the energy stored in the air gaps between the magnet and the journal, then performing a numerical perturbation to obtain a central difference of the energy change per unit position change. This gives the force in the direction of the perturbation.

The force for a magnet at an arbitrary location can be calculated. The calculation includes the following assumptions:

i. The permeability of the metal is infinite compared to that of the gaps, which is assumed equal to that of free space. This implies that all the energy is stored in the gaps.

ii. There is no flux leakage, but expansion of the flux lines beyond the gap edges is allowed.

iii. The coil current, therefore the MMF, is constant over a perturbation.

In an isotropic domain not containing currents, where time variations are only of low frequency, the magnetic field can be represented as the gradient of a scalar field $\phi(x,y)$.

The energy contained in the domain is given by Equation (2.3) above where the flux density B is given by

$$\vec{B} = -\nabla\phi \tag{2.2.1}$$

and the potential ϕ satisfies the governing equation

$$\nabla^2\phi = 0 \tag{2.2.2}$$

with the boundary conditions

$$\frac{\partial\phi}{\partial n} = 0 \text{ on free boundaries} \tag{2.2.3}$$

and, because of assumption (i) above

$$\phi = \Phi_1 \text{ on pole face 1}$$
$$\phi = \Phi_2 \text{ on pole face 2} \tag{2.2.4}$$
$$\phi = 0 \text{ on journal surface}$$
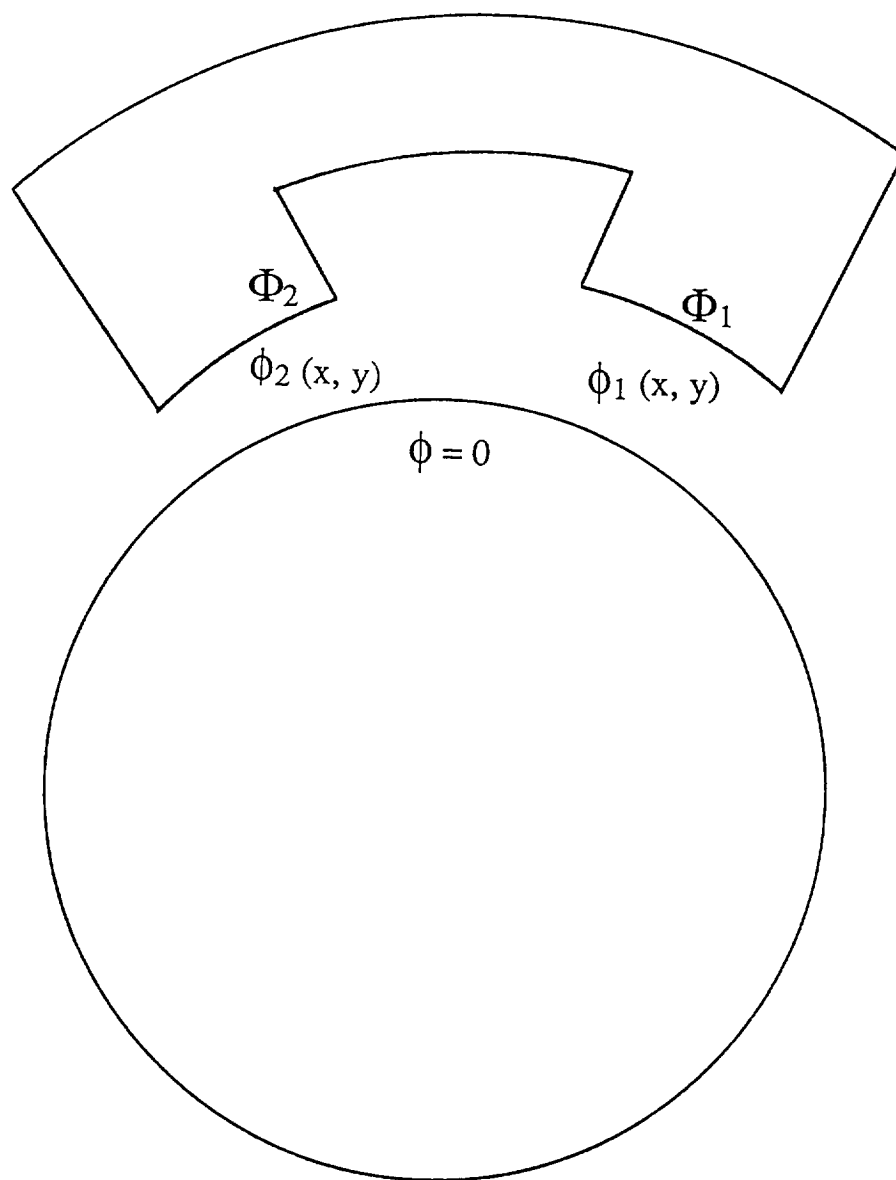
as shown in Figure 2.2.1.

Figure 2.2.1   Boundary conditions for numerical solution of magnetic potential.

Initially the boundary values of ϕ on the pole faces, Φ_1 and Φ_2, are not known, but must be determined in relation to the datum of $\phi=0$ on the journal surface. The problem is made tractable by the fact that the governing equation is a linear one, so that the values of ϕ internally are determined within a multiplicative constant even for an arbitrary choice of boundary condition values. The fact that the flux must be the same through the two gaps allows the ratio

$$\kappa = \frac{\Phi_2}{\Phi_1} \qquad (2.2.5)$$

to be determined. Then the fact that the difference between the two potentials is the magnetomotive force,

$$\Phi_1 - \Phi_2 = \zeta \qquad (2.2.6)$$

allows determination of the actual surface potentials. The variables are nondimensionalized so that $\Phi_1 = 1$. The procedure is as follows:

a. At an unperturbed position A, start with $\Phi_1 = 1$, $\Phi_2^* = 1$. An asterisk represents an initial guess or a calculated value based on an initial guess. Later the ratio

$$\kappa = \frac{\Phi_2}{\Phi_1} = \frac{\Phi_2}{\Phi_2^*} \qquad (2.2.7)$$

will be found.

b. Solve for the distribution of ϕ in each gap based on these boundary conditions: ϕ_1, ϕ_2^*. Note that $\phi_2 = \kappa\phi_2^*$.

c. Calculate the resulting flux density distributions and the energy stored in each gap, plus the flux through each pole face

$$\gamma_1 = \int_{A_1} \frac{-\partial\phi_1}{\partial n} \, dA \qquad (2.2.8)$$

$$\gamma_2^* = \int_{A_2} \frac{-\partial\phi_2^*}{\partial n} \, dA = \frac{1}{\kappa}\gamma_2 \qquad (2.2.9)$$

d. Since the actual dimensionless fluxes are the same magnitude ($\gamma_1 = -\gamma_2$), κ is uniquely determined as the ratio

$$\kappa = \frac{\gamma_1}{\gamma_2^*} \qquad (2.2.10)$$

e. The potential distribution in gap 2 is given by $\phi_2 = \kappa\phi_2^*$ and the flux density is related to the * distribution by the same ratio. The energy is therefore given by

$$\sigma_2 = \kappa^2 \sigma_2^* \qquad (2.2.11)$$

f. Note that the imposed mmf is the difference between the pole potentials

$$\zeta = \Phi_1 - \Phi_2 = (1 - \kappa)\Phi_1 \qquad (2.2.12)$$

or, since $\Phi_1 = 1$,

$$\zeta = (1 - \kappa) \qquad (2.2.13)$$

(If dimensional values are needed, the factor $(1 - \kappa)$ is also the ratio between mmf in amp-turns and the dimensional potential on pole face 1). For now, use the nondimensional ζ.

g. At a perturbed position B, start with $\Phi_1^* = 1$, $\Phi_2^{**} = 1$. The potential on pole 1 is now a guess, since only the mmf was maintained constant during the perturbation. Φ_2^{**} is a "double" guess because it is based on Φ_1^*

h. Use a procedure analogous to steps b through f to find the ratio

$$\lambda = \frac{\Phi_2^*}{\Phi_1^*} \qquad (2.2.14)$$

i. Use the calculated mmf ζ from step f above, which is still equal to the difference between the pole potentials, to write

$$\Phi_1 = \frac{\zeta}{1-\lambda} \qquad (2.2.15)$$

and define

$$\alpha = \frac{\Phi_1}{\Phi_1^*} = \frac{\Phi_2^*}{\Phi_2^{**}} \qquad (2.2.16)$$

j. Using the logic of step e

$$\sigma_1 = \alpha^2 \sigma_1^* \qquad (2.2.17)$$

and

$$\sigma_2 = \alpha^2 \lambda^2 \sigma_2^{**} \qquad (2.2.18)$$

k. Stored energies have now been calculated at position A and position B. A forward difference analogue to the force in the direction from A to B is therefore

$$F_{AB} = \frac{(\sigma_1 + \sigma_2)_B - (\sigma_1 + \sigma_2)_A}{\Delta x_{AB}} \qquad (2.2.19)$$

l. To return to dimensional values, use the factor $(1-\kappa)$ from step f above.

Although the description above uses a forward difference, a better result is obtained using a central difference, which is the method actually employed. This requires 4 perturbations to find the vector components of force in the x and y directions.

Although the calculation of forces with the inclusion of three dimensional effects, flux leakage and hysteresis will involve significantly more computations, the overall approach should be the same as that used above. It may be necessary to use a vector magnetic potential, and the assignment of boundary conditions will be considerably more complex, however.

2.3 Air Gap Method: Computer Program

The algorithm above is embodied in a FORTRAN computer program, GAPFOR1, which uses the finite element method for calculating the magnetic potential in two dimensions. For a given journal position the program calculates the gap height as a function of angular location and generates a finite element mesh for each gap. Flux fringing is allowed by extending the finite element domain beyond the edges of each pole face. Then the journal position is perturbed four times, first with positive dx and negative dx, then with positive dy and negative dy. At each step the mesh is regenerated and the energies are recalculated.

To achieve rapid computational speed and efficiency, a dedicated finite element program was written for this application. It includes a grid generation routine as well as a banded gauss elimination solver for the assembled equations. A listing of the algorithm is given in Appendix A.

2.4 Air Gap Method: Results

2.4.1 Test Case 1: parallel surfaces

The algorithm was tested by calculating the force in the case of a magnet and part having parallel faces, with no flux fringing allowed, shown in Figure 2.4.1. In this case an analytical expression approximates the force per unit depth of pole face as

$$F = \frac{\mu_g A_g N^2 i^2}{h_g^2} \qquad (2.4.1)$$

where
|		
F	=	force
μ_g	=	magnetic permeability of the gap
Ag	=	area of the gap
N	=	number of magnet coils
i	=	current
h	=	gap height

The computer program was run for the slightly different case of an annular clearance between a shaft and a magnet, corresponding to the case of a centered journal. For the sample case the equation gives F = 22.4 N, while the program predicts F = 20.9 N.

2.4.2 Test Case 2: Effects of element size and fringing

The algorithm was used to calculate the force from a single magnet acting on a journal, as in the experimental apparatus. The dimensions are given in Table 2.4.1. The effects of variations in element size were examined along with the effects of allowing fringing to occur by extending the domain of solution circumferentially beyond the ends of the pole faces as shown in Figure 2.4.2. Table 2.4.2 shows the results of these variations. The column A displays results without fringing, while column B shows results with fringing allowed in a domain extended 10% of the width of the pole face to either side. The results indicate that without fringing, the effect of decreasing the element size is small, but when fringing is to be accounted for, the element size is a significant parameter. The results of column B suggest that when fringing is allowed, the predicted force is smaller than when fringing is not considered. This might be expected, since fringing decreases the average flux density by increasing the volume of the energy storage area. Since the energy is related to the square of the flux density, an overall decrease in stored energy and in force seems appropriate.

2.4.3 Forces from one magnet of a bearing

The computer program has been used to predict the forces from one magnet acting on the journal at various positions of the journal within the clearance space. Half of the entire clearance space is mapped, since all positions of the journal with respect to a single
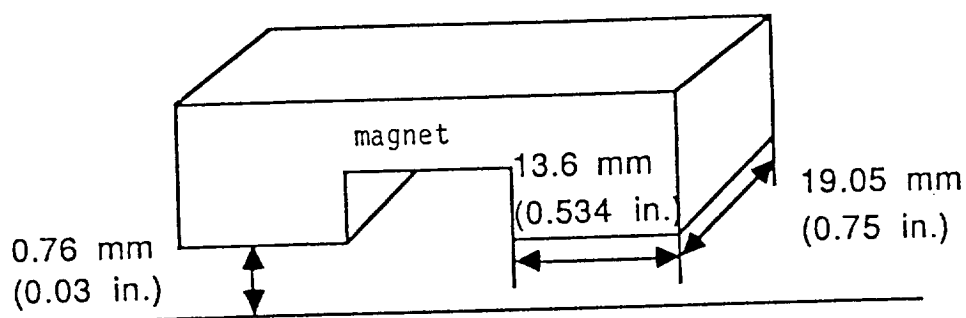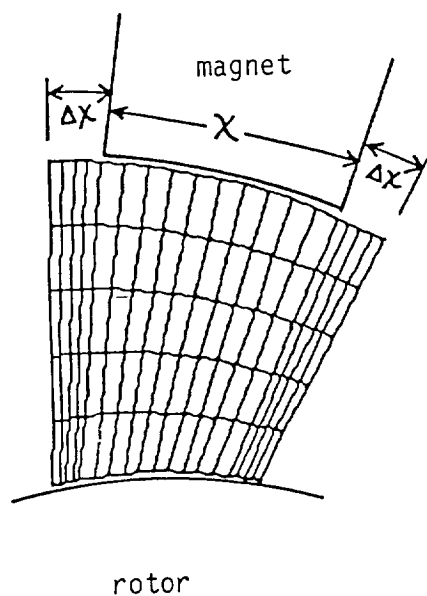
current: i=1 A
turn: N=200+200
magnetomotive force: mmf=400 turn-A

Analytical solution for a flat surface
by approximate equation
F_y=22.4 N (5.04 lb)

Numerical solution for annular clearance
F_y=20.9 N (4.70 lb)

Figure 2.4.1   Comparison of numerical and approximate analytical solutions for one
magnet.

magnet

GRID

n=10 circumferential divisions
m=5 radial divisions

ΔX=0.2X

(to allow fringing)

rotor

Figure 2.4.2 Sample grid (radial dimension exaggerated).

Pole depth	10.1 mm	0.750 in
Pole width	13.6 mm	0.534 in
Gap height	0.76 mm	0.03 in
Anglebetween poles	40°	
MMF	400 A-T	

Table 2.4.1 Parameters for sample calculations.

magnet can be represented in terms of positions in this half space. Figures 2.4.3 and 2.4.4 show maps of force versus x,y position. The magnet is the upper vertical magnet, and a steady

Attraction Force from One magnet Using Finite Simplex Method

Design Parameters:
R = 38.1 mm
c = 0.76 mm
L = 19.05 mm

$\theta_1 = 60^o$, $\theta_2 = 80^o$, $\alpha = 20^o$

Case	m	n	elements	global matrix	A No Fringing Fy	B With Fringing Fy
1	8	20	320	189 x 11	20.925	21.220
2	8	70	1120	639 x 11	20.927	20.635
3	8	150	2400	1359 x 11	20.927	19.881

Table 2.4.2 Effects of element size and fringing

current of 1 ampere through the coils is used. The dimensions and other parameters are the same as those of the experimental apparatus described below. The figure indicates that the force in the y-direction varies between 0 and 132 N as the journal is moved along the y axis. When the journal is also given an x-direction eccentricity, the y-force decreases significantly. Except at x=0, there is also a small x component to the force, shown in Figure 2.4.4.

In a subsequent section the predicted forces are compared with those measured in an experimental apparatus.

2.5 Full Magnet Method

Unlike the previous method the present section considers the magnetic flux within the metals in addition to that in the air gaps. This allows the examination of effects such as local magnetic saturation of the materials and residual magnetization. This approach presents two categories of difficult problems, however. The first category arises from consideration of finite permeability, which in the general case is a nonlinear and multivalued function of field intensity. The second is related to boundary conditions on magnetic field quantities, and a third concerns the source, or current density, term of the
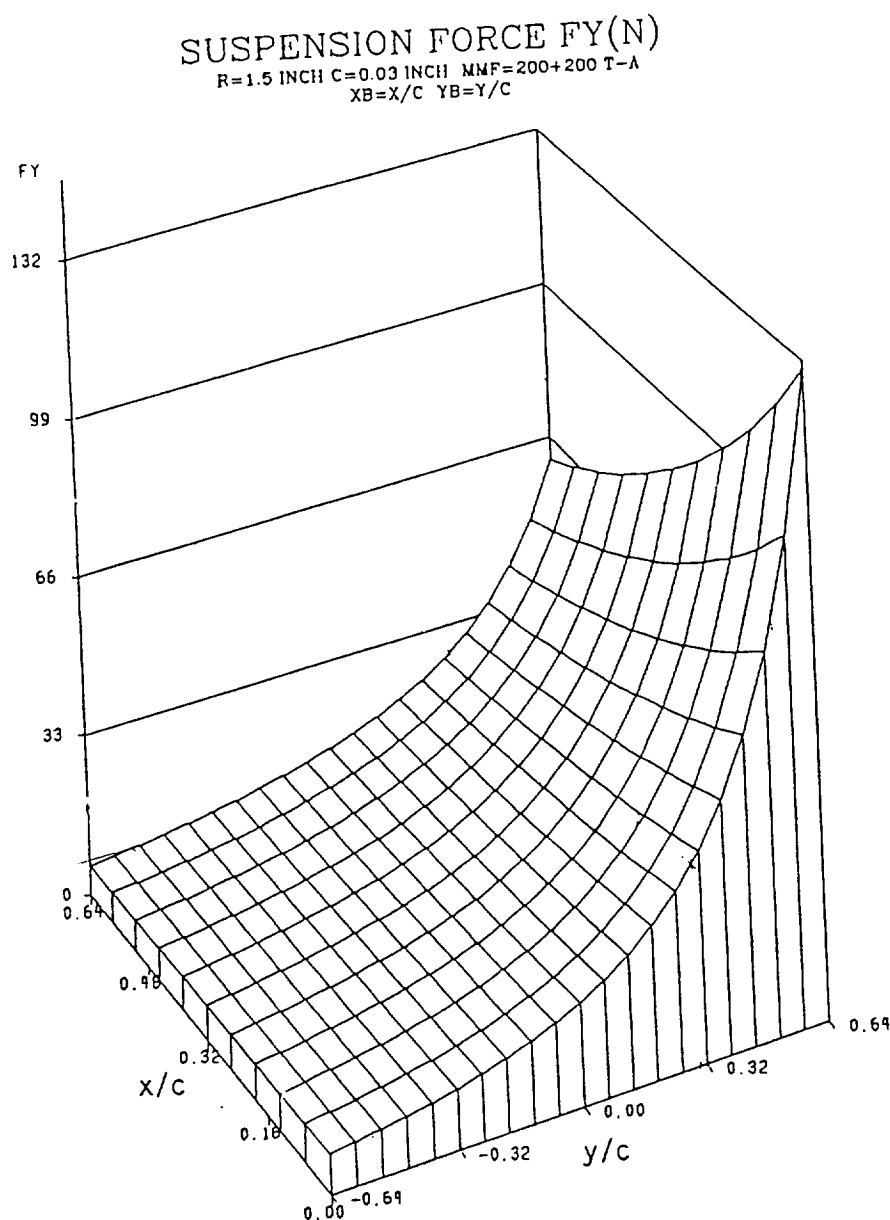
Figure 2.4.3   Vertical force of attraction from upper magnet with 1A current, by numerical calculation.

SUSPENSION FORCE FX(N)
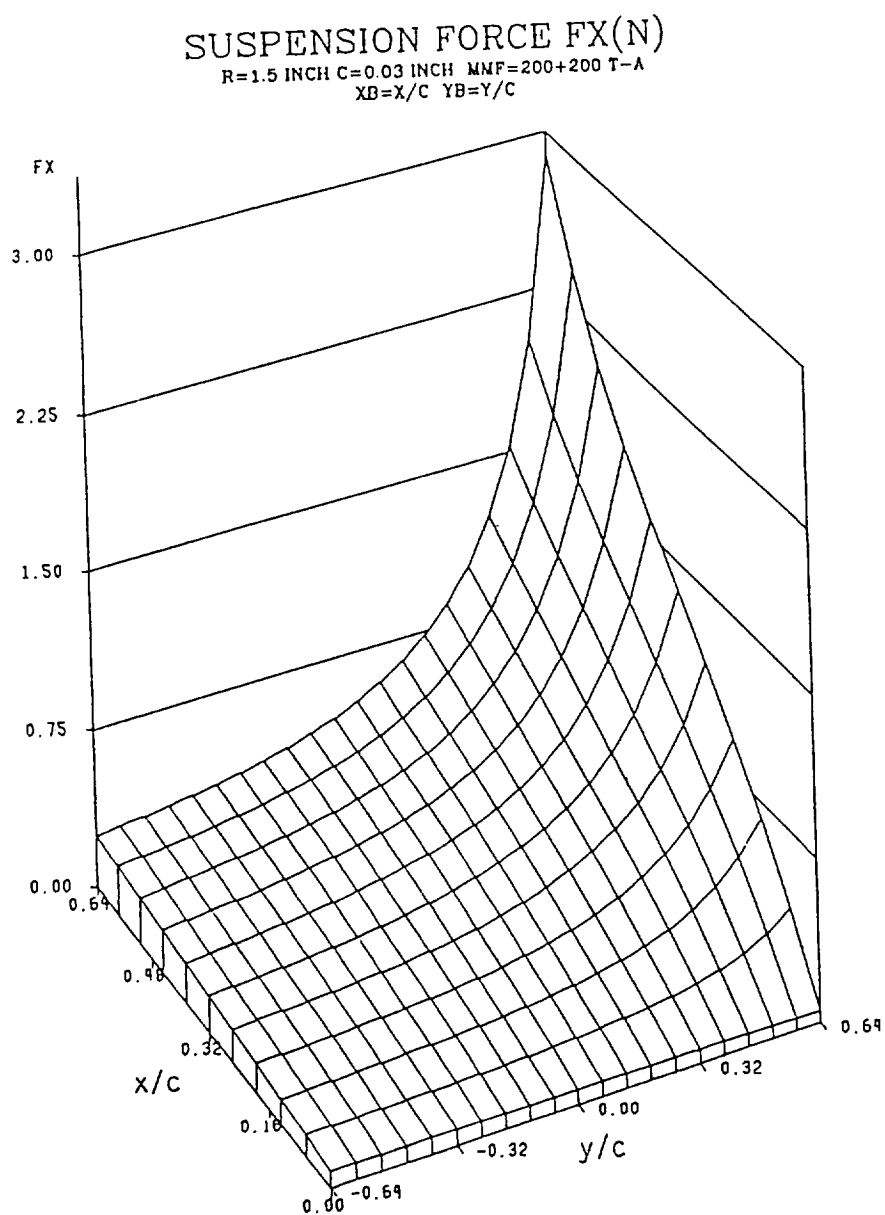R=1.5 INCH C=0.03 INCH MNF=200+200 T-A
XB=X/C YB=Y/C

Figure 2.4.4   Horizontal force of attraction from upper magnet with 1A current, by
numerical calculation.

governing equations. First the forms of the differential equations will be presented and then approximations and assumptions will be introduced to simplify the equations.

2.5.1 Differential Equations in 3-D

In the general three-dimensional case, the flux density $\vec{B}$, the field $\vec{H}$ and the current density $\vec{J}$ are related by

$$\nabla \times \vec{H} = \vec{J} \tag{2.5.1}$$

$$\vec{B} = \mu\vec{H} \tag{2.5.2}$$

$$\nabla \cdot \vec{B} = 0 \tag{2.5.3}$$

where

$$\mu = \mu(|\vec{H}|, t) \tag{2.5.4}$$

Assuming that a solution for $\vec{B}$ in all parts of the domain can be found, the method of force calculation described in Section 2.1 can be applied.

2.5.2 Two-dimensional Equations

For the next phase of the analysis, the solution domain is simplified from three dimensions to two dimensions. Successful finite element solutions for magnetic flux have been obtained in two dimensions (Chari and Silvester [61]) for cases of single valued permeability by making use of Equation (2.5.3) to write the flux density, or magnetization, vector as the curl of a vector magnetic potential

$$\vec{B} = \nabla \times \vec{A} \tag{2.5.5}$$

This equation is valid in three dimensions, but is more easily applied if the magnets and rotor are treated as infinitely long and the current is assumed to pass only in the coils of the magnets. Under these approximations both the vector potential and the current density have only one component (z), and Equations (2.5.1), (2.5.2) and (2.5.5) can be combined to write

$$\frac{\partial^2 A}{\partial x^2} + \frac{\partial^2 A}{\partial y^2} = \mu J \tag{2.5.6}$$

where A and J are magnitudes of the corresponding vector quantities. For given μ and J distributions and appropriate boundary conditions, this Poisson's equation can be solved by finite difference or finite element methods. In the present work the current density is assumed uniform within the coil windings and zero elsewhere. The coils are treated as isotropic solids, as shown in Figure 2.5.1.
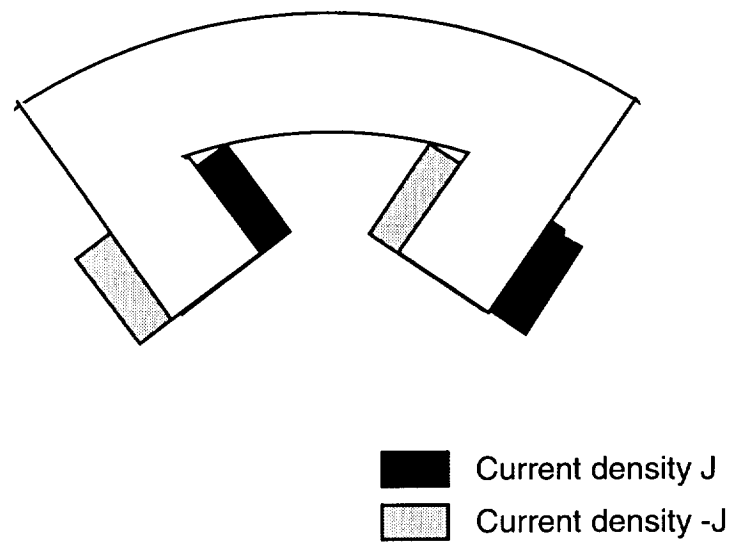
Current density J
Current density -J

Figure 2.5.1   Modelling of coils with uniform current density

At this point the two most difficult problems arise; determination of permeability and assignment of boundary conditions.

2.5.3 Permeability

In general, the permeability of a ferromagnetic material is a nonlinear, multivalued function of field intensity and, through the history of the field strength, of time. The magnetization of the material is often represented by the hysteresis loop (a) of Figure 2.5.2, adapted from Cullity [62] which shows the relationship between H and B for a particular time variation of H, namely a cyclic completely reversed variation that is sufficiently strong to cause the material to be saturated alternately in both directions. Although this figure gives some qualitative insight into the material's behavior, it does not fully characterize the response of a magnet to other types of time varying excitations. In fact, for an excitation H that does not fully saturate the material, the curve traced by the B function might take one of several other forms shown in Figure 2.5.2, depending on the material and the range of H.

For analytical purposes, it is most convenient to assume a linear variation of B with H, or a constant permeability ((a) of Figure 2.5.3). For this assumption the solution of Equation (2.5.6) is straightforward and obtainable by a direct method. Next in complexity is the consideration of B as a nonlinear but single valued function of H, as in (b). An iterative method is now required for the solution. In addition, the calculation of the energy in the magnetic field, Equation (2.1.2), requires integration using the actual magnetization function. The most general case, that where B can take on an infinity of values, depending on the history of H, is not considered in the present work. Therefore, in this report calculations are limited to single-valued functions of B vs. H.

2.5.4 Boundary Conditions

Far away from the magnets and rotor it is reasonable to assume that the magnetic flux intensity B is zero, which implies that

$$\frac{\partial A}{\partial x} = \frac{\partial A}{\partial y} = 0 \qquad (2.5.7)$$

It is feasible to extend the solution domain far enough to approximate this condition. Numerical studies of the effects of domain size were made as part of the analysis, and it was noted that the penetration of magnetic flux into the rotor is limited. A sample discretization is presented in Figure 2.5.4, where the boundary conditions given by
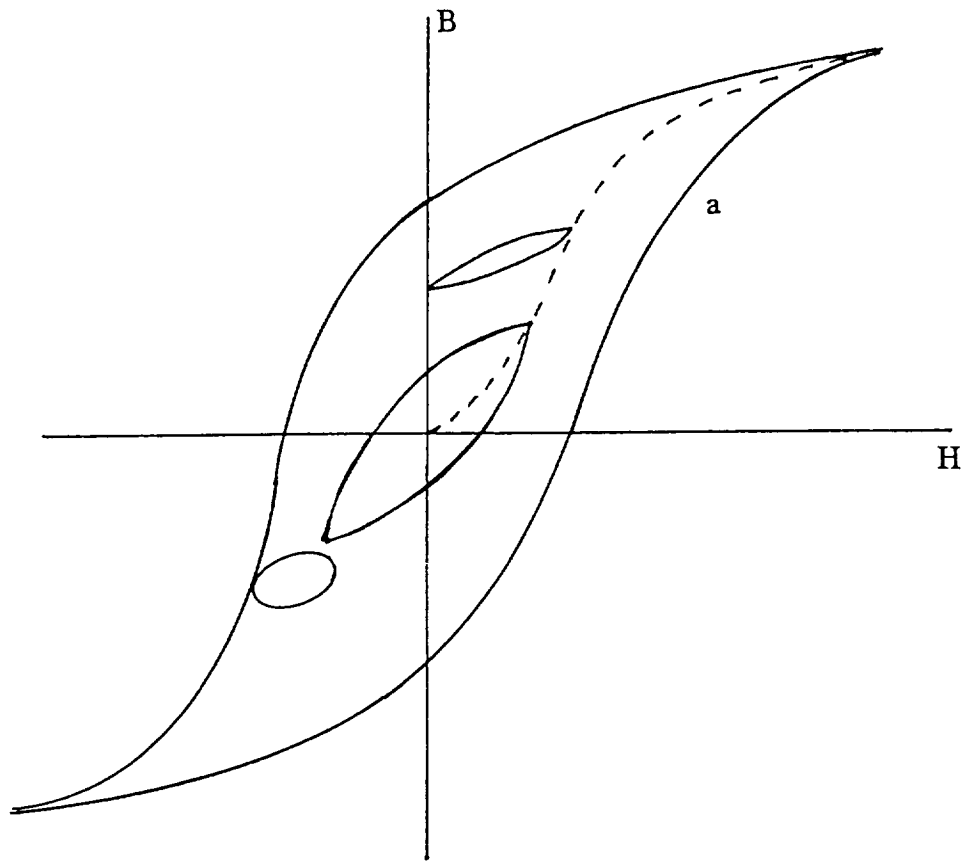
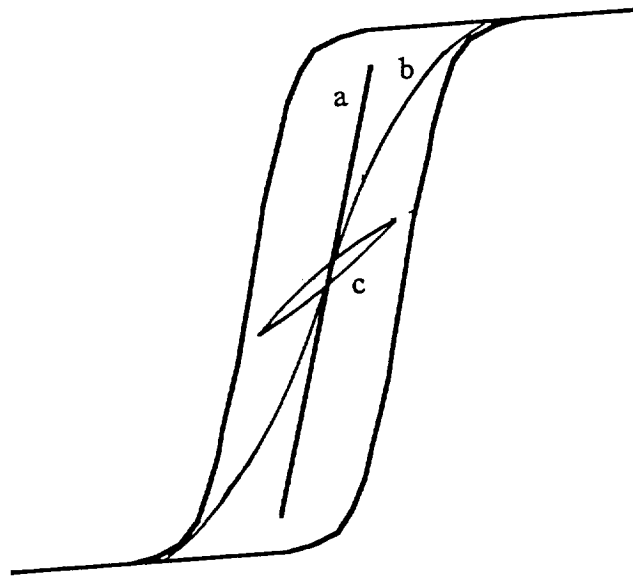Figure 2.5.2   Possible B-H loops in a real ferromagnetic material.

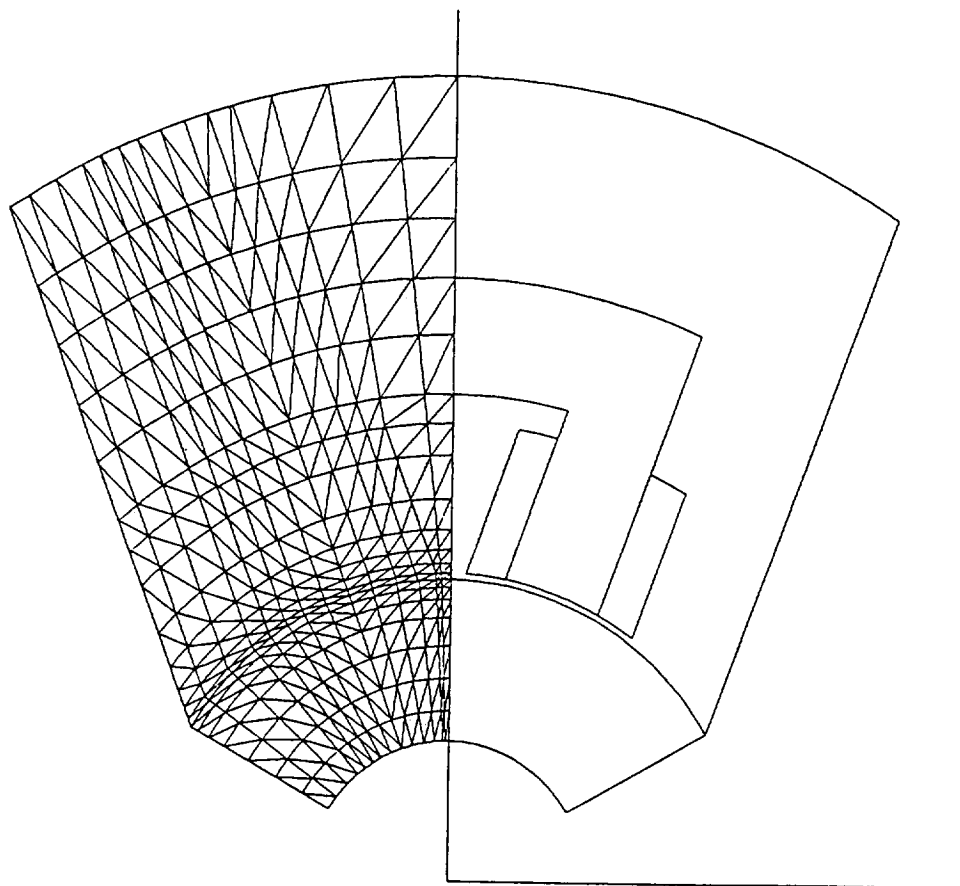Figure 2.5.3   Alternative models for magnetization characteristic.

Figure 2.5.4. Example of modified direct discretization of portion of domain.

Equation (2.5.7) are applied at an inner and an outer radius, as well as on the radial lines defining the edges of the domain.

2.5.5 Discretization

Parametric studies (Table 2.5.1) using the linear FEM solution of Section 2.3 indicate that in the linear case a discretization approximately as fine as 4 X 30 (240 elements) is needed in each gap to ensure that the force is not significantly affected by the grid size. In the nonlinear case an even finer grid may be needed to capture the distribution of flux near the metal surfaces. The region in and near the gap will require the most finely spaced grid and thus the bandwidth of the global matrix is largely determined by the gap spacing. Since the overall domain is large it is important to use a minimum number of elements in the gap. The principal difficulty is in numbering the nodes of the fine grid in the gap region so that connectivity is established between the fine grid elements and the adjacent coarser grid.

There are three primary considerations in choosing a discretization method: versatility in modelling different geometries; efficiency in computation; and ease of use. The easiest method is a direct discretization which would produce a fine grid over the entire annular arc sector that contains the gap. This method results in fine discretization in non-critical as well as critical regions, however, and leads to an unnecessarily large bandwidth. Some modification of this method may be used, as indicated in Figure 2.5.4, but the difficulty in automating the node numbering for optimized connectivity appears severe. Several more advanced methods from published literature were examined. These include automatic methods based on curvilinear coordinates as described by Ziekiewicz and Phillips [63], or the superelement method of Liu and Chen [64]. An automatic variable density method described by Cavendish [65], illustrated schematically in Figure 2.5.5, allows the user to specify the grid density in different regions. This may be the most flexible of the available methods, but it requires complex programming to be fully automatic (manual intervention was required in generating Figure 2.5.5). Methods of automatic bandwidth reduction by node renumbering [66] may be applied to one of the simpler methods to make it competitive with a complex scheme such as that of Cavendish.

In terms of the overall solution algorithm for computation of flux, it was decided to use the direct iteration method for determination of the distribution of permeability in the metals, regardless of the specific type of permeability model to be used.
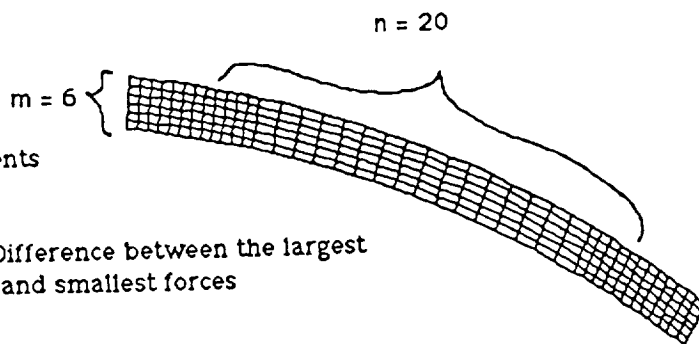
Two options were considered for the actual force calculation. One is based on the method already used in the linear FEM case; that is, a set of direct perturbations of the shaft

I = 1 A
x = 0.0 in.
y = -0.024 in.
Extra boundary 20 %
10 % with the fine elements
within the pole area

n = 20

m = 6 {

m x n	Force (N)	Difference between the largest and smallest forces
2 X 5	7.334	
2 X 15	6.557	1.353
2 X 20	6.361	
2 X 30	5.981	
4 X 5	7.397	
4 X 15	6.854	0.883
4 X 20	6.729	
4 X 30	6.514	
6 X 5	7.409	
6 X 15	6.933	0.713
6 X 20	6.845	
6 X 30	6.696	
8 X 5	7.413	
8 X 15	6.964	0.63
8 X 20	6.894	
8 X 30	6.783	
2 X 5	7.334	
4 X 5	7.397	0.079
6 X 5	7.409	
8 X 5	7.413	
2 X 30	5.981	
4 X 30	6.514	0.802
6 X 30	6.696	
8 X 30	6.783	

Table 2.5.1   Divisions and parametric study of grid size effects in gap region.
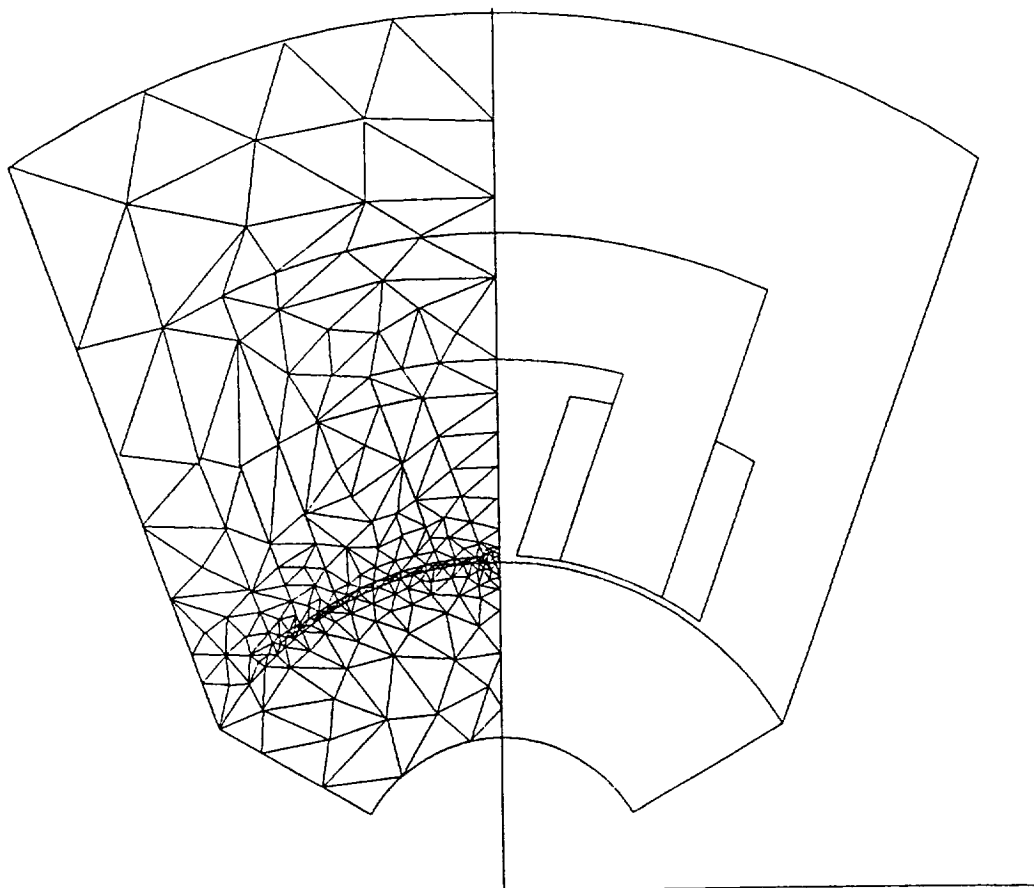
Figure 2.5.5. Example of variable density grid after Cavendish.

position followed by calculation of the forces based on changes in energy using a central difference approach, including the energy change due to flux distribution changes during the perturbation. In the case of larger domains having nonlinear permeability the computation time for this method would be large. The second method, which was actually adopted, holds the flux distribution constant and calculates the energy change due to the area changes of all the elements that are distorted during a perturbation. This method is much faster than the full numerical perturbation scheme, and has been shown [67] to have high accuracy.

2.6   Results of Linear Calculations

In Section 2.2, a method was described to calculate forces using a linear method, in which the air gaps only are treated and the flux distribution is calculated by the Laplace equation for the scalar magnetic potential. Results of calculations using this method were presented in Section 2.4. In Section 2.5, the linear method was extended to include regions of differing permeabilities, using the Poisson equation for flux distribution. The present section presents results of these calculations, along with experimental measurements. For a description of the experimental apparatus and methods, refer to Section 3. In that section, some of the calculations presented here will be shown again. The work presented in this section is also described in the paper "Determination of Forces in a Magnetic Bearing Actuator: Numerical computation with Comparison to Experiment," by Knight, Xia, McCaul and Hacker [68]. Only the Conclusion section of the paper is reiterated here.

Conclusion (of Reference [68])

Calculated and measured forces in a magnetic journal bearing actuator are presented. The calculations are based on two-dimensional finite element solutions of the magnetic flux distribution in both metals and free space. The measurements were made in an apparatus designed for direct force measurement by strain gage transducer assemblies supporting a non-rotating journal.

Comparison of numerical calculations with one-dimensional magnetic circuit theory indicates that as the gaps are made non-uniform by the approach of the journal to the magnet, two dimensional effects become significant and the two methods predict different forces. At relative permeabilities above 10^4, changes in permeability of the metal have little effect, but at lower

permeabilities the available force decreases dramatically with decreasing permeability.

Also predicted is that the effect of finite metal permeability is more strongly felt at small gaps than at large gaps.

The calculated principal attractive forces agree well with the measured forces when a relative permeability $\mu_r = 500$ is used, corresponding to highly saturated material. The measured normal forces, however, are higher than the calculated values even when a high permeability is used.

It seems reasonable that the permeability distribution in the metal is non-uniform. Future work is planned in which distributions of permeability will be examined.

After the submission of this paper, the numerical method was extended to model nonlinear distributions of permeability.

2.7 Nonlinear Force Calculation

An algorithm was developed to calculate the force exerted on a rotor by a magnet, considering the effects of a nonlinear magnetization characteristic for the rotor and magnet material. It uses the finite element method to solve the equation for vector magnetic potential in two dimensions. The force calculation part of the algorithm is based on the fast solution method proposed by Coulomb [67]. There are three primary operations involved in the force calculation: (a) modelling of the magnetization curve of the magnet and rotor material, (b) iteration for the distribution of vector magnetic potential consistent with the nonlinear permeability, and (c) application of the force calculation algorithm. These operations are outlined briefly below, but more complete descriptions of the methods are given in Appendix C.

This work is also described in a paper, "Forces in Magnetic Journal Bearings: Nonlinear Computation and Experimental Measurement," by Knight, Xia, and McCaul [69], presented at the Third International Symposium on Magnetic Bearings, Alexandria, VA, July 1992, and contained in the proceedings of that meeting.

2.7.1 Modelling of Magnetization Curve

For most of the calculations presented here, the magnetization function for silicon steel [62] has been used. Some calculations were also performed using an arbitrarily chosen function having sharp discontinuity in slope, to assess the effects of abrupt saturation.

The magnetization function of the steel is nonlinear but single-valued; that is it does not exhibit hysteresis. The function is represented by tabular data and is approximated by a cubic spline interpolation. At field intensities higher than 1200 A·t/m, the slope of the magnetization function is assumed to be the permeability of free space, μ_0. Figure 2.7.1 shows the actual magnetization data and the approximation.

For numerical calculations, a more useful representation of the magnetization function is that of Figure 2.7.2. The reluctivity of the material, H/B, or $1/\mu$, is plotted versus the square of the flux density. When this representation is used it is not necessary to calculate the field intensity at each location for every iteration, but only the flux distribution.

2.7.2 Calculation of Flux Distribution

The distribution of scalar magnetic potential, leading to the distribution of flux density, is calculated by the finite element method. The equation that models the potential is the nonlinear Poissons equation

$$\frac{\partial}{\partial x}\left(\frac{1}{\mu}\frac{\partial A}{\partial x}\right) + \frac{\partial}{\partial y}\left(\frac{1}{\mu}\frac{\partial A}{\partial y}\right) = J \qquad (2.7.1)$$

where A is the magnitude of the vector magnetic potential, which in the two-dimensional case has only one component, normal to the plane of the solution region. The flux density is related to the potential by

$$\overline{B} = \nabla \times \overline{A}. \qquad (2.7.2)$$

This relationship allows a convenient representation of flux density, since it implies that contours of constant A are also lines parallel to $\overline{B}$.

The source term J, current density, appears in those elements comprising the cross sections of the coils. The value of the total ampere-turns is divided by the nominal cross-section to arrive at this current density.

An iterative method is used to obtain a distribution that is consistent with the nonlinear magnetization function. The procedure is that recommended by Silvester [70], in which a Newton-Raphson iteration is applied to determination of the reluctivity. An initial approximation to the potential is made, then updated based on successive solutions of the Poissons equation for incremental changes in the A field that result from refinement of the reluctivity distribution.

When the flux distribution has been determined, the calculation of forces is performed using the method of Coulomb [67], in which only the energy changes in the distorted elements are considered during a virtual displacement. The method allows the force to be determined without multiple solutions for the flux distribution

Appendix C describes the numerical methods in more detail.

2.7.3 Results of Calculations

Calculations were performed based on the geometry of Figure 2.7.3, corresponding to the first experimental apparatus and the measurements described in [71]. The magnet under consideration is an upper vertical magnet, so forces in the y-direction are the principal forces, and forces in the x-direction are the normal forces. Also plotted in the figures are the results of the linear calculation described in previous reports and in [71]. The effect of saturation on the force is seen in Figure 2.7.4, which shows the attractive principal force as a function of the coil current, when the shaft is in a centered position with respect to the magnet pole faces. The gap between shaft and magnet poles is therefore constant at 0.03 inch. The dimensionless force is seen to increase with current, and below a current of 2.5 A (corresponding to 1000 A·t) the result of the nonlinear calculation is the same as that of the linear calculation. Above this value the force continues to increase, but at a much smaller rate than predicted by linear theory.

At current levels higher than 3 A the magnet material experiences saturation near the inner corners of the intersection between the pole legs and the magnet outer arc. As the current level is increased, the area of saturation expands across the cross section of the legs. Figure 2.7.5 shows those elements that have been saturated for the case of i = 3.5 A. At this level of MMF the area of saturation encompasses a complete layer of elements spanning the cross-section. For purposes of this plot, saturation is defined to correspond to a flux density of 1.4 T. At this point the slope of the magnetization function is assumed to be that of free space, so above this level of flux density the force can continue to increase with current, as indicated by Figure 2.7.4, but at a much slower rate.

For a given MMF the magnet may also experience saturation when the shaft is moved closer to the magnet. Such a displacement decreases the overall reluctance of the magnetic circuit by closing the gaps, and changes the gap shape as well. Figures 2.7.6 to 2.7.8 show the increase in number of saturated elements when the shaft is moved toward the magnet, for the constant current i = 2.0 A. Figure 2.7.6 corresponds to a shaft eccentricity of (X,Y) = (0, 0.5), which denotes a position on the magnet's axis of symmetry, half the distance from the center to the maximum possible eccentricity. There are two areas where elements are saturated; the inner corners of the horseshoe, and the part of the shaft near the inner edges of the pole faces. These edges are the points of closest proximity between the poles and the rotor. As the shaft is moved closer to the magnet the areas of saturation enlarge.   At an eccentricity of 0.6, Figure 2.7.7, the upper ends of the pole legs have been completely saturated, and the area of saturation at the rotor surface has expanded. As the eccentricity is further increased to 0.7, Figure 2.7.8 shows the saturation areas continuing to expand. The contour plot of Figure 2.7.9 reflects the saturation pattern. Comparison of
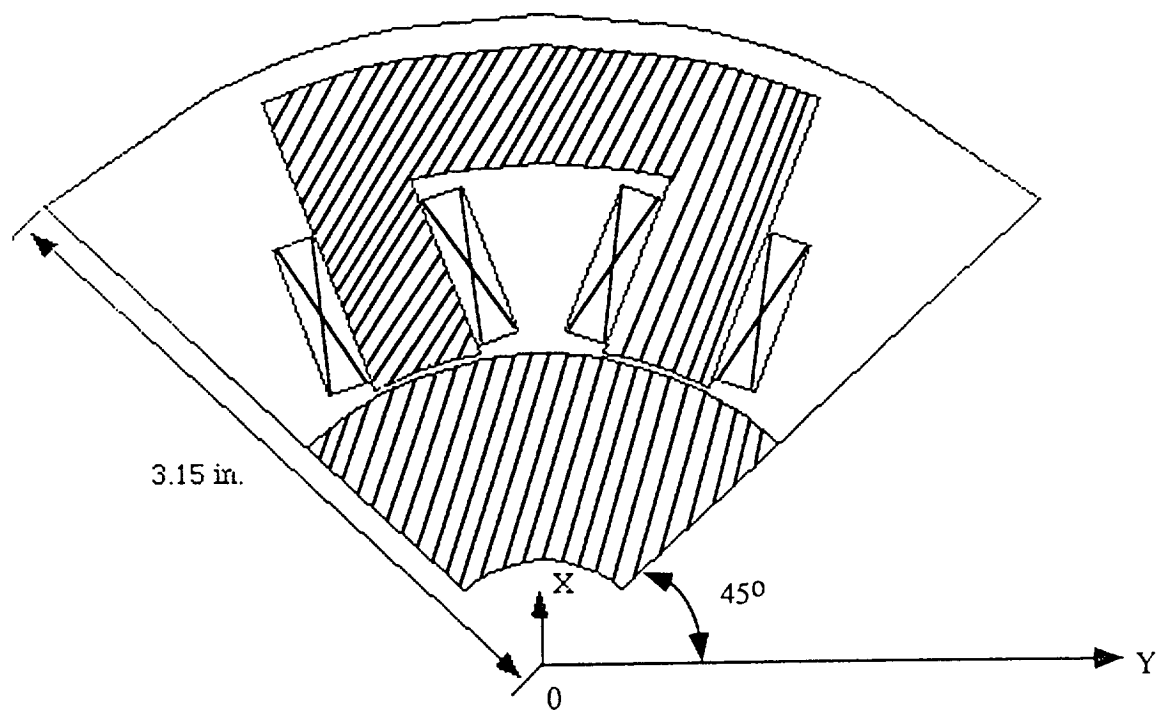
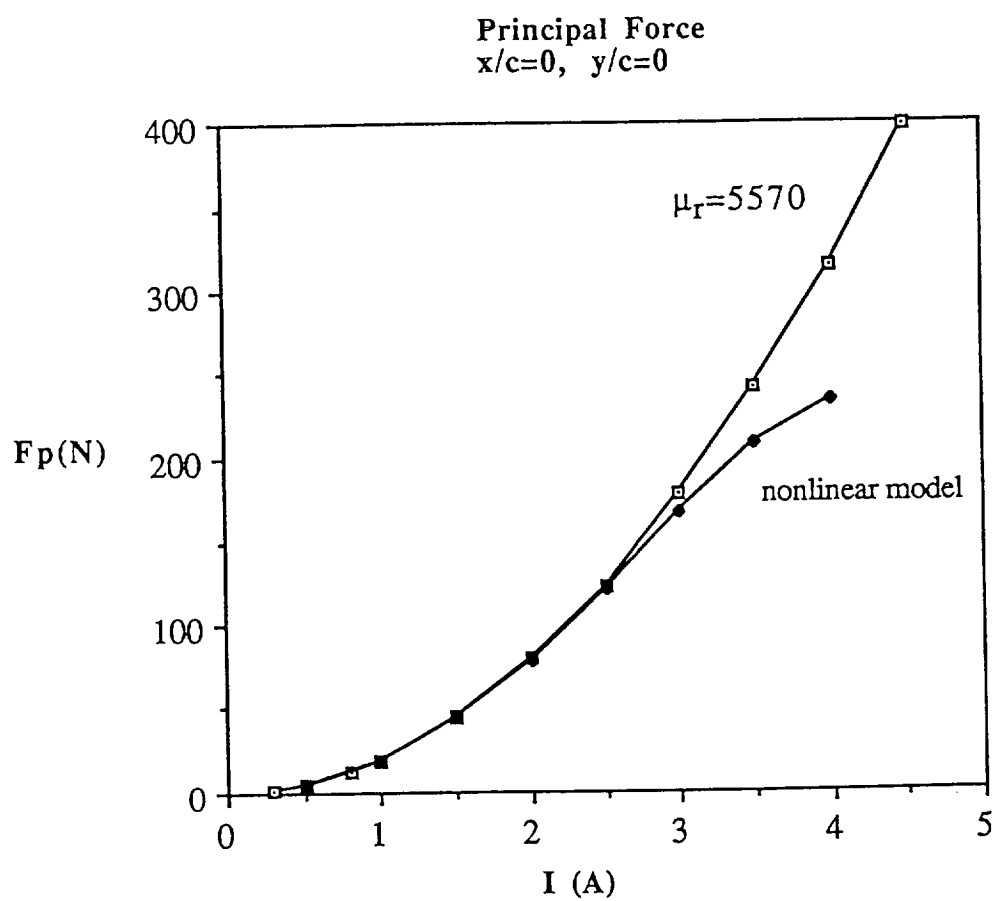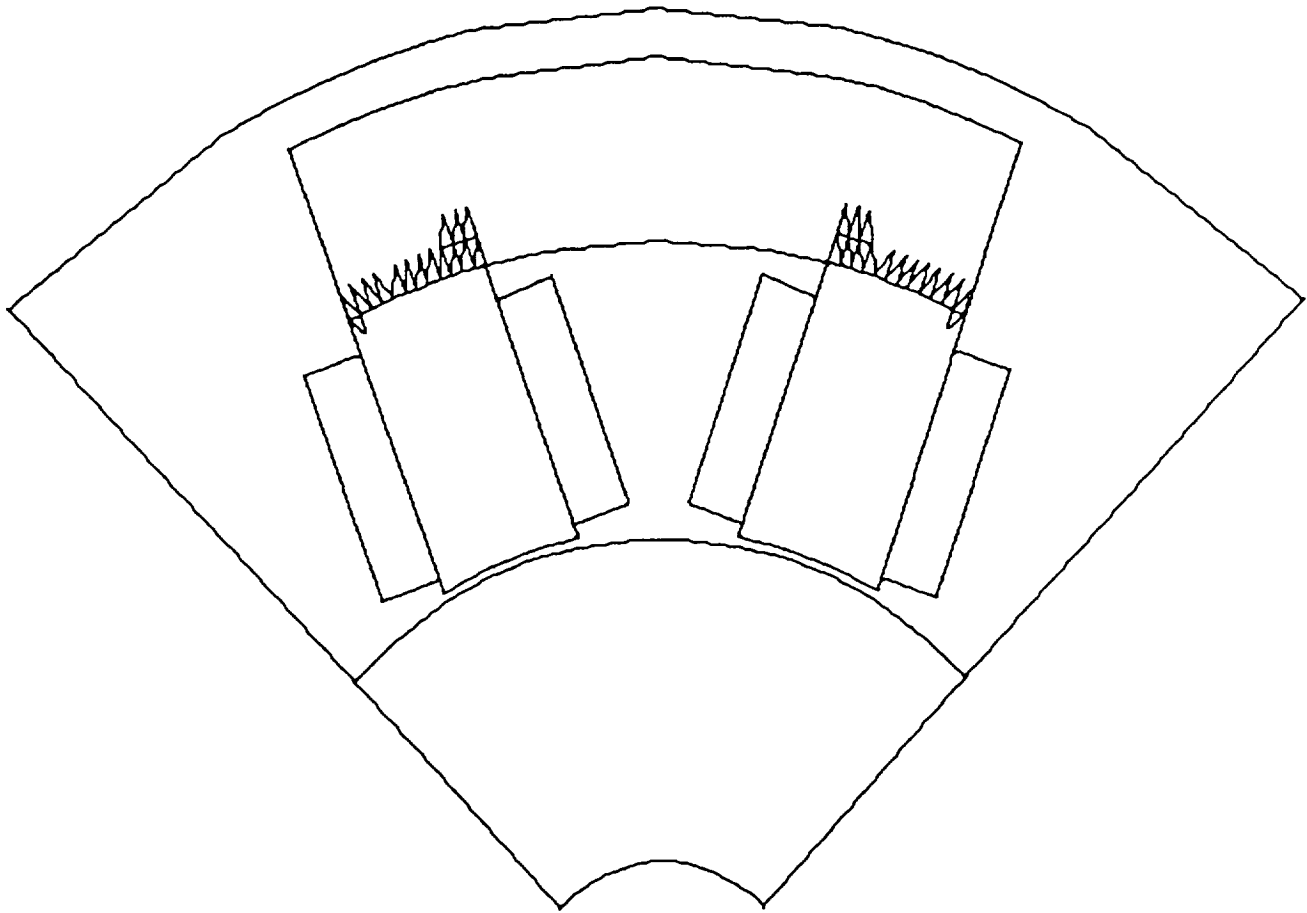Figure 2.7.3   Schematic of geometry for calculation.

Principal Force
x/c=0, y/c=0

Figure 2.7.4   Calculated principal force on centered shaft.

Saturated Elements

I	x/c	y/c	Fp(N)	Fn(N)
3.5A	0.	0.	208.35	0.0

Figure 2.7.5 Distribution of saturated elements at 3.5A current, centered rotor.

Saturated Elements
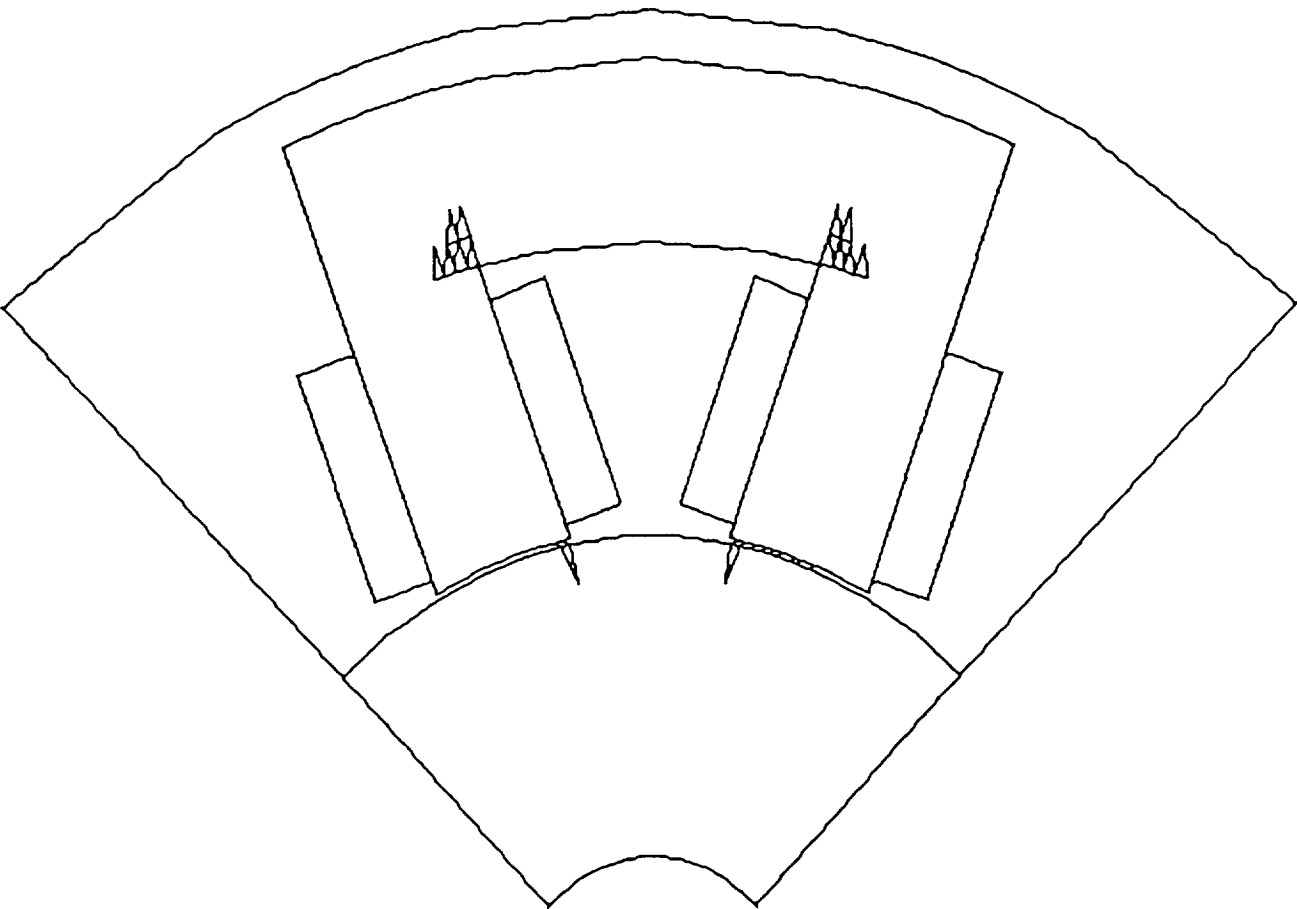
I	x/c	y/c	Fp(N)	Fn(N)
2A	0	0.5	239.34	0.0

Figure 2.7.6   Distribution of saturated elements at 2.0A current, with vertical
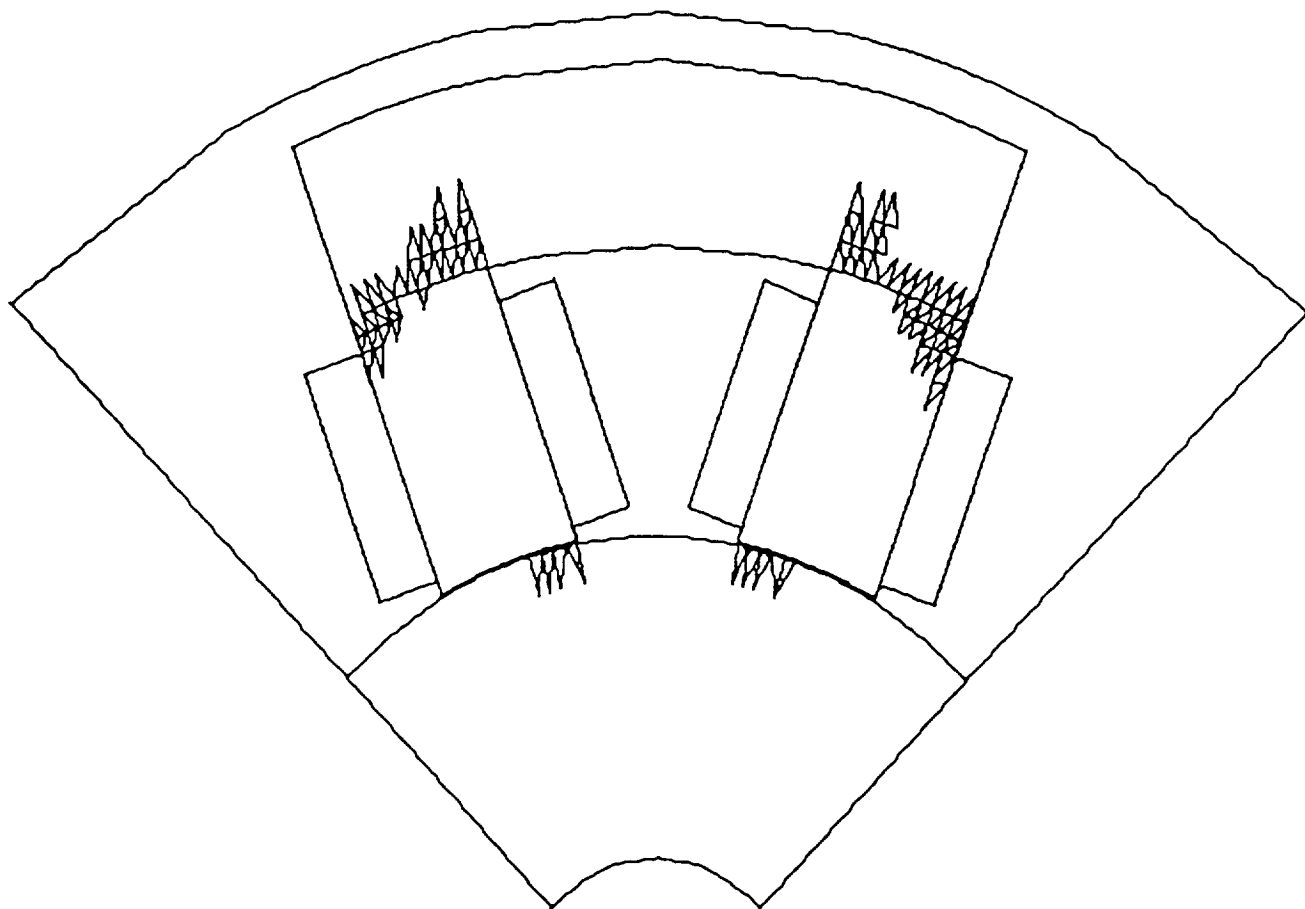displacement of 1/2 clearance.

Saturated Elements
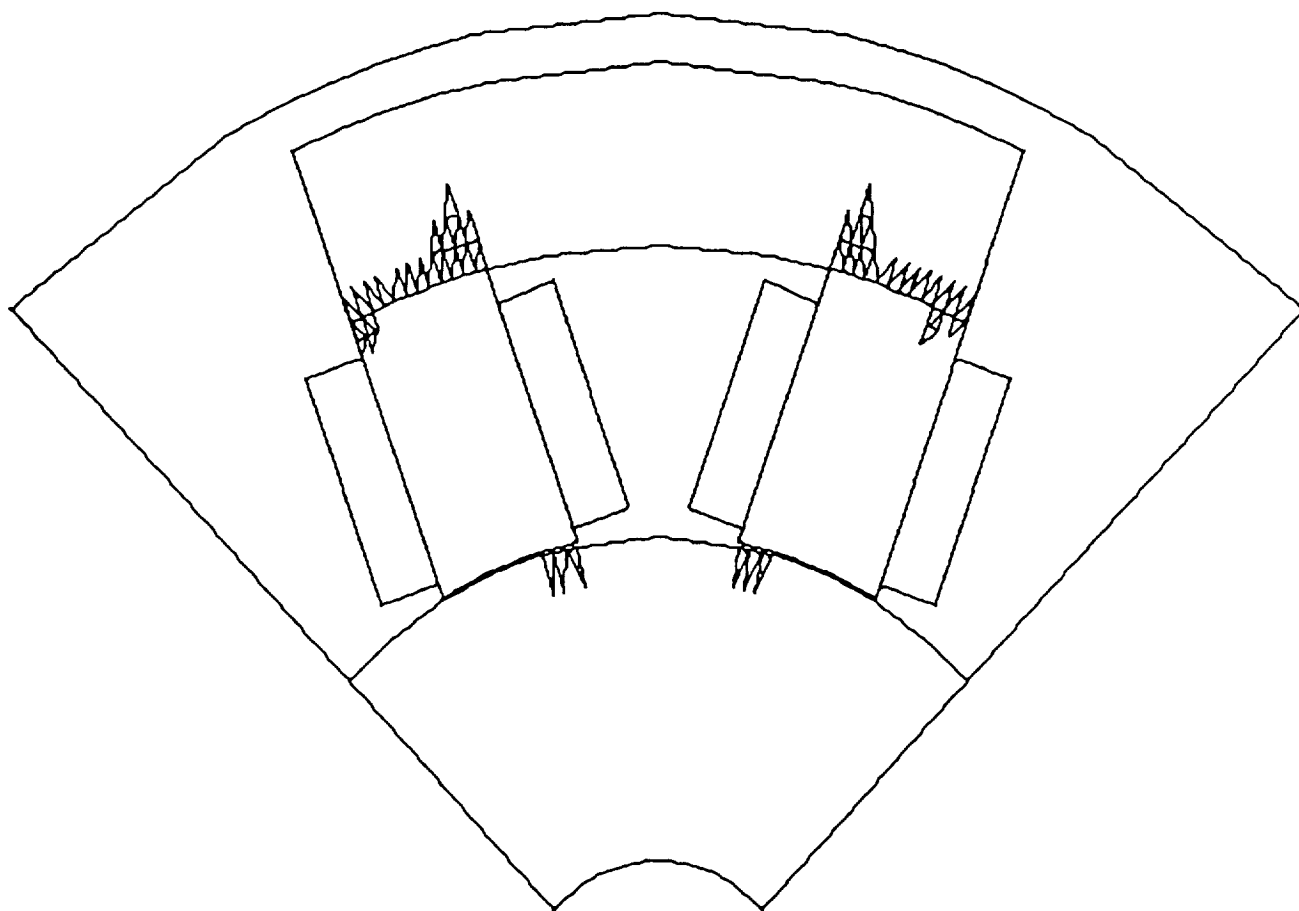
I	x/c	y/c	Fp(N)	Fn(N)
2A	0	0.6	264.84	0.0

Figure 2.7.7   Distribution of saturated elements at 2.0A current, with vertical
displacement of 0.6 clearance.

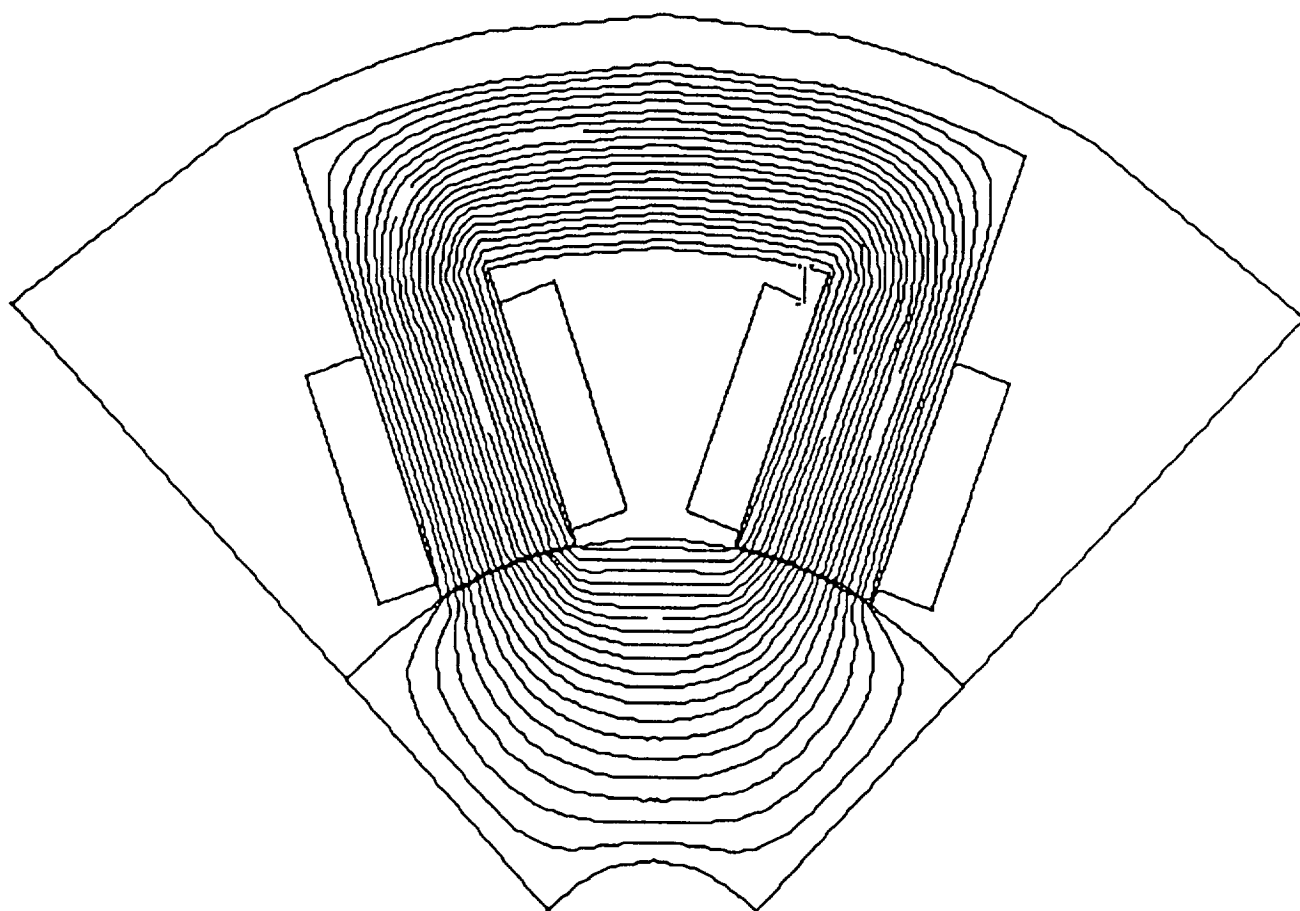# Saturated Elements

I	x/c	y/c	Fp(N)	Fn(N)
2A	0	0.7	289.07	0.0

Figure 2.7.8   Distribution of saturated elements at 2.0A current, with vertical displacement of 0.7 clearance.

Contour of Magnetic Potential

I	x/c	y/c
2A	0.	0.7

Figure 2.7.9   Nonlinear magnetic potential contours.

Figure 2.7.9 and Figure 2.7.10, which is the potential distribution obtained by a linear solution, shows how the flux distribution has changed in order for the flux lines to maintain a minimum curvature and to follow the easiest path, while minimizing local concentrations. The effect on the force is illustrated in Figure 2.7.11, where the nonlinear calculation is compared with the linear solution using a relative permeability of 5570 (corresponding to that of silicon steel at very low field intensity). Above an eccentricity of 0.4, the force continues to increase, but at a much lower rate than predicted by linear theory.

Asymmetry in the distribution of saturation develops when the rotor is given an eccentricity away from the magnet's symmetry axis. Figure 2.7.12 shows the saturation pattern when the shaft is moved to the right, to a position (0.45,0.7), a large eccentricity. The rotor near the inner corner of the left leg is saturated, as well as almost an entire layer of elements near the right leg. The saturation region at the upper ends of the legs has also changed slightly from that of Figure 2.7.8. Figure 2.7.13a shows the potential distribution for this case. Comparison with Figure 2.7.13b, which is the potential distribution obtained by a linear solution, illustrates the effect of saturation in excluding some of the flux from the corners and increasing the fringing at the poles.

The force in the normal direction is plotted in Figure 2.7.14 for one value of off-axis eccentricity, as a function of the y-position (along the symmetry axis). This force also is predicted to deviate from the linear theory above a y-displacement of 50 % of the clearance.

The ratio of normal force to principal force for this same normal eccentricity is plotted in Figure 2.7.15. Curves are shown for the nonlinear theory as well as for the linear theory at two different relative permeabilities, in addition to the experimental results. Although the nonlinear theory does not reflect the magnitudes of the ratio very accurately, the trend is appropriate: the nonlinear theory does indicate a very slight increase in this ratio as the eccentricity is made larger. The magnitude of the difference, however, is so small that it may not be significant in view of the numerical solution method.

Contour of Magnetic Potential

$$\mu_r=5570$$
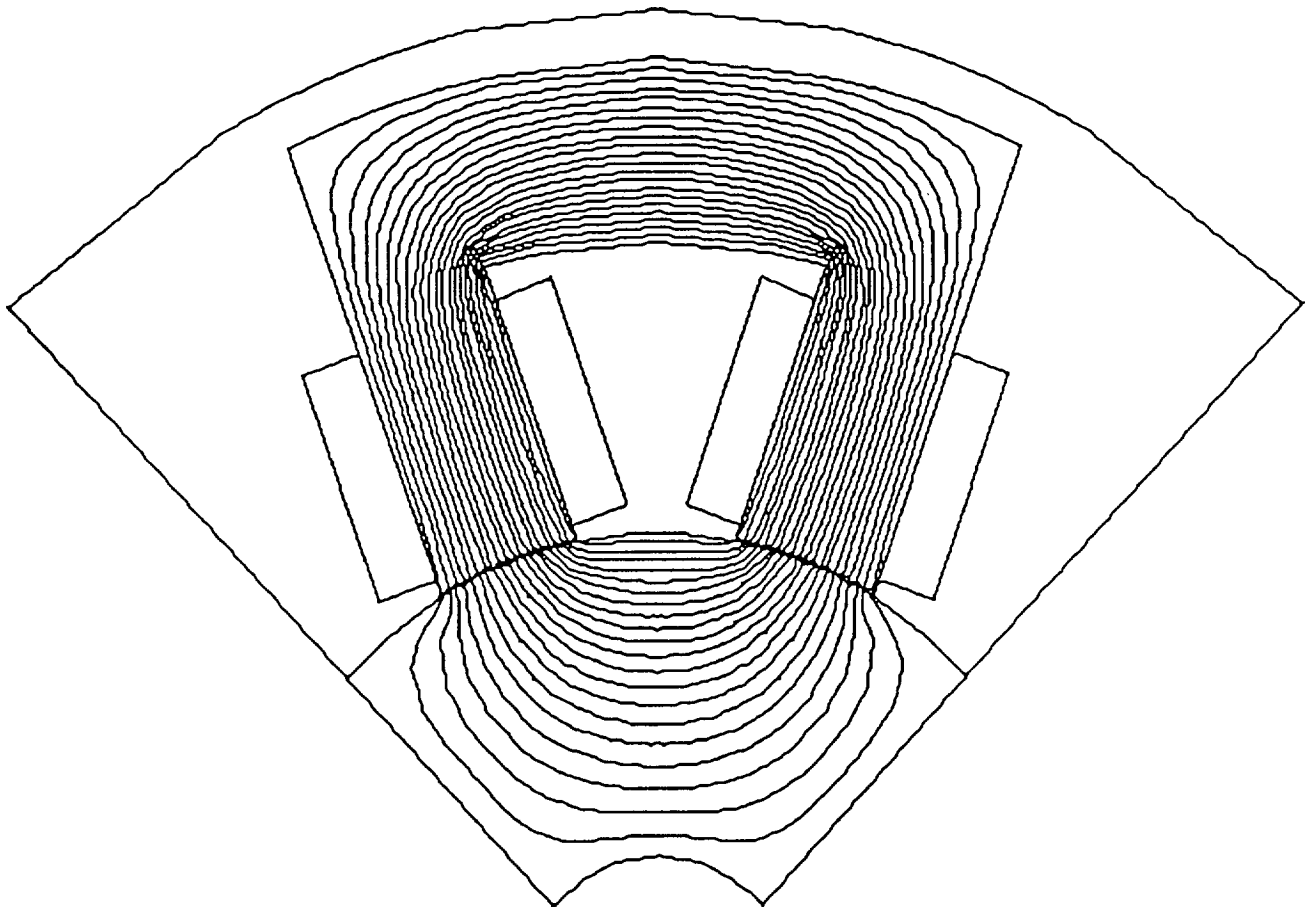
I	x/c	y/c
2A	0.	0.7

Figure 2.7.10 Linear magnetic potential contours.
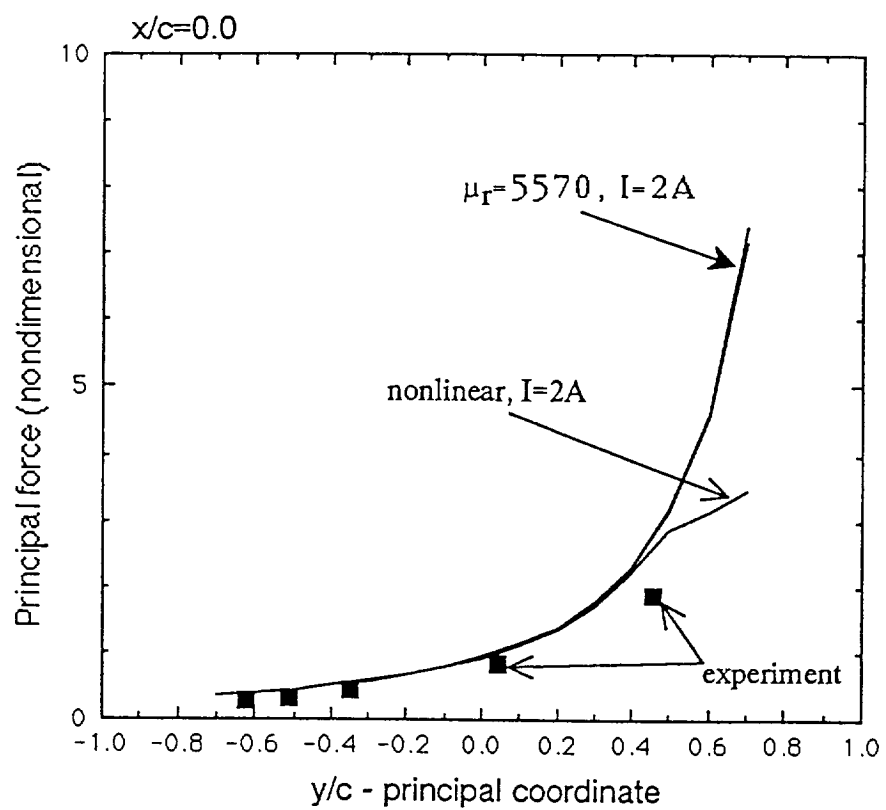
Figure 2.7.11 Principal force as a function of the principal coordinate.

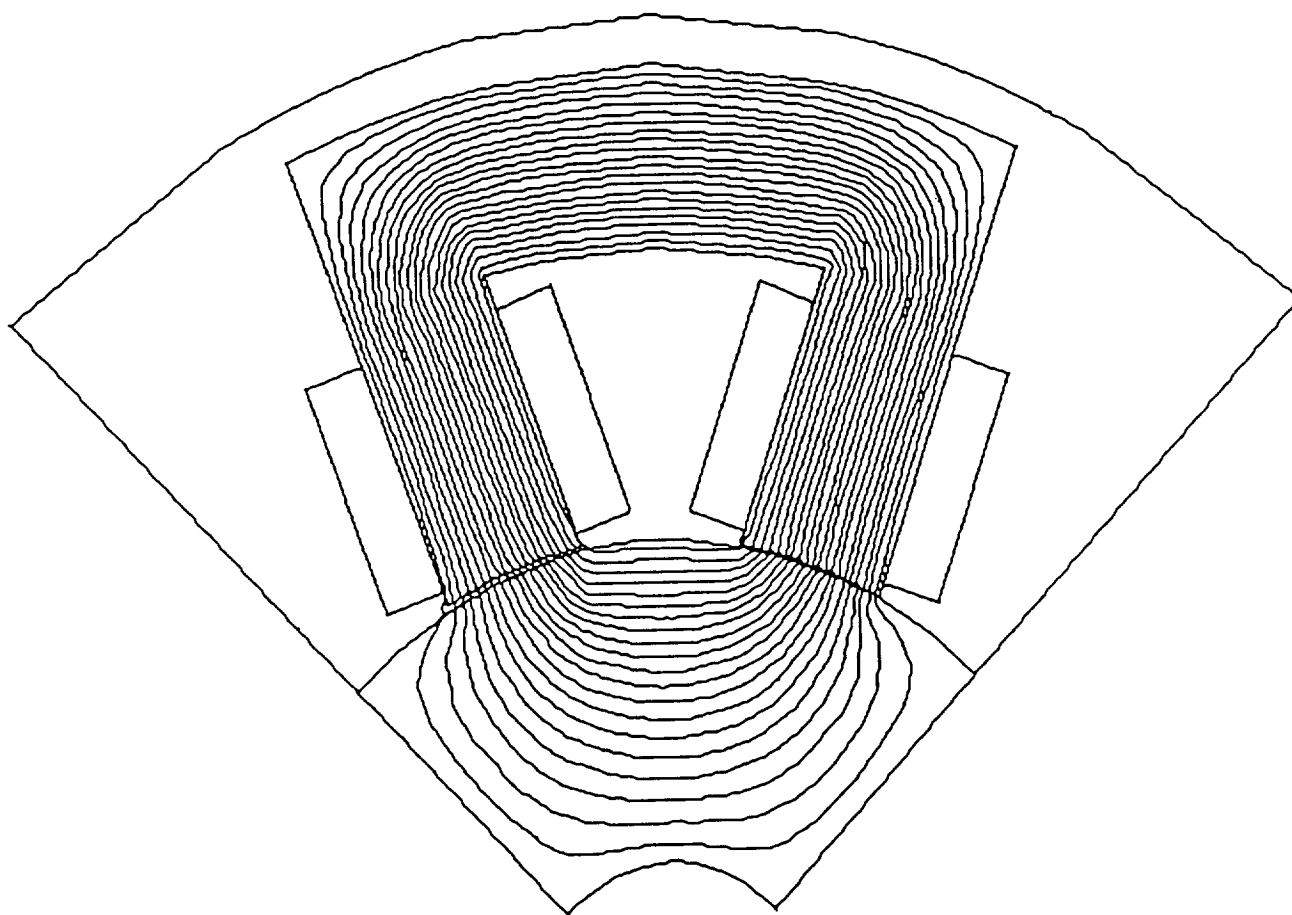## Saturated Elements
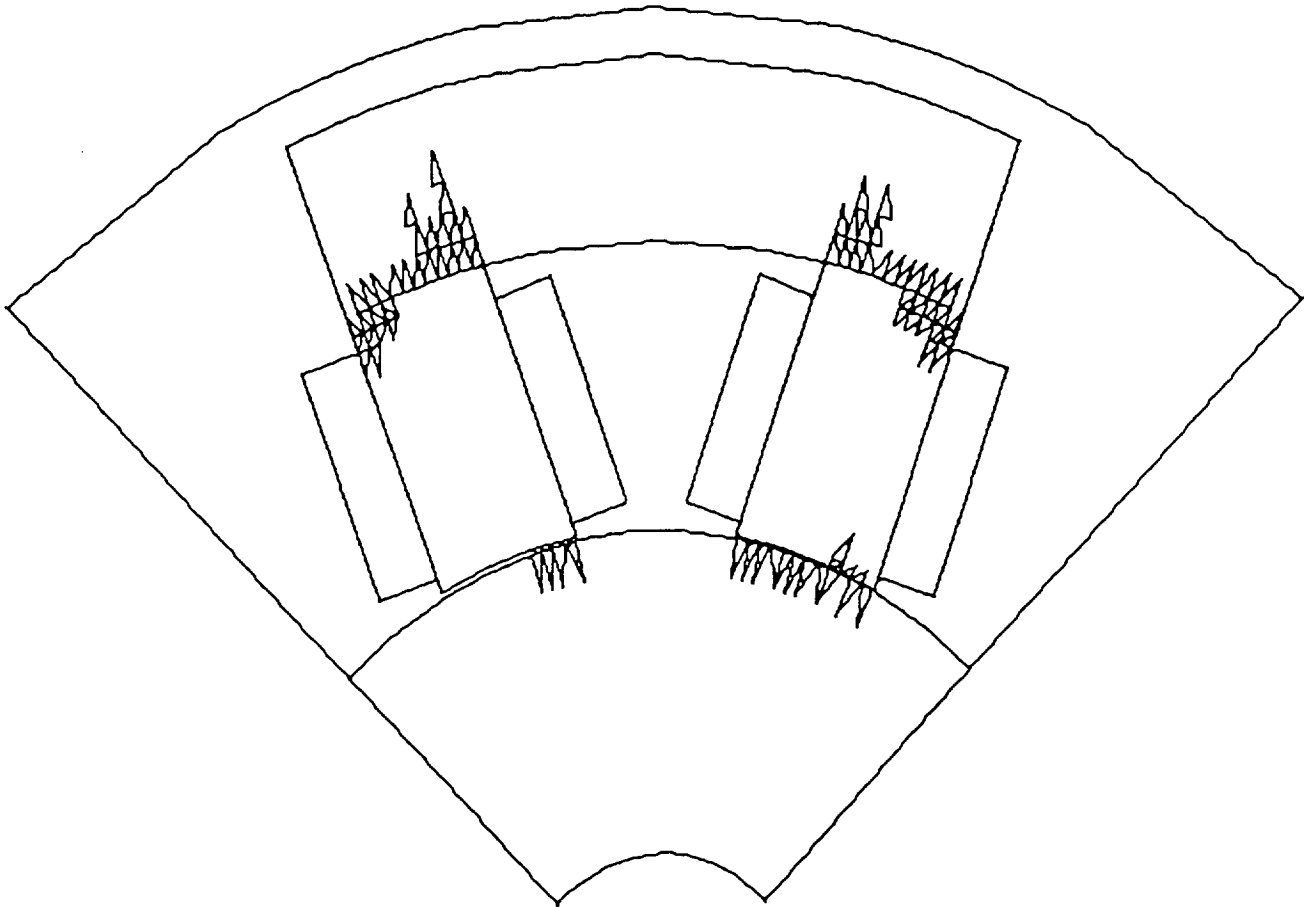
I	x/c	y/c	Fp(N)	Fn(N)
2A	0.45	0.7	283.213	8.714

Figure 2.7.12 Distribution of saturated elements at large eccentricity with normal component.

Contour of Magnetic Potential

I	x/c	y/c
2A	0.45	0.7

Figure 2.7.13a Nonlinear magnetic potential contours at large normal eccentricity.

Contour of Magnetic Potential

$$\mu_r = 5570$$
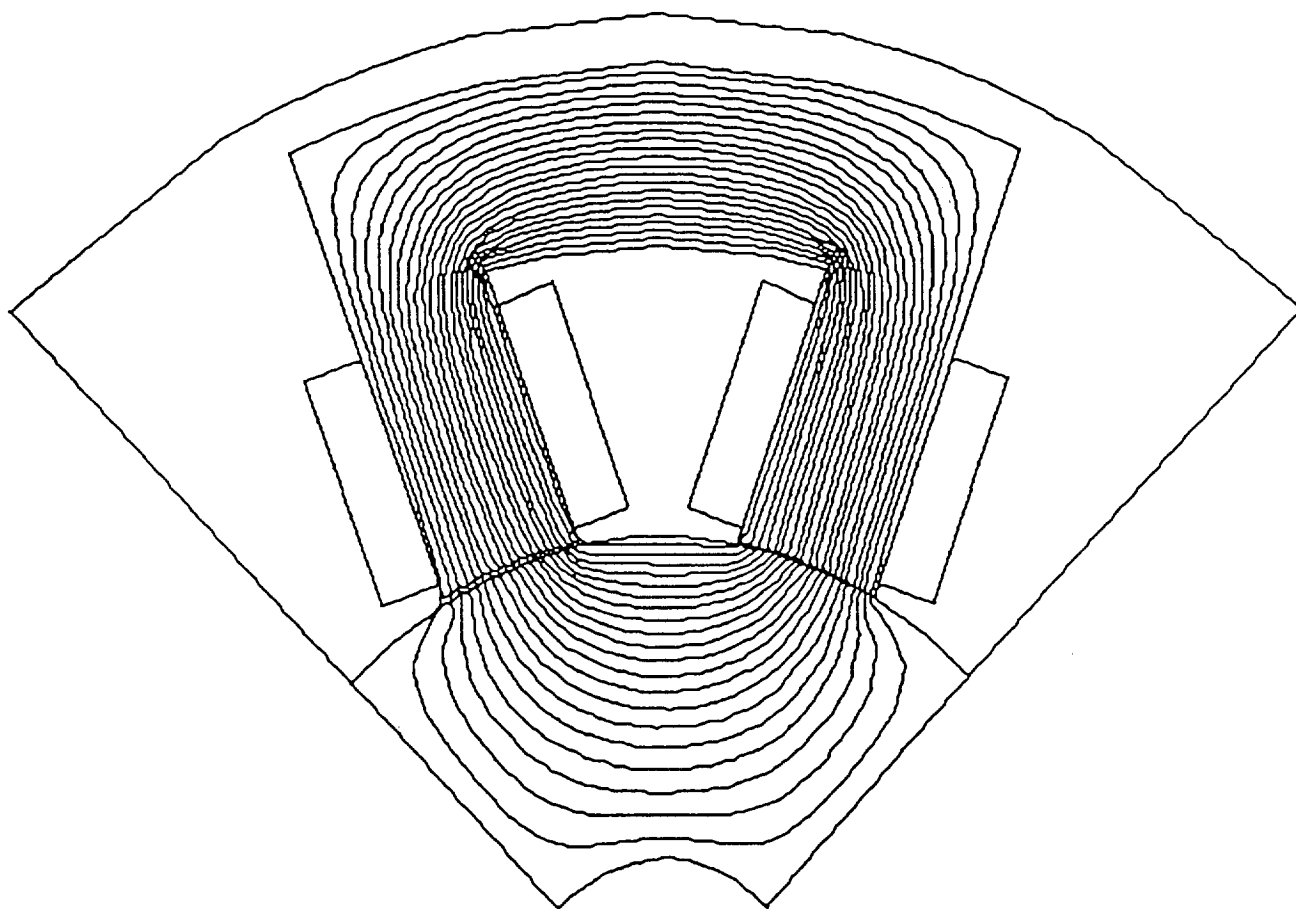
I	x/c	y/c
2A	0.45	0.7

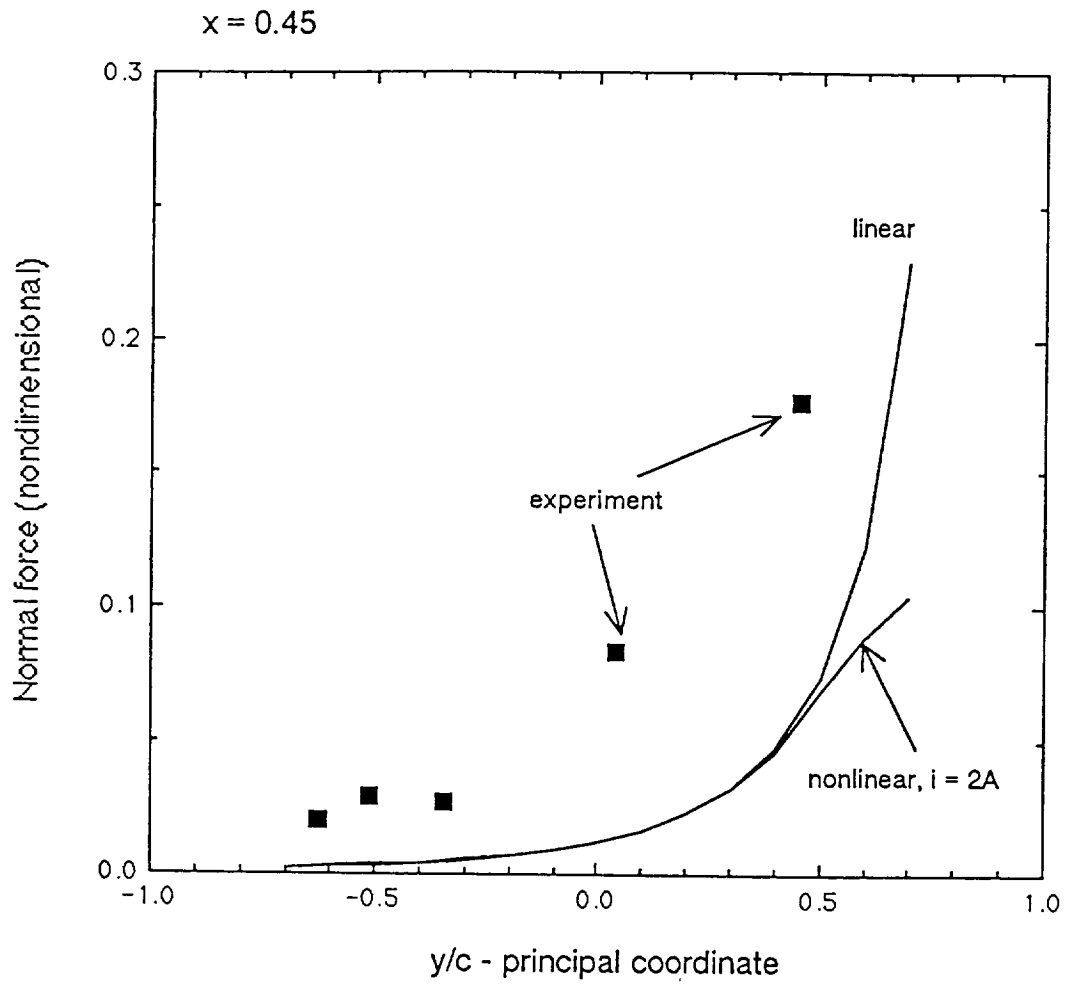Figure 2.7.13b Linear magnetic potential contours at large normal eccentricity.

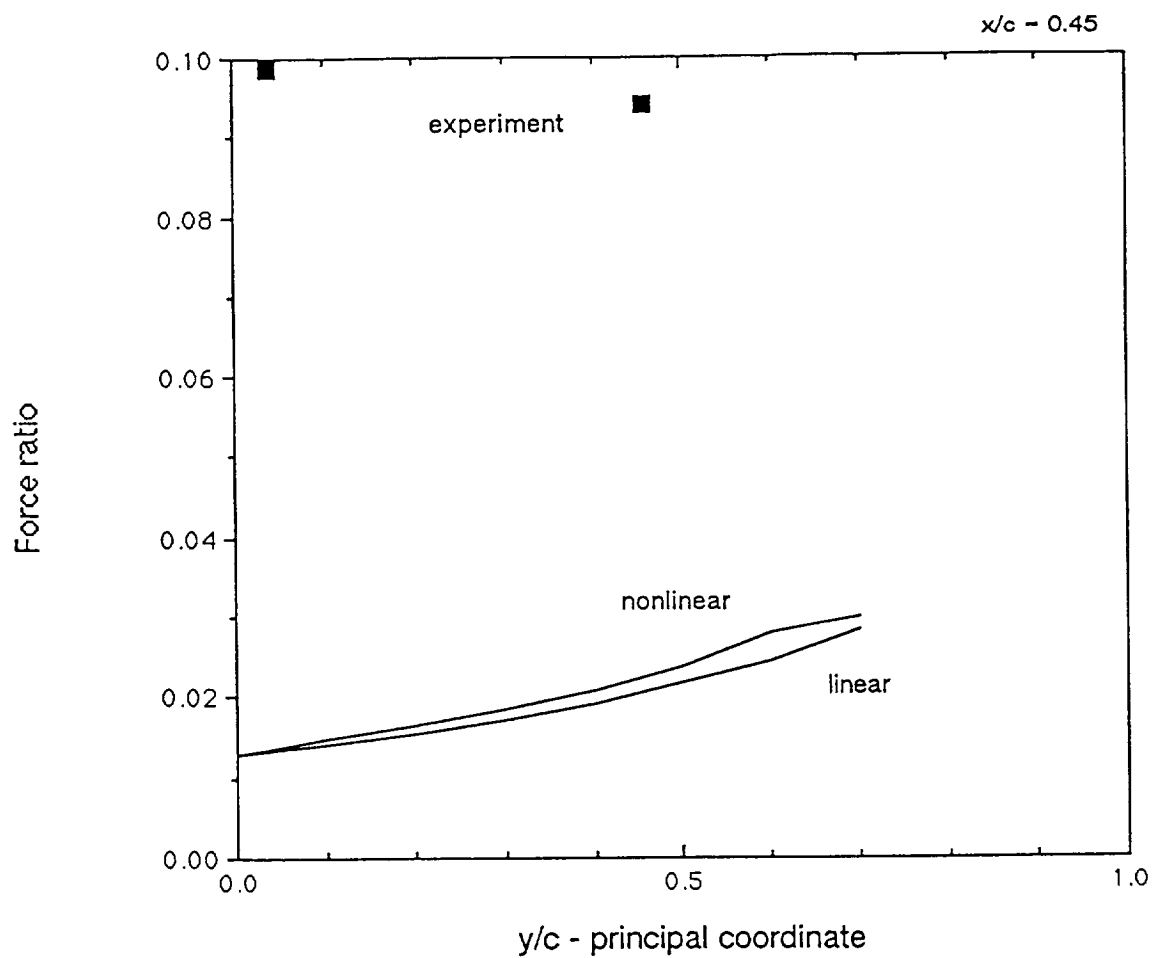Figure 2.7.14 Normal force at normal eccentricity of 0.45 .

Figure 2.7.15 Ratio of normal to principal force at large normal eccentricity.

2.8 Effects of Uncertainties and Property Variations

In earlier results, numerical calculations of forces using the nominal geometry of the experimental apparatus did not predict accurately the magnitudes of the normal forces. The measurements were in all cases considerably larger than predicted by calculation. Recent calculations have attempted to address the issues of uncertainty in the pole face geometry on the forces. The nominal geometry of the apparatus is shown in Figure 2.8.1, along with one possible type of geometric error. Suppose that each of the pole faces, while still consisting of a circular arc, is rotated a small amount from its nominal orientation. This rotation is distinct from the angular uncertainty described in section 2.2 above. This type of error, or an error of similar magnitude, might result from tolerances in machining, but would be unlikely to result from assembly errors.

Figures 2.8.2, 2.8.3 and 2.8.4 show the results of several series of calculations. Each figure is based on the same set of shaft positions and presents the force from one magnet when the shaft has a large normal eccentricity, as a function of position on the principal coordinate. These data are most easily compared with data from the first force measurement apparatus, because of the sequence of measurements. The four curves illustrate the effects of two different magnitudes of error in pole face orientation, 0.5° and 1.0°. These correspond to movement of the outer corner of each pole face a distance of 0.004 inch or 0.009 inch toward the shaft. A change of 0.5° therefore represents 15 % of the radial clearance. The effects of these changes on the calculated forces is shown for the case using the nominal magnetization function for the material, with a saturation flux density of 1.4 T (curves 1 and 4), and for the case using a saturation flux density reduced by 20 %, to 1.14 T. As a reference, the result for the linear calculation with no error in pole face geometry is included.

It is seen that the effect of this geometry change is to increase both the principal and normal forces, with a larger angular change causing larger forces as long as the nominal saturation flux density is maintained. The ratio of normal to principal force also increases. For an angular error of 1°, the ratio of forces has approached the ratio that was measured

When the calculation is performed using the lower value of saturation flux density, however, the result is similar up to the point where saturation is felt, then the ratio between the forces decreases with increasing principal coordinate. It is reasonable that a combination of geometric error and saturation flux density level can produce the force ratio observed in the experiment.

experimentally. In contrast to the experiment, however, the ratio shown in Figure 2.8.4 increases with principal coordinate, while the measurement does not indicate this trend.
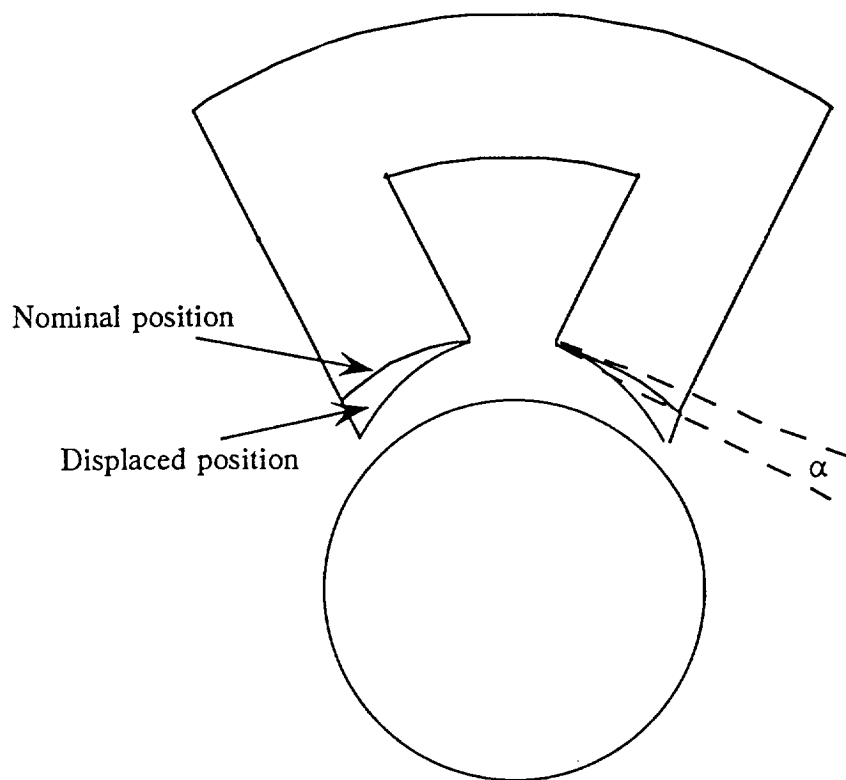
Figure 2.8.1   Schematic of possible error in pole face orientation.

Single Magnet
400 A turn
Normal coordinate = 0.45

$\alpha = 1^\circ$
$B_s = 1.14$ T

$\alpha = 1^\circ$
$B_s = 1.4$ T

Linear
$\mu_r = 5570$

$\alpha = 0.5^\circ$
$B_s = 1.4$ T

Principal Force (nondim)

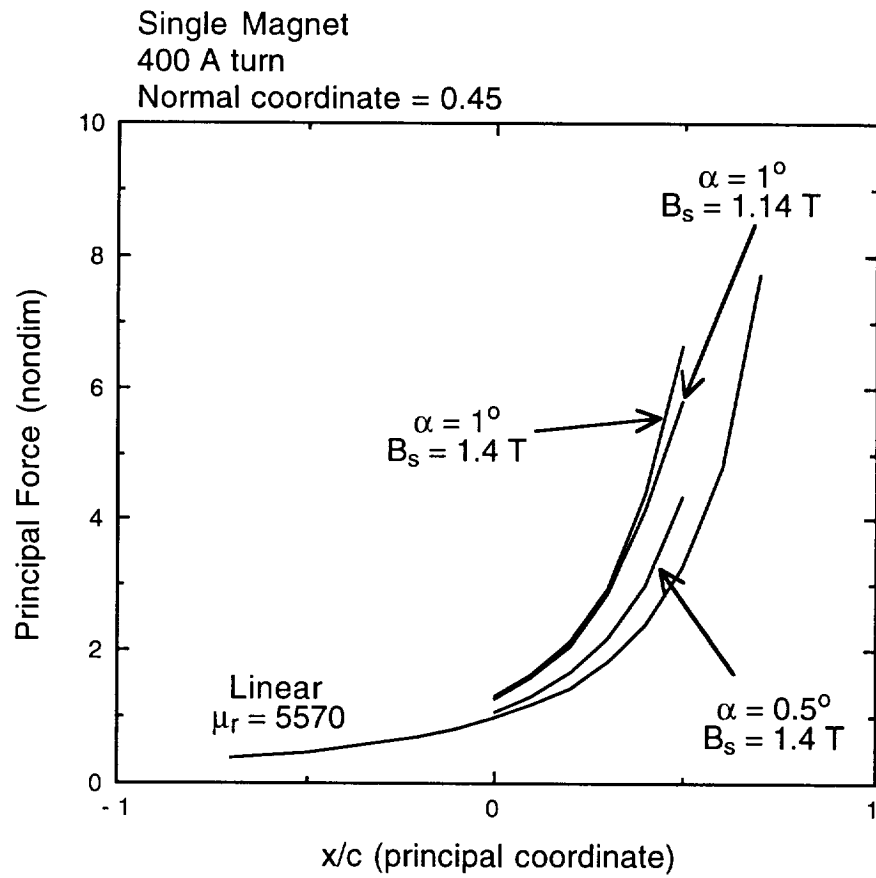x/c (principal coordinate)

Figure 2.8.2   Effect of rotation of pole faces on calculated principal force.
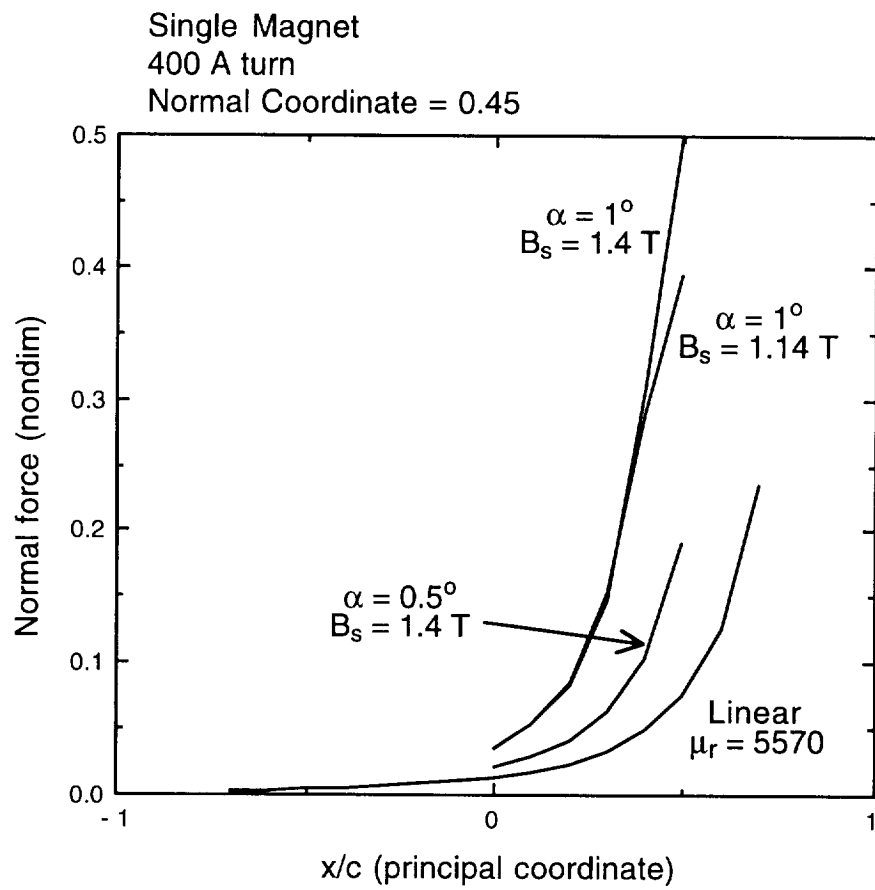
Figure 2.8.3   Effect of rotation of pole faces on calculated normal force.
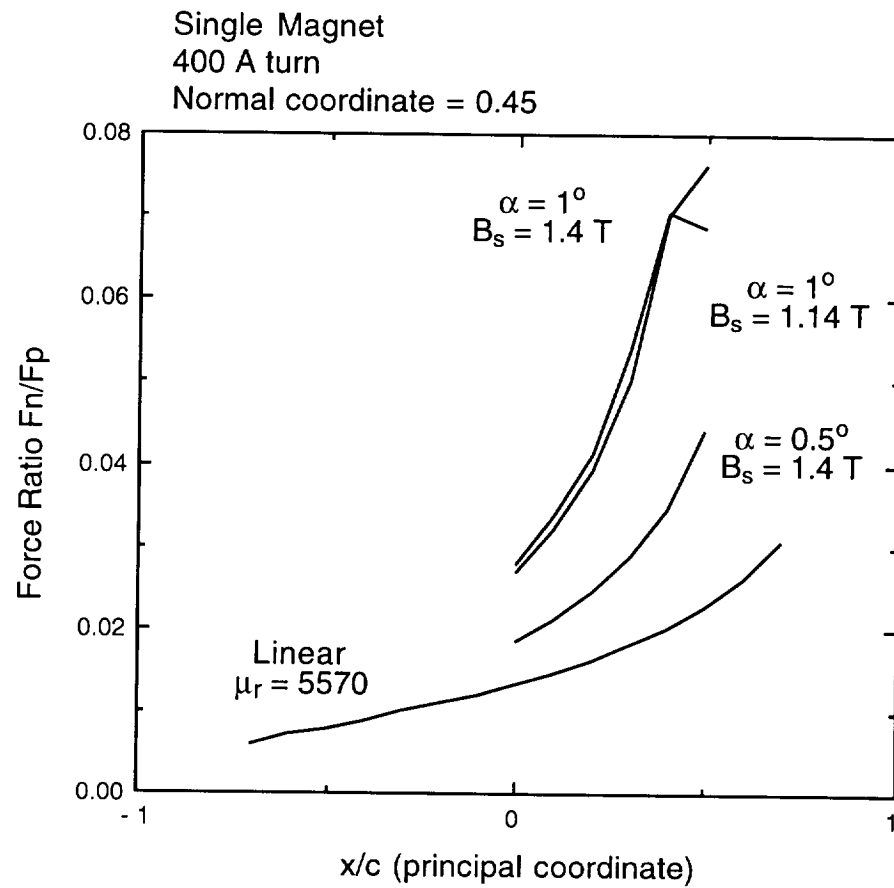
Figure 2.8.4 Effect of rotation of pole faces on calculated force ratio.

2.9 Conclusions (Analytical/Numerical)

Principal conclusions drawn from this phase of the work are: (1) that the distribution of saturation in the magnet core and the rotor influence both the principal attractive force and the force in the normal direction, (2) that the normal force measured experimentally is several times as large as the magnitude predicted at present by either linear or nonlinear theory, but that (3) the trend of nonlinear theory to predict larger normal forces in relation to principal forces is appropriate.

3. TECHNICAL FINDINGS: Experiments

Two different types of experimental apparatus were constructed to measure directly the forces exerted between magnets and shaft in the nonrotating case.

The first apparatus was made using a solid disk to approximate the rotor, and solid core magnets. This apparatus made use of strain gage instrumented support arms for the disk in order to measure the force directly.

The second apparatus was made with laminated disk and magnets, and used the principle of a calibrated deflecting beam to measure the forces indirectly.

Measurements of force on a stationary, non-rotating shaft were made as functions of position and current and the forces have been compared with corresponding numerical predictions. Where appropriate, measurements from the two rigs were also compared, and were found to be consistent with each other.

These apparatus and results are also described in the M.S. thesis of E. McCaul [72].

3.1 Magnet Apparatus I

Table 3.1.1 lists the design parameters of the apparatus for direct force measurement, Figures 3.1.1 and 3.1.2 show schematics, and Figure 3.1.3 shows an exploded view .

Rotor o.d.	0.076 m	3.00 in
Support shaft o.d.	0.016 m	0.625 in
Support shaft length	0.15 m	6.0 in
Magnet i.d.	0.0777 m	3.06 in
Magnet depth	0.019 m	0.5 in
Shaft clearance (diam)	1.52 mm	0.06 in
Pole width	0.013 m	0.5 in
Leg length	0.019 m	0.75 in
Coils	200 turns/leg, #22 copper	
Pole separation angle	40°	
Magnet centerlines	0° 90° 180° 270°	

Table 3.1.1 Design parameters of experimental apparatus I
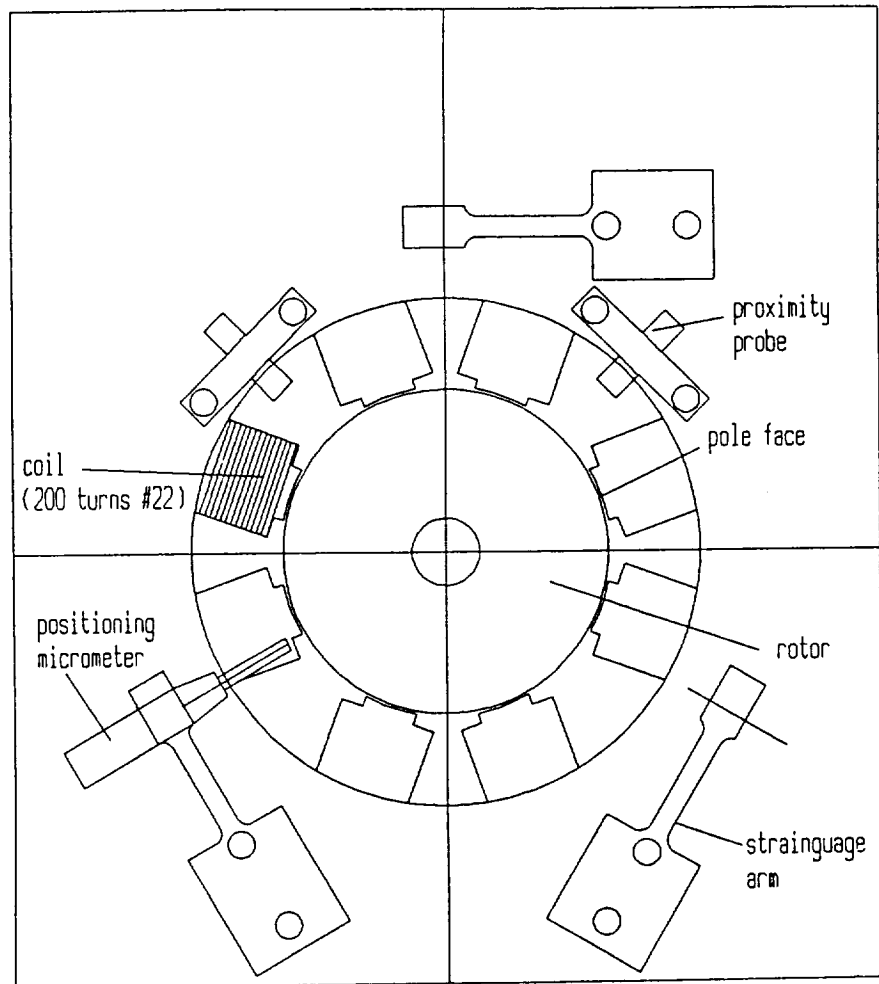
Figure 3.1.1   Schematic of experimental apparatus I.
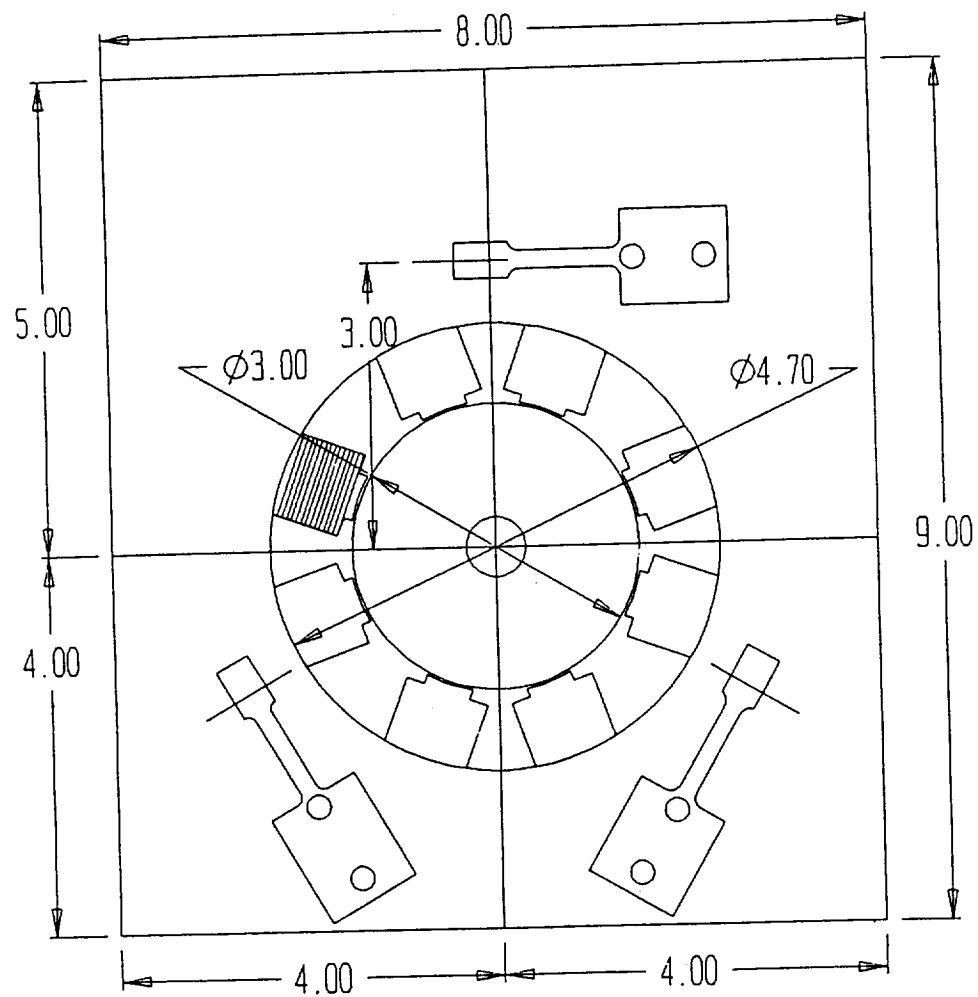
Figure 3.1.2   Dimensions (inches) of experimental apparatus I.

59

0.23 m

0.18 m

14 mm

Coil: 200 t each leg

Instrumented cantilever

Position Probe Holder

Side Panel

Magnet Core

Rotor: d = 76.2 mm
Clearance: 0.76 mm

Micrometer

Rolling Element Bearing

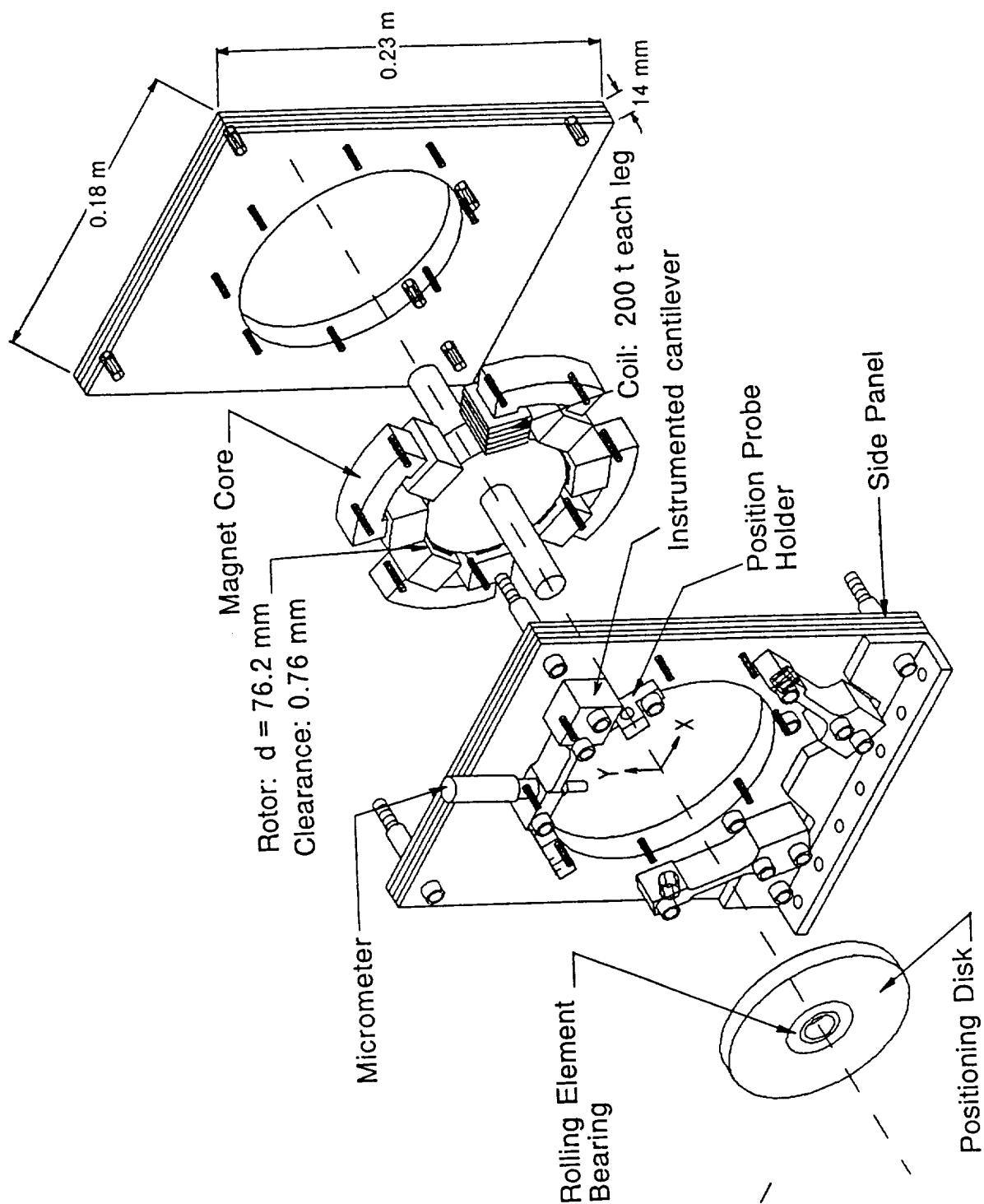Positioning Disk

X

Y

Figure 3.1.3   Assembly drawing of experimental apparatus I.

The magnets and the journal are cut from disks of solid 1020 steel. They are placed between two side panels that are laminated from 1/16" aluminum pieces. The magnets are held in place by locating pins that are press fitted into through holes. The hole positions were located prior to the cutting of the magnets from the solid disk. In this way careful control of the radial clearances and angular positions of the magnets was maintained.

Each magnet is independent and is wound with 400 turns capable of carrying current of 2.0 A in the steady state. The original design based on a sandwich construction was intended to allow flexibility in mounting magnets of different materials. In the steady force measurement mode, the rotor is held stationary by pressure from six micrometer heads (three on each end) that are in turn held by cantilever arms instrumented with strain guage bridges. Thus all mechanical force on the rotor passes through the strain guage arm transducers, and ideally all of the force on each micrometer tip is purely radial. In fact, it is likely that the transducer arms exert some force in the tangential direction because of static friction between the pusher tip and the support disk. Such force would not be sensed by the transducers, which are designed to measure only forces that cause bending moments. Attempts were made to minimize any frictional force by adding Teflon ball sockets with steel spheres between the pusher micrometers and the support disks.

Despite the difficulties encountered, a number of successful force measurements were made and useful conclusions have been drawn. Measurements from the second apparatus tended to confirm those of the first.

3.1.1 Method of Measurement

Measurement of the force at a given location x,y within the clearance space requires several steps:

i. Establish a datum position relative to the magnet from which the force is to be measured. This requires placement of the rotor in contact with the magnet along the inner corners of the pole faces. Visual alignment of the rotor is followed by application of a small steady current to the magnet to assure contact. The datum readings are then taken from the eddy current probes located at 45° to the vertical. Ideally, one datum would be sufficient for all positions and all magnets, but in reality because of machining tolerances and assembly allowances, the magnet pole faces are not located on a perfect circle. Measurements can only be made relative to one magnet at a time, therefore, and a separate datum is required for each magnet. This datum can be used for all positions relative to this magnet.

ii. Place the rotor in the desired position by adjusting the micrometer pushers, repeatedly computing the position from the probe readings and correcting as necessary. When the rotor is in position, all strain guage arms should be under a slight preload.

iii. Take readings of the strain guage voltages without current through the magnets. These will serve as datum values that contain all preloads including the rotor weight.

iv. Apply the desired current to the magnet. Take readings of the strain guage voltages and the position probe readings.

v. Compute the position from the probe readings and the forces from the strain guage voltages after subtracting the datum values.

vi. Apply an alternating current to the magnet coils to remove residual magnetization and return to step ii.

The intent was to automate the entire process of data taking and force calculation by using a microcomputer and digital data acquisition. Difficulties with the commercial A/D hardware, however, forced the use of manual data taking for this phase of the work. The raw outputs from the strain guages and position probes are processed using the same type of software as that intended for the automated process, but the data were entered manually.

3.2 Results of Measurements, Apparatus 1

Forces were measured at several locations and for several values of steady current. The figures referred to below display dimensional data as measured, with forces in Newtons plotted against y/c, the eccentricity ratio in the vertical direction. All of the forces measured in this apparatus are from the lower vertical magnet, so the vertical forces are in the negative y-direction. The eccentricities in the x-direction are all positive. Three traverses of the y-direction were made, at x/c positions of approximately 0.0, 0.24, and 0.45. Assessments of the errors in measurement are not complete; however, it is expected that the error in position measurement is no greater than plus or minus 0.05 in y/c and x/c, and that the error in force measurement is no greater that plus or minus 5 N. Errors in current level control are within 0.1 A. A larger series of measurements that were made before the addition of the ball/socket contacts was eventually discarded because the measurement error due to friction appeared to be significant.

The data support some of the anticipated relationships among the position, current and force variables but appear to disagree with other aspects of the present theory. Figure 3.2.1 shows the vertical force as a function of y/c for several values of current. The force

tends to increase roughly as the inverse square of the gap. The magnitudes of the forces, however, are considerably lower than those predicted either by the linear finite element theory or by the traditional theory based on assumption of uniform gaps, and the ratio between measured and predicted forces is not constant. Figure 3.2.2 is a comparison of the measured forces with those predicted by the finite element calculation. The results indicate that at large gap and/or small current the ratio between the measured and predicted forces is about 1.5, but at smaller gaps and/or higher currents this ratio increases, eventually exceeding 2.0 for all the three values of current that are plotted.

Several mechanisms may be operating to cause these discrepancies, including flux leakage, non-uniform permeability of the materials and magnetic saturation. Some part of the disagreement is likely the result of measurement errors, but the differences appear to be significant even after allowing for reasonable experimental error. These disagreements reinforce the need for additional work on force calculation.

The linear finite element theory predicts the existence of forces from a magnet that are normal to its axis of symmetry when the rotor is displaced from this symmetry axis, but the forces that are measured are considerably stronger than those predicted by calculation. Figure 3.2.3 shows the x component of force when the rotor is placed as closely as possible on the y-axis. The normal force appears to be somewhat stronger at higher current levels but all these forces are small, on the order of 5 % or less of the principal force, so it is difficult to attribute much significance to this ratio in view of the experimental uncertainty. At higher values of x/c, however, the normal force becomes much more significant. Figures 3.2.4 through 3.2.7 show the vertical and horizontal components of force when the x/c value is 0.24 or 0.45, and Figure 3.2.8 shows the value of the x force as a function of position for several values of x/c while the current is held constant at 1.0 A. In general it appears that the normal force increases significantly with increasing x/c, and at x/c = 0.24 and 0.45 the horizontal force is about 10 % of the principal force. Theory predicts a ratio of about 3 % to 5 %.

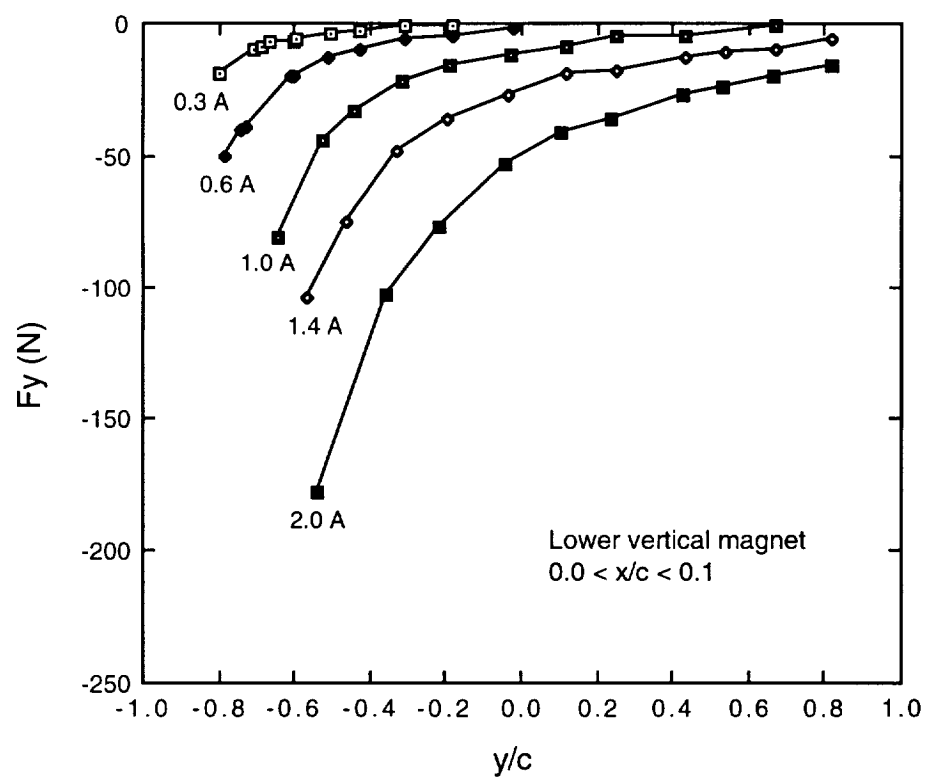Figure 3.2.1. Vertical force from lower vertical magnet at different values of current.
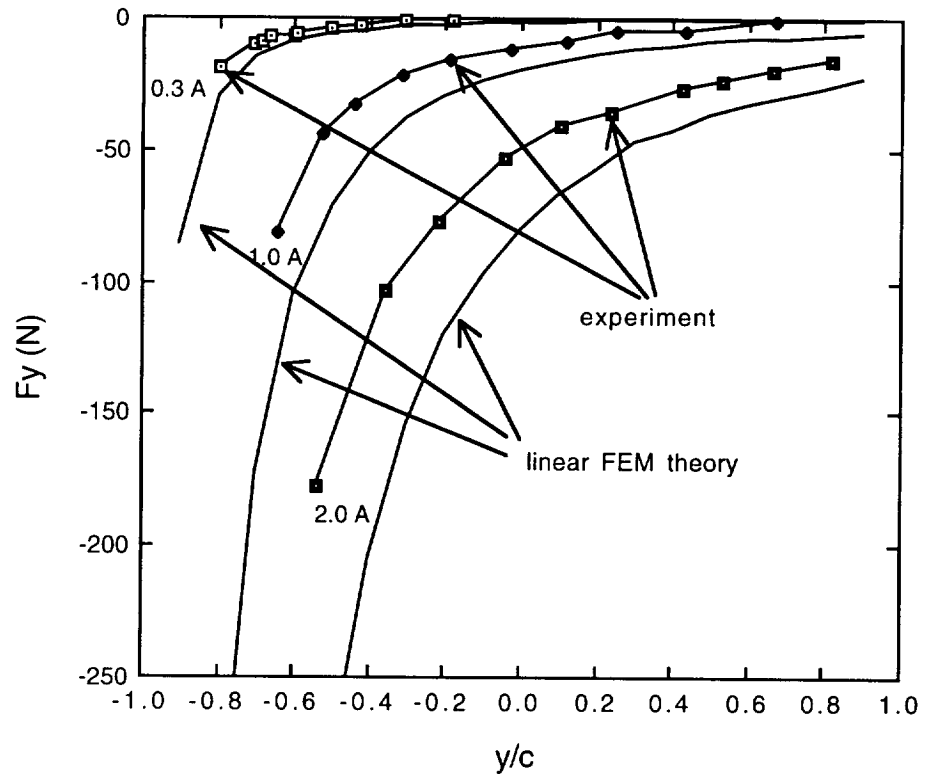
Figure 3.2.2. Measured forces and forces predicted by linear FEM calculation.

Figure 3.2.3. Horizontal force from lower vertical magnet at different values of current.

Figure 3.2.4. Vertical force from lower vertical magnet when x/c = 0.24.

Figure 3.2.5. Horizontal force from lower vertical magnet when x/c = 0.24.

Figure 3.2.6. Vertical force from lower vertical magnet when x/c = 0.45.

Figure 3.2.7. Horizontal force from lower vertical magnet when x/c = 0.45.
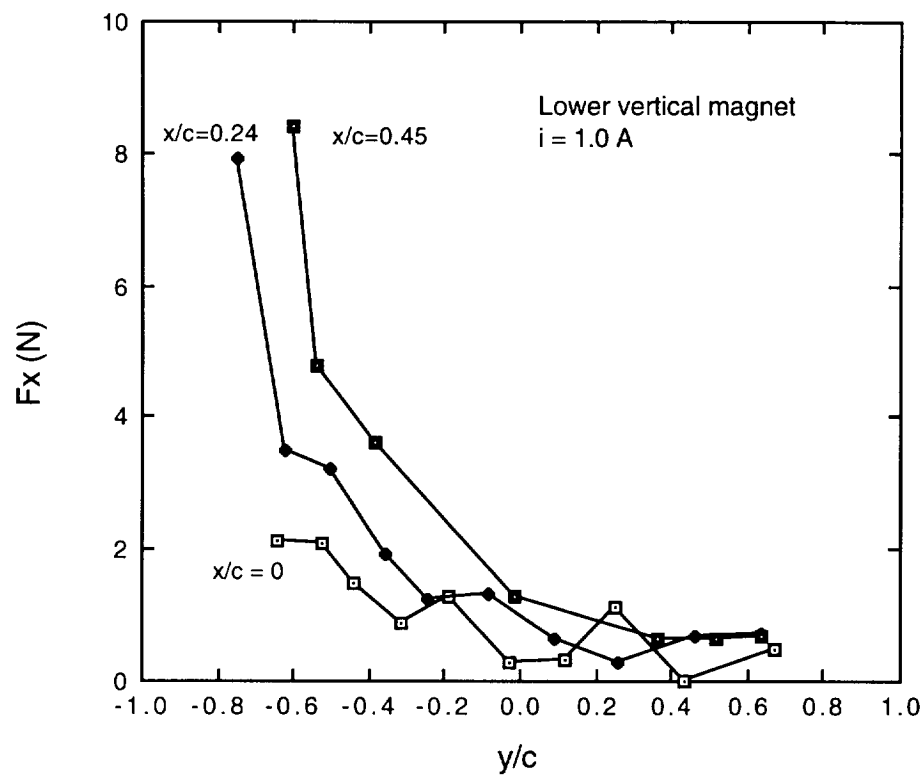
Figure 3.2.8. Horizontal force at different x positions with 1.0 A current.

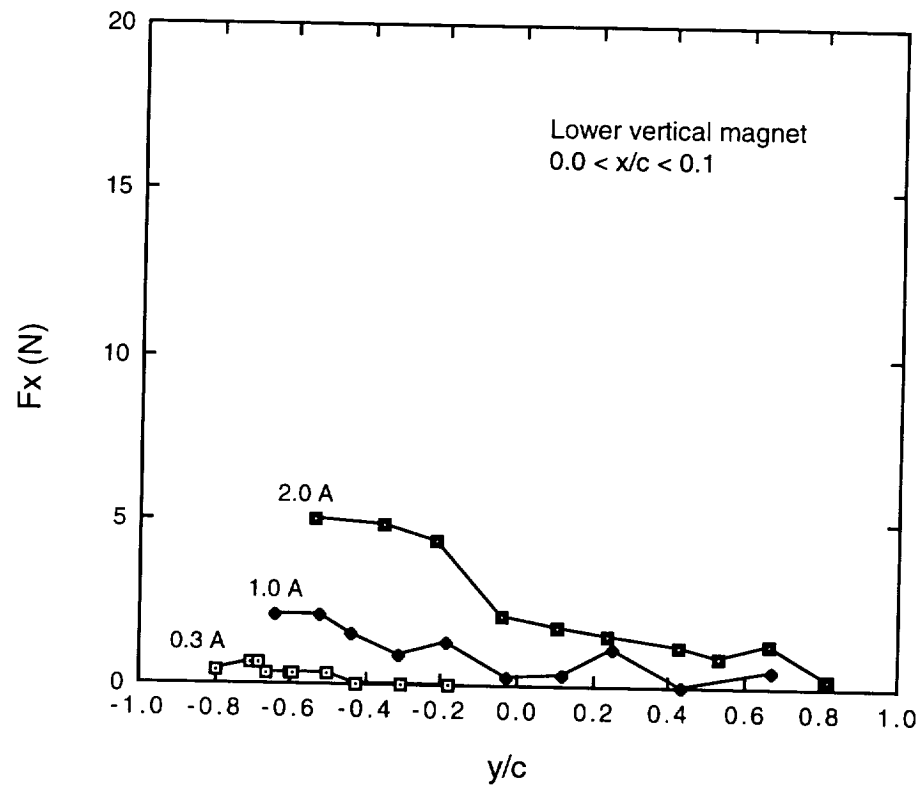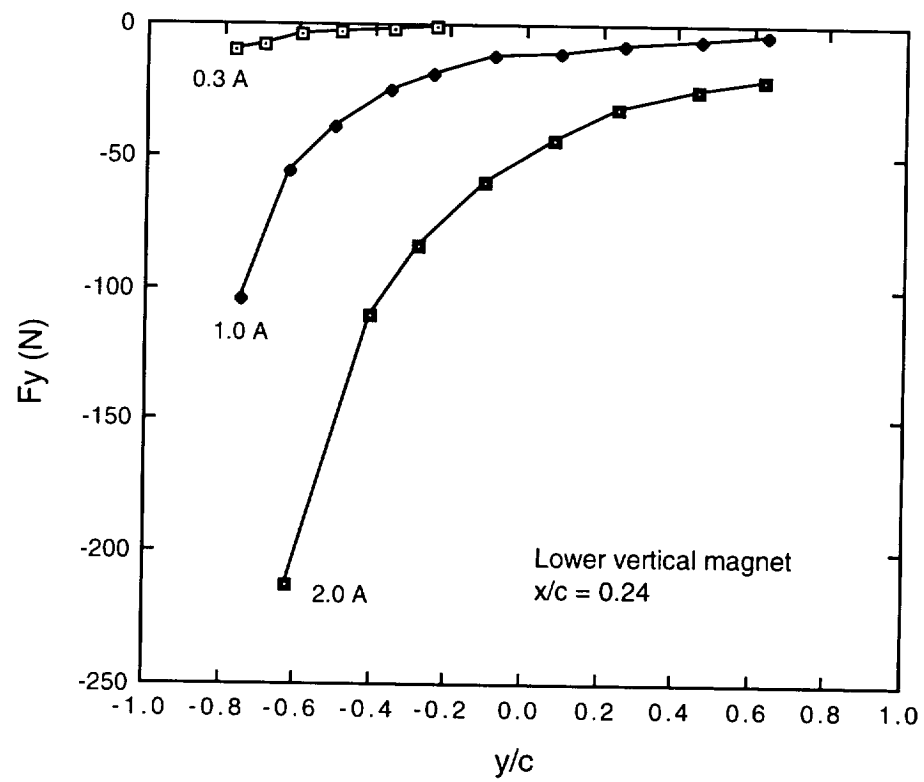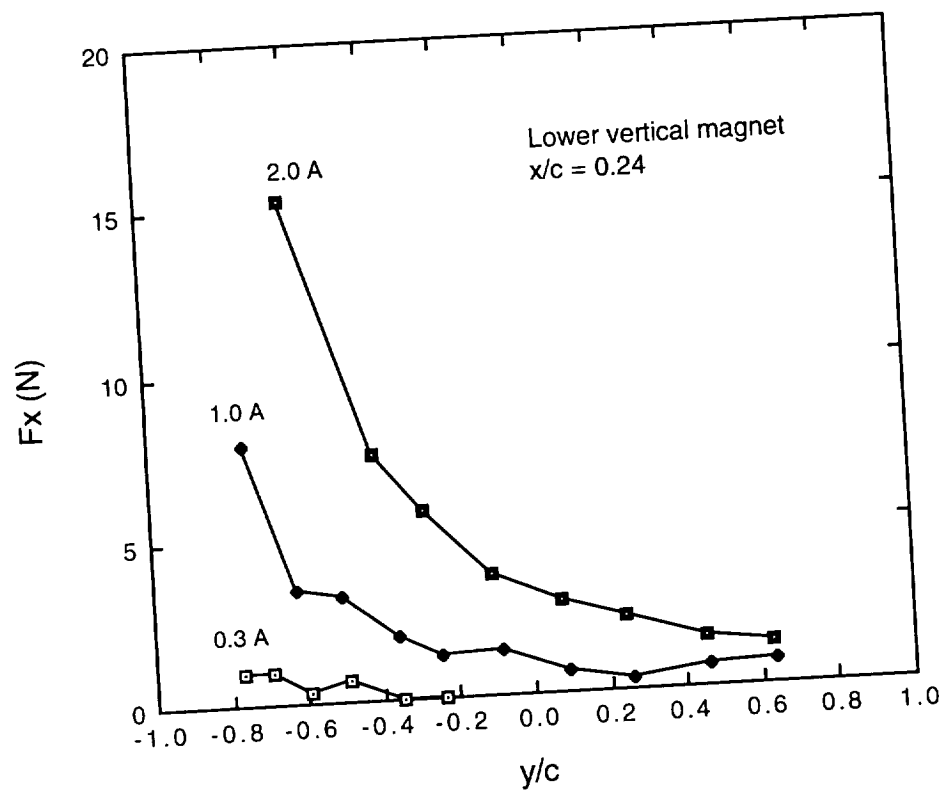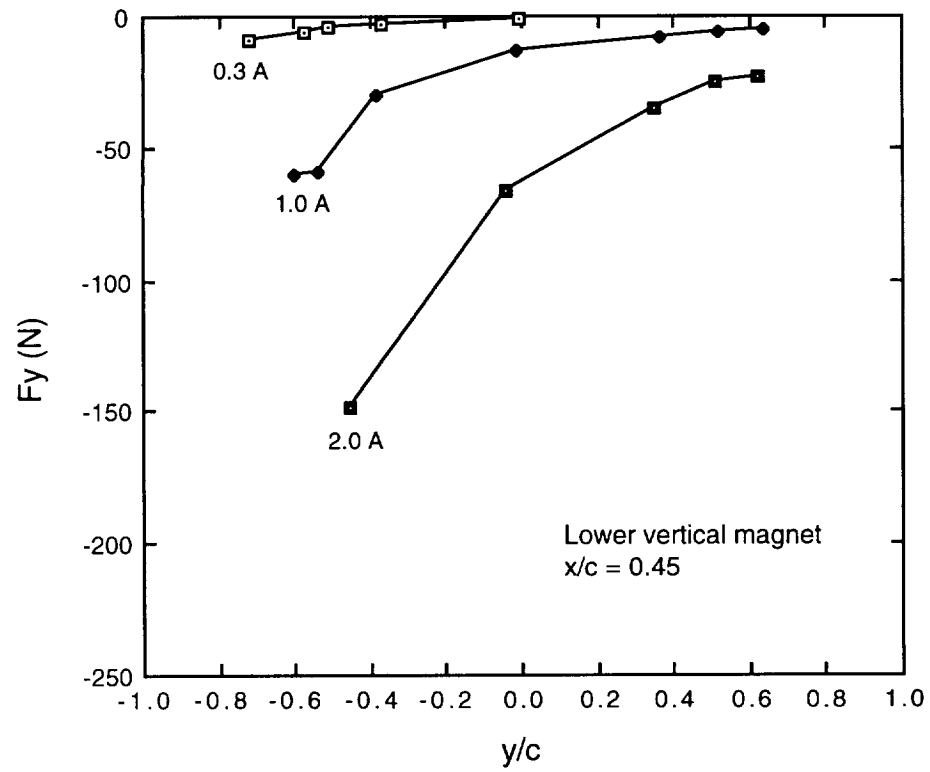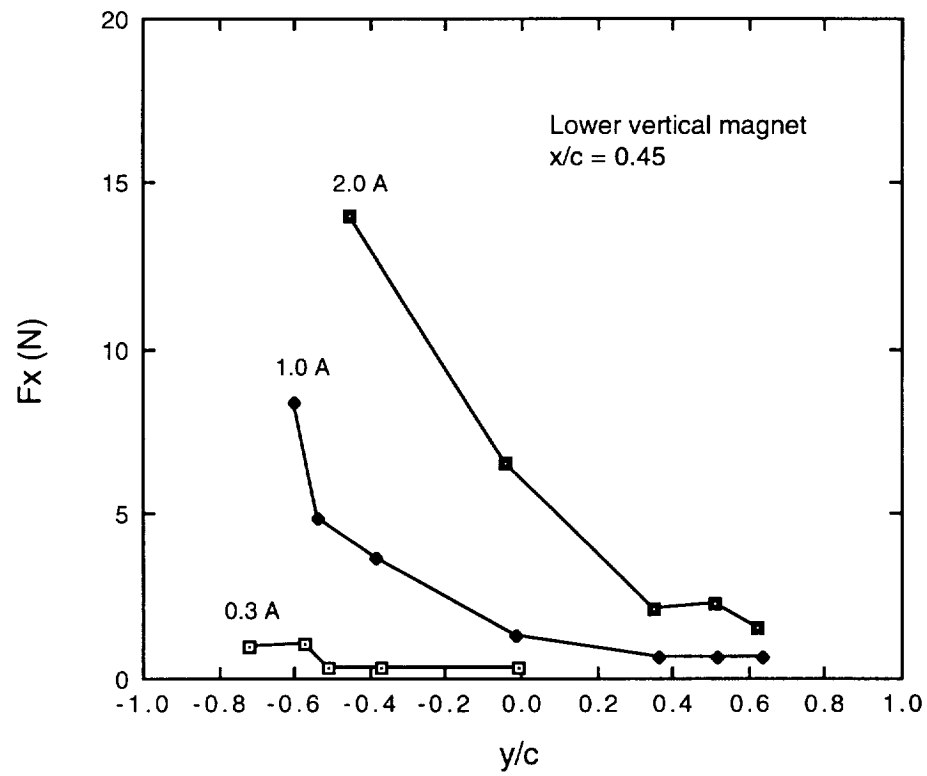An aspect of the measured forces that was not anticipated is the lack of degradation of principal force as the rotor is moved off the principal axis. Numerical calculations predict a significant decrease in the principal force under these conditions, but the measurements do not support this prediction. Figure 3.2.9 indicates that within measurement uncertainty there are not significant differences in the y-components of force at the three different values of x/c. A possible cause is that a self-correcting redistribution of flux along the pole faces occurs that allows the force to be maintained. The present theory assumes that the magnetic potential along the entire surface of each pole face is uniform. The mechanism of potential and flux redistribution should be studied further.

In summary, the general trends of the measured y-forces agree with the predictions of the theory while the magnitudes of forces are somewhat smaller than those predicted. Other aspects of theory are not confirmed by the measurements. The measured forces in the x direction appear to be significantly larger than those predicted by theory when the rotor has an x eccentricity. Also, the y forces do not appear to decrease significantly when the rotor is given an eccentricity in the x direction. These effects appear to be significant even after considering experimental uncertainty, and both of these phenomena were judged to warrant further study.
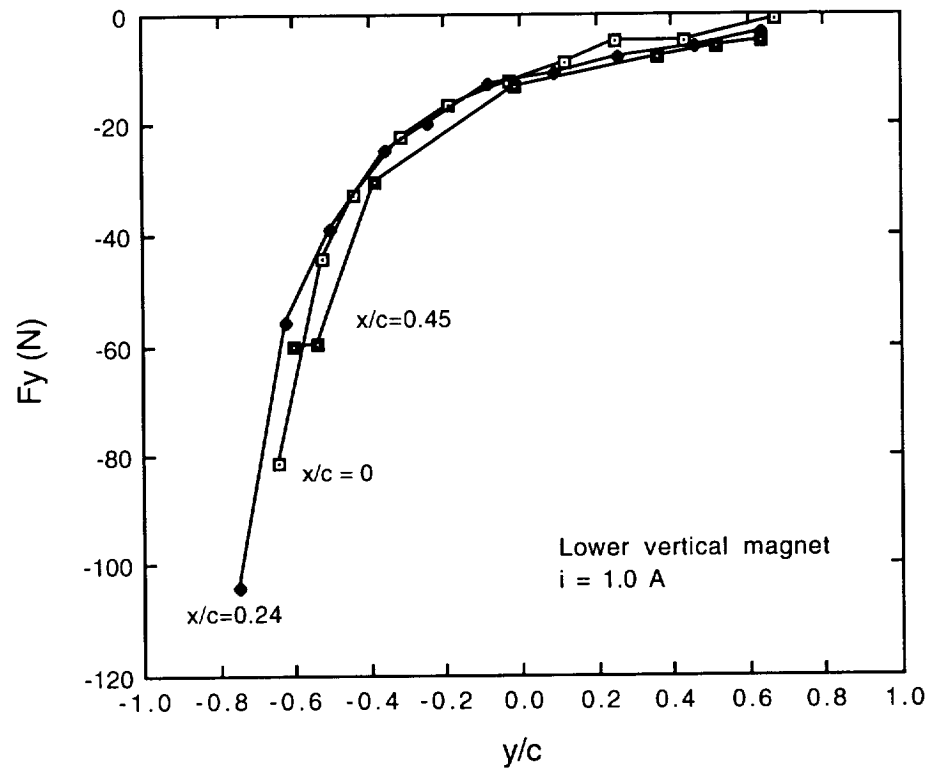
Figure 3.2.9. Vertical force at different x positions with 1.0 A current.

3.3 Measurement Apparatus II

Measurements of forces exerted by a magnet on a stationary, non-rotating rotor were made using a second apparatus that relied on a different measurement principle.

The magnet cores and the shaft are constructed of 0.014 inch laminations of silicon steel M15. Each magnet is wound with a total of 400 turns of #22 wire, arranged in two coils, one on each pole leg. The nominal dimensions of the magnets are the same as those of the first apparatus, which was of solid material, but the effective cross section is smaller in the new apparatus because of the laminated construction. At present its value has not been determined.

3.3.1 Deflecting Beam Apparatus

Figure 3.3.1 is a schematic of the apparatus for force measurement. The shaft is clamped at each end in two large pedestals that are fixed to a solid base. The magnets are assembled in a retaining shell and the entire magnet assembly is mounted on a slide mechanism allowing movement in the horizontal direction. The slide is mounted in turn on a laboratory jack that allows the assembly to be moved vertically. Thus the bearing assembly can be moved in two directions and positioned accurately with respect to the fixed shaft. The relative position of the bearing is measured by four proximity probes oriented at 45° to the vertical. These probes are connected to the bearing housing so they always measure the relative displacement of the rotor from the center of the bearing regardless of the deflection of the rotor support beam.

When one or more of the magnets is activated, the force causes a deflection of the beam from its static position. The components of this deflection in the vertical and horizontal directions are measured by a separate set of proximity probes that are connected directly to the base of the apparatus. The intention was to place the support beam in the pedestals to approximate the perfect clamped-clamped case, so the stiffness of the beam would be equal in all directions and could be calculated from simple beam theory. After assembly it was found, however, that manufacturing tolerances resulted in unequal stiffnesses, so the force vs. deflection relationship was directly calibrated independently in both directions. Although the deflections were different in the two directions, the relationships were linear over the range required for measurements, so the calibrations yield a constant horizontal and a constant vertical stiffness.
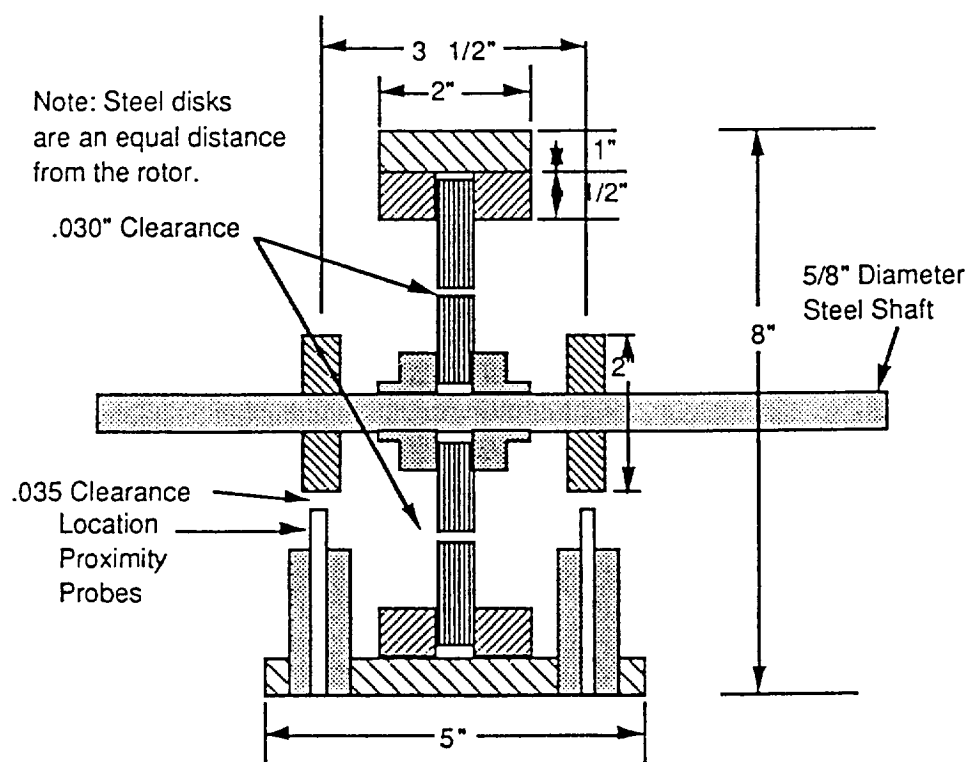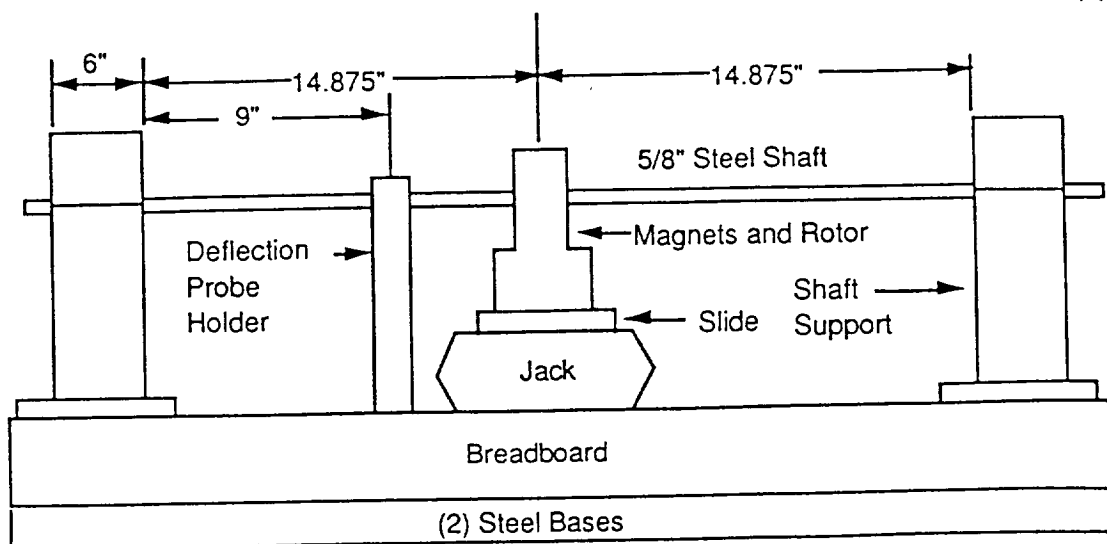
Figure 3.3.1 Schematic of experimental apparatus II.

3.3.2 Measurement Method

Before conducting any force measurements, the location of the bearing center is determined by noting the readings of the position probes when the shaft is placed against the pole faces of the magnets and interpolating to find the center. Also, the undeflected shaft position is noted.

To measure the force at a particular current level, the magnet/rotor assembly is first degaussed using alternating current in the coils of the magnet, with peak amplitude of at least twice the highest current used. To avoid destructive vibrations while degaussing, the shaft is rigidly fixed relative to the magnets by using a temporary clamp. The magnets are then activated and the proximity probe outputs are read to determine the final shaft position relative to the magnets and also the absolute shaft deflection.

3.3.3 Measurements Using One Magnet

The apparatus described above was used to measure the force between a single magnet and the shaft for a variety of positions of the shaft with respect to the center of curvature of the magnet pole faces. Particular attention was paid to the forces when the shaft was given an eccentricity with respect to the axis of symmetry of the magnet. Such relative positions, which will be seen as undesirable, may nevertheless result from three causes: misalignment of the magnets during assembly (note that this is a strong argument for manufacture of magnets having poles attached to a continuous backing ring), from dynamic motion of the shaft, or from errors in biasing.

Measurements were made at several levels of current in the magnet coils, and over a range of shaft positions within the clearance space. After assembly it was found that the magnets lacked a common center because of assembly tolerances. All the measurements therefore were conducted using one of the side magnets. At present the numerical calculation method described above has not been applied to the geometry of the new apparatus, so the results presented below are measurements only. A limited discussion of the trends of the normal forces in relation to the previous experiment as well as to the calculations that have been performed will be attempted, however.

The results of these measurements are presented in a slightly different way from the results of the Section 2.1 above, reflecting a different sequence of shaft repositioning from that used in the first series of experiments. Each group of symbols corresponds to a constant x position and therefore represents a traverse of the vertical direction (the normal direction in this case). By executing traverses of the normal direction it was possible to

plot the ratio of normal force to principal force as a function of the distance away from the axis of symmetry.

In the plots below,the value of X, or x/c, listed in the legend gives the position of the rotor along the axis of symmetry of the magnet. The largest possible value is 1.0, but it was not possible to approach this value closely with the present design of the apparatus. A discussion of possible redesign to alleviate this difficulty, as well as to achieve some other goals, is presented in a later section. For the present, however, most of the values of X in this and subsequent plots are negative, and some extrapolation is necessary to visualize trends as the rotor approaches the magnet. Some of the values of y/c that are presented are smaller than -1.0, corresponding to a location so far from symmetry axis that it is outside the clearance space. While this would not be possible in an actual design, the steady state apparatus can accommodate such large displacement.

Figure 3.3.2 shows the measured force in the principal direction and Figure 3.3.3 shows the force in the normal direction at a current level of 1.0A (400 A·t). The principal force is seen to be significantly larger at larger values of X, or rotor locations closer to the magnet. The force increases slightly as the rotor is moved away from the axis of symmetry, toward one of the poles. This trend was predicted by the original linear theory based on gap regions only, but has not been predicted by the nonlinear theory. The magnitude of the normal force increases strongly with an increase in distance away from the symmetry axis. Figure 3.3.4 shows the ratio of the normal force to the principal force. Linear fits to the data of each traverse were calculated. To avoid confusion only one fit is shown, but the slope of this line is equal to the average of the slopes of all the fits.

Figures 3.3.5 through 3.3.16 show the corresponding results for other values of coil currents. Similar trends are observed in all the cases. In each of the plots of force ratio a linear fit is provided, and in each case the slope of the fit chosen is the same as the average of the slopes of all the individual fits.

Over the ranges of position examined, the data indicate an approximately linear relationship between the normal eccentricity of the shaft and the ratio of normal to principal force. The constant of proportionality seems to be larger at lower currents, but for all cases examined its value is between 0.14 and 0.17. The nonlinear theory has predicted the existence of normal forces, but has not predicted such a large constant of proportionality for the ratio.
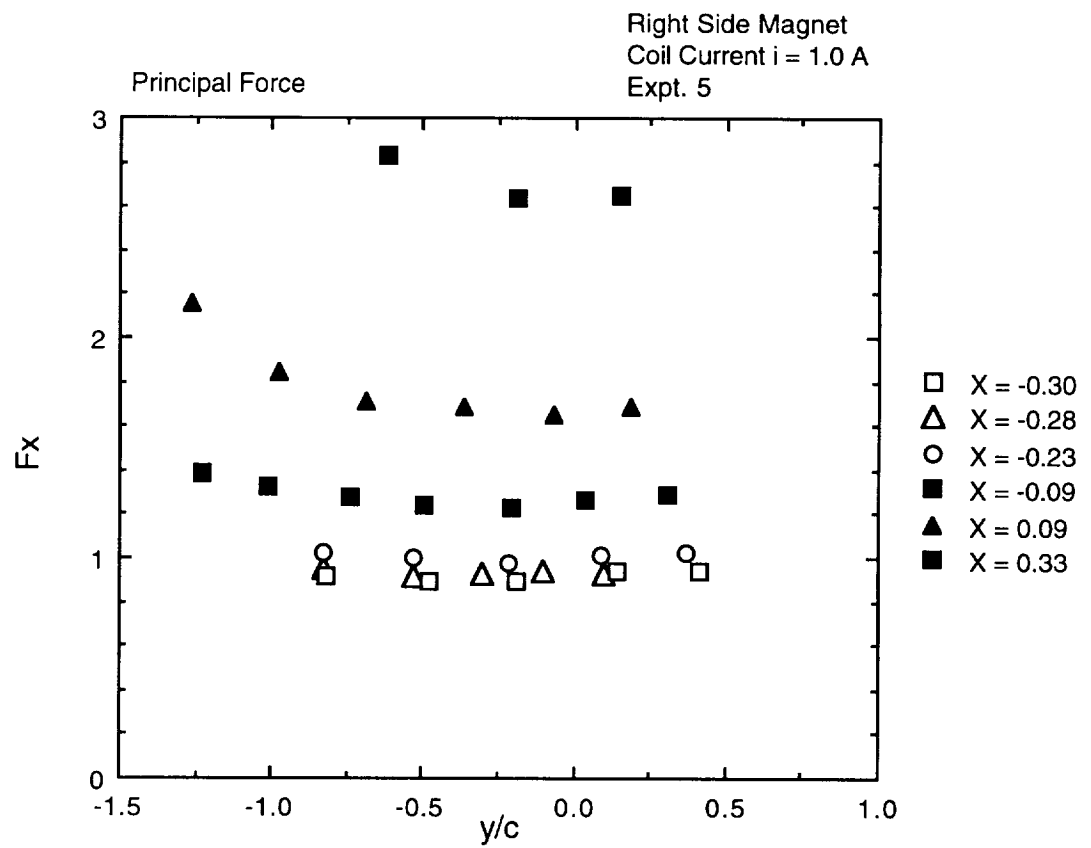
Figure 3.3.2 Principal force from single magnet at 1.0 Ampere (400 A-turns).
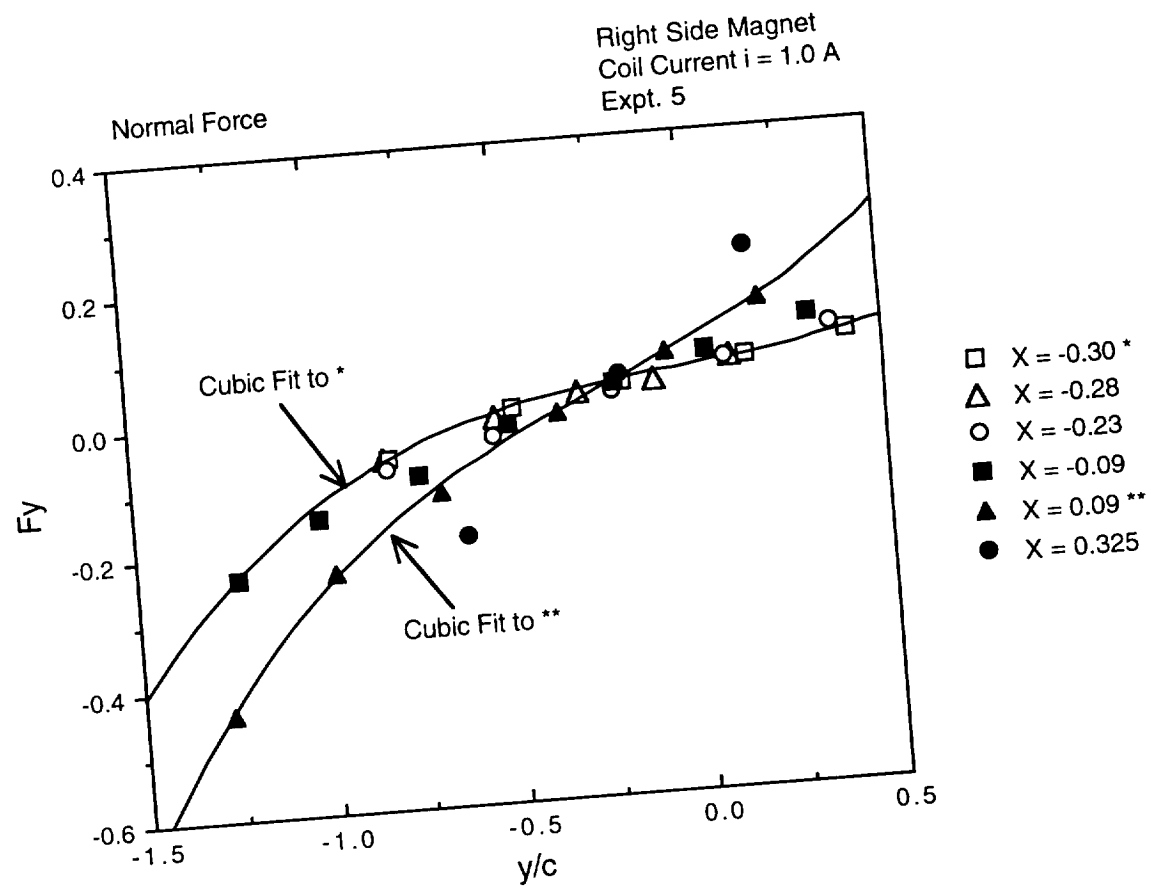
Figure 3.3.3 Normal force from single magnet at 1.0 Ampere (400 A-turns).
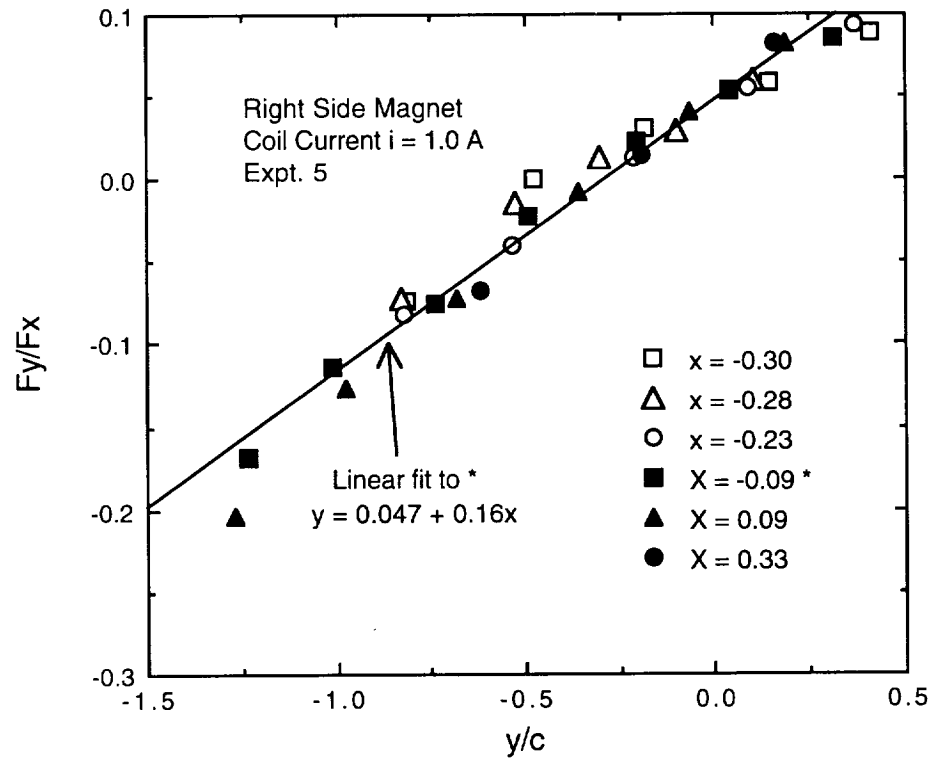
Figure 3.3.4 Ratio of normal to principal force, single magnet, 400 A-turns.
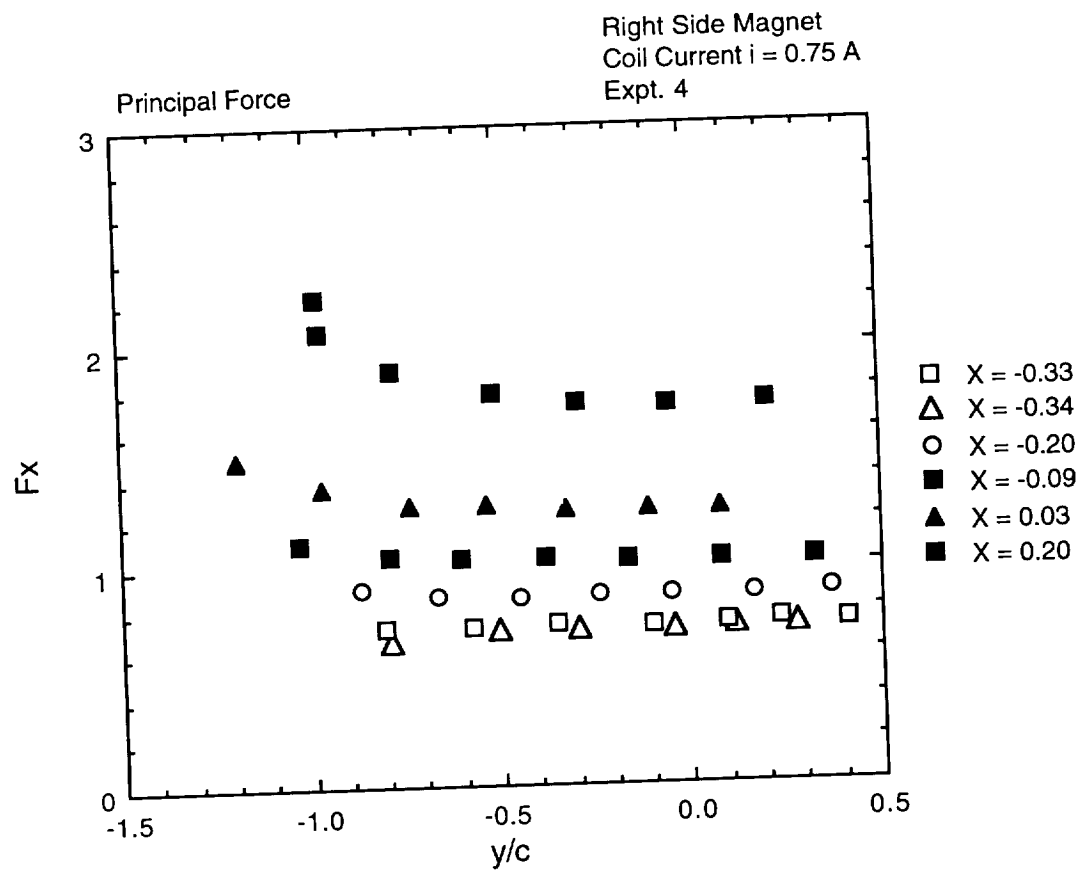
Figure 3.3.5 Principal force from one magnet at 0.75 A (300 A-turns).
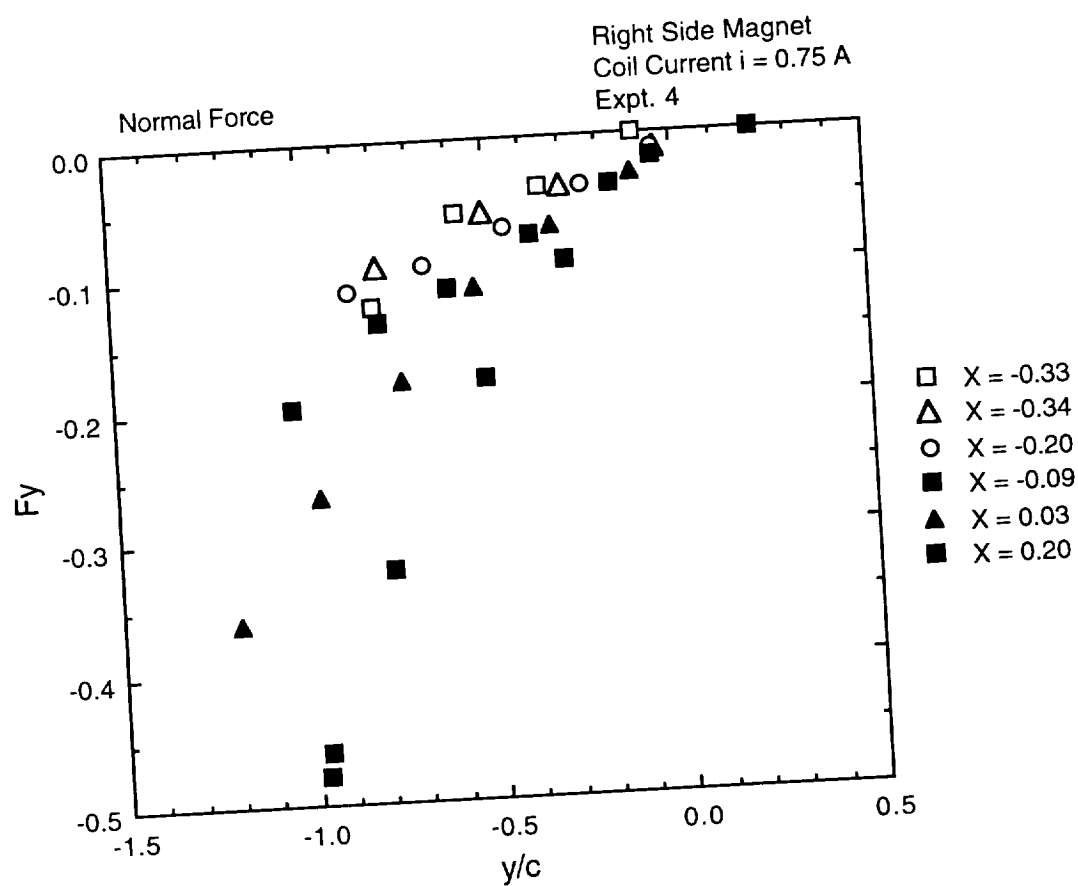
Figure 3.3.6 Principal force from one magnet at 0.75 A (300 A-turns).
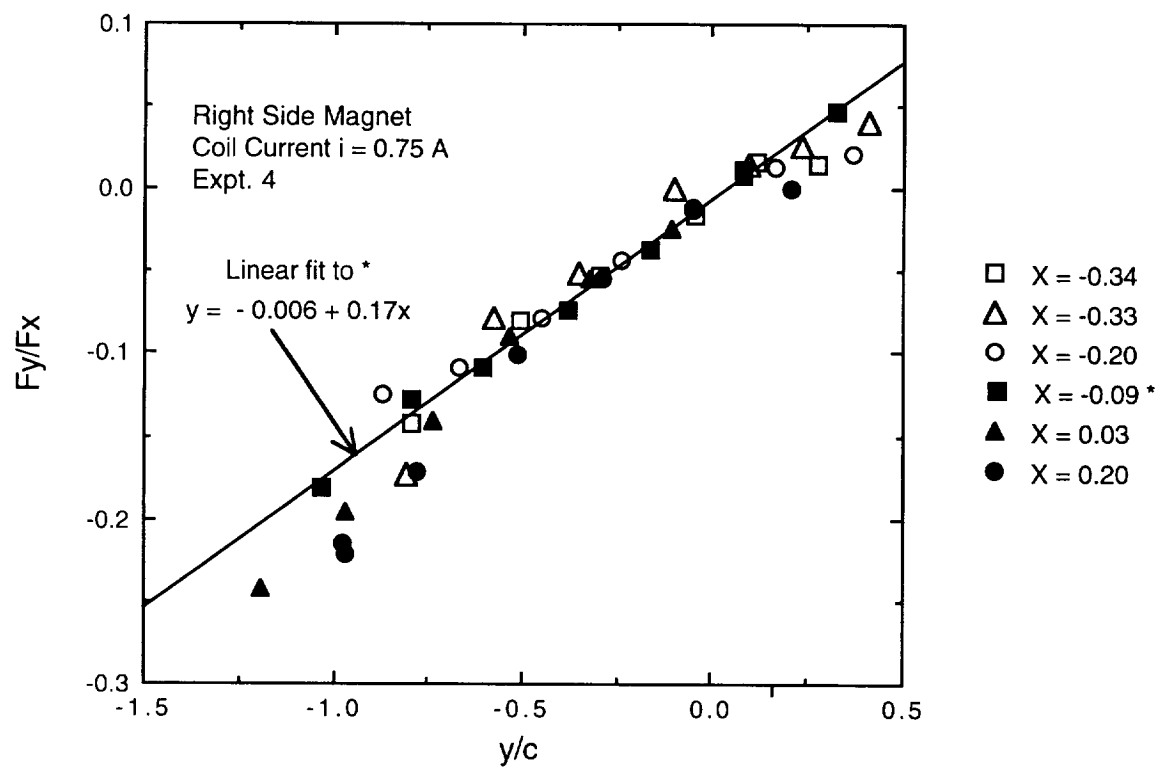
Figure 3.3.7 Ratio of normal to principal force, one magnet, 300 A-turns.
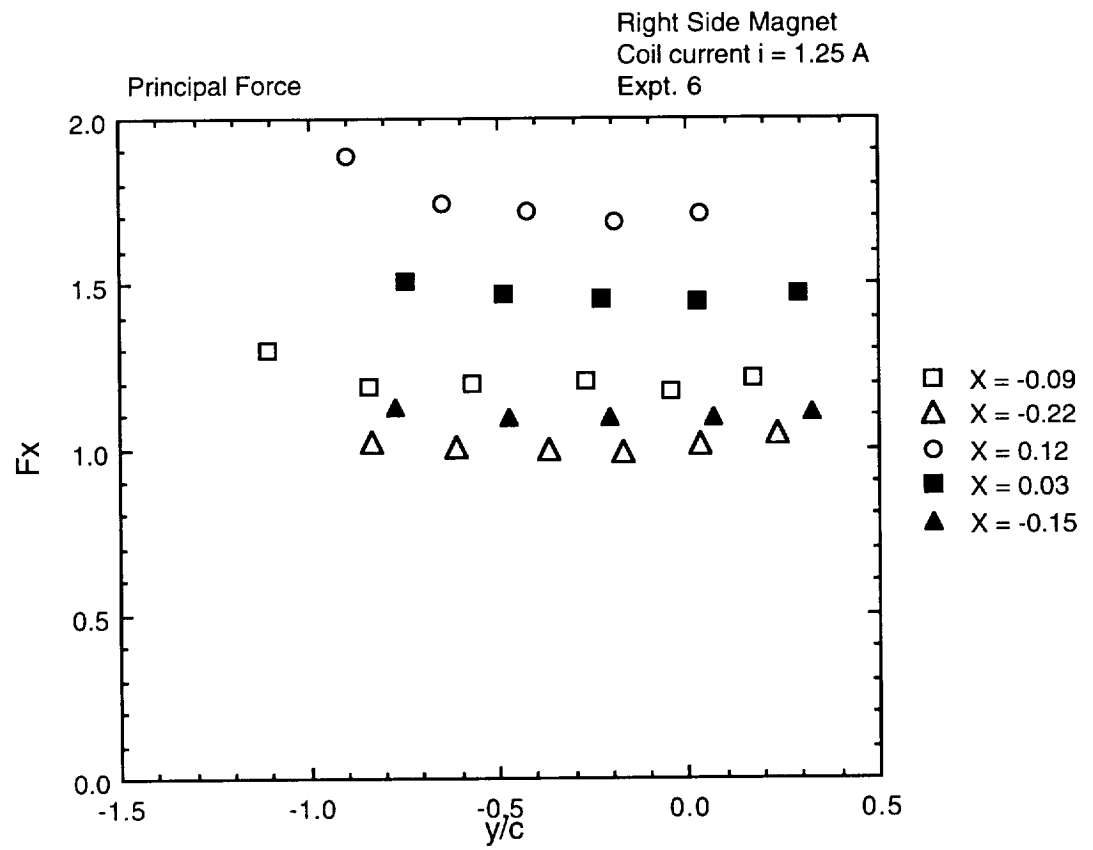
Figure 3.3.8 Principal force from single magnet at 1.25 Ampere (500 A-turns).
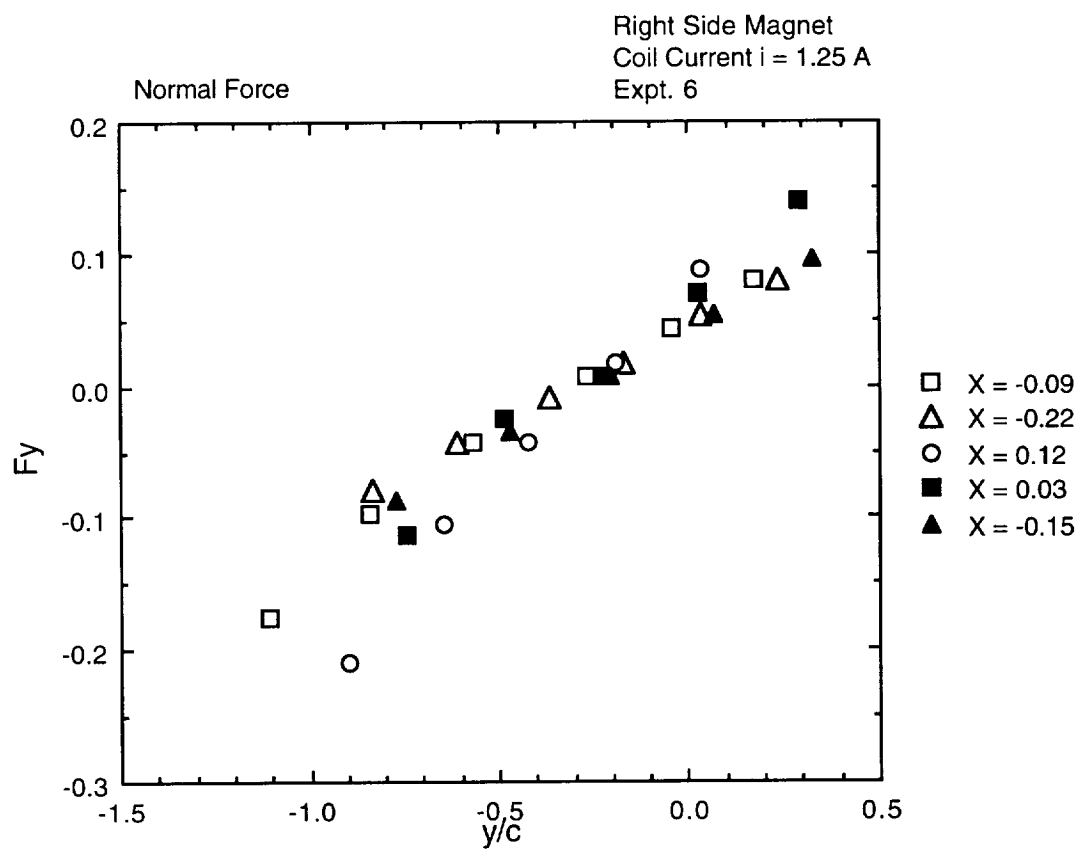
Figure 3.3.9 Normal force from single magnet at 1.25 Ampere (500 A-turns).
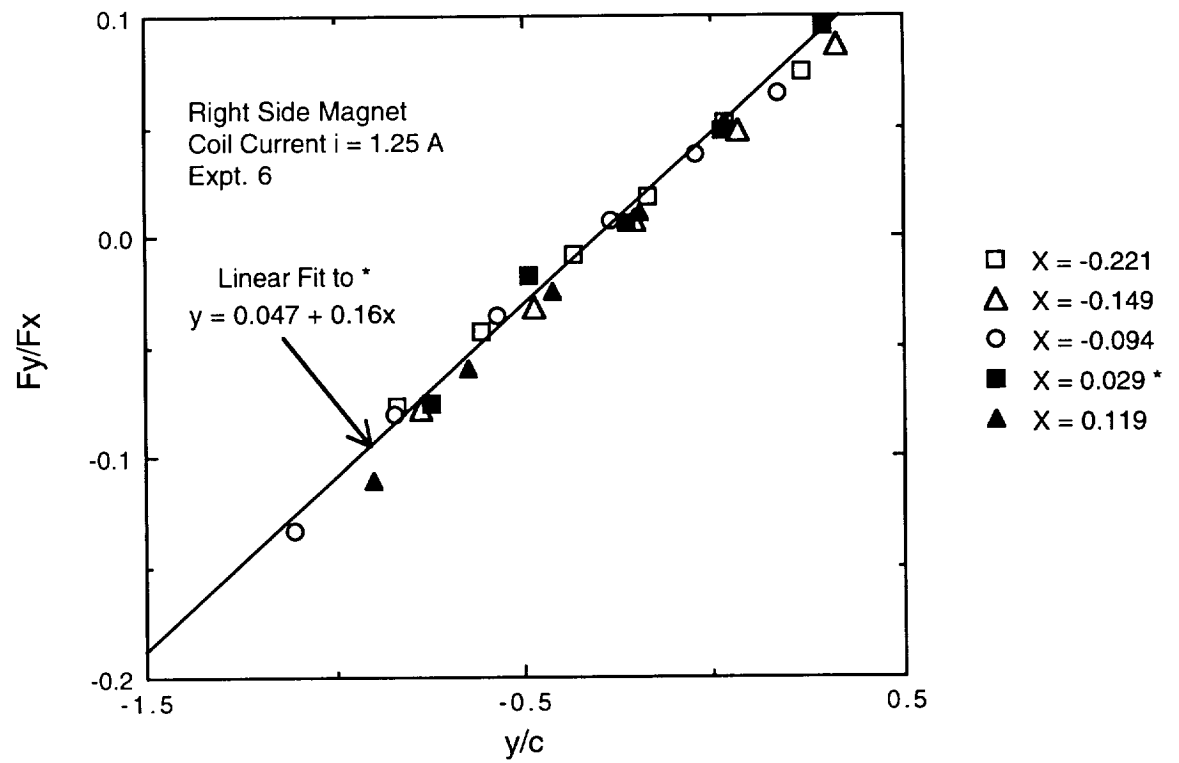
Figure 3.3.10 Ratio of normal to principal force,single magnet, 500 A-turns.
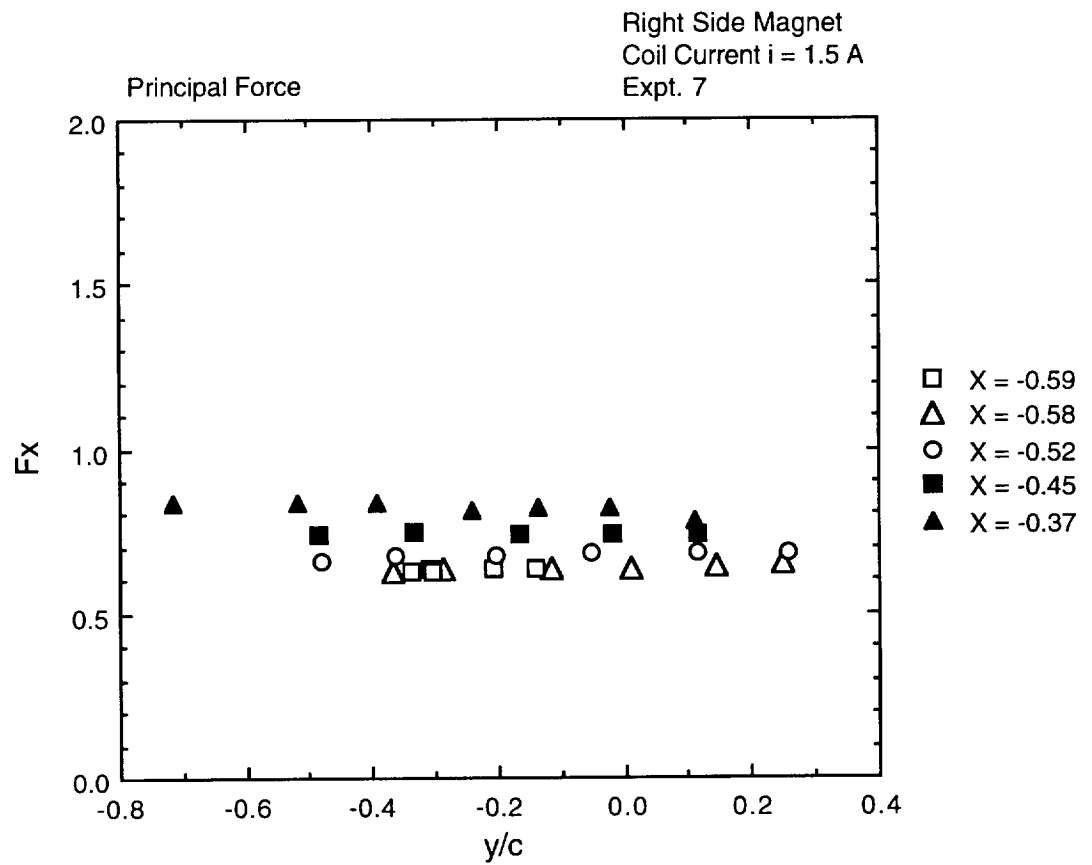
Figure 3.3.11 Principal force from single magnet at 1.5 Ampere (600 A-turns).
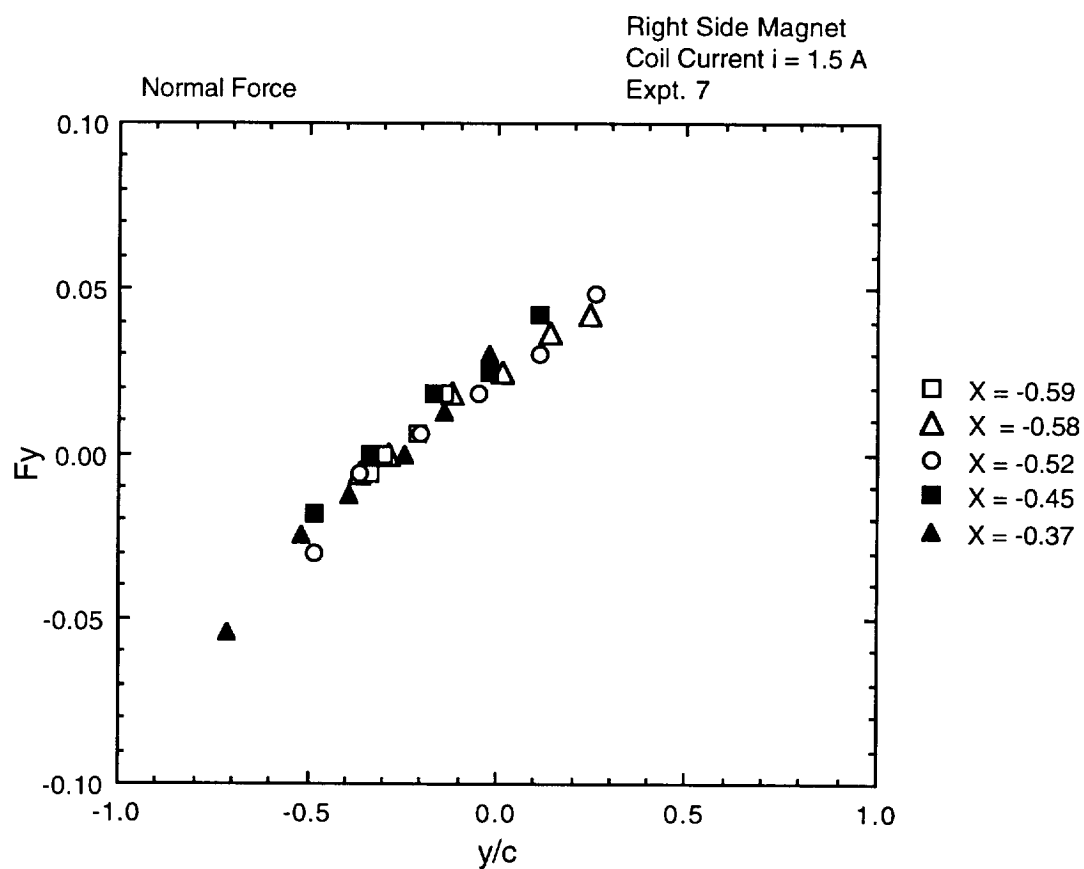
Figure 3.3.12 Normal force from single magnet at 1.5 Ampere (600 A-turns).
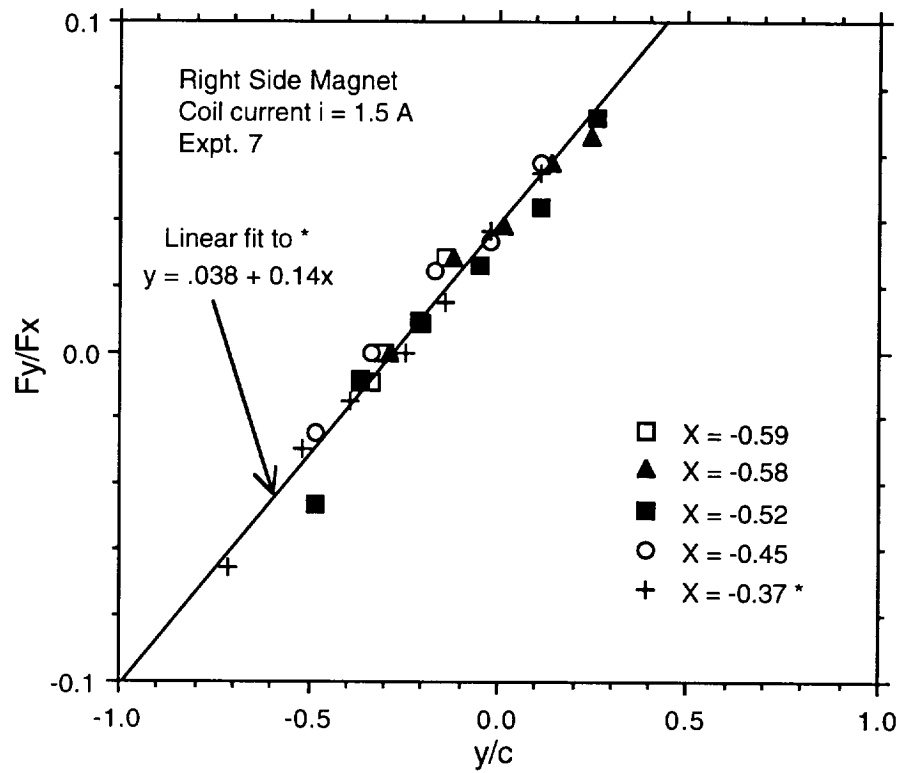
Figure 3.3.13 Ratio of normal to principal force, single magnet, 600 A-turns.

Normal Force
(nondimensional)

Right Side Magnet
Coil Current i = 1.75 A
Expt. 8

Cubic Fit to *

Cubic Fit to **

Fy

0.1

0.0

-0.1

-0.8   -0.6   -0.4   -0.2   0.0   0.2   0.4

y/c

□ X = -0.43 *
△ X = -0.30
○ X = -0.24
■ X = -0.22
▲ X = -0.07 **
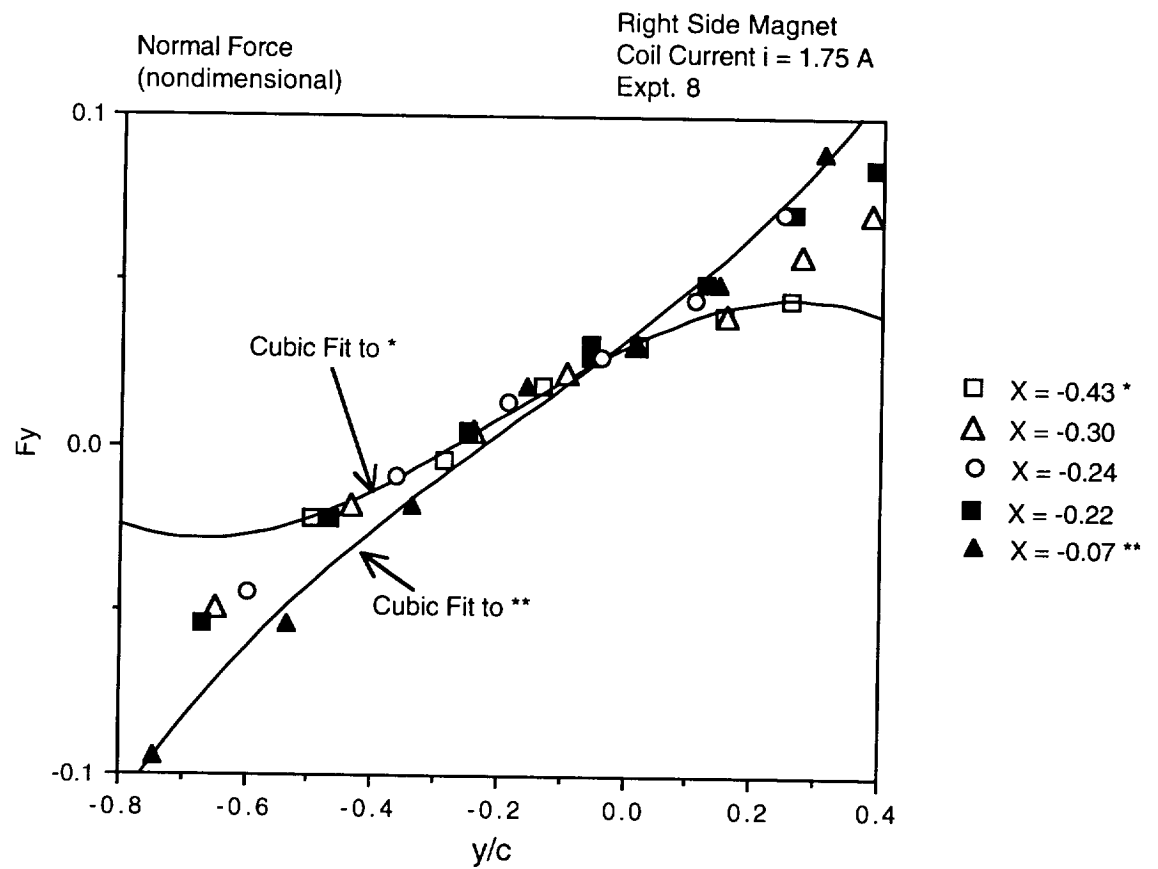
Figure 3.3.15 Normal force from single magnet at 1.75 Ampere (700 A-turns).
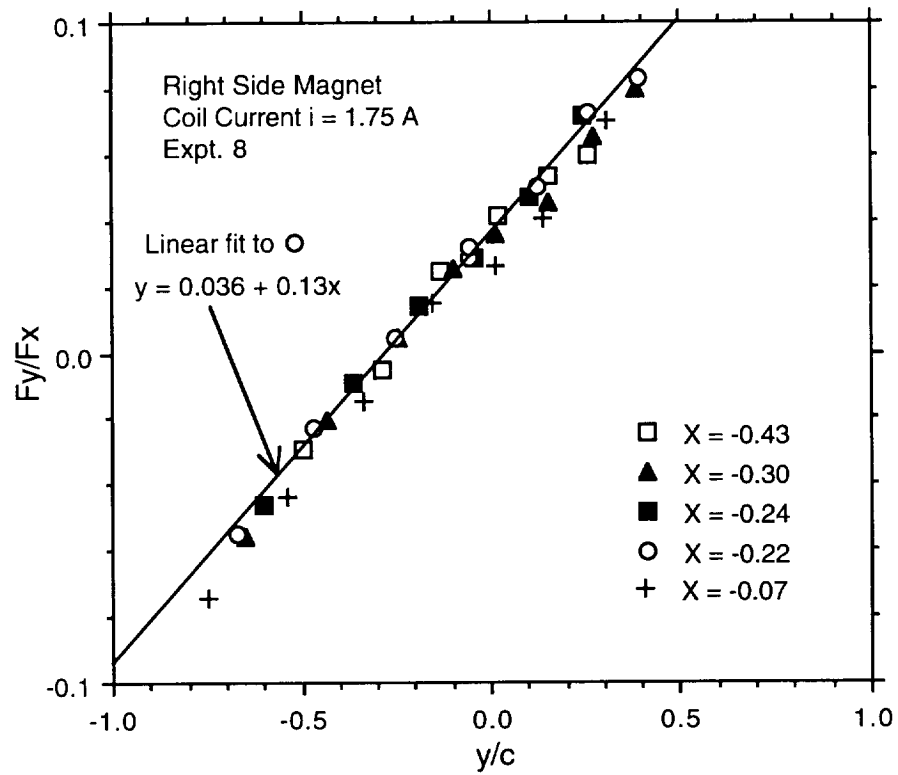
Figure 3.3.16 Ratio of principal to normal force,single magnet, 700 A-turns.

3.3.4   Measurements Using Two Magnets

The result that the normal force seems to be approximately proportional to the product of principal force and normal eccentricity indicated that the normal forces would be even more significant in the case of a strongly biased, opposed magnet pair, where the principal forces are approximately balanced. To examine this possibility a new set of experiments was conducted using two opposed magnets at the same current.

Figure 3.3.17 is a plot of the principal force exerted by the magnet pair as a function of the normal coordinate, at several values of the principal coordinate, along the symmetry axis. At small eccentricity, the force in the principal direction is near zero, as expected, since the shaft is equidistant from the two magnets. As the shaft is moved toward either of the magnets, there is a resultant force in the direction of that magnet. This force is a relatively weak function of the normal coordinate, but is seen to be largest in magnitude when both normal and principal eccentricities are large.

The normal forces exerted under these conditions are shown in Figure 3.3.18. The intercept of these force plots with the axes would nominally be at (0,0), and the precise cause of their displacement from that intercept is not yet clear, although its most likely cause seems to be uncertainty in the angular positions of the magnets around the clearance circle. This possibility is discussed further below, but it is felt that the magnitudes of the forces observed in this plot remain significant after considering this uncertainty, because all the normal forces do in fact change sign as anticipated, at some point. The magnitude of the normal force is the same order as the resultant principal force at small eccentricities and is significantly larger than the principal force at large eccentricities, as illustrated by the plot of Figure 3.3.19, which shows the ratio of normal to principal force. This occurs because the normal forces from the two magnets are additive, while the principal forces are of opposite sign.

The displacement from zero of the intercepts of the normal forces with the axes in Figure 3.3.19 and the locations of minima of the principal forces in Figure 3.3.17 have been considered in terms of possible angular uncertainty in magnet placement. The apparatus, further described in the earlier progress report, was assembled by positioning all of the magnet pole faces against a plastic mandrel and then clamping the magnet laminations in place. The mandrel was then carefully removed. Because of the method of assembly, it is felt that the uncertainty in radial position of each pole face is small, on the order of 1 % of the clearance. The largest uncertainty is that of the angular position of each magnet.

Opposed Magnet Pair
400 A turn

Figure 3.3.17 Measured principal force from opposed magnet pair at 400 A·t.

Figure 3.3.18. Measured normal force from opposed magnet pair at 400 A·t.
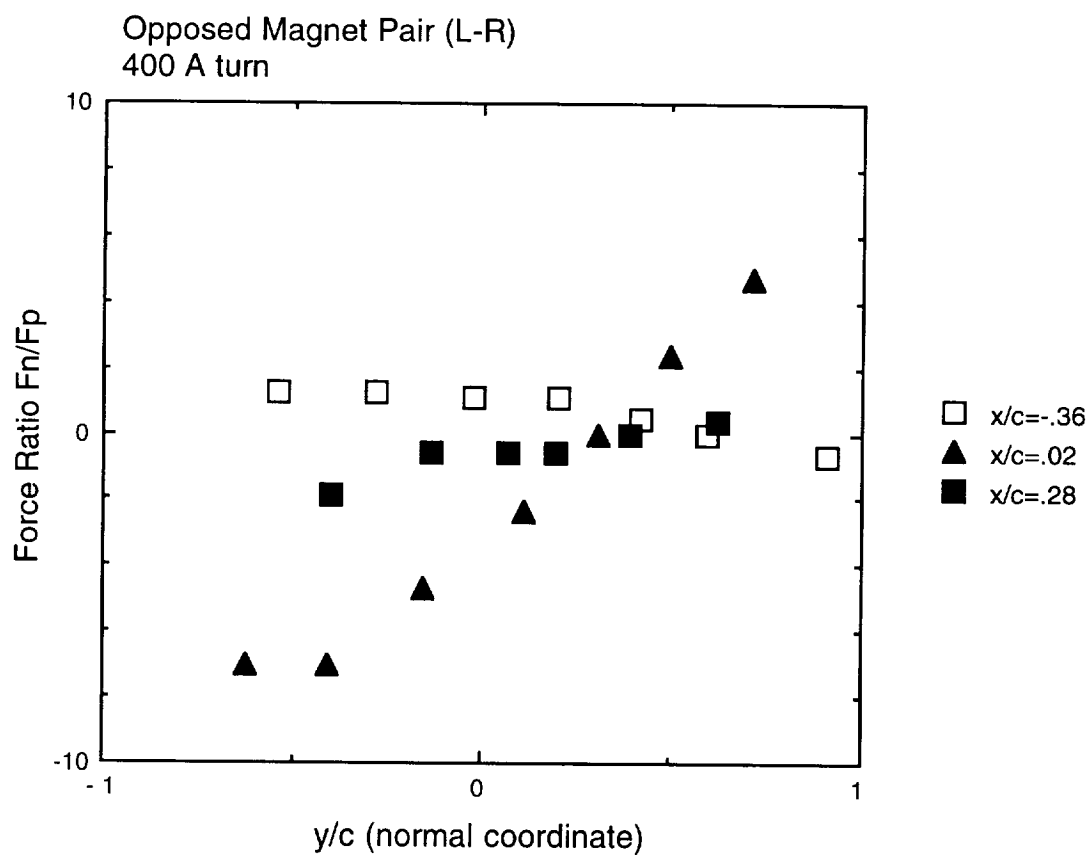
Figure 3.3.19. Force ratio from opposed magnet pair at 400 A·t.

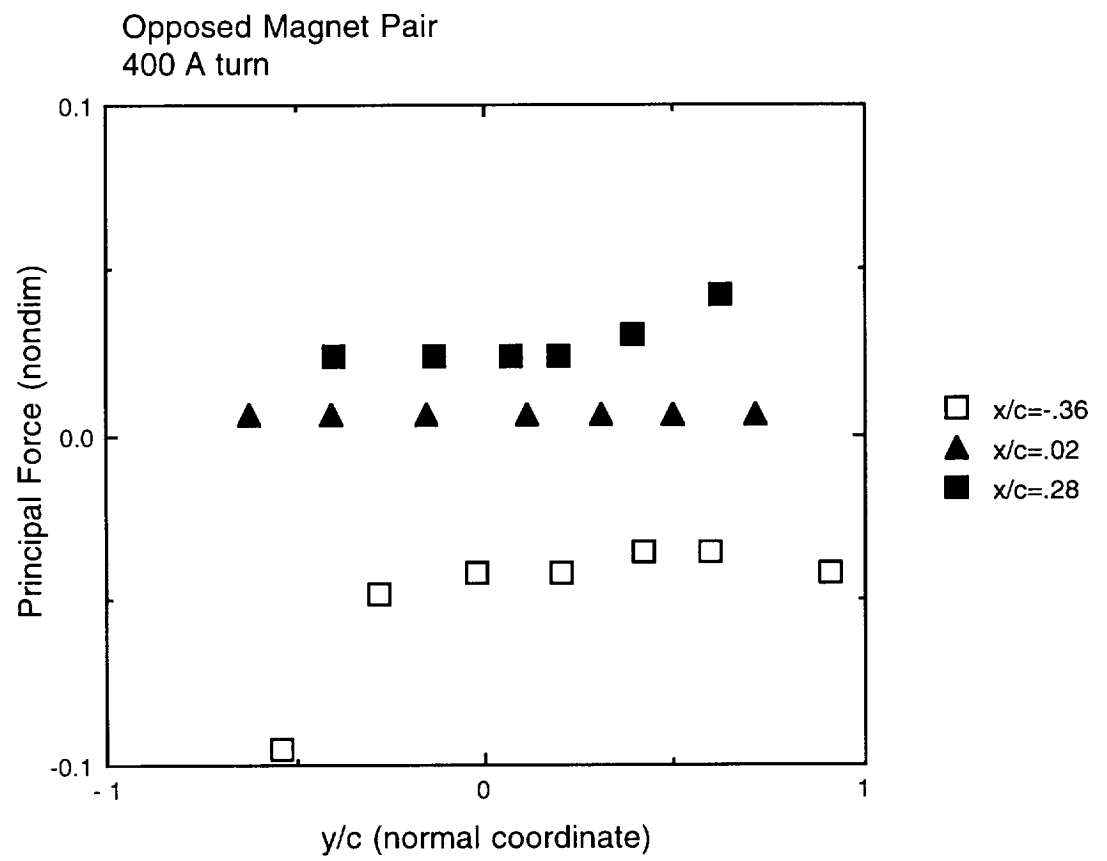Ideally, each magnet should be 90° from each of its neighbors, but in fact, assembly tolerances may have resulted in errors of up to 3° from the nominal positions. This would result in an uncertainty in orientation of the force vector associated with each magnet. Such a 3° uncertainty would result in an increase or decrease in the *normal* force component of approximately 2 % of the *principal* force from each magnet of the pair. Using a principal force of 1.0 at zero of the principal coordinate, a 3° uncertainty in principal force orientation would result in a change in the normal force of 0.06 nondimensional force units. This is an uncertainty of the same order as the displacement of intercepts of the measured normal force data from the (0,0) position in Figure 3.3.18.

If this uncertainty in angular position is the cause of the displacement of the data, it would be expected that forces measured at other current levels would behave similarly. Additional measurements were made at two other current levels, and indeed the data all are displaced by approximately the same amount. These data are shown in Figures 3.3.20 through 3.3.22, for MMF of 300 A·t, and in Figures 3.3.23 through 3.3.25, for MMF of 500 A·t (each magnet). It is therefore believed that a small error in angular positioning is present.

In interpreting the measurements of Figures 3.3.17 through 3.3.25, then, it must be remembered that this uncertainty of angular orientation may be playing a role. Nevertheless, the magnitudes of the normal forces are still significant. Those on the negative side of the plots are apparently increased by the error, but those on the positive side are apparently decreased. Therefore, it may be conservatively stated that the magnitudes of normal forces in a magnet pair that is perfectly aligned will be at least as large as those on the positive side of the plots presented. Under this interpretation the normal forces are of significant magnitude. In addition, the very fact that the system is shown to be highly sensitive to such angular errors should receive some emphasis. This factor must be considered in designing the actuator and in determining the level of robustness or the type of algorithms required for controlling the bearing. It is a strong argument, in fact, for the use of magnets made with a continuous outer ring, which would practically preclude this type of uncertainty.

The coordinate coupling illustrated in the force ratio plots has serious implications for the design of magnetic bearings and magnetically supported flexible rotor systems because it is primarily dependent not on the control currents, but on the bias currents. Since it is widely believed that magnetic bearings must be biased rather strongly in order to provide a greater degree of linearity and to improve their stability characteristics, the coordinate coupling in these systems could be strong. In flexible rotor dynamics,

coordinate coupling in bearings is regarded as an undesirable characteristic because of the potential for excitation at multiples of the running speed as well as for self-excited whirl.
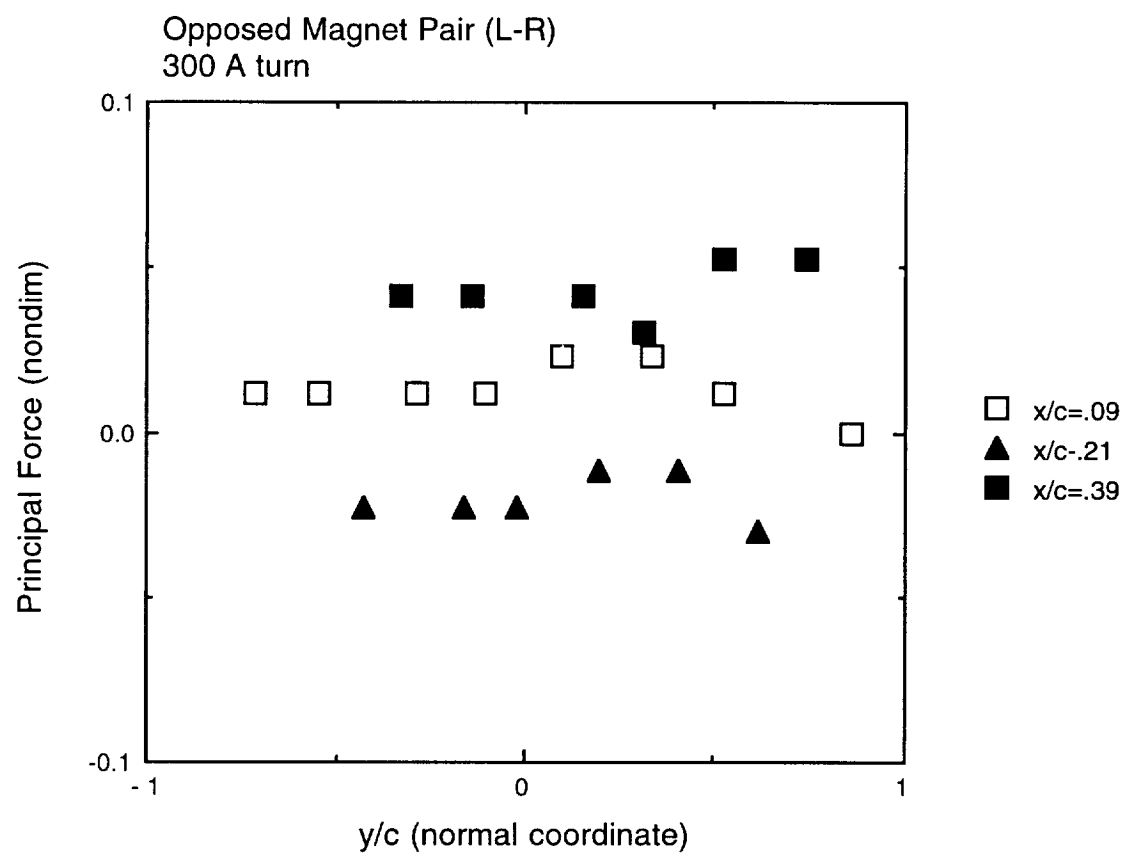
Figure 3.3.20. Measured principal force from opposed magnet pair at 300 A·t.
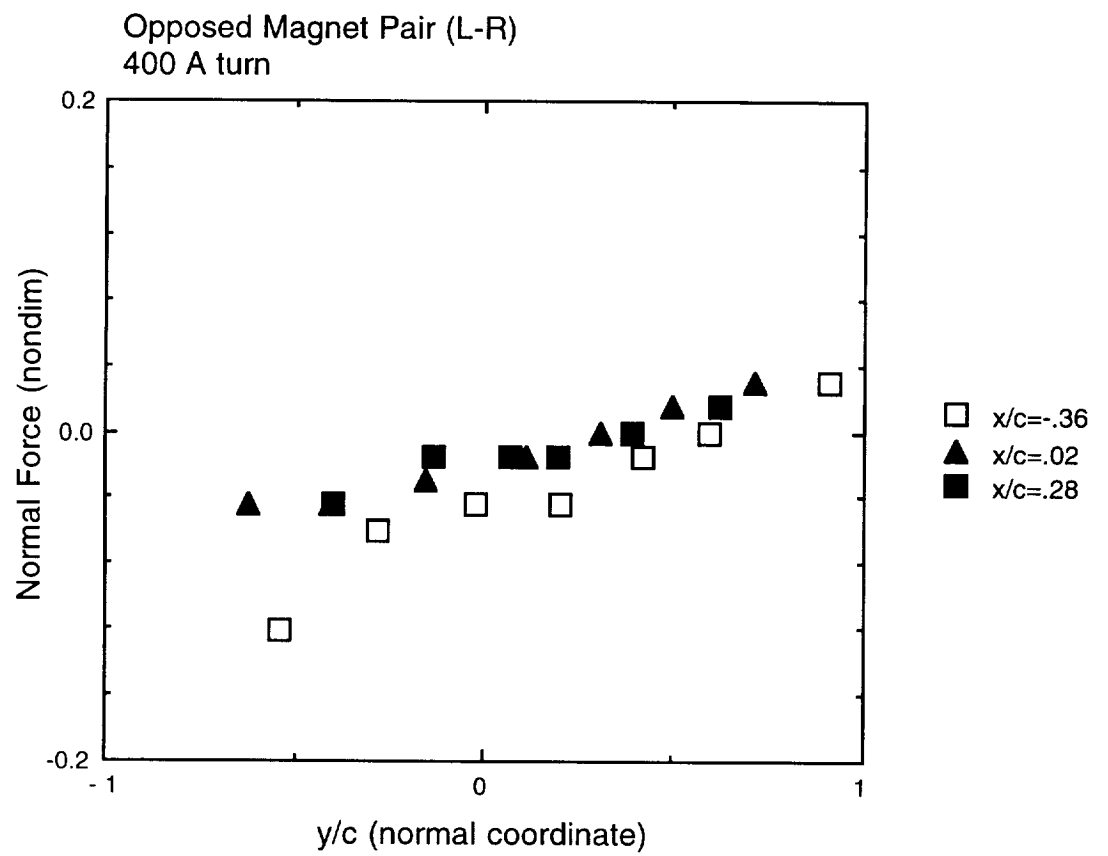
Opposed Magnet Pair (L-R)
300 A turn
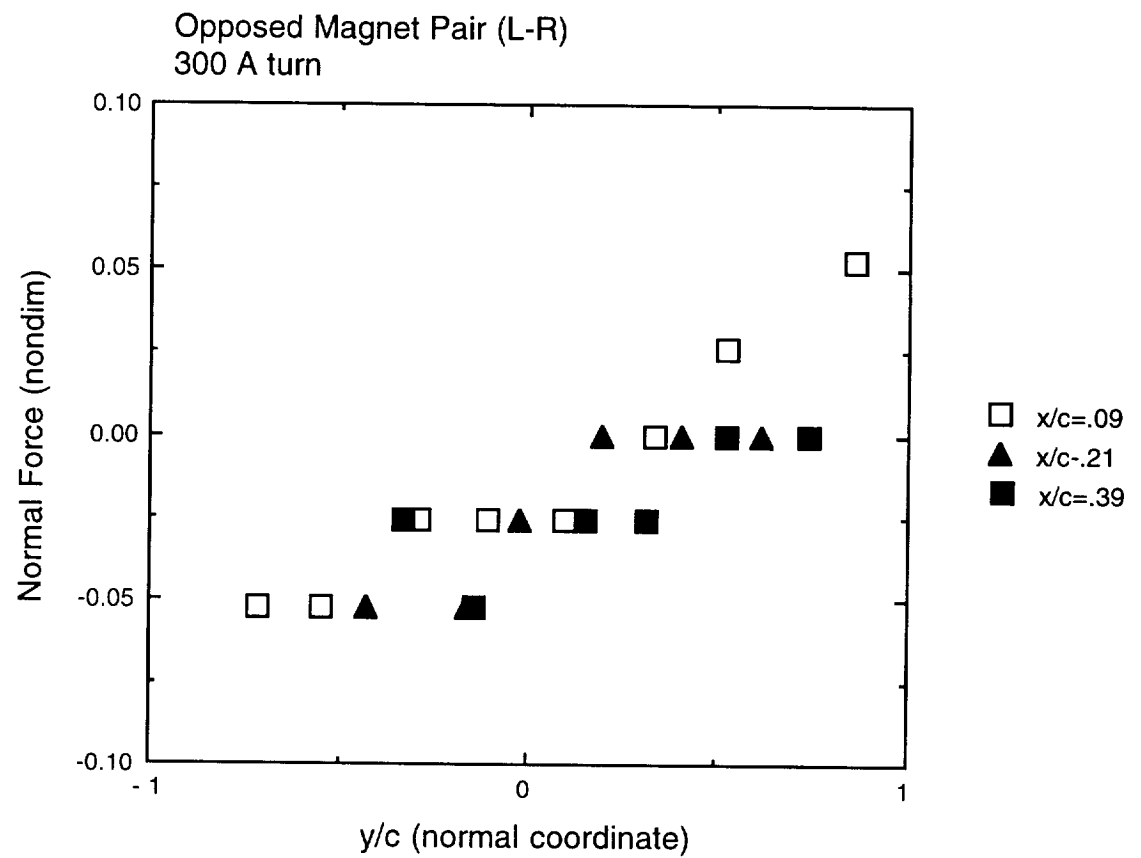
Figure 3.3.21. Measured normal force from opposed magnet pair at 300 A·t.
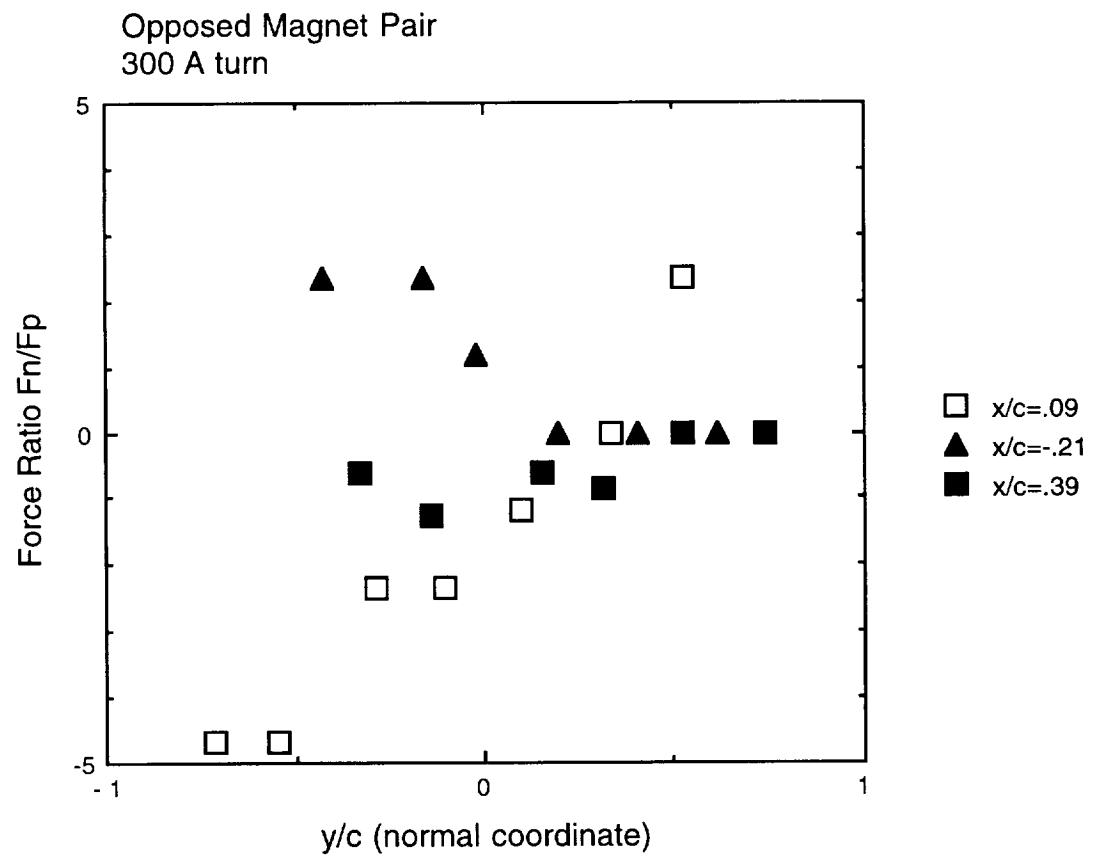
Figure 3.3.22. Force ratio from opposed magnet pair at 300 A·t.
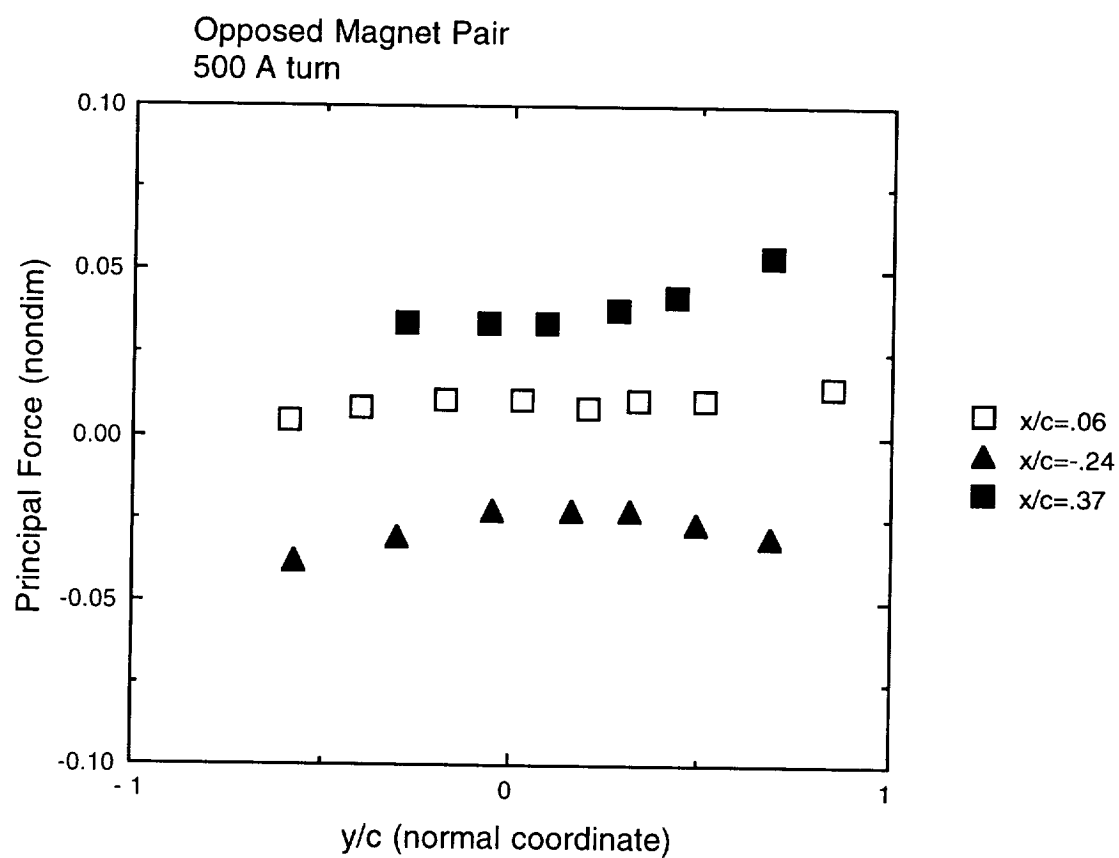
Figure 3.3.23. Measured principal force from opposed magnet pair at 500 A·t.
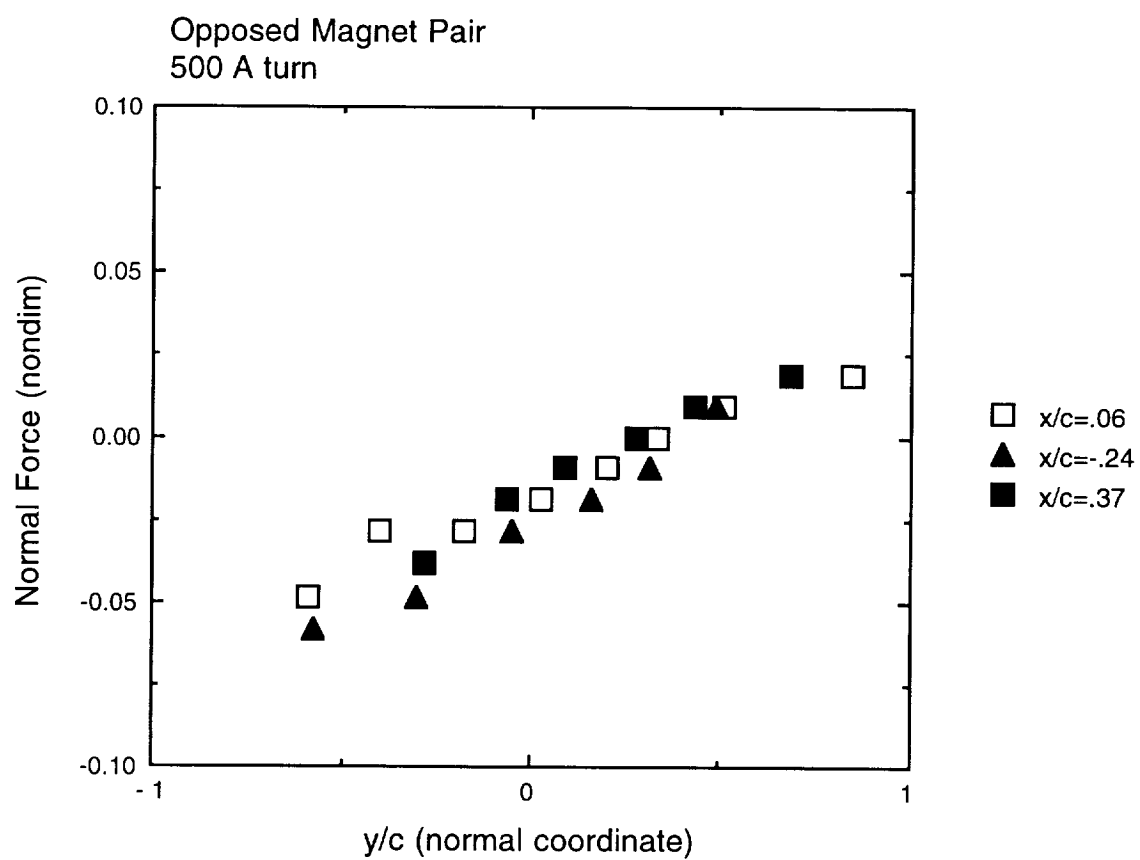
Figure 3.3.24. Measured normal force from opposed magnet pair at 500 A·t.
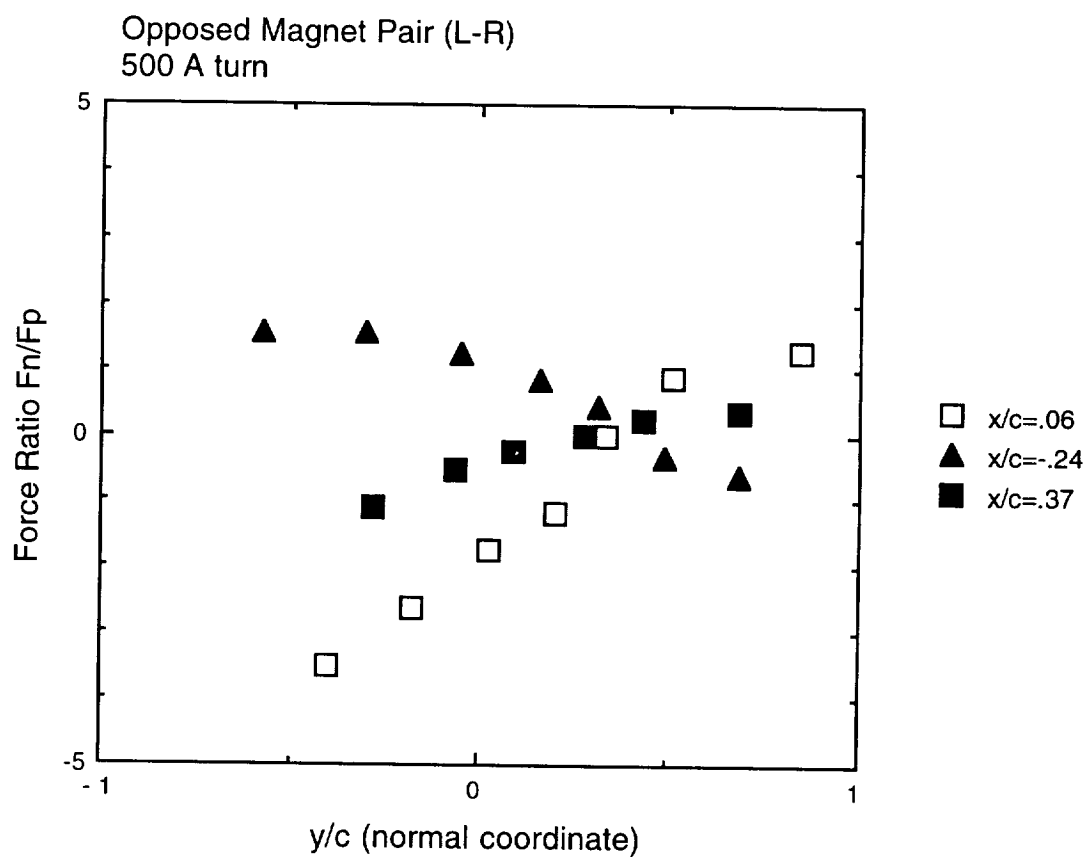
Figure 3.3.25. Force ratio from opposed magnet pair at 500 A·t.

The type of coupling illustrated by these measurements would not tend to cause whirl, because the coupling coefficients have the same sign, unlike the case of a fluid film bearing, where the normal stiffness coefficients often have opposite signs. They would, however, tend to cause an excitation at multiples of the running speed. This possibility must be considered when designing magnetic bearings for flexible rotor applications, such as gas turbines and other turbomachinery.

4. CLOSURE

4.1 Summary of Technical Findings

Both numerical and experimental studies were done to determine the characteristics of the forces exerted on a stationary shaft by a magnetic bearing actuator. The numerical studies were based on finite element computations and were of three types:

(1) Calculations based only on energy stored in air gaps.

(2) Calculations including metal parts, with locally constant magnetic permeability.

(3) Calculations including nonlinear magnetization function, with the possibility of saturation .

Principal conclusions from the analytical/numerical studies are:

(1) The distribution of saturation in the magnet core and the rotor influences both the principal attractive force and the normal force

(2) The computed normal force is considerably smaller than that measured experimentally

(3) The trend of nonlinear theory to predict larger normal forces in relation to principal forces is appropriate.

Measurements of the force versus position of the shaft were made using two separate measurement rigs, one based on strain guage measurement of forces, the other based on deflections of a calibrated beam. All measurements were static, using steady currents and a nonrotating shaft. Principal conclusions from the experimental studies, taken in conjunction with the numerical studies, are:

(4) The trends of the measured principal (y) forces agree with the predictions of the theory while the magnitudes of forces are somewhat smaller than those predicted. The y forces do not appear to decrease significantly as predicted by theory when the rotor is given an eccentricity in the x direction.

(5) The measured forces in the x direction are significantly larger than those predicted by theory when the rotor has an x eccentricity.

(6) Over the ranges of position examined, there is an approximately linear relationship between the normal eccentricity of the shaft and the ratio of normal to principal force. The constant of proportionality was not the same for all cases, but its value was consistently between 0.14 and 0.17. The nonlinear computations predicted the existence of normal forces, but did not predict such a large ratio.

(7) The type of coupling illustrated by these measurements probably would not tend to cause whirl, but they might tend to cause other kinds of nonsynchronous excitation This possibility must be considered when designing magnetic bearings for flexible rotor applications, such as gas turbines and other turbomachinery.

Further work was conducted beyond the nominal work period of this proposal, in which simulations of 2DOF systems were performed subject to these force models. The results, attached as Appendix C, show that significant nonlinear behavior can occur, including multiple coexisting solutions, bifurcations in response as the stabilities of the respective solutions change, and self-similarity in stability boundaries.

4.2 Documentation

In the course of this project, one master's thesis and one Ph.D. dissertation were completed. Edward McCaul received the degree Master of Science after defending the thesis entitled "Measurement of Forces in a Magnetic Journal Bearing" [72]. Harold Xia received the degree Doctor of Philosophy after defending the dissertation "Numerical Investigation of Suspension Force in a Magnetic Journal Bearing Actuator" [60].

Five interim progress reports were filed with NASA as this work proceeded

Presentations of results of the research performed under this grant were made at three technical meetings:

1. NASA Workshop on Aerospace Applications of Magnetic Suspension at Langley Research Center, September 1990
2. ROMAG'91 Conference on Magnetic Bearings and Dry Gas Seals, in Alexandria, VA, March 1991
3. ASME/STLE Joint Tribology Conference in St. Louis, Missouri, October 1991 (also published in ASME Journal of Tribology) [68]

In addition, related work on nonlinear dynamic simulation of magnetic bearing systems that makes direct use of the results obtained in this project have been presented at three technical conferences:

1. Third International Symposium on Magnetic Bearings, Alexandria, VA 1992 [69]
2. NASA Second International Symposium on Magnetic Suspension Technology, Seattle, WA, August 1993 [73]
3. ASME International Gas Turbine and Aeroengine Congress, The Hague, 1994 (also published in ASME Journal of Engineering for Gas Turbines and Power) [74]

5. REFERENCES

1. Dussaux, M., "The Industrial Applications of the Active Magnetic Bearings Technology," 2nd Int'l. Symposium on Magnetic Bearings, Tokyo, July 1990.

2. Habermann, H. and Liard, G., "An Active Magnetic Bearing System," Tribology International, April 1980, pp. 85-89.

3. Beams, J., "Magnetic Suspension for Small Rotors," The Review of Scientific Instruments, Vol. 21, No. 7, February 1949, pp. 182-184.

4. Tournier, P., "Magnetic Suspension for Model in a Wind Tunnel," La Recherche Aeronautique, No. 59, July-August 1957, Paris.

5. Nikolajsen, J. L., Holmes, R., and Gondhalekar, V., "Investigation of an Electromagnetic Damper for Vibration Control of a Transmission Shaft," Institution of Mechanical Engineers, Vol. 193, No. 31, 1979, pp. 331-336.

6. Schweitzer, G. and Lange, R., "Characteristics of a Magnetic Rotor Bearing for Active Vibration Control," First International Conference on Vibrations in Rotating Machinery, Institution of Mechanical Engineers, London, Cambridge, 1980.

7. Bleuler, H. and Schwietzer, G., "Decentralized Control," Applied Control and Identification Symposium, IASTED, Copenhagen, 1983.

8. Salm, J. and Schweitzer, G., "Modeling and Control of a Flexible Rotor with Magnetic Bearings," Third International Conference on Vibrations in Rotating Machinery, Institution of Mechanical Engineers, York, September 1984, Paper C277/80.

9. Allaire, P. E., Lewis, D. W., and Jain, V. K., "Feedback Control of a Single Mass Rotor on Rigid Supports," Journal of the Franklin Institute, Vol. 312, 1981 pp. 1-11.

10. Allaire, P. E., Lewis, D. W., and Knight, J. D., "Active Vibration Control of the Single Mass Rotor on Flexible Supports," Journal of the Franklin Institute, Vol. 315, 1983, pp. 211-222.

11. Heinzmann, J. et. al., "The Implementation of Automatic Vibration Control in a High Speed Rotating Test Facility," presented at ASME Winter Annual Meeting, November, 1980.

12. Kelm, R. D., "Analysis and Testing of a Magnetic Bearing for Flexible Rotors," M.S. Thesis, University of Virginia, 1986.

13. Connor, K. A. and Tichy, J. A., "Analysis of an Eddy Current Journal Bearing," ASME Jnl. of Tribology, paper 87-Trib-10.

14. Chen, H. M. and M. S. Darlow, "Magnetic Bearing with Rotating Force Control," ASME Jnl. of Tribology, paper 87-Trib-7.

15. Walowit, J. A. and Pinkus, O., "Analytical and Experimental Investigation of Magnetic Support Systems. Part 1: Analysis," ASME Jnl. of Lubrication Technology, Vol. 104, No. 2, July 1982, pp. 418-428.

16. Albrecht, P. R., Walowit, J. and Pinkus, O., "Analytical and Experimental Investigation of Magnetic Support Systems. Part 2: Experimental Investigation," ASME Jnl. of Lubrication Technology, Vol. 104, No. 2, July 1982, pp. 429-437.

17. Keith, F. J., Williams R. D. and Allaire, P. E., "Digital Control of Magnetic Bearings Supporting a Multimass Flexible Rotor," STLE prepring 89-AM-1B-3.

18. Maslen, E., Hermann, P., Scott, M. and Humphris, R.R., "Practical Limits to the Performance of Magnetic Bearings: Peak Force, Slew Rate and Displacement Sensitivity," ASME Journal of Tribology, in press.

19. Schweitzer, G., (ed), Magnetic Bearings: Proceedings of the First International Symposium, ETH Zurich, Switzerland, June 6-8, 1988, Springer-Verlag, Berlin, 1989.

20. Hisatani, M., "Identification and Optimization of Active Magnetic Bearing Systems using Measured Nyquist Diagrams," Magnetic Bearings: Proceedings of the First International Symposium, ETH Zurich, Switzerland, June 6-8, 1988, Springer-Verlag, Berlin, 1989.

21. Wagner, N. G. and Pietruszka, W. D., "Identification of Rotordynamic Parameters on a Test Stand with Active Magnetic Bearings," Magnetic Bearings: Proceedings of the First International Symposium, ETH Zurich, Switzerland, June 6-8, 1988, Springer-Verlag, Berlin, 1989.

22. Lewis, D. W., Maslen, E., and Humphris, R. R., "Dynamic Response of Magnetically Supported Rotor," Magnetic Bearings: Proceedings of the First International Symposium, ETH Zurich, Switzerland, June 6-8, 1988, Springer-Verlag, Berlin, 1989.

23. Nakajima, A., "Research and Development of Magnetic Bearing Flywheels for Attitude Control of Spacecraft," Magnetic Bearings: Proceedings of the First International Symposium, ETH Zurich, Switzerland, June 6-8, 1988, Springer-Verlag, Berlin, 1989.

24. Bichler, U. and Eckhardt, T., "A 3(5) Degree of Freedom Electrodynamic - Bearing Wheel for 3-Axis Spacecraft Attitude Control Application," Magnetic Bearings: Proceedings of the First International Symposium, ETH Zurich, Switzerland, June 6-8, 1988, Springer-Verlag, Berlin, 1989.

25. Dussaux, M., "The Industrial Applications of the Active Magnetic Bearings Technology," ROMAG '91 Conference on Magnetic Bearings and Dry Gas Seals, Washington, March 1991.

26. Higuchi, T., (ed.) "Proceedings of the Second International Symposium on Magnetic Bearings," Tokyo, Japan, July 1990.

27. Bichler, U. J., "A Low Noise Magnetic Bearing Wheel for Space Application," 2nd Int'l. Symposium on Magnetic Bearings, Tokyo, July 1990.

28. Zmood, R. B., Pang, D., Anand D. K., and Kirk, J. A., "Robust Magnetic Bearings for Flywheel Energy Storage Systems," 2nd Int'l. Symposium on Magnetic Bearings, Tokyo, July 1990.

29. Möller, B., "Using High-speed Electrospindles with Active Magnetic Bearings for boring of Noncircular Shapes," 2nd Int'l. Symposium on Magnetic Bearings, Tokyo, July 1990.

30. Ota, M., Ando, S., and Oshima, J., "Monitoring and Actuating Function of the Internal Grinding Spindle with Magnetic Bearing," 2nd Int'l. Symposium on Magnetic Bearings, Tokyo, July 1990.

31. Siegwart, R., Larsonneur, R., and Traxler, A., "Design and Performance of a High Speed Milling Spindle in Digitally Controlled Active Magnetic Bearings," 2nd Int'l. Symposium on Magnetic Bearings, Tokyo, July 1990.

32. McGinnis, G., Cooper, P., Janik. G., Jones, G., and Shultz, R., "Application of Magnetic Bearings in a Multistage Boiler Feed Pump," 2nd Int'l. Symposium on Magnetic Bearings, Tokyo, July 1990.

33. Schmied, J., "Experience with Magnetic Bearings Supporting a Pipeline Compressor," 2nd Int'l. Symposium on Magnetic Bearings, Tokyo, July 1990.

34. Bührer, P., Engel, J., and Glass, D., "The MALVE Experimental Circulator - The First Large Nuclear Component with Active Magnetic Bearings," 2nd Int'l. Symposium on Magnetic Bearings, Tokyo, July 1990.

35. Youcef-Toumi, K., Reddy, S., and Vithiananthan, I., "A Digital Time Delay Controller for Active Magnetic Bearings," 2nd Int'l. Symposium on Magnetic Bearings, Tokyo, July 1990.

36. Brunet, M. and Rioland, J., "Self-tuning Digital State Controller for Active Magnetic Bearings," 2nd Int'l. Symposium on Magnetic Bearings, Tokyo, July 1990.

37. Higuchi, T., Mizuno, T., and Tsukamoto, M., "Digital Control System for Magnetic Bearings with Automatic Balancing," 2nd Int'l. Symposium on Magnetic Bearings, Tokyo, July 1990.

38. Keith, F. J., Maslen, E. H., Humphris, R. R., and Williams, R. D., "Switching Amplifier Design for Magnetic Bearings," 2nd Int'l. Symposium on Magnetic Bearings, Tokyo, July 1990.

39. Bardas, T., Harris T., Oleksuk, C., Eisenbart, G., and Geerligs, J., "Problems, Solutions and Applications in the Development of a Wide Band Power Amplifier for Magnetic Bearings," 2nd Int'l. Symposium on Magnetic Bearings, Tokyo, July 1990.

40. LaRocca, P. Fermental, D., and Cusson, E., "Performance Comparison Between Centralized and Decentralized Control of the Jeffcott Rotor," 2nd Int'l. Symposium on Magnetic Bearings, Tokyo, July 1990.

41. Matsumura, F., Fujita, M. and Okawa, K., "Modeling and Control of Magnetic Bearing Systems Achieving a Rotation Around the Axis of Inertia," 2nd Int'l. Symposium on Magnetic Bearings, Tokyo, July 1990.

42. Murakami, C., "A Design Method of a Dynamic Compensator of Conical Modes for Magnetic Bearings of a Rigid Spinning Rotor," 2nd Int'l. Symposium on Magnetic Bearings, Tokyo, July 1990.

43. Nonami, K. and Yamaguchi, H., "Active Vibration Control of Flexible Rotor for High Order Critical Speeds Using Magnetic Bearings," 2nd Int'l. Symposium on Magnetic Bearings, Tokyo, July 1990.

44. Herzog, R., and Bleuler, H., "Stiff AMB Control Using an H^{∞} Approach," 2nd Int'l. Symposium on Magnetic Bearings, Tokyo, July 1990.

45. Fujita, M., Matsumura, F., and Shimizu, M., "H^{∞} Robust Control Design for a Magnetic Suspension System," 2nd Int'l. Symposium on Magnetic Bearings, Tokyo, July 1990.

46. Ueyama, H., and Fujimoto, Y., "Iron Losses and Windy Losses of High Rotational Speed Rotor Suspended by Magnetic Bearings," 2nd Int'l. Symposium on Magnetic Bearings, Tokyo, July 1990.

47. Zhang, H., Nagata, T., Okada, Y., and Tani, J., "Flexible Shell Structured Rotor Controlled by Digital Magnetic Bearings (Transputer Control)," 2nd Int'l. Symposium on Magnetic Bearings, Tokyo, July 1990.

48. Chen, H. M., Wilson, D., Lewis, P., and Hurley, J., "Stability Analysis for Rotors Supported by Active Magnetic Bearings," 2nd Int'l. Symposium on Magnetic Bearings, Tokyo, July 1990.

49. Satoh, I., Murakami, C., Nakajima A., and Kanemitsu, Y., "A Self-excited Vibration of Magnetic Bearing System with Flexible Structure," 2nd Int'l. Symposium on Magnetic Bearings, Tokyo, July 1990.

50. Ziegler Jr., E., "Active Noise Cancellation with Magnetic Bearings," ROMAG '91 Conference on Magnetic Bearings and Dry Gas Seals, Washington, March 1991.

51. Knospe, C., "Controller Design for Microgravity Isolation," ROMAG '91 Conference on Magnetic Bearings and Dry Gas Seals, Washington, March 1991.

52. Gniady, J., "Optical Table Vibration Cancellation Using Electromagentic Thrust Bearings," ROMAG '91 Conference on Magnetic Bearings and Dry Gas Seals, Washington, March 1991.

53. Barrett, L., "The Application of Magnetic Bearings to Gas Turbine Aircraft Engines," ROMAG '91 Conference on Magnetic Bearings and Dry Gas Seals, Washington, March 1991.

54. Lang, K. W., "Study on Magnetic Bearings for Rocket Engine Turbopumps," ROMAG '91 Conference on Magnetic Bearings and Dry Gas Seals, Washington, March 1991.

55. Kirk, G., and Rawal, D., "Evaluation of AMB Rotor Response Considering Sensor Non-collocation," ROMAG '91 Conference on Magnetic Bearings and Dry Gas Seals, Washington, March 1991.

56. Kanemitsu, Y., Ohsawa, M., Watanabe, K., and Shirao, Y.,"Active Control of a FLexible Rotor by a Magnetic Bearing - Effect of Power Amplifier on Unbalance Response of Rotor," ROMAG '91 Conference on Magnetic Bearings and Dry Gas Seals, Washington, March 1991.

57. Maslen, E., "Contollability for Rotors," ROMAG '91 Conference on Magnetic Bearings and Dry Gas Seals, Washington, March 1991.

58. Allaire, P. E., ed. "Proceedings of the Third International Symposium on Magnetic Bearings," July 29-31, 1992, Technomic Publishing, 1992.

59. "Proceedings of Mag '93: Magnetic Bearings, Magnetic Drives and Dry Gas Seals Conference and Exhibition," July 29-30, 1993, Technomic Publishing, 1993.

61. Chari, M. V. K. and Silvester, P., "Analysis of Turboalternator Magnetic Fields by Finite Elements," IEE Trans. on Power Apparatus and Systems, V. PAS-90, No. 2, March/April 1971, pp. 454-464.

62. Cullity, B., Introduction to Magnetic Materials, Addison-Wesley, Reading, Pa., 1973.

63. Zienkiewicz, O. C. and Phillips, D. V., "An Automatic Mesh Generation Scheme for Plane and Curved Surfaces by Isoparametric Coordinates," Int'l. Jnl. for Numerical Methods in Engineering, V. 3, pp. 519-528 (1971).

64. Liu, Y. and Chen, K., "A Two-Dimensional Mesh Generator for Variable Order Triangular and Rectangular Elements," Computers and Structures, V. 29, No. 6, pp 1033-1053, 1988.

65. Cavendish, J. C., "Automatic Triangularization of Arbitrary Planar Domains for the Finite Element Method," Int'l Jnl. for Numerical Methods in Ingeneering, V. 8, pp. 679-696 (1974).

66. Collins, R. J. "Bandwidth Reduction by Automatic Renumbering," Int'l. Jnl. for Numerical Methods in Engineering, V. 6, pp. 345-356 (1973).

68. Knight, J. D., Xia, Z., McCaul, E. and Hacker, H., "Determination of Forces in a Magnetic Bearing Actuator: Numerical Computation with Comparison to Experiment," Journal of Tribology, V 114, No. 4 , October 1992, pp. 796-801.

67. Coulomb, J. L., "A Methodology for the Determination of Global Electromechanical Quantities from a Finite Element Analysis and Its Application to the Evaluation of Magnetic Forces, Torques and Stiffness," IEEE Trans. on Magnetics, V. MAG-19, No. 6, Nov. 1983, pp. 2514-2519.

70. Silvester, P. and Chari, V.K., "Finite Element Solution of Saturable Magnetic Field Problems," IEEE Trans. on Power Apparatus and Systems, Vol. PAS-90, No. 2, March/April 1971, pp. 454-464.

72. McCaul, E. B., Measurement of Forces in a Magnetic Journal Bearing, Master's Thesis, Duke University, 1991.

60. Xia, H. Z., Numerical Investigation of Suspension Force in a Magnetic Journal Bearing Actuator, Ph.D. Thesis, Duke University, 1992.

71. Knight, J. D., McCaul, E., and Xia, Z., "Measurement and Calculation of Forces in a Magnetic Journal Bearing Actuator," Proceedings of ROMAG'91 Conference on Magnetic Bearings and Dry Gas Seals, March 1991.

69. Knight, J. D., Xia, Z., and McCaul, E., "Forces in Magnetic Journal Bearings: Nonlinear Computation and Experimental Measurement," Third International Symposium on Magnetic Bearings, Alexandria, VA, July 1992.

73. Knight, J. D., Walsh, T., and Virgin, L. N., "Dynamic Analysis of a Magnetic Bearing System with Flux Control," proceedings, 2nd International Symposium on Magnetic Suspension Technology, Seattle, WA, August 1993.

74. Virgin, L. N., Knight, J. D., and Walsh, T., "Nonlinear Behavior of a Magnetic Bearing System," paper 94-GT-341, ASME Gas Turbine Conference, The Hague, June 1994, accepted for ASME Journal of Engineering for Gas Turbines and Power.

APPENDICES (individually page numbered)

APPENDIX A -   **PROGRAM FOR FORCE CALCULATION USING AIR GAPS ONLY**

APPENDIX B -   **COMPUTATIONAL METHODS INCLUDING METAL REGIONS**

APPENDIX C -   **MASTER'S THESIS OF THOMAS WALSH**

APPENDIX A -   PROGRAM FOR FORCE CALCULATION USING AIR GAPS ONLY

```
C$$$$$$$$$$$$$$$$$$$$$$$$$$$$$$$$$$$$$$$$$$$$$$$$$$$$$$$$$$$$$$$$$$$$$$$$$
$
C
C                        GAPFOR                        SEPT. 1990
C
C    THIS ALGORITHM CALCULATES THE MAGNETIC SUSPENSION FORCE FOR A
C    MAGNETIC JOURNAL BEARING ACTUATOR.  THE CALCULATION REGION
INVOLVES
C    THE AIR GAP BETWEEN THE MAGNET POLE-FACES AND THE ROTOR WHERE THE
C    MAGNETIC FIELD IS DOMINATED BY LAPLACE EQUATION.  MAGNETIC FORCE
C    IS DETERMINED BY USING VIRTUAL WORK PRINCIPLE.
C
C$$$$$$$$$$$$$$$$$$$$$$$$$$$$$$$$$$$$$$$$$$$$$$$$$$$$$$$$$$$$$$$$$$$$$$$$$
$
C
C                        INPUT
C
C    LINE1-TITLE
C    LINE2- E: ECCENTRICITY OF SHAFT CENTER
C           C: CLEARENCE(IN.)
C           R: JOURNAL RADIUS(IN.)
C           ANG1,ANG2: LOCATION OF THE MAGNET POLE 2(DEGREES)
C           EBC: CODE USED FOR EXPANDING PART AS A PERCENTAGE OF THE
C               GAP REGION
C               (A) 0: 10% OF THE GAP REGION
C               (B) 1: 20% OF THE GAP REGION
C           CURRENT: CURRENT IN COILS(A)
C           NCOIL: # OF TURNS(EACH COIL)
C    LINE3- N: CIRCUMFERENTIAL ELEMENT DIVISIONS
C           M: RADIAL ELEMENT DIVISIONS
C           ALPHA: ANGLE BETWEEN POLES
C           NBON: SPECIFIED BOUNDARIES
C           PHISTAR1: ARBITRARILY ASSUMED B.C ALONG POLE 1
C           PHIR: BOUNDARY CONDITION ALONG ROTOR CURVATURE
C           MG_DETH: MAGNET DEPTH
C
C
C                        OUTPUT
C
C    PHI---------MAGNETIC POTENTIAL FIELD
C    BETA--------MAGNETIC FLUX DENSITY
C    GAMMA-------MAGNETIC FLUX
C    SIGMA-------MAGNETIC ENERGY
C    FORCE-------MAGNETIC SUSPENSION FORCE
C
C                        SUBROUTINES
C
C    COORD-------GRID GENERATION
C    ELEMOD------ELEMENT NODAL SPECIFICATION
C    ASSEML------GLOBAL BANDED COEFFICENT MATRIX
C    MODMAT------MODIFIED BANDED MATRIX
C    GAUSS2------GAUSS ELEMINATION METHOD FOR BANDED MATRIX
C    FLUXEG------MAGNETIC FLUX & ENERGY
C
```

```
C$$$$$$$$$$$$$$$$$$$$$$$$$$$$$$$$$$$$$$$$$$$$$$$$$$$$$$$$$$$$$$$$$$$$$$$$$$
$
C
      IMPLICIT DOUBLE PRECISION(A-H,O-Z)
      REAL*8 KAPPA1,KAPPA2,MMF,MG_DETH,MU
      REAL*8 BETA(1000),AL(1000),PHI(800),PHIS(800),XJJ(50),YJJ(50,50)
      REAL*8 X(800),Y(800),FJJ(50,50),RECMAT(800,100),REMMAT(800,100)
      REAL*8 RX(300,10),RY(300,10),RPHI(300,10),XPLOT(500,4)
      REAL*8 YPLOT(500,4),PHIPLOT(500,4),BETAPLOT(1000)
      REAL*8 ANGPLOT(1000),XBETA(1000),YBETA(1000)
      INTEGER EB,EBC,EM,ELEMT,B1,B2
      INTEGER X_NUMBER,X_POINT,Y_POINT,Y_P
      INTEGER II(1000),JJ(1000),KK(1000),IBOUND(2,800)
      IN=1
      IO=9
C
      WRITE(IO,5)
5     FORMAT(1H1,10X,'*** MAGNETIC FORCE CALCULATION--LINEAR MODEL
***')
      READ(IN,7)TITLE
7     FORMAT(30A4)
      READ(IN,10)E,C,R,ANG1,ANG2,EBC,CURRENT,NCOIL
10    FORMAT(5F10.4,I4,F10.4,I6)
      WRITE(*,20)E,C,R,ANG1,ANG2
20    FORMAT(1X,'E=',F5.3,1X,'C=',F5.3,1X,'R=',F5.2,1X,
     &'ANG1=',F5.2,1X,'ANG2=',F5.2)
      WRITE(*,25)EBC,CURRENT,NCOIL
25    FORMAT(1X,'EBC=',I4,1X,'CURRENT=',F8.4,1X,'NUMBER OF COIL=',I6)
      READ(IN,30)N,M,ALPHA,NBON,PHISTAR1,PHIR,MG_DETH
30    FORMAT(2I10,F10.4,I10,3F10.4)
      WRITE(*,35)M,N,ALPHA,NBON
35    FORMAT(1X,'M=',I4,1X,'N=',I4,1X,'ALPHA=',F7.2,1X,'NBON=',I4)
      WRITE(*,37)PHISTAR1,PHIR,MG_DETH
37    FORMAT(1X,'PHISTAR1=',F7.2,1X,'PHIR=',F7.2,
     &1X,'MAGNET DEPTH=',F7.4)
      CONVER=0.0254D0
      E=E*CONVER
      C=C*CONVER
      R=R*CONVER
      MG_DETH=MG_DETH*CONVER
      PI=4.0D0*ATAN(1.0D0)
      MU=4.*PI*1.0E-7
      D_A=(ANG2-ANG1)*PI/180.D0
      POLE_L=D_A*(R+C)
      WRITE(*,55)POLE_L
55    FORMAT(1X,'POLE_L=',F15.9)
      IF(EB.EQ.0)GOTO 40
      EB=5
      NR=N/EB
      GOTO 50
40    EB=10
      NR=N/EB
50    B1=NR*2+1
      B2=N+B1
      N1=B2+NR*2
      M1=M+1
C  TOTAL NODAL POINTS(INCLUDING EXPANDED BOUNDARY AREA)
      NODE=N1*(M1)
```

```
            N2=N1-1
     C   TOTAL ELEMENTS
            ELEMT=2*N2*M
            WRITE(*,80)NODE,ELEMT
      80    FORMAT(1X,'NODE=',I10,1X,'ELEMT=',I10)
     C
     C$$$$$$$$$$$$$$$$$$$$$$$$$$$$$$$$$$$$$$$$$$$$$$$$$
     C   ARRAY OF POINTS FOR FORCE DISTRIBUTION
     C$$$$$$$$$$$$$$$$$$$$$$$$$$$$$$$$$$$$$$$$$$$$$$$$$$$
     C
            DELTA=C/10.D0
            CHANGE=CONVER*1.0D-7
            DO 3010 I=1,8
            XJJ(I)=.0D0
            DO 3010 J=1,15
     3010 YJJ(I,J)=.0D0
            DO 3020 I=1,1
     C      XJJ(I)=(I-1)*DELTA
            XJJ(I)=.0135D0*CONVER
            DO 3020 J=1,15
     3020 YJJ(I,J)=.021D0*CONVER-(J-1)*DELTA
     C3020 WRITE(*,3022)XJJ(I),YJJ(I,J)
     3022 FORMAT(2X,'XJJ=',F12.8,2X,'YJJ=',F12.8)
     C
     C$$$$$$$$$$$$$$$$$$$$$$$$$$$$$$$$$$$$$$$
     C   LOOP ON FORCE CALCULATION
     C$$$$$$$$$$$$$$$$$$$$$$$$$$$$$$$$$$$$$$$
     C
            DO 1050 I=1,1
            DO 1050 J=1,1
     C
     C$$$$$$$$$$$$$$$$$$$$$$$$$$$$$$$$$$$$$$$$$$$$$$$$$$$$$$$$$$$$$$$$$$$$$$$$$$$$$$
     C   CALCULATION OF BOUNDARY CONDITIONS FOR BACKWAORD PERTURBATION
     C$$$$$$$$$$$$$$$$$$$$$$$$$$$$$$$$$$$$$$$$$$$$$$$$$$$$$$$$$$$$$$$$$$$$$$$$$$$$$$
     C
            XJ=XJJ(I)-CHANGE
            YJ=YJJ(I,J)
            A1=ANG1+ALPHA
            A2=ANG2+ALPHA
     C
     C----------------------------------------------------------------------
     -
            CALL COORD(B1,B2,N1,EB,N,M,C,R,A1,A2,PI,XJ,YJ,X,Y,RANG1,RANG2,
          &          RX,RY)
     C----------------------------------------------------------------------
     -
     C
     C---------------------------------------------
            CALL ELEMOD(M,N2,II,JJ,KK,ELEMT)
     C---------------------------------------------
     C
     C   CHECK ORDER OF VERTICES WITHIN ELEMENTS
            WRITE(IO,8000)
     8000 FORMAT(2X,'CHECK ORDER OF VERTICES WITHIN ELEMENTS')
            DO 82 ITEST=1,ELEMT
            WRITE(IO,84)II(ITEST),JJ(ITEST),KK(ITEST)
            WRITE(IO,85)X(II(ITEST)),X(JJ(ITEST)),X(KK(ITEST))
      82    WRITE(IO,85)Y(II(ITEST)),Y(JJ(ITEST)),Y(KK(ITEST))
```

```
  84    FORMAT(1X,(3I6,1X))
  85    FORMAT(1X,(6F8.5,1X))
C  BANDWIDTH OF GLOBAL RECTANGULAR MATRIX
       NWID=M1+2
       WRITE(*,135)NWID
 135   FORMAT(1X,'NWID=',I6)
C
C----------------------------------------------------------------
-
       CALL ASSEML(M,N,NWID,ELEMT,X,Y,EB,NODE,II,JJ,KK,RECMAT,PHI,AL,
     &             PHISTAR1,PHIR,PHIS,IBKK,IBJJ,IBOUND)
C----------------------------------------------------------------
-
C
C      DO 110 K=1,NODE
C110    WRITE(*,120)(RECMAT(K,KJ),KJ=1,NWID),PHI(K)
 120   FORMAT(1X,7F8.2,2X,F8.2)
C
C----------------------------------------------------------------
-
       CALL MODMAT(NWID,NBON,PHI,NODE,RECMAT,REMMAT,PHIS,IBOUND,
     &             IBKK,IBJJ,M,N,EB)
C----------------------------------------------------------------
-
C
C----------------------------------------------------
C      CALL GAUSS2(REMMAT,PHI,NODE,NWID)
C----------------------------------------------------
C
C      WRITE(IO,140)M1,N1
 140   FORMAT(3X,I5,',',I5)
       MNODE=NODE-M
C      DO 150 IPOT=1,M1
C      DO 160 JPOT=IPOT,MNODE,M1
C      X(JPOT)=X(JPOT)/CONVER
C      Y(JPOT)=Y(JPOT)/CONVER
C160    WRITE(IO,170)X(JPOT),Y(JPOT),PHI(JPOT)
C150    MNODE=MNODE+1
 170   FORMAT(3X,2(F7.3,','),F7.3)
C
C----------------------------------------------------------------
-
       CALL FLUXEG(EB,ELEMT,II,JJ,KK,RANG1,RANG2,N,AL,PHI,X,Y,GAMMA,
     $SIGMA,BETA,M,R,C,NODE,MG_DETH,ANGPLOT,XBETA,YBETA)
C----------------------------------------------------------------
-
C
       GAMMASTAR1=GAMMA
C      WRITE(*,220)GAMMASTAR1
 220   FORMAT(1X,'GAMMASTAR1=',F12.4)
       PHISTAR2=-PHISTAR1
       A1=ANG1
       A2=ANG2
C
C----------------------------------------------------------------
-
       CALL COORD(B1,B2,N1,EB,N,M,C,R,A1,A2,PI,XJ,YJ,X,Y,RANG1,RANG2,
     &             RX,RY)
```

```
C-----------------------------------------------------------------------
-
C
C-----------------------------------------------------
      CALL ELEMOD(M,N2,II,JJ,KK,ELEMT)
C-----------------------------------------------------------------------
-
C
C-----------------------------------------------------------------------
      CALL ASSEML(M,N,NWID,ELEMT,X,Y,EB,NODE,II,JJ,KK,RECMAT,PHI,AL,
     &            PHISTAR2,PHIR,PHIS,IBKK,IBJJ,IBOUND)
C-----------------------------------------------------------------------
-
C
C-------------------------------------------------------------------
      CALL MODMAT(NWID,NBON,PHI,NODE,RECMAT,REMMAT,PHIS,IBOUND,
     &            IBKK,IBJJ,M,N,EB)
C---------------------------------------------------------------------
C
C--------------------------------------------------
      CALL GAUSS2(REMMAT,PHI,NODE,NWID)
C-----------------------------------------------
C
C-----------------------------------------------------------------------
      CALL FLUXEG(EB,ELEMT,II,JJ,KK,RANG1,RANG2,N,AL,PHI,X,Y,GAMMA,
     $SIGMA,BETA,M,R,C,NODE,MG_DETH,ANGPLOT,XBETA,YBETA)
C-----------------------------------------------------------------------
-
C
C     DO 230 I=EM,1,-M2
C230  WRITE(*,240)(BETA(J),J=I,I+M2-1)
C
C-----------------------------------------------------------
C  CALCULATE PARAMETERS TO DECIDE BOUNDARY CONDITION
C-----------------------------------------------------------
C
      GAMMASTAR2=GAMMA
C     WRITE(*,250)GAMMASTAR2
 250  FORMAT(1X,'GAMMASTAR2=',F12.4)
      KAPPA1=GAMMASTAR1/PHISTAR1
      KAPPA2=GAMMASTAR2/PHISTAR2
      MMF=CURRENT*FLOAT(NCOIL)
      PHIP1=MMF/(1.-KAPPA1/KAPPA2)
      PHIP2=PHIP1-MMF
C
C$$$$$$$$$$$$$$$$$$$$$$$$$$$$$$$$$$$$$$$$$$$$$$$$$$$$$$$$$$$$$$$$$$$$$$$$$$
$
C  CALCULATION OF MAGNETIC FLUX AND ENERGY FOR BACKWARD PERTURBATION
C$$$$$$$$$$$$$$$$$$$$$$$$$$$$$$$$$$$$$$$$$$$$$$$$$$$$$$$$$$$$$$$$$$$$$$$$$$
$
C
      XJ=XJJ(I)-CHANGE
      YJ=YJJ(I,J)
      A1=ANG1+ALPHA
      A2=ANG2+ALPHA
C
C-----------------------------------------------------------------------
-
```

```
          NK=1
          DO 650 IPLOT=1,N2
          DO 660 JPLOT=1,M
          XPLOT(NK,1)=RX(IPLOT+1,JPLOT)
          XPLOT(NK,2)=RX(IPLOT,JPLOT)
          XPLOT(NK,3)=RX(IPLOT,JPLOT+1)
          XPLOT(NK,4)=RX(IPLOT+1,JPLOT+1)
          YPLOT(NK,1)=RY(IPLOT+1,JPLOT)
          YPLOT(NK,2)=RY(IPLOT,JPLOT)
          YPLOT(NK,3)=RY(IPLOT,JPLOT+1)
          YPLOT(NK,4)=RY(IPLOT+1,JPLOT+1)
          PHIPLOT(NK,1)=RPHI(IPLOT+1,JPLOT)
          PHIPLOT(NK,2)=RPHI(IPLOT,JPLOT)
          PHIPLOT(NK,3)=RPHI(IPLOT,JPLOT+1)
          PHIPLOT(NK,4)=RPHI(IPLOT+1,JPLOT+1)
  660     NK=NK+1
  650     CONTINUE
          NUMELE=ELEMT/2
C         WRITE(IO,670)NUMELE
 670      FORMAT(3X,I5)
C         DO 680 IPLOT=1,NUMELE
C         DO 685 JCON=1,4
C         XPLOT(IPLOT,JCON)=XPLOT(IPLOT,JCON)/CONVER
C685      YPLOT(IPLOT,JCON)=YPLOT(IPLOT,JCON)/CONVER
C
C$$$$$$$$$$$$$$$$$$$$$$$$$$$$$$$$$$$$$$$$$$
C  DATA OUTPUT FOR CONTOUR GRAPHICS
C$$$$$$$$$$$$$$$$$$$$$$$$$$$$$$$$$$$$$$$$$$
C
C         WRITE(IO,8010)
C8010 FORMAT(2X,'CONTOUR PLOT')
C         WRITE(IO,690)(XPLOT(IPLOT,JPLOT),JPLOT=1,4),
C     &               (YPLOT(IPLOT,JPLOT),JPLOT=1,4)
C680   WRITE(IO,700)(PHIPLOT(IPLOT,JPLOT),JPLOT=1,4)
 690      FORMAT(3X,7(F7.3,','),F7.3)
 700      FORMAT(3X,3(F10.4,','),F10.4)
          A1=ANG1
          A2=ANG2
C
C---------------------------------------------------------------------
-
          CALL COORD(B1,B2,N1,EB,N,M,C,R,A1,A2,PI,XJ,YJ,X,Y,RANG1,RANG2,
     &            RX,RY)
C---------------------------------------------------------------------
-
C
C-------------------------------------------------
          CALL ELEMOD(M,N2,II,JJ,KK,ELEMT)
C-------------------------------------------------
C
C---------------------------------------------------------------------
-
          CALL ASSEML(M,N,NWID,ELEMT,X,Y,EB,NODE,II,JJ,KK,RECMAT,PHI,AL,
     &            PHIP2,PHIR,PHIS,IBKK,IBJJ,IBOUND)
C---------------------------------------------------------------------
-
C
C---------------------------------------------------------------------
```

```
      CALL MODMAT(NWID,NBON,PHI,NODE,RECMAT,REMMAT,PHIS,IBOUND,
     &              IBKK,IBJJ,M,N,EB)
C------------------------------------------------------------
C
C-------------------------------------------
      CALL GAUSS2(REMMAT,PHI,NODE,NWID)
C-------------------------------------------
C
C--------------------------------------------------------------------
      CALL FLUXEG(EB,ELEMT,II,JJ,KK,RANG1,RANG2,N,AL,PHI,X,Y,GAMMA,
     $SIGMA,BETA,M,R,C,NODE,MG_DETH,ANGPLOT,XBETA,YBETA)
C--------------------------------------------------------------------
C
      GAMMA_2A=GAMMA
      SIGMA_2A=SIGMA
      WRITE(*,310)GAMMA_2A,SIGMA_2A
 310  FORMAT(1X,'GAMMA_2A=',F12.4,1X,'SIGMA_2A=',F12.4)
C
C$$$$$$$$$$$$$$$$$$$$$$$$$$$$$$$$$$$$$$$$$$$$$$$$$$$$$$$$$$$$$$$$$$$$$$$$
C  CALCULATION OF BOUNDARY CONDITIONS FOR FORWARD PERTURBATION
C$$$$$$$$$$$$$$$$$$$$$$$$$$$$$$$$$$$$$$$$$$$$$$$$$$$$$$$$$$$$$$$$$$$$$$$$
C
      XJ=XJJ(I)+CHANGE
      YJ=YJJ(I,J)
      A1=ANG1+ALPHA
      A2=ANG2+ALPHA
C
C--------------------------------------------------------------------
      CALL COORD(B1,B2,N1,EB,N,M,C,R,A1,A2,PI,XJ,YJ,X,Y,RANG1,RANG2,
     &          RX,RY)
C--------------------------------------------------------------------
C
C-------------------------------------------
      CALL ELEMOD(M,N2,II,JJ,KK,ELEMT)
C-------------------------------------------
C
C--------------------------------------------------------------------
      CALL ASSEML(M,N,NWID,ELEMT,X,Y,EB,NODE,II,JJ,KK,RECMAT,PHI,AL,
     &          PHISTAR1,PHIR,PHIS,IBKK,IBJJ,IBOUND)
C--------------------------------------------------------------------
C
C----------------------------------------------------------
      CALL MODMAT(NWID,NBON,PHI,NODE,RECMAT,REMMAT,PHIS,IBOUND,
     &              IBKK,IBJJ,M,N,EB)
C------------------------------------------------------------
C
C-------------------------------------------
      CALL GAUSS2(REMMAT,PHI,NODE,NWID)
C-------------------------------------------
C
C--------------------------------------------------------------------
```

```
      CALL FLUXEG(EB,ELEMT,II,JJ,KK,RANG1,RANG2,N,AL,PHI,X,Y,GAMMA,
     $SIGMA,BETA,M,R,C,NODE,MG_DETH,ANGPLOT,XBETA,YBETA)
C---------------------------------------------------------------------
-
C
      M2=M*2
      EM=ELEMT-M2+1
      GAMMASTAR1=GAMMA
C     WRITE(*,410)GAMMASTAR1
 410  FORMAT(1X,'GAMMASTAR1=',F12.4)
      PHISTAR2=-PHISTAR1
      A1=ANG1
      A2=ANG2
C
C---------------------------------------------------------------------
-
      CALL COORD(B1,B2,N1,EB,N,M,C,R,A1,A2,PI,XJ,YJ,X,Y,RANG1,RANG2,
     &          RX,RY)
C---------------------------------------------------------------------
-
C
C-------------------------------------------------
      CALL ELEMOD(M,N2,II,JJ,KK,ELEMT)
C-------------------------------------------------
C
C---------------------------------------------------------------------
-
      CALL ASSEML(M,N,NWID,ELEMT,X,Y,EB,NODE,II,JJ,KK,RECMAT,PHI,AL,
     &          PHISTAR2,PHIR,PHIS,IBKK,IBJJ,IBOUND)
C---------------------------------------------------------------------
-
C
C---------------------------------------------------------------------
      CALL MODMAT(NWID,NBON,PHI,NODE,RECMAT,REMMAT,PHIS,IBOUND,
     &          IBKK,IBJJ,M,N,EB)
C---------------------------------------------------------------------
-
C
C--------------------------------------------------
      CALL GAUSS2(REMMAT,PHI,NODE,NWID)
C--------------------------------------------
C
C---------------------------------------------------------------------
-
      CALL FLUXEG(EB,ELEMT,II,JJ,KK,RANG1,RANG2,N,AL,PHI,X,Y,GAMMA,
     $SIGMA,BETA,M,R,C,NODE,MG_DETH,ANGPLOT,XBETA,YBETA)
C---------------------------------------------------------------------
-
C
      GAMMASTAR2=GAMMA
C     WRITE(*,420)GAMMASTAR2
 420  FORMAT(1X,'GAMMASTAR2=',F12.4)
      KAPPA1=GAMMASTAR1/PHISTAR1
      KAPPA2=GAMMASTAR2/PHISTAR2
      MMF=CURRENT*FLOAT(NCOIL)
      PHIP1=MMF/(1.-KAPPA1/KAPPA2)
      PHIP2=PHIP1-MMF
C     WRITE(*,430)KAPPA1,KAPPA2,FP1,FP2
```

```
  430  FORMAT(1X,'KAPPA1=',F12.4,1X,'KAPPA2=',F12.4,1X,
      &'FP1=',F12.4,1X,'FP2=',F12.4)
C
C$$$$$$$$$$$$$$$$$$$$$$$$$$$$$$$$$$$$$$$$$$$$$$$$$$$$$$$$$$$$$$$$$$$$$$$$$$$
C  CALCULATION OF MAGNETIC FLUX AND ENERGY FOR FORWARD PERTURBATION
C$$$$$$$$$$$$$$$$$$$$$$$$$$$$$$$$$$$$$$$$$$$$$$$$$$$$$$$$$$$$$$$$$$$$$$$$$$$
C
       XJ=XJJ(I)+CHANGE
       YJ=YJJ(I,J)
       A1=ANG1+ALPHA
       A2=ANG2+ALPHA
C
C--------------------------------------------------------------------
-
       CALL COORD(B1,B2,N1,EB,N,M,C,R,A1,A2,PI,XJ,YJ,X,Y,RANG1,RANG2,
      &          RX,RY)
C--------------------------------------------------------------------
-
C
C-------------------------------------------
       CALL ELEMOD(M,N2,II,JJ,KK,ELEMT)
C-------------------------------------------
C
C--------------------------------------------------------------------
-
       CALL ASSEML(M,N,NWID,ELEMT,X,Y,EB,NODE,II,JJ,KK,RECMAT,PHI,AL,
      &          PHIP1,PHIR,PHIS,IBKK,IBJJ,IBOUND)
C--------------------------------------------------------------------
-
C
C--------------------------------------------------------------------
       CALL MODMAT(NWID,NBON,PHI,NODE,RECMAT,REMMAT,PHIS,IBOUND,
      &          IBKK,IBJJ,M,N,EB)
C--------------------------------------------------------------------
C
C-------------------------------------------
       CALL GAUSS2(REMMAT,PHI,NODE,NWID)
C-------------------------------------------
C
C--------------------------------------------------------------------
-
       CALL FLUXEG(EB,ELEMT,II,JJ,KK,RANG1,RANG2,N,AL,PHI,X,Y,GAMMA,
      $SIGMA,BETA,M,R,C,NODE,MG_DETH,ANGPLOT,XBETA,YBETA)
C--------------------------------------------------------------------
-
C
       GAMMA_1B=GAMMA
       SIGMA_1B=SIGMA
       WRITE(*,330)GAMMA_1B,SIGMA_1B
  330  FORMAT(1X,'GAMMA_1B=',F12.4,1X,'SIGMA_1B=',F12.3)
       A1=ANG1
       A2=ANG2
C
C--------------------------------------------------------------------
-
       CALL COORD(B1,B2,N1,EB,N,M,C,R,A1,A2,PI,XJ,YJ,X,Y,RANG1,RANG2,
      &          RX,RY)
```

```
C------------------------------------------------------------------
-
C
C-----------------------------------------------
      CALL ELEMOD(M,N2,II,JJ,KK,ELEMT)
C---------------------------------------
C
C------------------------------------------------------------
-
      CALL ASSEML(M,N,NWID,ELEMT,X,Y,EB,NODE,II,JJ,KK,RECMAT,PHI,AL,
     &          PHIP2,PHIR,PHIS,IBKK,IBJJ,IBOUND)
C------------------------------------------------------------------
-
C
C--------------------------------------------------------------
      CALL MODMAT(NWID,NBON,PHI,NODE,RECMAT,REMMAT,PHIS,IBOUND,
     &          IBKK,IBJJ,M,N,EB)
C-------------------------------------------------------------
C
C-----------------------------------------------
      CALL GAUSS2(REMMAT,PHI,NODE,NWID)
C-----------------------------------------------
C
C------------------------------------------------------------------
-
      CALL FLUXEG(EB,ELEMT,II,JJ,KK,RANG1,RANG2,N,AL,PHI,X,Y,GAMMA,
     $SIGMA,BETA,M,R,C,NODE,MG_DETH,ANGPLOT,XBETA,YBETA)
C------------------------------------------------------------------
-
C
      GAMMA_2B=GAMMA
      SIGMA_2B=SIGMA
      WRITE(*,340)GAMMA_2B,SIGMA_2B
 340  FORMAT(1X,'GAMMA_2B=',F12.4,1X,'SIGMA_2B=',F12.3)
C
C   FORCE CALCULATION
C
      DELTA_SIGMA=(SIGMA_1B+SIGMA_2B)-(SIGMA_1A+SIGMA_2A)
      FORCE=DELTA_SIGMA/CHANGE
      FORCE=MU*FORCE/4.
      FJJ(I,J)=FORCE
      WRITE(*,1070)XJJ(I),YJJ(I,J),FJJ(I,J)
 1050 CONTINUE
      DO 1060 I=1,1
      XJJ(I)=XJJ(I)/C
      DO 1060 J=1,15
      YJJ(I,J)=YJJ(I,J)/C
      WRITE(IO,8050)
 8050 FORMAT(1X,4X,'X',12X,'Y',17X,'FORCE')
 1060 WRITE(IO,1070)XJJ(I),YJJ(I,J),FJJ(I,J)
 1070 FORMAT(1X,F12.8,1X,F12.8,1X,F12.3)
      STOP
      END
C
C*********************************************************************
*
      SUBROUTINE COORD(B1,B2,N1,EB,N,M,C,R,ANG1,ANG2,PI,XJ,YJ,X,Y,
     &RANG1,RANG2,RX,RY)
```

```
C***********************************************************************
*
C
      IMPLICIT DOUBLE PRECISION(A-H,O-Z)
      REAL*8 X(800),Y(800),RY(300,10),H(300),RX(300,10)
      INTEGER EB,B1,B2
      IO=9
      RANG1=ANG1*PI/180.
      RANG2=ANG2*PI/180.
      RANG=(ANG2-ANG1)/FLOAT(EB)*PI/180.
      THETA1=RANG1-RANG
      THETA2=RANG2+RANG
      THETA=THETA1
      DO 20 I=1,N1
      IF(I.NE.1)GO TO 30
      H(I)=C-XJ*COS(THETA)-YJ*SIN(THETA)
      GO TO 35
   30 IF(I.LE.B1)GO TO 40
      IF(I.GT.B2)GO TO 40
      DELTA_TH=(RANG2-RANG1)/FLOAT(N)
      GO TO 50
   40 DELTA_TH=(RANG2-RANG1)/FLOAT(N)*0.5
   50 THETA=THETA+DELTA_TH
      H(I)=C-XJ*COS(THETA)-YJ*SIN(THETA)
   35 CC=COS(THETA)
      DELTA_H=H(I)/FLOAT(M)
      DO 80 J=1,M+1
      RX(I,J)=(R+C-H(I)+DELTA_H*(J-1))*COS(THETA)
      RY(I,J)=(R+C-H(I)+DELTA_H*(J-1))*SIN(THETA)
   80 CONTINUE
   20 CONTINUE
      K=1
      DO 120 I=1,N1
      DO 130 J=1,M+1
      X(J+(K-1)*(M+1))=RX(I,J)
  130 Y(J+(K-1)*(M+1))=RY(I,J)
  120 K=K+1
      RETURN
      END
C
C***********************************************************************
*
      SUBROUTINE ELEMOD(M,N2,II,JJ,KK,ELEMT)
C***********************************************************************
*
C
      INTEGER II(1000),JJ(1000),KK(1000),ELEMT,ENDE
      INTEGER STARTE,T,END
      IO=9
      M1=M+1
      STARTE=1
      ENDE=STARTE+(M-1)*2
      K=1
      END=ELEMT-1
   20 CONTINUE
      T=0
      DO 30 I=STARTE, ENDE,2
      II(I)=K+T
```

```
            JJ(I)=II(I)+M1+1
            KK(I)=JJ(I)-1
            II(I+1)=II(I)
            JJ(I+1)=II(I+1)+1
            KK(I+1)=JJ(I)
     30     T=T+1
            IF(ENDE.EQ.END)GO TO 40
            STARTE=ENDE+2
            ENDE=ENDE+M*2
            K=K+M+1
            GO TO 20
     40     CONTINUE
            RETURN
            END
C
C**********************************************************************
*
            SUBROUTINE ASSEML(M,N,NWID,ELEMT,X,Y,EB,NODE,II,JJ,KK,RECMAT,PHI,
         &                   AL,PHISTAR1,PHIR,PHIS,IBKK,IBJJ,IBOUND)
C**********************************************************************
*
C
            IMPLICIT DOUBLE PRECISION(A-H,O-Z)
            REAL*8 X(800),Y(800),B(3),C(3),AL(1000),PHI(800)
            REAL*8 RECMAT(800,100),BDBMAT(1000,3,3)
            REAL*8 PHISTAR1,PHIR,PHIS(800)
            INTEGER IBOUND(2,800),ELEMT,EB
            INTEGER II(1000),JJ(1000),KK(1000),INELE(3,1000)
            IO=9
            DO 10 I=1,NODE
            DO 10 J=1,NWID
     10     RECMAT(I,J)=0.0
            DO 20 I=1,NODE
     20     PHI(I)=0.0
            M1=M+1
            M2=(N/EB*2+1)*M1
            M3=NODE-N/EB*2*M1
            IBKK=1
            DO 30 I=M2,M3,M1
            PHIS(I)=PHISTAR1
            IBOUND(1,IBKK)=I
     30     IBKK=IBKK+1
            IBKK=IBKK-1
            IBJJ=1
            DO 40 I=1,NODE,M1
            PHIS(I)=PHIR
            IBOUND(2,IBJJ)=I
     40     IBJJ=IBJJ+1
            IBJJ=IBJJ-1
            DO 50 NN=1,ELEMT
            I=II(NN)
            J=JJ(NN)
            K=KK(NN)
C           WRITE(IO,41)X(I),X(J),X(K),Y(I),Y(J),Y(K)
     41     FORMAT(1X,(6F8.6,1X))
            AL(NN)=0.5*(X(I)*Y(J)+X(J)*Y(K)+X(K)*Y(I)-X(I)*Y(K)-X(K)*Y(J)-
    Y(I)
         &*X(J))
```

```
C        WRITE(IO,42)AL(NN)
  42     FORMAT(1X,F12.8)
         B(1)=Y(J)-Y(K)
         B(2)=Y(K)-Y(I)
         B(3)=Y(I)-Y(J)
         C(1)=X(K)-X(J)
         C(2)=X(I)-X(K)
         C(3)=X(J)-X(I)
         INELE(1,NN)=II(NN)
         INELE(2,NN)=JJ(NN)
         INELE(3,NN)=KK(NN)
         DO 60 NR=1,3
         DO 60 NC=1,3
  60     BDBMAT(NN,NR,NC)=(B(NR)*B(NC)+C(NR)*C(NC))/(4.0*AL(NN))
  50     CONTINUE
         DO 70 NN=1,ELEMT
         DO 80 IN=1,3
         DO 80 JN=1,3
         ID=INELE(IN,NN)
         JD=INELE(JN,NN)
         IF(JD.LT.ID)GO TO 85
         RECMAT(ID,JD+1-ID)=RECMAT(ID,JD+1-ID)+BDBMAT(NN,IN,JN)
         GOTO 80
  85     DO 100 NEWB=1,IBKK
         IF(JD.NE.IBOUND(1,NEWB))GOTO 100
         PHI(ID)=PHI(ID)-BDBMAT(NN,IN,JN)*PHIS(JD)
 100     CONTINUE
  80     CONTINUE
  70     CONTINUE
         RETURN
         END
C
C****************************************************************
*
         SUBROUTINE MODMAT(NWID,NBON,PHI,NODE,RECMAT,REMMAT,PHIS,
        &                  IBOUND,IBKK,IBJJ,M,N,EB)
C****************************************************************
*
C
         IMPLICIT DOUBLE PRECISION(A-H,O-Z)
         REAL*8 PHI(800),RECMAT(800,100),PHIS(800),REMMAT(800,100)
         INTEGER MM(10),NEND(10),IBOUND(2,800),IIBOUND(2,800)
         INTEGER BON1,BON2,EB
         IO=9
         M1=M+1
         M2=(N/EB*2+1)*M1
         M3=NUMN-N/EB*2*M1
         DO 40 I=1,NODE
         DO 40 J=1,NWID
  40     REMMAT(I,J)=RECMAT(I,J)
         NEND(1)=IBOUND(1,IBKK)
         NEND(2)=IBOUND(2,IBJJ)
         MM(1)=M2
         MM(2)=1
         DO 100 NN=1,NBON
         BON1=MM(NN)
         DO 110 I=1,NODE
         IF(I.GT.NEND(NN))GO TO 110
```

```
           IF(I.EQ.BON1)GO TO 130
           SUM=0.0
           BON2=BON1
           JJ=NWID+I-1
           DO 140 J=I,JJ
           IF(BON2.GT.NEND(NN))GO TO 140
           IF(J.NE.BON2)GO TO 140
           SUM=SUM+REMMAT(I,J+1-I)*PHIS(J)
           BON2=BON2+M1
           REMMAT(I,J+1-I)=0.0
   140     CONTINUE
           PHI(I)=PHI(I)-SUM
           GO TO 110
   130     CONTINUE
           DO 170 J=1,NWID
           IF(J.EQ.1)GO TO 170
           REMMAT(I,J)=0.0
   170     CONTINUE
           PHI(I)=REMMAT(I,1)*PHIS(I)
           BON1=BON1+M1
   110     CONTINUE
   100     CONTINUE
           RETURN
           END
C
C*********************************************************************
*                              .
           SUBROUTINE GAUSS2(E,V,NNODES,NWID)
C*********************************************************************
*
C
           IMPLICIT DOUBLE PRECISION(A-H,O-Z)
           REAL*8 E(800,100),V(800),U(800)
C
C          TRIANGULARIZE
C
           NWIDM=NWID-1
           ISTOP=NNODES-1
           ISTOP=NNODES-1
           DO 1000 ID=1,ISTOP
           DO 1000 JD=1,NWIDM
           QUO=E(ID,JD+1)/E(ID,1)
           V(ID+JD)=V(ID+JD)-QUO*V(ID)
           KSTOP=NWID-JD
           DO 1000 KD=1,KSTOP
           E(ID+JD,KD)=E(ID+JD,KD)-QUO*E(ID,KD+JD)
  1000 CONTINUE
C
C      BACK SUBSTITUTE
C
           U(NNODES)=V(NNODES)/E(NNODES,1)
           DO 3000 ID=2,NNODES
           SUM=0.
           IN=NNODES+1-ID
           DO 2500 JD=2,NWID
           SUM=SUM+E(IN,JD)*U(IN+JD-1)
  2500 CONTINUE
           U(IN)=(V(IN)-SUM)/E(IN,1)
```

```
 3000 CONTINUE
      DO 4000 ID=1,NNODES
      V(ID)=U(ID)
 4000 CONTINUE
      RETURN
      END
C
C*******************************************************************
*
      SUBROUTINE FLUXEG(EB,ELEMT,II,JJ,KK,RANG1,RANG2,N,AL,PHI1,X,Y,
     $GAMMA,SIGMA,BETA,M,RR,CL,NODE,MG_DETH,ANGPLOT,XBETA,YBETA)
C*******************************************************************
*
C
      IMPLICIT DOUBLE PRECISION(A-H,O-Z)
      REAL*8 AL(1000),PHI1(800),X(800),Y(800),MG_DETH,ANGPLOT(1000)
      REAL*8 BETA(1000),BETAX(1000),BETAY(1000),B(800),C(800)
      REAL*8 XBETA(1000),YBETA(1000)
      REAL*8 RANG1,RANG2,GAMMA,SIGMA,RR,CL,DELTA_TH,DELTA_L
      INTEGER ELEMT,EB,II(1000),JJ(1000)
      INTEGER KK(1000)
      IO=9
      DO 20 I=1,ELEMT
      BETAX(I)=0.0
 20   BETAY(I)=0.0
C
C  CALCULATE ELEMENT CENTER
C
      DO 25 ICENT=1,ELEMT,2
      IE=II(ICENT)
      JE=JJ(ICENT)
      KE=KK(ICENT)
      XMID=(X(IE)+X(KE))/2.
      YMID=(Y(IE)+Y(KE))/2.
      XBETA(ICENT)=(XMID+0.5*X(JE))/1.5
      YBETA(ICENT)=(YMID+0.5*Y(JE))/1.5
      IE=II(ICENT+1)
      JE=JJ(ICENT+1)
      KE=KK(ICENT+1)
      XMID=(X(IE)+X(KE))/2.
      YMID=(Y(IE)+Y(KE))/2.
      XBETA(ICENT+1)=(XMID+0.5*X(JE))/1.5
      YBETA(ICENT+1)=(YMID+0.5*Y(JE))/1.5
 25   CONTINUE
C
C  CALCULATE FLUX DENSITY
C
      DO 30 NN=1,ELEMT
      I=II(NN)
      J=JJ(NN)
      K=KK(NN)
      B(I)=Y(J)-Y(K)
      B(J)=Y(K)-Y(I)
      B(K)=Y(I)-Y(J)
      C(I)=X(K)-X(J)
      C(J)=X(I)-X(K)
      C(K)=X(J)-X(I)
      BETAX(NN)=-(B(I)*PHI1(I)+B(J)*PHI1(J)+B(K)*PHI1(K))/(2.*AL(NN))
```

```
         BETAY(NN)=-(C(I)*PHI1(I)+C(J)*PHI1(J)+C(K)*PHI1(K))/(2.*AL(NN))
C        WRITE(*,100)BETAX(NN),BETAY(NN)
  100    FORMAT(2X,'BX=',F15.4,1X,'BY=',F15.4)
         ANGPLOT(NN)=ATAN(BETAY(NN)/BETAX(NN))
   30    BETA(NN)=SQRT(BETAX(NN)**2+BETAY(NN)**2)
C        WRITE(*,110)
  110    FORMAT(2X)
         DELTA_TH=(RANG2-RANG1)/FLOAT(N)*0.5
         DELTA_L=2.*(RR+CL)*SIN(DELTA_TH)
C        DELTA_L=0.1
C        WRITE(*,38)DELTA_TH,DELTA_L
   38    FORMAT(1X,'DELTA_TH=',F12.9,1X,'DELTA_L=',F12.9)
         GAMMA=0.0
         M2=M*2
         NSTART=M2*(N/EB*2+1)
         NEND=ELEMT-N/EB*2*M2
         DO 40 I=NSTART,NEND,M2
   40    GAMMA=GAMMA+BETA(I)
         GAMMA=DELTA_L*GAMMA*MG_DETH
C        GAMMA=GAMMA*MG_DETH
         SIGMA=0.0
         DO 50 I=1,ELEMT
   50    SIGMA=SIGMA+(BETAX(I)**2+BETAY(I)**2)*AL(I)*MG_DETH
         RETURN
         END
C
C*******************************************************************
         SUBROUTINE GAUSS1(E,V,NNODES,NWID)
C*******************************************************************
C
         IMPLICIT DOUBLE PRECISION(A-H,O-Z)
         REAL*8 E(200,200),V(800),U(800)
C
C        TRIANGULARIZE
C
         NWIDM=NWID-1
         DO 1000 ID=1,NNODES
         DO 1000 JD=1,NWIDM
         QUO=E(ID+JD,ID)/E(ID,ID)
         IDP=ID+NWIDM
         V(ID+JD)=V(ID+JD)-QUO*V(ID)
         DO 1000 KD=ID,IDP
         E(ID+JD,KD)=E(ID+JD,KD)-QUO*E(ID,KD)
 1000    CONTINUE
C
C        BACK SUBSTITUTE
C
         U(NNODES)=V(NNODES)/E(NNODES,NNODES)
         DO 2000 ID=2,NWID
         SUM=0.
         IN=NNODES+1-ID
         NSTOP=NNODES
         INP=IN+1
         DO 1500 JD=INP,NSTOP
         SUM=SUM+E(IN,JD)*U(JD)
 1500    CONTINUE
         U(IN)=(V(IN)-SUM)/E(IN,IN)
 2000    CONTINUE
```

```
      NWIDP=NWID+1
      DO 3000 ID=NWIDP,NNODES
      SUM=0.
      IN=NNODES+1-ID
      NSTOP=IN+NWID-1
      INP=IN+1
      DO 2500 JD=INP,NSTOP
      SUM=SUM+E(IN,JD)*U(JD)
 2500 CONTINUE
      U(IN)=(V(IN)-SUM)/E(IN,IN)
 3000 CONTINUE
      DO 4000 ID=1,NNODES
      V(ID)=U(ID)
 4000 CONTINUE
      RETURN
      END
```

APPENDIX B -   COMPUTATIONAL METHODS INCLUDING METAL REGIONS

B.1 Modelling of Magnetization Curve

If hysteresis and anisotropic effects are neglected, the magnetization function, or B vs. H function, for a ferromagnetic material can be represented as a continuous, single-valued nonlinear function. It is difficult, however, to find a single analytical expression that accurately represents the function over the entire useful range. A procedure using cubic spline fits recommended by Silvester et al.[B1] is used in the present work to model the magnetization characteristic of silicon sheet steel. The graphical data for the characteristic were taken from Smith [B2].

The procedure for modelling the experimentally determined relationship between B and H is as follows:

First, convert the data from a permeability representation (B vs. H) to a reluctivity v vs. B^2, the square of the flux density. The two methods of representing the data are shown in Figure B1 and Figure B2.
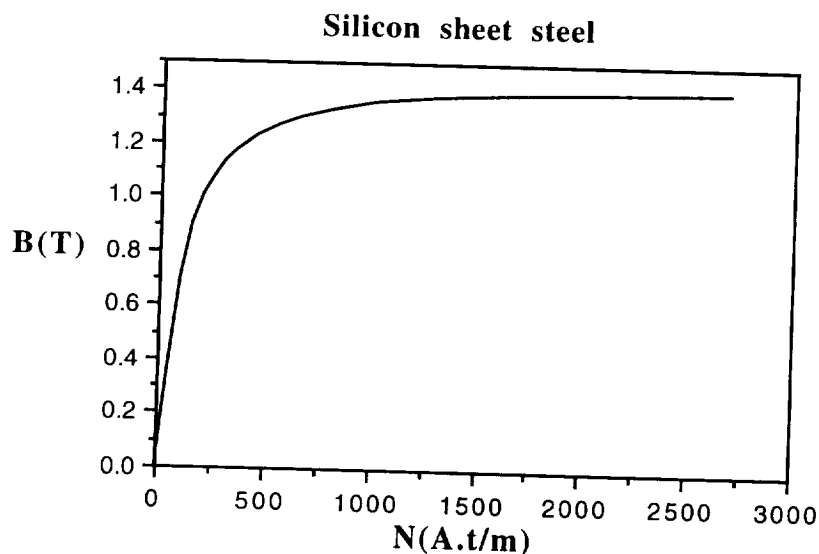
Figure B1. Magnetization of silicon sheet steel
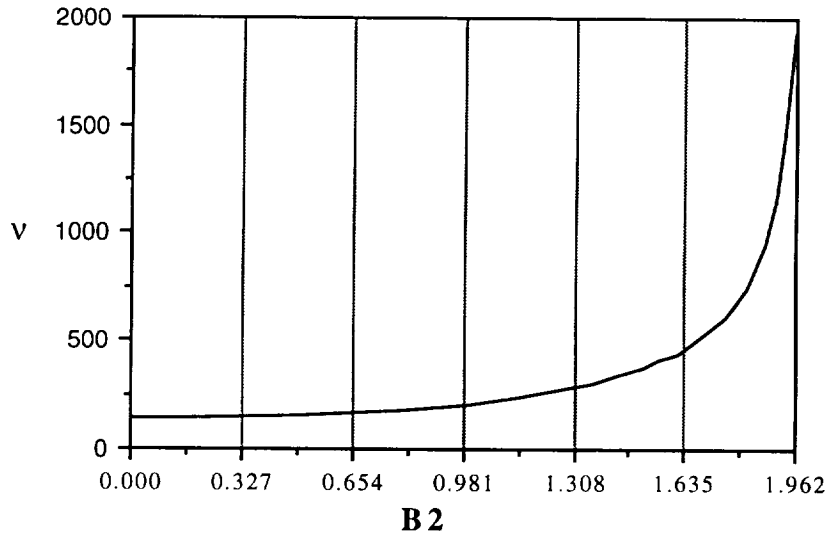
Figure B2. Reluctivity vs. square of flux density

Next, evenly divide B^2 into n subintervals. Then within an interval between end points i1 and i2 the value of v and the slope κ of the v-B^2 curve can be calculated by the cubic interpolation formulae

$$x = \frac{B^2 - B_{i1}^2}{B_{i2}^2 - B_{i1}^2} \tag{1.1}$$

$$v(x) = \left(2x^3 - 3x^2 + 1\right) v_{i1} + \left(-2x^3 + 3x^2\right) v_{i2} + \left(x^3 - 2x^2 + x\right) \kappa_{i1} + \left(x^3 - x^2\right) \kappa_{i2} \tag{1.2}$$

$$\kappa(x) = \frac{dv}{dB^2} = \frac{1}{B_{i2}^2 - B_{i1}^2} \{\left(6x^2 - 6x\right) v_{i1} + \left(-6x^2 + 6x\right) v_{i2} + \left(3x^2 - 4x + 1\right) \kappa_{i1} + \left(3x^2 - 2x\right) \kappa_{i2}\} \tag{1.3}$$

$$\frac{d\kappa}{dB^2} = (12x-6) v_{i1} + (-12x+6) v_{i2} + (6x-4) \kappa_{i1} + (6x-2) \kappa_{i2} \tag{1.4}$$

The values of v_i are known from the B-H curve and κ_i of (2) and (3) can be obtained by setting a constraint that the slope of κ with respect to B^2 must to be continuous at the interval ends. For instance, if v-B^2 is divided into 6 sub-segments as shown in Fig. 2, for two adjacent intervals from node i-1 to node i and from node i to node i+1, the gradient at the right end (x=1) is evaluated using (1.4)

$$\left[\frac{d\kappa}{dB^2}\right]_i = 6v_{i-1} - 6v_i + 2\kappa_{i-1} + 4\kappa_i \tag{1.5}$$

Similarly, calculating the quantity at node i at x=0 in the second interval

$$\left[\frac{d\kappa}{dB^2}\right]_i = -6v_i + 6v_{i+1} - 4\kappa_i - 2\kappa_{i+1} \tag{1.6}$$

Equating (5) and (6)

$$\kappa_{i-1} + 4\kappa_i + \kappa_{i+1} = 3v_{i+1} - 3v_{i-1} \tag{1.7}$$

For a v-B^2 curve with 6 subintervals, expanding (7) leads to

$$\kappa_1 + 4\kappa_2 + \kappa_3 = 3v_3 - 3v_1$$
$$\kappa_2 + 4\kappa_3 + \kappa_4 = 3v_4 - 3v_2$$
$$\kappa_3 + 4\kappa_4 + \kappa_5 = 3v_5 - 3v_3$$
$$\kappa_4 + 4\kappa_5 + \kappa_6 = 3v_6 - 3v_4$$
$$\kappa_5 + 4\kappa_6 + \kappa_7 = 3v_7 - 3v_5$$

a set of 5 simultaneous linear equations with 7 unknowns. However, for the leftmost node at B=0, v can be easily obtained as a constant from B-H curve, leading to $\kappa_1 = 0$. For κ_7, different values must be tried until the series of κ_i from (7) are positive and monotonic. With the above special treatment of leftmost and rightmost nodes, the unknowns are reduced to five

$$4\kappa_2 + \kappa_3 = 3v_3 - 3v_1$$
$$\kappa_2 + 4\kappa_3 + \kappa_4 = 3v_4 - 3v_2$$
$$\kappa_3 + 4\kappa_4 + \kappa_5 = 3v_5 - 3v_3$$
$$\kappa_4 + 4\kappa_5 + \kappa_6 = 3v_6 - 3v_4$$
$$\kappa_5 + 4\kappa_6 = 3v_6 - 3v_4 - \kappa_7$$

Finally, use the calculated κ_i in (1.2) and (1.3) to check the predicted the curve of H vs. B as illustrated in Figure B3.

Silicon sheet steel
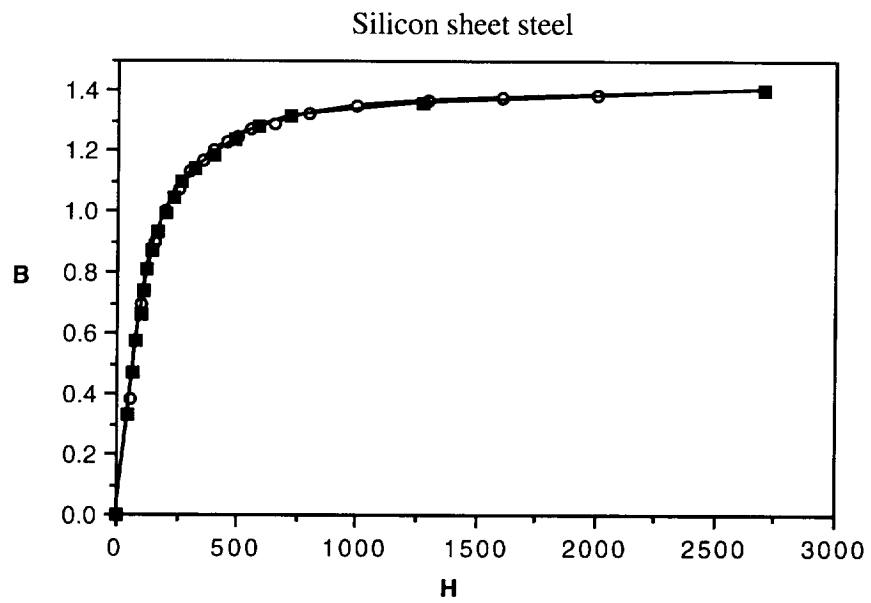
Figure B3. Comparison of material sample test and curve modelling,

circle-----material sample test
square----curve modelling.

B.2   Iteration for Flux Distribution: Newton-Raphson Method

To calculate the forces from a magnet accurately it is necessary to obtain solutions to the Poisson equation consistent with the magnetization characteristic of the metal. A Newton-Raphson iteration algorithm has been developed by Silvester et al.[B1] and is suggested by many researchers working in this field due to its rapid convergence and unconditional stability. After evaluation of several iteration methods, the Newton-Raphson algorithm was found to converge faster and more stably than other methods, but it can not well constrain the saturated magnetic flux density because of the sharp increase of the reluctivity beyond the saturation point. However, with an undercorrecting parameter for the residual part of the iteration as well as an additional successive overrelaxation (SOR) form for a weighted combination of the reluctivity obtained at step n and step n+1, the Newton-Raphson algorithm offers a satisfactory solution.

A summary of the iteration algorithm based on [B1] is presented below.

As presented in the previous report, the magnetic potential field will be obtained by minimizing the energy functional

$$\xi(A) = \int_R (W - JA) \, d\Omega \tag{2.1}$$

here W is the density of magnetically stored energy

$$W = \int_0^B H \, dB \tag{2.2}$$

The requirement to minimize functional (2.1) is equivalent to demanding

$$\frac{\partial \xi}{\partial A_i} = 0. \tag{2.3}$$

Expanding (2.3) will yield N simultaneous nonlinear equations whose solution A describes the desired result.

To construct an iteration process, expand (2.3) in a Taylor series

$$\left(\frac{\partial \xi}{\partial A_i}\right)_{A+\Delta A} = \left(\frac{\partial \xi}{\partial A_i}\right)_A + \sum_j \left(\frac{\partial^2 \xi}{\partial A_i \partial A_j}\right)_A \Delta A_j \ ....$$
(2.4)

Neglecting those terms beyond the second derivative term will yield a matrix equation

$$\Delta A_j = -\left(\frac{\partial^2 \xi}{\partial A_i \partial A_j}\right)_{A+\Delta A}^{-1} \left(\frac{\partial \xi}{\partial A_i}\right)_{A+\Delta A}$$
(2.5)

Then a successive correction will be formed based on (2.5):

$$A^{(n+1)} = A^{(n)} - \left(\frac{\partial^2 \xi}{\partial A_i \partial A_j}\right)_{A+\Delta A}^{-1} \left(\frac{\partial \xi}{\partial A_i}\right)_{A+\Delta A}$$
(2.6)

To apply the iteration process (2.6) for finite element formulation, we calculate the first and second derivatives of (2.1)

$$\frac{\partial \xi}{\partial A_i} = \int_R \left(\frac{\partial W}{\partial A_i} - J\right) d\Omega$$
(2.7)

$$\frac{\partial^2 \xi}{\partial A_i \partial A_j} = \int_R \frac{\partial^2 W}{\partial A_i \partial A_j} d\Omega$$
(2.8)

The field vector **H** is related to the flux density B by nonlinear reluctivity,

$$\mathbf{H} = v(B^2) \ \mathbf{B}$$
(2.9)

Therefore (2.2) will become

$$W = \frac{1}{2} \int_0^{B^2} v(B^2) \ d(B^2)$$
(2.10)

Within an element, the potential is given by an interpolation form suitable for finite element calculations

$$A = \sum_i A_i N_i$$
(2.11)

Then the squared flux density in the element will be given by

$$B^2 = \sum_i \sum_j A_i A_j \nabla N_i \cdot \nabla N_j \tag{2.12}$$

Differentiating by the chain rule,

$$\frac{\partial W}{\partial A_i} = \nu(B^2) \sum_k A_k \nabla N_i \cdot \nabla N_k \tag{2.13}$$

$$\frac{\partial^2 W}{\partial A_i \partial A_j} = \nu \nabla N_i \cdot \nabla N_j + 2\frac{d}{dB^2}\sum_m \sum_n A_m A_n \left(\nabla N_m \cdot \nabla N_i\right)\left(\nabla N_n \cdot \nabla N_j\right) \tag{2.14}$$

Hence the residual vectors of the iterative process (2.6) will be formed by joining the individual element contributions formed according to (2.7) and (2.13)

$$\int_R \left(\frac{\partial W}{\partial A_i} - J\right) d\Omega = \sum_k A_k \int_R \nu \nabla N_k \cdot \nabla N_i d\Omega - \int_R J \, d\Omega \tag{2.15}$$

$$\int_R \frac{\partial^2 W}{\partial A_i \partial A_j} d\Omega = \int_R \nu \nabla N_i \cdot \nabla N_j + 2\sum_m \sum_n A_m A_n \int_R \frac{d\nu}{dB^2}\left(\nabla N_m \cdot \nabla N_i\right)\left(\nabla N_n \cdot \nabla N_j\right) d\Omega$$

For a first-order triangular element, define

$$\int_R \frac{\partial^2 W}{\partial A_i \partial A_j} d\Omega = \int_R \nu \nabla N_i \cdot \nabla N_j + 2\int_R \nabla N_m \cdot \nabla N_j \, d\Omega = S_{mj} \tag{2.17}$$

and then the matrix contribution will be

$$\int_R \frac{\partial W}{\partial A_k} d\Omega = \nu \sum_i S_{ki} A_i \tag{2.18}$$

$$\int_R \frac{\partial^2 W}{\partial A_i \partial A_j} d\Omega = \nu S_{ij} + \frac{2}{A_r dB^2} \frac{dv}{m} \sum_m \sum_n A_m A_n S_{im} S_{jn} \qquad (2.19)$$

The second term of (2.19) can be simplified to

$$\frac{2}{A_r dB^2} \frac{dv}{} \sum_m \sum_n A_m A_n S_{im} S_{jn} = U_i U_j \qquad (2.20)$$

where

$$U_i = \sum_j S_{ij} A_j \qquad (2.21)$$

So that the Jacobian matrix contributions are given, finally, by

$$P_{ij} = \nu \, S_{ij} + \frac{2}{A_r} \frac{dv}{dB^2} U_i U_j \qquad (2.22)$$

Within every iteration, the reluctivity ν is weighted by SOR:

$$\nu^{(n+1)} = \nu^{(n)} + \omega\left(\nu^* - \nu^{(n)}\right) \qquad (2.23)$$

where ν^* is calculated from the approximate magnetization characteristic.
The iteration process is illustrated by the program flow chart of Figure B4.

```
┌─────────────────────────────┐
│ Compute element coeff.       │
│ matrices and source vectors  │
└─────────────────────────────┘
              │
┌─────────────────────────────┐
│ Set initial $A_i$ and $v_n$ and slop $k_n$ │
└─────────────────────────────┘
              │
        ┌──────────────┐
        │ Calculate $B^2$ │
        └──────────────┘
              │
┌─────────────────────────────────────────────┐
│ Predict $v_n^{i+1}$ and $\kappa_n^{i+1}$ using curve fitting │
└─────────────────────────────────────────────┘
              │
┌───────────────────────────────┐
│ Calculate $v_n^{i+1}$ using SOR │
└───────────────────────────────┘
              │
      ┌──────────────────┐
      │ Calculate residual │
      │ $\mathbf{Y=SA-J}$  │
      │ Jacobian matrix    │
      │ $\mathbf{P}$       │
      └──────────────────┘
              │
      ┌──────────────────┐
      │ Modify $\mathbf{P}$ with B.C. │
      └──────────────────┘
              │
      ┌──────────────────────────┐
      │ Solve $\delta\mathbf{A=P^{-1}Y}$ │
      └──────────────────────────┘
              │
      ┌──────────────────────────┐
      │ $A_n^{i+1}=A_n^i+\omega\delta A_n$ │
      └──────────────────────────┘
              │
No    ┌──────────────────┐
──────│ Test convergence │
      └──────────────────┘
              │ Yes
        ┌────────┐
        │ Exit   │
        └────────┘
```
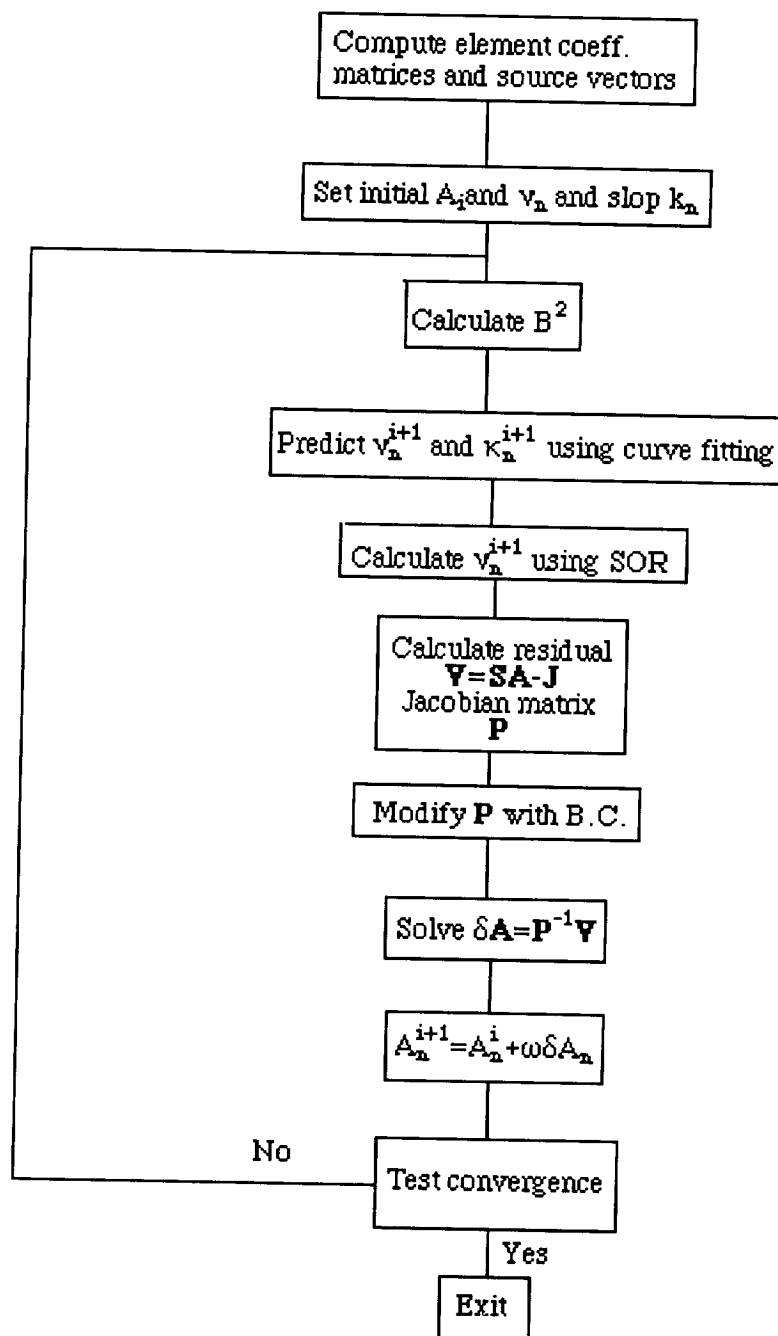
Figure B4. Program flow chart

B.3 Efficient Calculation of Force

In static electromagnetic field analysis, the virtual work principle is commonly used to calculate magnetic force acting on a rigid, current-free and movable body:

$$F_s = -\frac{\partial W}{\partial s} \tag{3.1}$$

where ∂s is an infinitesimal distance along the s-direction and W is the magnetic energy stored within the computation region. Therefore, to obtain magnetic force, the suspended body is subjected to a virtual displacement, then the field quantities are computed at both positions. A general procedure is first to solve the governing equation of a field problem with specified boundary conditions. For example, a static 2-D magnetic field will be expressed as a partial differential equation of Poisson's type:

$$\nabla v \nabla A_z(x,y) = J_z. \tag{3.2}$$

Then the magnetic flux density will be obtained by calculating the curl of the vector magnetic potential

$$\overline{B} = \nabla \times \overline{A}. \tag{3.3}$$

Magnetic energy finally is calculated by an integration over the volume containing the total distributed magnetic energy in terms of field quantities

$$W = \frac{1}{2} \int_v \frac{B^2}{\mu} \, dv. \tag{3.4}$$

In a numerical analysis for an electromagnetic field problem, the computation region may be bounded by irregular contours and may also involve several different materials. So a discretization of the domain may require many elements and the resulting force calculation would be very time-consuming. The problem becomes even more severe when an iterative method must be used to deal with nonlinearities such as the magnetization characteristics of different magnetic materials. To develop a more efficient and forthright algorithm for magnetic force calculation, Coulomb derived an elegant formula for implementing the virtual work principle without the need for a second field solution

[B3,B4]. A mapping approach is used so that the calculations of differential terms of the field quantities have been switched to the calculations of differential changes of the coordinates in the Jacobian matrix. This approach not only saves the time that would be required for the second field solution, but may also improve the accuracy of the solution. It reduces the computer round-off error since the domain of the force calculation includes only the distorted elements during a virtual displacement. In the present research the principle of Coulomb's work is applied to derive the force calculation equations for two theoretical models: a linear solution for magnetic potential based on Laplace's equation, which was described in detail in a previous report, and a nonlinear Poisson's equation model.

B.3.1. Force Calculation using Linear Potential Model

With an assumption of infinite permeability of magnetic material, the computation region will only involve the air gap between the magnet poles and the suspended rotor. The fundamental equation of the source-free field then represents the curl-free nature of the magnetic field intensity

$$\nabla \times \overline{H} = 0.. \tag{3.5}$$

With the vector identity

$$\nabla \times \nabla \phi = 0,. \tag{3.6}$$

the field intensity can be written as the gradient of the magnetic potential

$$\overline{H} = -\nabla \phi. \tag{3.7}$$

Since the divergence of magnetic flux density is zero everywhere

$$\nabla \cdot \overline{B} = \nabla \cdot \mu_0 \overline{H} = 0. \tag{3.8}$$

substitution of (3.8) into (3.7) gives the Laplace equation

$$\nabla^2 \phi = 0. \tag{3.9}$$

If the triangular linear interpolation formula

$$\phi(x,y) = \sum_i N_i(x,y)\ \Phi_i, \tag{3.10}$$

is used to approximate the potential field and then the energy functional

$$\xi = \int_R \frac{1}{2}\nu\left[\nabla\phi\right]^2 dR, \tag{3.11}$$

is minimized as explained in the previous report, the solution of nodal potential values is found

$$\overline{\Phi}^T_{min} = \left[\Phi_1, \Phi_2, \dots, \Phi_N\right]. \tag{3.12}$$

Using the energy from equation (4), the force can be calculated from the virtual work principle of (1)

$$F_s = \frac{\partial W}{\partial s} = \frac{\partial}{\partial s}\left\{\sum_i^M \int_R \frac{B^2}{2\mu_0} dR\right\}. \tag{3.13}$$

where M is the total number of the elements. The Jacobian matrix can be used to transfer the global coordinates into local ones and to map a function between global and local coordinates

$$\int_R f(x,y)\ dR = \int_\Omega f(x(L_1,L_2),y(L_1,L_2))\ |J|\ dL_1 dL_2.. \tag{3.14}$$

The force then can be expressed as a function of flux density and local coordinates

$$F_s = \frac{\partial}{\partial s}\left[\sum_i^M \int_\Omega \frac{B^2}{2\mu_0} |\overline{J}|\, dL_1 dL_2\right]$$

$$= \sum_i^M \int_\Omega \left[\frac{\partial}{\partial s}\left(\frac{B^2}{2\mu_0}\right)|\overline{J}| + \frac{B^2}{2\mu_0}\frac{\partial|\overline{J}|}{\partial s}\right] dL_1 dL_2. \qquad (3.15)$$

The first term inside of the integral will be

$$\frac{\partial}{\partial s}\left(\frac{B^2}{2\mu_0}\right) = \overline{B}^T \cdot \frac{\partial \overline{H}}{\partial s}. \qquad (3.16)$$

With the equations of the mapping given as

$$\frac{\partial \phi_\beta}{\partial L_1} = \frac{\partial \phi_\beta}{\partial x}\frac{\partial x}{\partial L_1} + \frac{\partial \phi_\beta}{\partial y}\frac{\partial y}{\partial L_1},$$

$$(3.17)$$

$$\frac{\partial \phi_\beta}{\partial L_2} = \frac{\partial \phi_\beta}{\partial x}\frac{\partial x}{\partial L_2} + \frac{\partial \phi_\beta}{\partial y}\frac{\partial y}{\partial L_2},$$

or in a matrix form:

$$\left\{\begin{array}{c} \dfrac{\partial \phi_\beta}{\partial L_1} \\[2ex] \dfrac{\partial \phi_\beta}{\partial L_2} \end{array}\right\} = \overline{J}\left\{\begin{array}{c} \dfrac{\partial \phi_\beta}{\partial x} \\[2ex] \dfrac{\partial \phi_\beta}{\partial y} \end{array}\right\}, \qquad (3.18)$$

where the Jacobian matrix is

$$\bar{J} = \begin{bmatrix} \dfrac{\partial x}{\partial L_1} & \dfrac{\partial y}{\partial L_1} \\[2ex] \dfrac{\partial x}{\partial L_2} & \dfrac{\partial y}{\partial L_2} \end{bmatrix},$$

(3.19)

The intensity field can therefore be expressed in terms of the inverse of the Jacobian matrix and the derivatives of local coordinates as

$$\bar{H} = -\nabla\phi = -\bar{J}^{-1} \begin{Bmatrix} \dfrac{\partial\phi}{\partial L_1} \\[2ex] \dfrac{\partial\phi}{\partial L_2} \end{Bmatrix},$$

(3.20)

So from (1-14),

$$\frac{\partial\bar{H}}{\partial s} = -\frac{\partial\bar{J}^{-1}}{\partial s} \begin{Bmatrix} \dfrac{\partial\phi}{\partial L_1} \\[2ex] \dfrac{\partial\phi}{\partial L_2} \end{Bmatrix},$$

(3.21)

In order to eliminate the differential terms of ϕ over L, the unit matrix is used

$$\frac{\partial}{\partial s}\left(\bar{J}\,\bar{J}^{-1}\right) = \frac{\partial\bar{J}}{\partial s}\bar{J}^{-1} + \bar{J}\frac{\partial\bar{J}^{-1}}{\partial s} \equiv 0,$$

(3.22)

so that

$$\frac{\partial\bar{J}^{-1}}{\partial s} = -\bar{J}^{-1}\frac{\partial\bar{J}}{\partial s}\bar{J}^{-1}.$$

(3.23)

Substituting (1-17) into (1-16), we find

$$\frac{\partial \overline{H}}{\partial s} = - \overline{J}^{-1} \frac{\partial \overline{J}}{\partial s} \overline{H} \tag{3.24}$$

and then substituting (1-18) into (1-12), we finally have

$$F_s = \sum_i^M \int_R \left[-\overline{B}^T \overline{J}^{-1} \frac{\partial \overline{J}}{\partial s} \overline{H} + \frac{B^2}{2\mu_0} |\overline{J}|^{-1} \frac{\partial |\overline{J}|}{\partial s} \right] dR . \tag{3.25}$$

Following a general routine of a calculation for the Jacobian matrix, we have

$$\overline{J} = \begin{bmatrix} X_{13} & Y_{13} \\ X_{23} & Y_{23} \end{bmatrix}, \tag{3.26}$$

where X,Y are nodal coordinates and the following forms are used to simplify the expression

$$X_{ij} = X_i - X_j, \quad Y_{ij} = Y_i - Y_j. \tag{3.27}$$

With an infinitesimal displacement of the nodal coordinates, we can write

$$\frac{\partial \overline{J}}{\partial s} = \begin{bmatrix} \dfrac{\Delta X_{13}}{\Delta s} & \dfrac{\Delta Y_{13}}{\Delta s} \\[2mm] \dfrac{\Delta X_{23}}{\Delta s} & \dfrac{\Delta Y_{23}}{\Delta s} \end{bmatrix} \tag{3.28}$$

and

$$\frac{\partial |\overline{J}|}{\partial s} = \frac{\Delta(X_{13} Y_{23} - Y_{13} X_{23})}{\Delta s} \tag{3.29}$$

Geometrically, a suspension system undergoing a virtual displacement could be represented by three parts, a region of the magnet as a fixed part, a region of the levitated body as an entirely moving part and a free space region between the fixed and moving parts

as a distorted part. Equations (1-21) and (1-22) are discussed separately for each of these three different regions.

A. For a fixed element

$$\Delta X_{ij} = \Delta Y_{ij} = 0, \qquad (3.30)$$

so

$$\frac{\partial \overline{J}}{\partial s} = \frac{\partial |J|}{\partial s} = 0. \qquad (3.31)$$

B. For an element within an entirely moving body, the element shape will not be changed at all, as illustrated in Fig.B5,
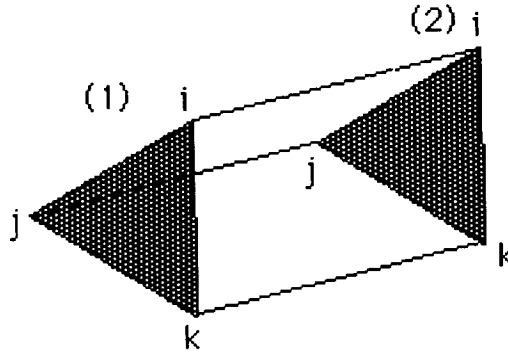
Figure B5. An element in a rigid moving body is moved from location 1 to 2.

so

$$\Delta X_{ij} = X_i^{(2)} - X_i^{(1)} - \left(X_j^{(2)} - X_j^{(1)} \right) = \Delta X - \Delta X = 0, \qquad (3.32)$$

$$\Delta Y_{ij} = Y_i^{(2)} - Y_i^{(1)} - \left(Y_j^{(2)} - Y_j^{(1)} \right) = \Delta Y - \Delta Y = 0, \qquad (3.33)$$

where the superscript represents the moment before and after the displacement. For the same reason,

$$\Delta[X_{ij}Y_{nj} - Y_{ij}X_{nj}] = (X_{ij}Y_{nj})^{(2)} - (X_{ij}Y_{nj})^{(1)} - \left\{ (Y_{ij}X_{nj})^{(2)} - (Y_{ij}X_{nj})^{(1)} \right\} = 0, \qquad (3.34)$$

since

$$X_{ij}^{(2)} = X_{ij}^{(1)}, \ Y_{nj}^{(2)} = Y_{nj}^{(1)}, \ X_{nj}^{(2)} = X_{nj}^{(1)}, \ Y_{ij}^{(2)} = Y_{ij}^{(1)} = 0. \qquad (3.35)$$

So the same conclusion is reached:

$$\frac{\partial \bar{J}}{\partial s} = \frac{\partial |\bar{J}|}{\partial s} = 0. \tag{3.36}$$

Applying the above results for (1-19), all those elements in the moving and fixed bodies can be neglected during the virtual displacement. Only the distorted elements need to be considered for the force calculation:

$$F_s = \sum_{\text{distor.}} \int_R \left[-\bar{B}^T \bar{J}^{-1} \frac{\partial \bar{J}}{\partial s} \bar{H} + \frac{B^2}{2\mu_0} |\bar{J}|^{-1} \frac{\partial |\bar{J}|}{\partial s} \right] dR \,. \tag{3.37}$$

Since the distortion of the free space is arbitrarily decided, we may just take one layer of the elements surrounding the moving part as shown in Fig.B6 where, for more accurate calculations, the diagonals of the gap 1 and 2 are symmetrically arranged.
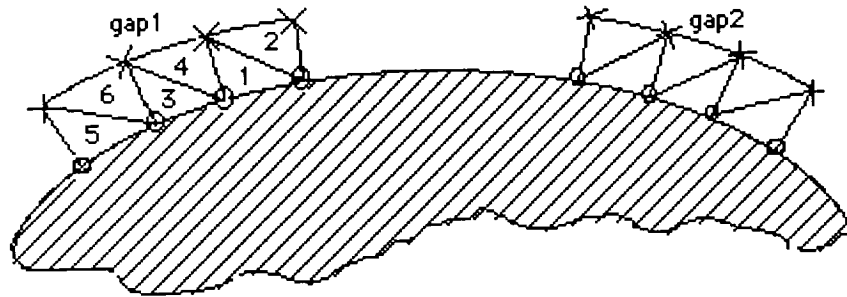
Figure B6. Geometry of one layer of elements surrounding the rotor where,

x———— fixed node

o———— moving node.

If the first term of (1-23) is expanded to matrix form

$$\text{term1}=\left[-\overline{B}^T\,\overline{J}^{-1}\,\frac{\partial\overline{J}}{\partial s}\,\overline{H}\right]A_a=-\frac{\mu_0}{2}\left[\phi_x,\phi_y\right]\left[\begin{array}{cc}Y_{23} & Y_{31}\\X_{32} & X_{13}\end{array}\right]\left[\begin{array}{cc}\dfrac{\Delta X_{13}}{\Delta s} & \dfrac{\Delta Y_{13}}{\Delta s}\\[2mm]\dfrac{\Delta X_{23}}{\Delta s} & \dfrac{\Delta Y_{23}}{\Delta s}\end{array}\right]\left\{\begin{array}{c}\phi_x\\\phi_y\end{array}\right\},\;(3.38)$$

where A_a is the element area, all the quantities in term 1 are known except for the derivative of the Jacobian matrix. Since one rectangular shape consists of two triangular elements which have different ranges of fixed nodes and moving nodes, the matrix has to be determined separately according to the elements with odd or even numbers. An example of the nodal range is shown in Fig.B7.
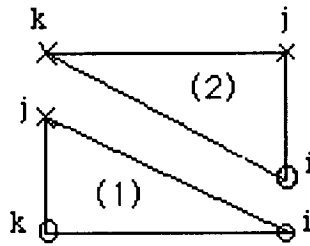
Figure B7. The range of fixed and moving nodes of the elements.

For element = 1,3,5,......, odd numbers, if s = x, since

$$\frac{\Delta X_{ij}}{\Delta x}=\frac{X_i^{(2)}-X_i^{(1)}-\left(X_j^{(2)}-X_j^{(1)}\right)}{\Delta x},\qquad(3.39)$$

it is easy to determine that

$$\frac{\Delta X_{13}}{\Delta x}=0,\;\frac{\Delta X_{23}}{\Delta x}=-1,\;\frac{\Delta Y_{13}}{\Delta x}=\frac{\Delta Y_{23}}{\Delta x}=0.\qquad(3.40)$$

So we have

$$\frac{\partial \bar{J}}{\partial x} = \begin{bmatrix} 0 & 0 \\ -1 & 0 \end{bmatrix}.$$

(3.41)

Repeating the above calculations, we obtain the matrix for s = y

$$\frac{\partial \bar{J}}{\partial x} = \begin{bmatrix} 0 & 0 \\ 0 & -1 \end{bmatrix}.$$

(3.42)

The elements with even numbers and furthermore, the second term of (1-23), also can be handled with the same calculation above. The final forms of the force components along x and y-directions respectively as a summation of one layer elements are obtained as

$$F_x = \frac{D\mu_0}{2} \left\{ \sum_{odd} \left[\phi_x(\phi_x Y_{31} + \phi_y X_{13}) + \frac{1}{2}(\phi_x^2 + \phi_y^2)Y_{13} \right] + \sum_{even} \left[-\phi_x(\phi_x Y_{23} + \phi_y X_{32}) + \frac{1}{2}(\phi_x^2 + \phi_y^2)Y_{23} \right] \right\},$$

3.43a

$$F_y = \frac{D\mu_0}{2} \left\{ \sum_{odd} \left[\phi_y(\phi_x Y_{31} + \phi_y X_{13}) - \frac{1}{2}(\phi_x^2 + \phi_y^2)X_{13} \right] - \sum_{even} \left[\phi_y(\phi_x Y_{23} + \phi_y X_{32}) + \frac{1}{2}(\phi_x^2 + \phi_y^2)X_{23} \right] \right\},$$

(3.43b)

where D is the depth of the magnet.

To examine the accuracy of the equations (1-24), the magnetic suspension force of an uniform magnet shown in Fig.B8 has been calculated and a comparison between analytical and numerical results is shown in Table B1.

MMF=1A x 400T
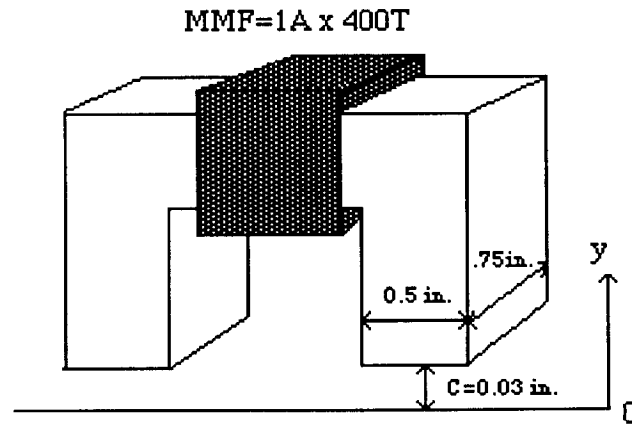
Figure B8. Test electromagnet

Table B1. Comparison of Analytical and Numerical results

	Force(N) y/c=0.0	Force(N) y/c=0.7	CPU	Charge($)
Analytical solution	19.68087	218.67681	_____	_____
Numerical one layer solution	19.68088	218.67640	1.80 sec.	1.27
Numerical whole region solution	19.68109	218.70340	1.87 sec.	1.30

2. Force Calculation using Nonlinear Flux Model

The methods described above will applied to the case where the flux is determined by Poisson's equation. The only difference is that the magnetic field is no longer current-free and the flux density will be the curl of the vector potential

$$\overline{B} = \nabla \times \overline{A}. \tag{3.44}$$

If there is only a z-component of current density, then

$$B_x = \frac{\partial \phi}{\partial y}, \quad B_y = -\frac{\partial \phi}{\partial x}. \tag{3.45}$$

The computation region for the force calculation will be one layer of elements adjacent to the movable rotor and the final equations are expressed in the form of (1-27).

$$F_x = \frac{D}{2\mu_0} \left\{ \sum_{\text{odd}} \left[\phi_y(\phi_x(X_{32}+X_{13})-\phi_y(Y_{23}+Y_{31}))+\frac{1}{2}(\phi_x^2+\phi_y^2)(Y_{23}-Y_{13}) \right] \right. $$
$$\left. + \sum_{\text{even}} \left[-\phi_y(\phi_y Y_{23}-\phi_x X_{32})+\frac{1}{2}(\phi_x^2+\phi_y^2)Y_{23} \right] \right. \tag{3.46}$$

$$F_y = \frac{D}{2\mu_0} \left\{ \sum_{\text{odd}} \left[\phi_x(\phi_y(Y_{23}+Y_{31})-\phi_x(X_{32}+X_{13}))+\frac{1}{2}(\phi_x^2+\phi_y^2)(X_{13}-X_{23}) \right] \right. $$
$$\left. + \sum_{\text{even}} \left[\phi_x(\phi_y Y_{23}-\phi_x X_{32})-\frac{1}{2}(\phi_x^2+\phi_y^2)X_{23} \right] \right. \tag{3.47}$$

A comparison of the results of this method to those of the original method, in which the energy contained in the entire solution region is used in calculating the virtual work involved, and the new one is displayed in Table B2.

Table B2. Comparison of whole region and one layer calculations

	Force(N) y/c=0.0	Force(N) y/c=0.7 x/c=0.7	CPU	Charge($)
One laye calculation	19.59116	186.24043	42.99 sec.	11.40
Whole region calculation	19.67500	186.90760	1min38 sec	26.79

References

B1. Silvester, P., Cabayan, H.S., and Browne, B.T., 1973, "Efficient Techniques for Finite Element Analysis of Electric Machines," IEEE Trans. Power Apparatus Syst., Vol. PAS-92, No.4, pp.1274-1281, July/Aug.

B2. Smith, R. S., Circuits, Devices and Systems, 3d ed.,Wiley, New York, 1976.

B3. Coulomb, J.L., "A methodology for the Determination of Global Electromechanical Quantities from A Finite Element Analysis and Its Application to The Evaluation of Magnetic Forces, Torques and Stiffness", IEEE Transactions on Magnetics, Vol. MAG-19, No.6, November 1983, PP. 2514-2519.

B4. Coulomb, J.L, "Finite Element Implementation on Virtual Work Principle for Magnetic or Electric Force and Torque Computation", IEEE Transactions on Magnetics, Vol. MAG-20, No.5, September 1984, pp. 1894-1896.
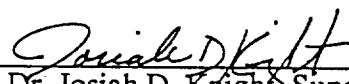
NONLINEAR DYNAMIC ANALYSIS OF A MAGNETIC BEARING SYSTEM WITH FLUX CONTROL: THE EFFECTS OF COORDINATE COUPLING
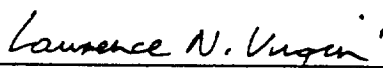
by
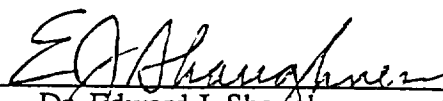
Thomas F. Walsh

Department of Mechanical Engineering and Materials Science
Duke University

Date: 26 April 1993 .
Approved:

_____
Dr. Josiah D. Knight, Supervisor

_____
Dr. Lawrence N. Virgin

_____
Dr. Edward J. Shaughnessy

A thesis submitted in partial fulfillment of the
requirements for the degree of Master of Science
in the Department of Mechanical Engineering and Materials Science
in the Graduate School of
Duke University

1993

Abstract

Active magnetic journal bearings are increasingly being used in a wider variety of turbomachinery applications because their magnetic forces can be controlled and thus, can be used to minimize any rotor vibration. However, most magnetic bearing research has ignored the curved shape of the magnet and has consequently inappropriately modeled its forces. By using an accurate model of the two-dimensional forces of the curved magnets, this paper models the unbalanced rotating dynamic motion of the shaft which is being minimized by two opposed pairs of axis independent, proportional-derivative flux controlled magnetic bearings. The nonlinear dynamic behavior of the rotor is then examined using the resulting equations of motion via numerical simulation and the harmonic balance method. This dynamic analysis consists of examining the shaft's free vibration and its potential energy and maximum steady-state amplitude versus the natural frequency ratio for varying control and system parameters.

Acknowledgments

I would first like to thank both of my advisor's, Dr. Josiah Knight and Dr. Lawrence Virgin, for their time, guidance and help. Without their assistance this thesis would certainly never have been completed. I would also like to thank the other member of my committee, Dr. Edward Shaughnessy as well as Holly Hammarstrom, Michael Todd and William Parizeau for the time that they spent either answering my questions or proofing my paper. Lastly, I would like to thank my parents and the rest of my family for their support and help throughout my undergraduate and graduate education.

Table of Contents

List of Figures

List of Symbols

a	Cross-sectional area of the pole face
B_1	Magnetic flux density of magnet one
B_{1b}	Bias magnetic flux density of magnet one
B_{1c}	Control magnetic flux density of magnet one
B_3	Magnetic flux density of magnet three
B_{3b}	Bias magnetic flux density of magnet three
B_{3c}	Control magnetic flux density of magnet three
B_b	Bias magnetic flux density of any magnet
B_c	Control magnetic flux density of any magnet
c	Distance from the outer edge of the rotor to the inner edge of the magnetic bearing
e	Mass unbalance in the shaft
E	Nondimensional mass unbalance in the shaft
F_{x1}	X-directional force resulting from magnet one
F_{x3}	X-directional force resulting from magnet three
F_{x13}	X-directional force resulting from magnets one and three
F_{x24}	X-directional force resulting from magnets two and four
F_{y1}	Y-directional force resulting from magnet one
F_{y3}	Y-directional force resulting from magnet three
F_{y13}	Y-directional force resulting from magnets one and three

F_{y24} Y-directional force resulting from magnets two and four

m   Mass of the shaft

R   Nondimensional radial displacement

t   Time

T   Nondimensional time

x   Horizontal displacement

X   Nondimensional horizontal displacement

X_{max} Nondimensional maximum displacement of either X or Y

X_o Nondimensional initial horizontal displacement

$\dot{x}$ Horizontal velocity

X' Nondimensional horizontal velocity

$\ddot{x}$ Horizontal acceleration

X'' Nondimensional horizontal acceleration

y   Vertical displacement

Y   Nondimensional vertical displacement

Y_o Nondimensional initial vertical displacement

$\dot{y}$ Vertical velocity

Y' Nondimensional vertical velocity

$\ddot{y}$ Vertical acceleration

Y'' Nondimensional vertical acceleration

α_1 Normal force proportionality constant of magnet one

α_3 Normal force proportionality constant of magnet three

α Normal force proportionality constant of any magnet

A   Nondimensional normal force proportionality constant of any magnet

ϕ Angle measured from the positive x-axis

γ Derivative control coefficient

Γ Nondimensional derivative control coefficient

κ Proportional control coefficient

K Nondimensional proportional control coefficient

μ_o Permeability of the free space

τ Natural period ratio

ω Forcing frequency

ω_{ln} Natural frequency of the linear system

ω_n Natural frequency of the uncoupled system

Ω Frequency ratio

Chapter 1

Introduction

A typical magnetic suspension system, see Figure 1.1, is comprised of two main parts, the actuator and the controller. The actuator, which often consists of two opposed pairs of magnets, see Figure 1.2, is responsible for levitating the shaft. While the controller, which consists of the feedback sensor(s), control electronics, and power amplifier(s), is used to regulate the forces of the actuator by using the signal from the sensor(s) and, depending on what is needed to minimize the shaft vibration, either increases or decreases the current supplied to each of the magnets.

In recent years, this general type of active magnetic bearing has increasingly been used in a variety of applications. They are now found in centrifugal compressors, electric power plants, petroleum refining, machine tools, satellites and military weapons (O'Connor (1992)). This rise in popularity can mainly be attributed to two advantages that magnetic bearings have over the more conventional fluid film bearings. First, because in the magnetic actuator the rotor is levitated and no contact occurs between it and the magnets, there is practically no friction and thus, there is no wear and no need for lubricants. The other benefit of magnetic bearings is that they have the ability to minimize any shaft vibration. In recent years, this control of the shaft vibration has been the main topic of most of the magnetic suspension research

1
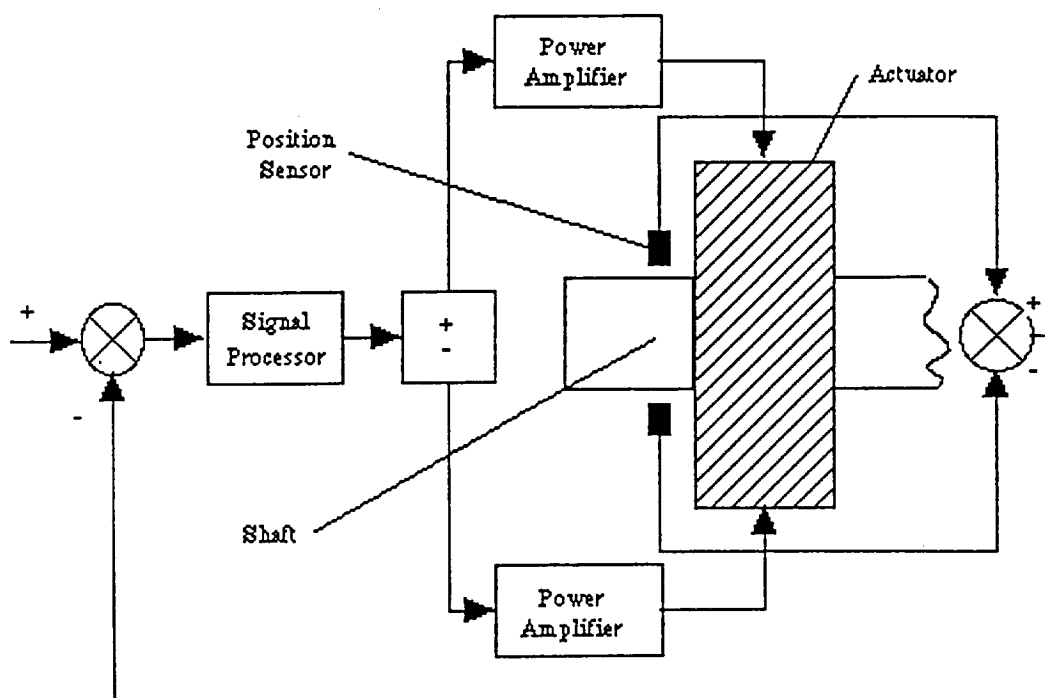
Figure 1.1: Block diagram of the active magnetic bearing.
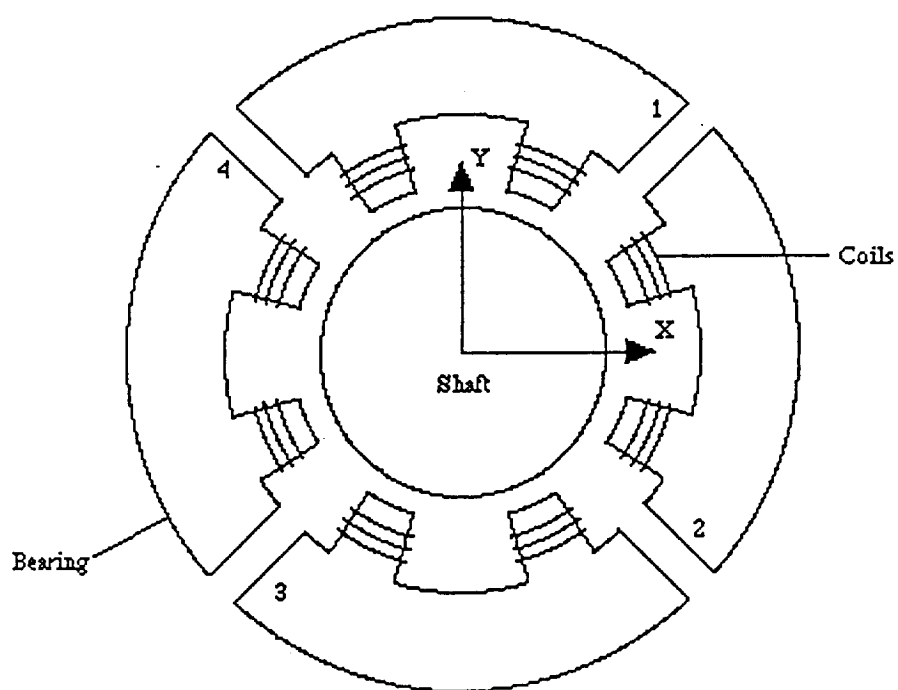
Figure 1.2: Active magnetic bearing and shaft.

and has focused on two distinct subareas:

      1. The most suitable controller and control strategy

      2. Theoretically investigating the effectiveness of the control scheme.

In trying to determine the optimal magnetic bearing control system, most researchers have experimented with digital and analog controllers and variations on proportional-derivative (pd) schemes. For example, Williams et al. (1991) experimentally compared the differences of using digital and analog pd controllers to reduce the amplitudes of a multimass flexible rotor. They found that in both control systems, increasing the stiffness tended to decrease the response at low speeds and increase the amplitudes at high speeds and increasing the damping minimized the maximum displacement for every forcing frequency. Williams et al. (1991) also concluded that including second derivative feedback in a digital pd controller gave the system a wider bandwidth while introducing integral feedback only affected the amplitude at the first critical speed. The possibility of using a digital pd controller was also experimentally examined by Scudiere et al. (1986); however, in their system the previous inputs were given uneven weight. The results showed that when the most recent inputs are heavily weighted the output responds slowly but is very smooth and that if the previous inputs are given less weight then the motion becomes less damped but responds much more quickly.

The other popular magnetic bearing research topic is to theoretically investigate controlling the motion of a flexible rotor with a magnetic bearing. Lee and Kim (1992) designed a suboptimal output feedback controller based on a truncated modal equation of the distributed parameter system. This control scheme minimized the displacement at the first critical speed but was inadequate at other supercritical frequencies. Nonami et al. (1990) experienced similar problems at high frequencies as Lee and Kim (1992). Their flexible rotor model was based on the finite-element

method and the control scheme was formulated by using eigenvalue analysis. Maslen and Bielk (1992) also examined the stability of a rotor supported by a magnetic bearing. They took into account sensor-actuator noncollocation and controller bandwidth; however, the performance of the model was not tested.

However, with the exception of Imlach et al. (1991) and Knight et al. (1992) there has been very little research completed which has measured the forces of the magnet. Imlach et al. (1991) compared predicted stiffness and force values in a closed-loop controlled magnetic bearing with their experimental counterparts. The agreement was good at small eccentricities; however, as the eccentricity increased the predicted and measured values began to diverge. Knight et al. (1992) also measured the forces from a magnet. They found that a single curved magnet produced forces in both the horizontal and vertical directions and that the horizontal force, assuming that the center of the magnet is situated directly on the y- or vertical axis (see magnet one in Figure 1.2), is proportional to the vertical force multiplied by the horizontal displacement. Most magnetic bearing papers, including Lee and Kim (1992), Nonami et al. (1990) and Maslen and Bielk (1992), have ignored this additional force component in their formulation of the vibration of the rotor.

This thesis will show that including the often ignored normal force of a curved magnet in a magnetic bearing model will cause the motion of the unbalanced shaft to be significantly different than was previously estimated by earlier linear models. This will be accomplished by first using the conclusions of Knight et al. (1992) to derive brand new equations of motion for a shaft which is encircled by a flux controlled magnetic journal bearing, chapter 2. Then in chapter 3, the resulting coupled, nonlinear equations of motion and two techniques, numerical simulation (fourth-order Runge-Kutta) and the harmonic balance method, will be used to examine how the introduction of the normal force component changes the potential energy and

4

dynamic motion of the shaft for varying control as well as physical parameters. In the final section, chapter 4, the results from these two chapters will be briefly summarized and some suggestions will be made concerning future work.

Chapter 2

Modeling Shaft Vibration

The magnetic bearing model used in the upcoming analysis is comprised of a shaft and two opposed pairs of flux controlled magnets, see Figure 2.1. Each of the
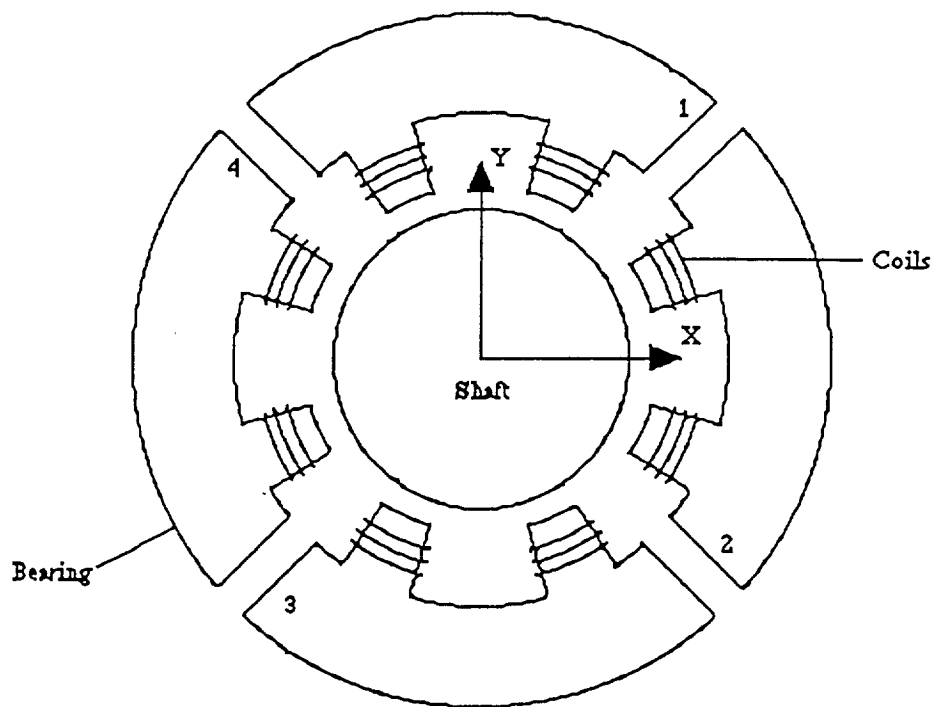
Figure 2.1: Magnetic bearing and shaft coordinate system.

magnet pairs is identical and is subjected independently to proportional and

6

derivative axis control. In addition, the circular shaft is being externally rotated and its center of mass is not necessarily coincident with its actual geometric center. This rotating unbalance of the shaft, in addition to the forces of the magnetic actuator, cause the rotor to vibrate. The following section models these forces and the motion of the shaft, nondimensionalizes the resulting equations and analyzes appropriate parameter values.

2.1 Dimensional Equation Derivation

The magnets in Figure 2.1 are labeled one through four. In the initial portion of the equation derivation, the opposed pair two and four will be ignored and full attention will be given to the forces from the magnet pair of one and three.

2.1.1 The Vertical Forces of Magnets One and Three

The y-directional forces of these two magnets, F_{y1} and F_{y3}, are approximated by one-dimensional magnetic circuit theory and are written as

$$F_{y1} = \frac{aB_1^2}{\mu_o} \tag{2.1}$$

and

$$F_{y3} = -\frac{aB_3^2}{\mu_o} \tag{2.2}$$

where B is the magnetic flux density of each magnet, a is the cross-sectional area of the pole face and μ_o is the permeability of the free space. The total vertical force produced by the pair of one and three is simply the sum of (2.1) and (2.2),

7

$$F_{y13} = \frac{a\left(B_1^2 - B_3^2\right)}{\mu_o}.$$

Both flux densities in this expression are equivalent to the sum of their bias and control flux densities, denoted by subscripts b and c respectively,

$$B_1 = B_{1b} + B_{1c} \qquad (2.3)$$

and

$$B_3 = B_{3b} + B_{3c}, \qquad (2.4)$$

and can be replaced to give

$$F_{y13} = \frac{a}{\mu_o}\left[\left(B_{1b} + B_{1c}\right)^2 - \left(B_{3b} + B_{3c}\right)^2\right]. \qquad (2.5)$$

Since both magnets are identical, their bias flux densities must also be equivalent, $B_{1b} = B_{3b} = B_b$. The control flux densities of the two magnets however, will have opposite signs, $B_{1c} = -B_{3c} = B_c$, so that each magnet will force the shaft toward the origin. By replacing B_{1b}, B_{1c}, B_{3b} and B_{3c} in equation (2.5), with their equivalent, either B_b or B_c, expanding the bracketed terms and simplifying, F_{y13} can be rewritten as

$$F_{y13} = \frac{4a}{\mu_o}B_b B_c. \qquad (2.6)$$

The control flux, B_c, is a function of the vertical displacement, y, and velocity, $\dot{y}$, the bias flux density, B_b, the proportional control coefficient, κ, and the derivative

8

control coefficient, γ, and is equivalent to

$$B_c = -\kappa B_b y - \gamma B_b \dot{y}. \qquad (2.7)$$

Replacing B_c in equation (2.6) with (2.7) yields the most useful representation of the vertical force caused by the magnet pair one and three,

$$F_{y13} = -\frac{4a}{\mu_o} B_b^2 (\kappa y + \gamma \dot{y}). \qquad (2.8)$$

2.1.2 The Horizontal Forces of Magnets One and Three

It was stated earlier, that Knight et al. (1992) found that a curved magnet produced a normal force (in the x-direction for magnets one and three and in the y-direction for magnets two and four) which was proportional to its normal displacement multiplied by the principal force (the force perpendicular to the normal force) of the same magnet; thus, the x-directional forces from magnets one and three can be written as

$$F_{x1} = \alpha_1 x |F_{y1}| \qquad (2.9)$$

and

$$F_{x3} = \alpha_3 x |F_{y3}| \qquad (2.10)$$

where α_1 and α_3 are the normal force proportionality constants and x denotes the horizontal component of displacement. The total x-directional force from these two magnets is simply obtained by summing (2.9) and (2.10),

$$F_{x13} = x\left(\alpha_1 |F_{y1}| + \alpha_3 |F_{y3}|\right).$$

Because both magnets are identical, and therefore must have the same physical properties, α_1 and α_3 can be replaced by α to give

$$F_{x13} = \alpha x\left(|F_{y1}| + |F_{y3}|\right).$$

F_{x13} can be rewritten as

$$F_{x13} = \frac{a}{\mu_o} \alpha x\left(B_1^2 + B_3^2\right)$$

by substituting the absolute of equations (2.1) and (2.2) for F_{y1} and F_{y3}. It is also useful to substitute (2.3) and (2.4) for B_1 and B_3,

$$F_{x13} = \frac{a}{\mu_o} \alpha x\left[(B_{1b} + B_{1c})^2 + (B_{3b} + B_{3c})^2\right]. \qquad (2.11)$$

This expression can be further reduced by replacing each flux density term with its respective equivalent, either B_b or B_c, and simplifying,

$$F_{x13} = \frac{2a}{\mu_o} \alpha x\left(B_b^2 + B_c^2\right). \qquad (2.12)$$

Finally, replacing the control flux density in (2.12) with (2.7) and expanding puts F_{x13} in its most practical form,

10

$$F_{x13} = \frac{2a}{\mu_o} \alpha x B_b^2 \left(1 + \kappa^2 y^2 + 2\kappa\gamma y\dot{y} + \gamma^2 \dot{y}^2\right).$$ (2.13)

2.1.3 All Other Forces Acting on the Shaft

A similar procedure can be used to obtain the vertical and horizontal magnetic forces from magnets two and four,

$$F_{y24} = \frac{2a}{\mu_o} \alpha y B_b^2 \left(1 + \kappa^2 x^2 + 2\kappa\gamma x\dot{x} + \gamma^2 \dot{x}^2\right)$$ (2.14)

and

$$F_{x24} = -\frac{4a}{\mu_o} B_b^2 (\kappa x + \gamma\dot{x}).$$ (2.15)

These two equations, along with (2.8) and (2.13), represent an accurate mathematical description of the forces from the magnetic actuator which act on the shaft. The shaft however, will also be subjected to an additional force which results from it being rotated and its mass being unevenly distributed. This additional load is analogous to rotating unbalance in rotor dynamics and its components can be written as $me\omega^2 \sin\omega t$, in the y-direction, and $me\omega^2 \cos\omega t$, in the x-direction, where m is the mass of the shaft, e is the distance from the geometrical center of the shaft to its center of gravity and ω is the forcing frequency. By applying Newton's second law of motion, $\sum F = ma$, in each direction, the nonlinear, coupled equations of motion which describe a shaft that is unbalanced, rotating and subjected to flux controlled magnetic fields are obtained,

$$m\ddot{y} = -\frac{4a}{\mu_o} B_b^2 \left[\kappa y + \gamma\dot{y} - \frac{\alpha}{2} y \left(1 + \kappa^2 x^2 + 2\kappa\gamma x\dot{x} + \gamma^2 \dot{x}^2\right) \right] + me\omega^2 \sin\omega t$$ (2.17)

11

$$m\ddot{x} = -\frac{4a}{\mu_o}B_b^2\left[\kappa x + \gamma\dot{x} - \frac{\alpha}{2}x\left(1 + \kappa^2 y^2 + 2\kappa\gamma y\dot{y} + \gamma^2\dot{y}^2\right)\right] + me\omega^2\cos\omega t. \quad (2.18)$$

In both of these equations, note that all of the linear displacement and velocity terms are a direct result of the principal forces of the four magnets (the forces which can be modeled using one-dimensional magnetic circuit theory). In contrast, the normal forces are responsible for every coupling and nonlinear term in (2.17) and (2.18); thus, including the normal forces in the equations of motion of the shaft introduces the system to instabilities by decreasing its linear restoring forces, i.e. making it less stiff.

2.2 Nondimensionalization of the Equations of Motion

To make the upcoming analysis easier and the results more physically meaningful, (2.17) and (2.18) will be nondimensionalized by replacing the variables in both equations with the following,

$$x = Xc \qquad\qquad y = Yc$$
$$t = T/\omega_n \qquad\qquad \omega = \Omega/\omega_n$$
$$\kappa = K/c \qquad\qquad \gamma = \Gamma/c\omega_n$$
$$\alpha = A/c \qquad\qquad e = Ec,$$

where all capitals represent the nondimensional quantities, c is the radial clearance between the rotor and the inner surface of the controlling magnets and the uncoupled natural frequency ($\alpha = 0$) is equal to

$$\omega_n = \sqrt{\frac{4a\kappa B_b^2}{m\mu_o}}.$$ (2.19)

Making these substitutions results in the following ordinary differential equations,

$$cm\omega_n^2 Y'' = -\frac{4aB_b^2}{\mu_o}\left(KY + \Gamma Y' - \frac{A}{2}Y\left(1 + K^2 X^2 + 2K\Gamma XX' + \Gamma^2 X'^2\right)\right) + cm\omega_n^2 E\Omega^2 \sin\Omega T$$

and

$$cm\omega_n^2 X'' = -\frac{4aB_b^2}{\mu_o}\left(KX + \Gamma X' - \frac{A}{2}X\left(1 + K^2 Y^2 + 2K\Gamma YY' + \Gamma^2 Y'^2\right)\right) + cm\omega_n^2 E\Omega^2 \cos\Omega T$$

where a prime denotes differentiation with respect to nondimensional time. By dividing both of the two previous expressions by $cm\omega_n^2$ and replacing the remaining squared uncoupled natural frequency terms in the resulting equations with (2.19) gives

$$Y'' = -\frac{4am\mu_o B_b^2}{4acm\kappa\mu_o B_b^2}\left(KY + \Gamma Y' - \frac{A}{2}Y\left(1 + K^2 X^2 + 2K\Gamma XX' + \Gamma^2 X'^2\right)\right) + E\Omega^2 \sin\Omega T$$

and

$$X'' = -\frac{4am\mu_o B_b^2}{4acm\kappa\mu_o B_b^2}\left(KX + \Gamma X' - \frac{A}{2}X\left(1 + K^2 Y^2 + 2K\Gamma YY' + \Gamma^2 Y'^2\right)\right) + E\Omega^2 \cos\Omega T$$

The most useful forms of the nondimensional equations of motion are obtained by canceling all like terms and replacing $c\kappa$ with K,

13

$$Y'' = -\frac{1}{K}\left(KY + \Gamma Y' - \frac{A}{2}Y\left(1 + K^2X^2 + 2K\Gamma XX' + \Gamma^2 X'^2\right)\right) + E\Omega^2 \sin\Omega T \quad (2.20)$$

$$X'' = -\frac{1}{K}\left(KX + \Gamma X' - \frac{A}{2}X\left(1 + K^2Y^2 + 2K\Gamma YY' + \Gamma^2 Y'^2\right)\right) + E\Omega^2 \cos\Omega T \quad (2.21)$$

Note that, in obtaining (2.20) and (2.21), c and the uncoupled natural frequency, ω_n, were chosen as the two variables which were used to aid in the nondimensionalization of equations (2.17) and (2.18). Both variables were selected over other parameters for different reasons. First, the choice of c allows the dependent variables in the governing equations of motion to become X, $\dot{X}$, Y, $\dot{Y}$ and T. As a result, the numerical solution becomes more meaningful, because both X and Y, x / c and y / c respectively, are real physical properties and both are constrained to remain within the range of negative to positive one. In contrast, ω_n was chosen as a nondimensionalizing parameter because it will present the least amount of problems in the following analysis. Its only real drawback is that when the dimensionless normal force proportionality constant is varied, Ω will not shift with it. Fortunately, because A is generally much smaller than K (their magnitudes will be discussed in the next section.), the actual shift in the forcing frequency ratio due to varying A is extremely small. The only other reasonable choice to use in place of ω_n is the linear natural frequency,

$$\omega_{ln} = \sqrt{\left(K - \frac{\alpha}{2}\right)\frac{4aB_b^2}{m\mu_o}}.$$

Although this would allow the effect of A on Ω to be incorporated into the solution of (2.20) and (2.21), it would also mean that the equations of motion would have

14

$1/\left(K-\dfrac{A}{2}\right)$ in place of both of the $1/K$ and thus, some values would become cumbersome. For example, the uncoupled stiffness would change from a value of one to $K/\left(K-\dfrac{A}{2}\right)$.

2.3 Appropriate Variable Ranges

A significant part of the upcoming analysis is to examine how A, K, Γ and E affect dynamic behavior of the unbalanced rotating shaft. This will be accomplished by varying the four parameters within the following practical limits.

The dimensionless normal force proportionality coefficient, A, for a single magnet was determined by Knight et al. (1992) to be approximately equal to 0.15. Its value for opposed magnets was less exact, so during the analysis, it will be varied from 0.05 to 0.25. The values of the dimensionless proportional and derivative control coefficients, unlike A, are less defined, although their selection does affect certain bearing properties and must be chosen accordingly. For example, magnetic bearings are often characterized by low damping; thus, to achieve an uncoupled damping ratio, $\Gamma/2K$, of 0.1 to 0.3 for a K equal to one, Γ must fall within the range of 0.2 to 0.6. K on the other hand is inversely proportional to the uncoupled damping ratio, so it would be advantageous to have large values of K which would decrease the damping in the bearing. Unfortunately, K is also equal to the inverse of the available displacement before the magnetic force becomes zero for $\Gamma=0$, so to balance the two competing effects, K in the upcoming analysis will be limited to values under five. The fourth and final variable to consider, the nondimensionalized mass eccentricity, is dependent on the imperfection of the shaft, e, and the distance from the rotor to the magnet, c. Generally, e, the dimensional rotating mass

15

unbalance, is an extremely small number compared to c; however, c is solely dependent on the magnetic actuator design and in some instances may also be very small. It is unlikely, nevertheless, that in a magnetic actuator magnitude of e will approach that of c. A more reasonable situation is that the dimensionless mass unbalance is going to be equal to or less than 0.05; however, to be on the safe side, E will be given values as high as 0.15.

Chapter 3

Results And Analysis

3.1 Potential Energy

If it exists (or can be derived), a useful tool in many dynamic analyses is a graphical representation of the potential energy, V, of the system. The dimensionless potential energy, which can be derived from the restoring forces in the conservative form of the governing equations, is

$$V = \frac{1}{K}\left[\left(\frac{K}{2} - \frac{A}{4}\right)\left(X^2 + Y^2\right) - \frac{A}{4}K^2X^2Y^2\right] \qquad (3.1)$$

In addition to the vertical and horizontal displacements, note that V is a function of A and K. Consequently, fluctuations in either variable should lead to changes in the form of the potential energy.

As A is increased from 0.05 to 0.25, with K held fixed, the potential energy wells, Figures 3.1a to 3.1c, become increasingly shallow. Thus, as expected, when the dimensionless normal force proportionality coefficient is increased the deviation of the potential energy from the linear case becomes more pronounced. This departure from the linear case is also increasingly evident at larger displacements. Also note

17
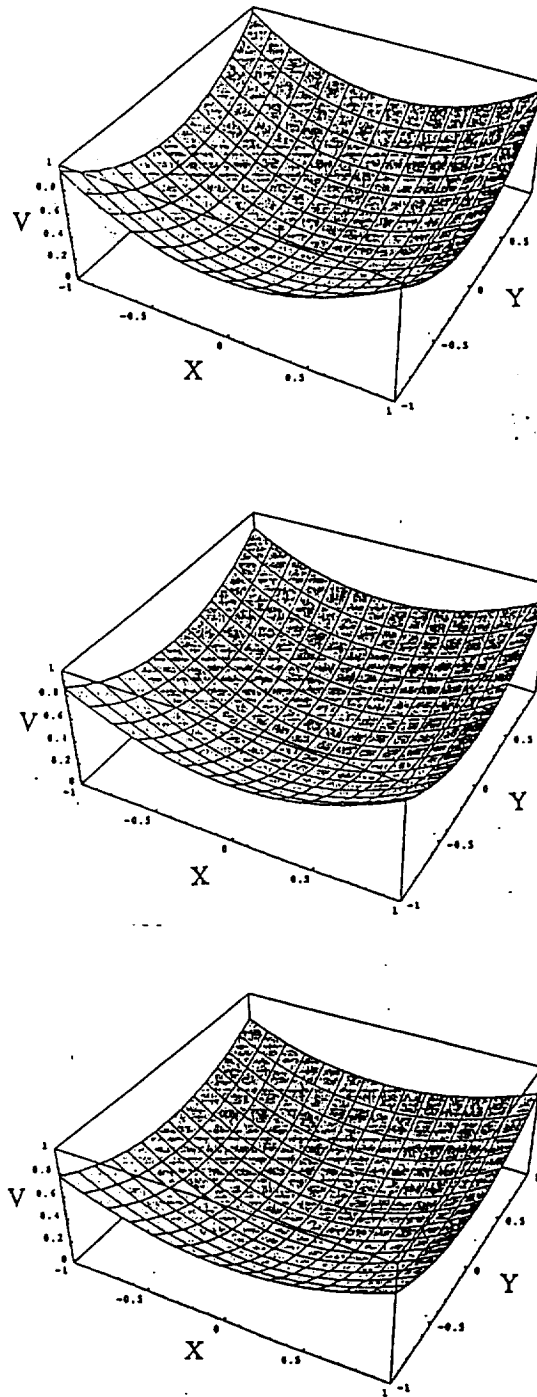
Figure 3.1: Potential energy wells where K=3 and a. A=0.05 b. A=0.15 c. A=0.25.

that in Figure 3.1 the potential functions, unlike some nonlinear systems, do not contain any unstable regions, i.e. a local maximum, and only have one equilibrium point, the origin, within the physical system.

If K is now varied while A is held constant, Figure 3.2, the changes in the potential wells are similar to those observed in Figure 3.1. This may be somewhat surprising given the fact that typically, when something thought to be analogous to stiffness, such as the dimensionless proportional control coefficient, is increased, an increase *not* a decrease in stiffness should occur. However, it is important to remember that because of the nondimensionalization, the linear stiffnesses in (2.20) and (2.21) are equal to $1 - \dfrac{A}{2K}$ and thus, a reasonable increase in K will only affect the potential wells slightly. If K is now increased to twenty, Figure 3.3, there exists the possibility that the mass can enter an unstable area at high absolute values of X and Y. In the magnetic actuator, the likelihood that K will reach such a high magnitude is small; however, if the physical boundary of the dynamic system is increased, then the unstable equilibrium points corresponding to

$$(X, Y) = (\pm\sqrt{\frac{2K - A}{AK^2}}, \pm\sqrt{\frac{2K - A}{AK^2}})$$

will need to be avoided.

3.2 Dynamic Motion of the Shaft

In the following two sections, two different techniques will be used to examine the free and forced nonlinear dynamic behavior of the circular shaft and the effects of K, A, Γ and E on this motion. The initial analysis will be based on the Runge-Kutta
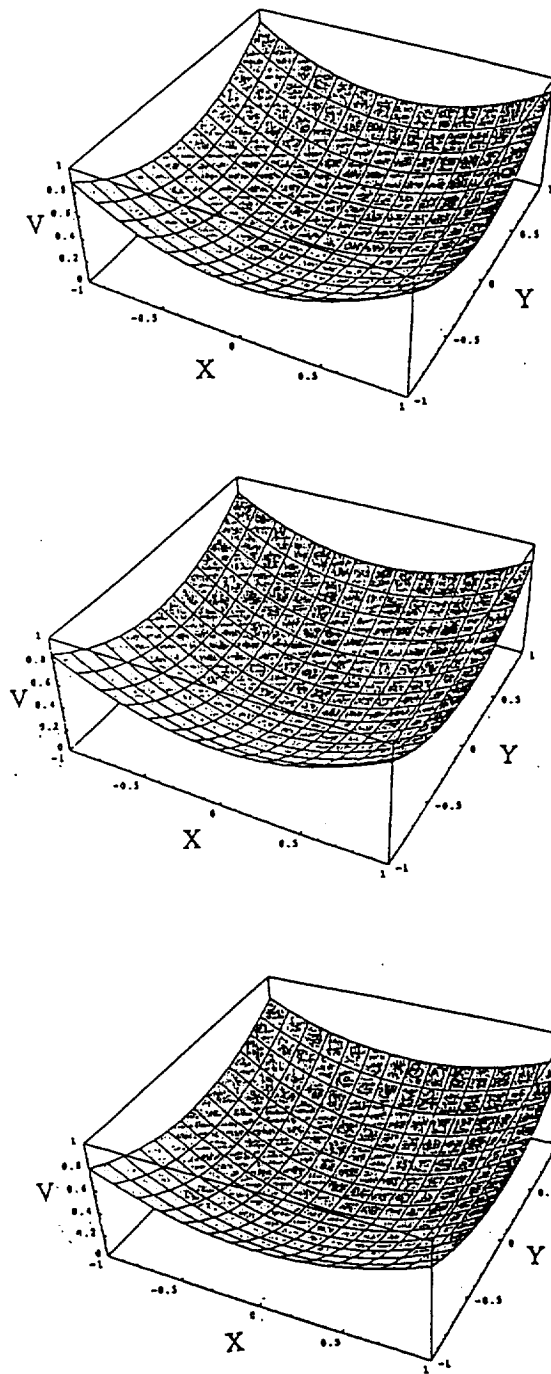
Figure 3.2: Potential energy wells where A=0.15 and a. K=1 b. K=3 c. K=5.
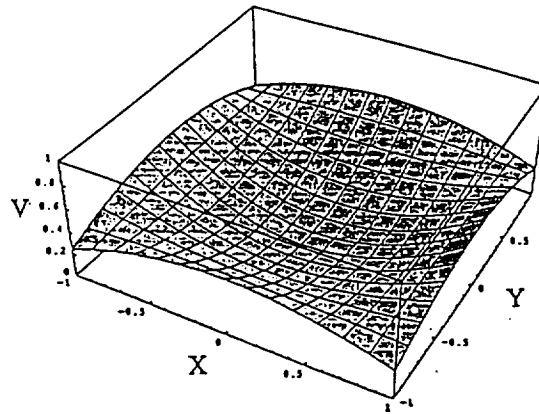
Figure 3.3: Potential energy well where K=20 and A=0.15.

routine which is a highly accurate numerical method for solving differential equations and is described in Appendix A. In the second section, the results will be calculated using an approximate but sometimes extremely valuable analytical technique called the harmonic balance method.

3.2.1 Runge-Kutta Method Free Vibration Results

Often when investigating nonlinear systems, such as a pendulum undergoing large amplitude swings, it is useful to examine how the natural period changes with amplitude. Unfortunately, explicitly solving for the natural period in this case cannot be achieved because of the nonlinearity in the equations of motion of the shaft. However, by using numerical simulation, an accurate estimate of the natural period of the shaft as a function of the initial conditions can be obtained. An additional tool in the construction of these graphs is to use the symmetry of the system. For example, in Figure 3.3, the quartered section where both X and Y are positive, call it region one,

has the same shape as the other quarters of the well and within region one, its two halves are mirror images of each other. Because of this symmetry, only an eighth of the initial conditions need to be analyzed to garner a complete understanding of the total behavior of the system. These initial conditions are defined as

$$Y_o = R\sin\phi$$

and

$$X_o = R\cos\phi$$

where R is the nondimensional radial distance of the shaft and ϕ is the angle measured from the x-axis to the radial distance vector, see Figure 3.4.
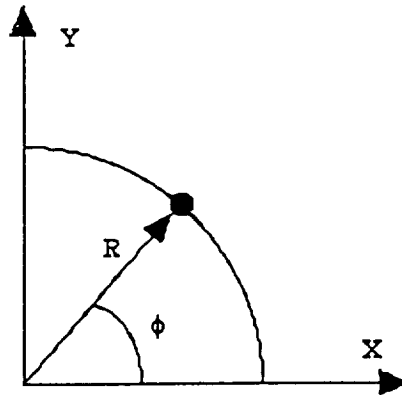
Figure 3.4: Summary of natural period initial conditions.

In Figure 3.5a, ϕ is fixed at 22.5 degrees and the radius is increased from zero to one while both of the initial velocities are held at zero. For each increment in R the natural period ratio, τ, for both displacements is determined by measuring the time between consecutive peak amplitudes and by dividing this result with the linearized natural period, $2\pi / \sqrt{1 - \dfrac{A}{2K}}$,. Unlike the linear case, the τ of both displacements is initial condition dependent and the values of the two natural period ratios diverge and

22
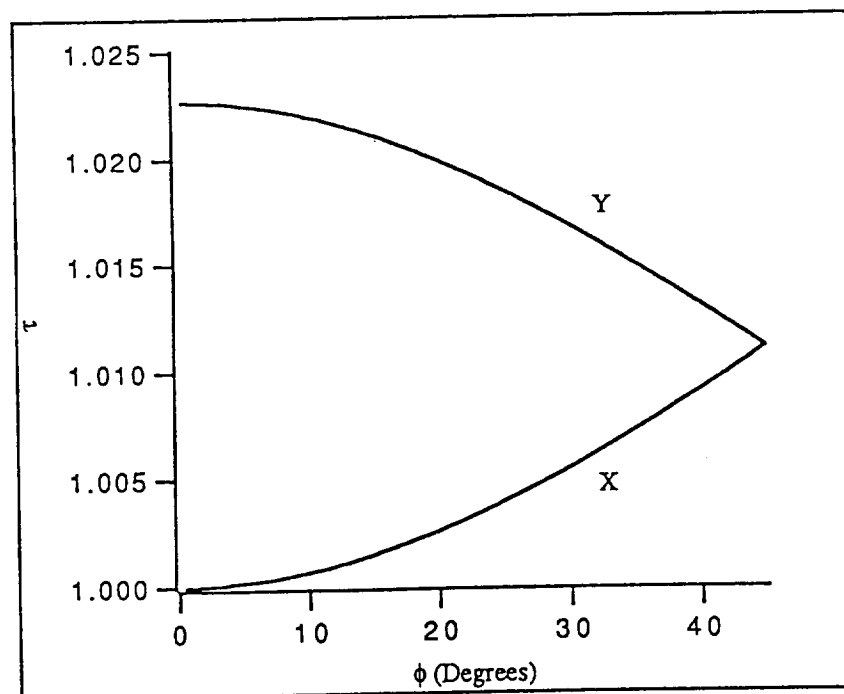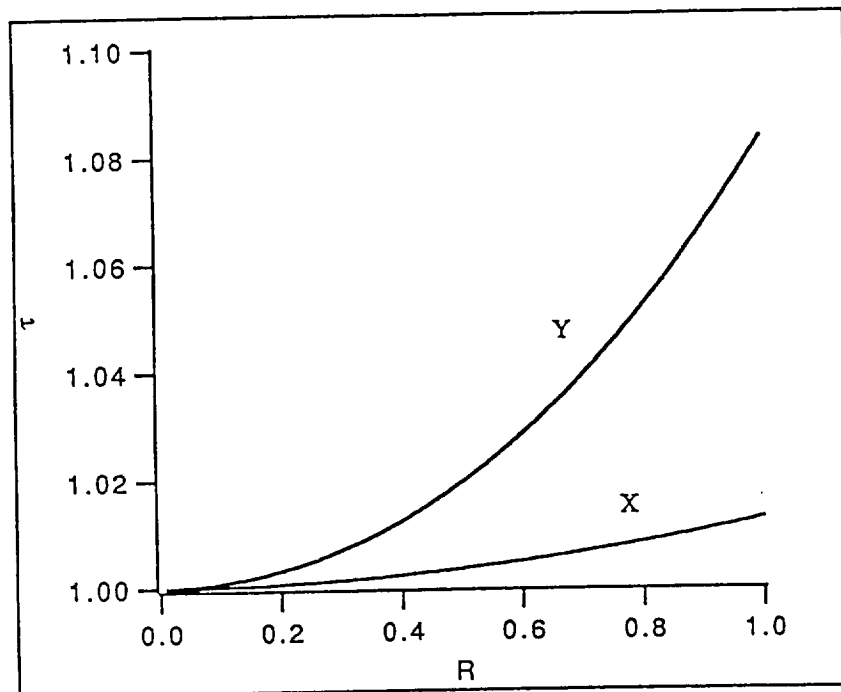
Figure 3.5: Numerically obtained natural period for K=3, A=0.15, a. φ=22.5 and varying R
b. R=0.5 and varying φ.

thus become more nonlinear as the radius increases. If the radius is now held fixed at 0.5 and τ for both X and Y is measured for each increment in ϕ, a graphical display of the angle versus the ratio is obtained, Figure 3.5b. Only when ϕ is equal to $\frac{\pi}{4}(2n-1)$ radians, where n is any integer, is there any agreement between the natural period ratios of the two displacements. At every other angle the ratios are different suggesting that the undamped, unforced motion of the shaft will not repeat every period like the linear system. Instead, the behavior, see Figures 3.6a and 3.6b, will be analogous to beating, which occurs in harmonically forced linear systems where the natural and forcing frequencies are extremely close but not exact, and results in a trajectory which is not an ellipse or a circle but is closed and passes over a large portion of area, Figure 3.6c.

3.2.2 Runge-Kutta Method Forced Vibration Results

A useful tool for investigating how the nonlinearities affect the rotating dynamic behavior of the shaft over ranges of system parameters is to construct amplitude response curves for varying values of K, A, Γ and E. This graph plots the maximum steady-state nondimensionalized horizontal and vertical displacements versus the frequency ratio, Ω and Figures 3.7 to 3.15 are obtained by numerically simulating the nondimensional equations of motion and by picking off both maximum displacements after 400 cycles (to allow for transients to decay). Unfortunately, contrary to their linear counterparts, the maximum amplitudes in nonlinear systems are initial condition dependent. Thus, to make the analysis easier, all of the following amplitude response curves will be constructed using the initial conditions $X(0) = Y(0) = \dot{X}(0) = \dot{Y}(0) = 0$, the rest state, unless stated otherwise.

A comparison of Figures 3.7a to 3.7c, amplitude response curves where only K is

24
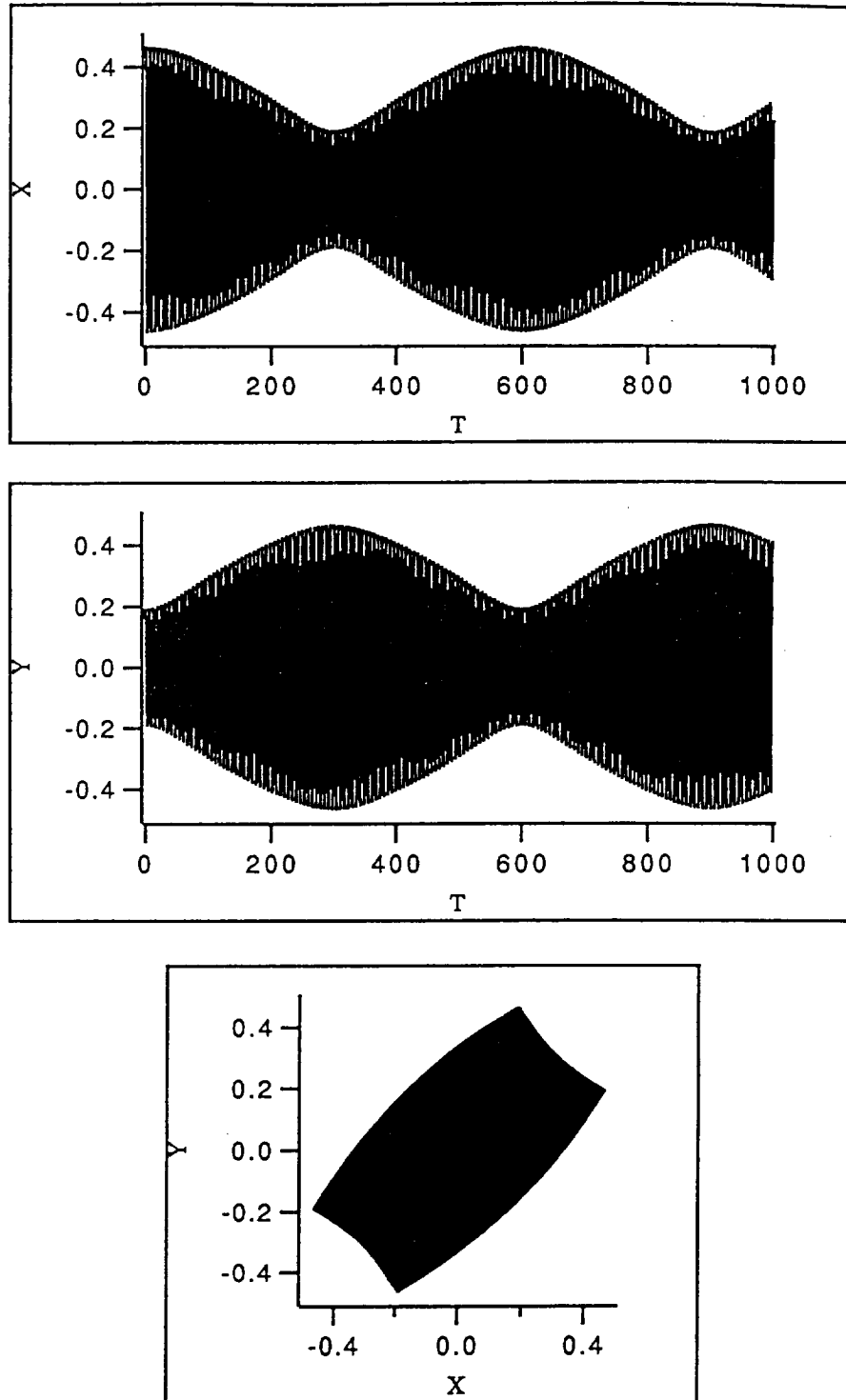
Figure 3.6: Numerical free vibration a. Time series of X b. Time series of Y
c. Trajectory where K=3, A=0.15, R=0.5 and φ=22.5.
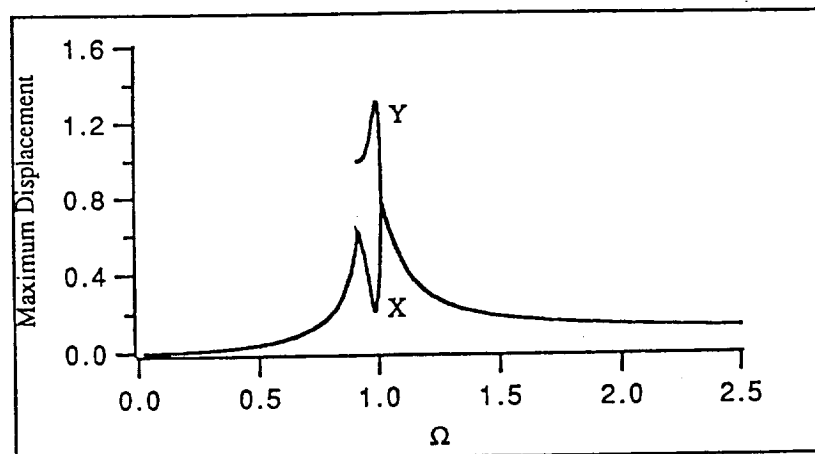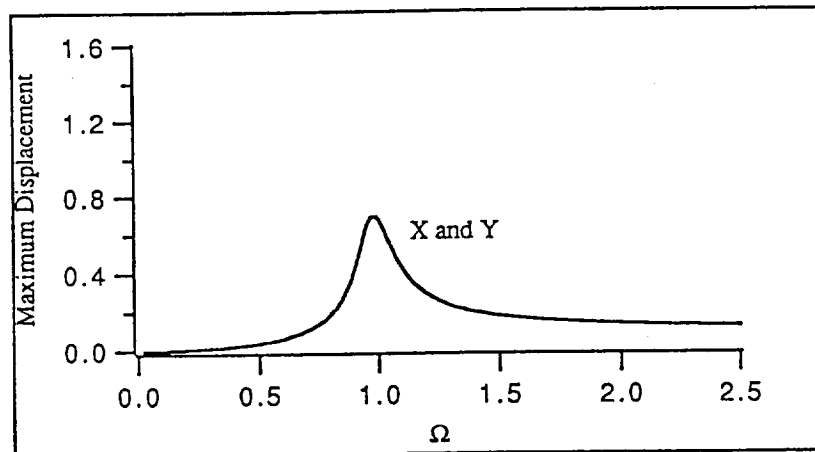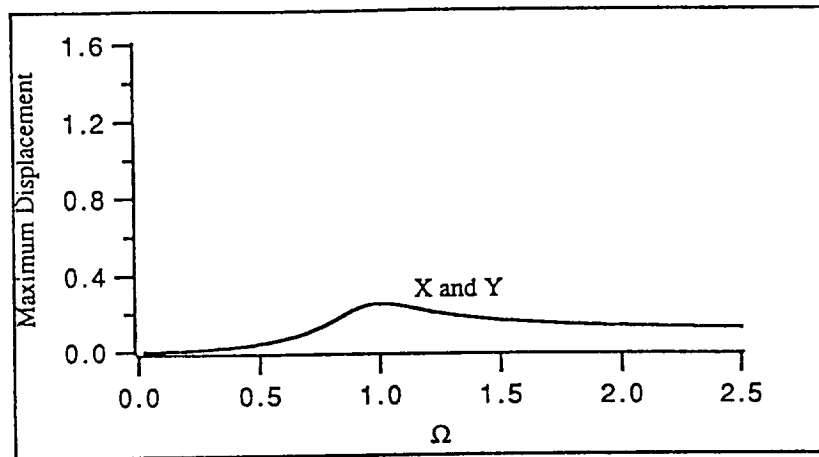
Figure 3.7: Numerical amplitude response curves where A=0.15, Γ=0.4,
E=0.1 and a. K=1 b. K=3 and c. K=5.
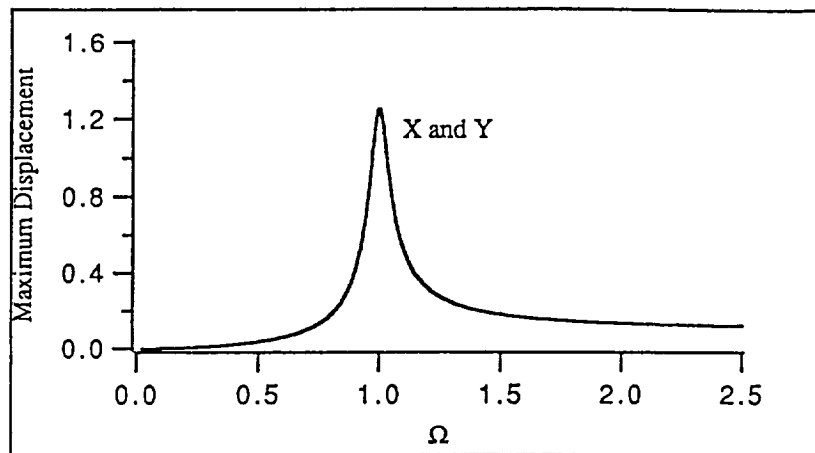
Figure 3.8: Uncoupled amplitude response curve where K=5, A=0, Γ=0.4 and E=0.1.

varied, yields some interesting results. First, as the dimensionless proportional control coefficient is increased the amplitudes grow, especially near resonance. This behavior may be somewhat surprising if K is again thought of in terms of stiffness or proportional feedback; however, because of the nondimensionalization of (2.20) and (2.21), K is actually more closely related to the inverse of the uncoupled damping ratio, $\Gamma/2K$, in each equation; therefore, the growing amplitudes near resonance make sense for increasing values of K. The most surprising feature of graphs 3.7a to 3.7c is the difference in the maximum amplitudes of X and Y for K = 5. In the analogous uncoupled linear case, A = 0, the maximum amplitudes are identical, Figure 3.8; thus, the amplitude split in Figure 3.7c can be attributed to the nonlinearity of the equations of motion. It is not completely surprising that this behavior only occurred when K was large. For increased values of K, larger amplitudes are expected and earlier, while examining the potential wells, larger displacements meant the nonlinearity of the equations became more pronounced.

The time series, trajectories and phase projections of the nonlinear and linear K = 5 cases at comparable frequency ratios, Figures 3.9 and 3.10 respectively, yield
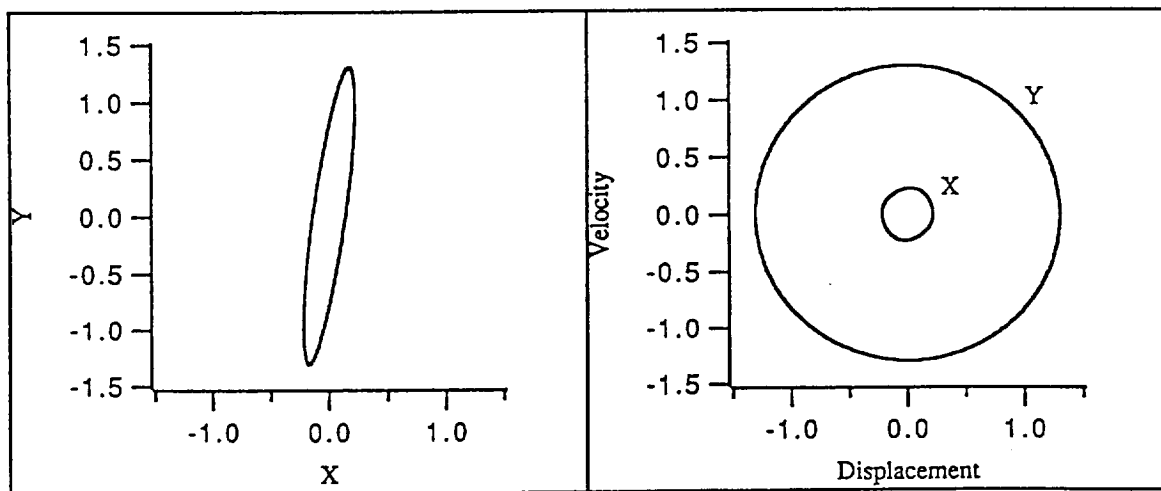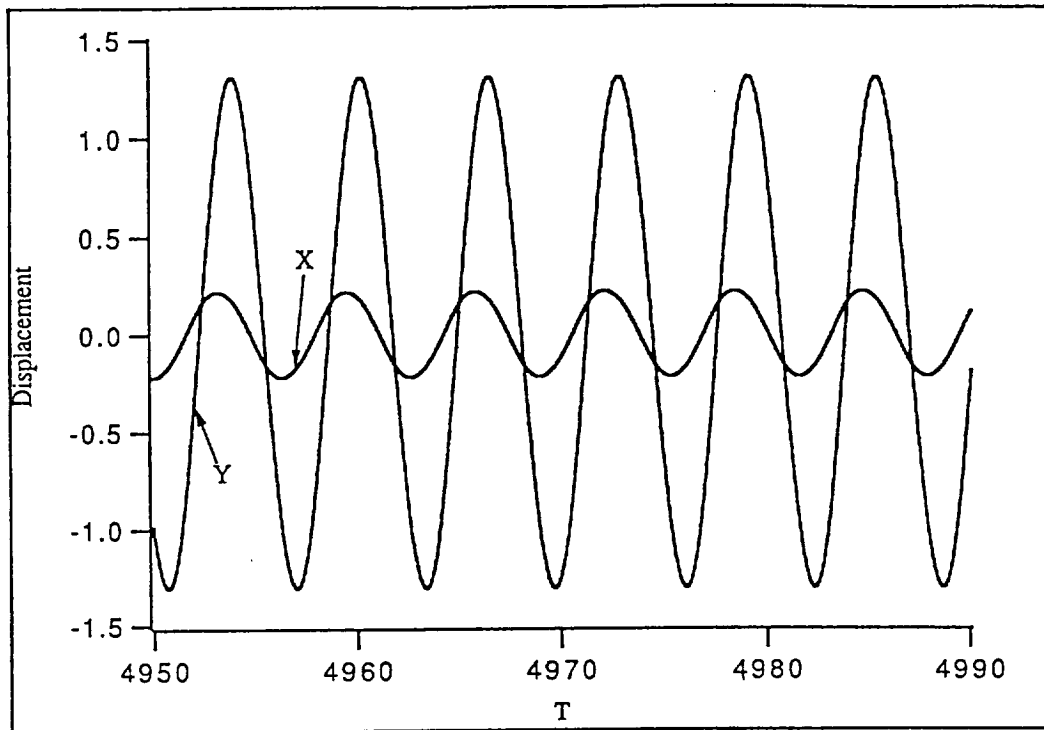
Figure 3.9: Numerical steady-state a. Time series b. Trajectory c. Phase portrait where K=5, A=0.15, Γ=0.4, E=0.1 and Ω=0.9925.
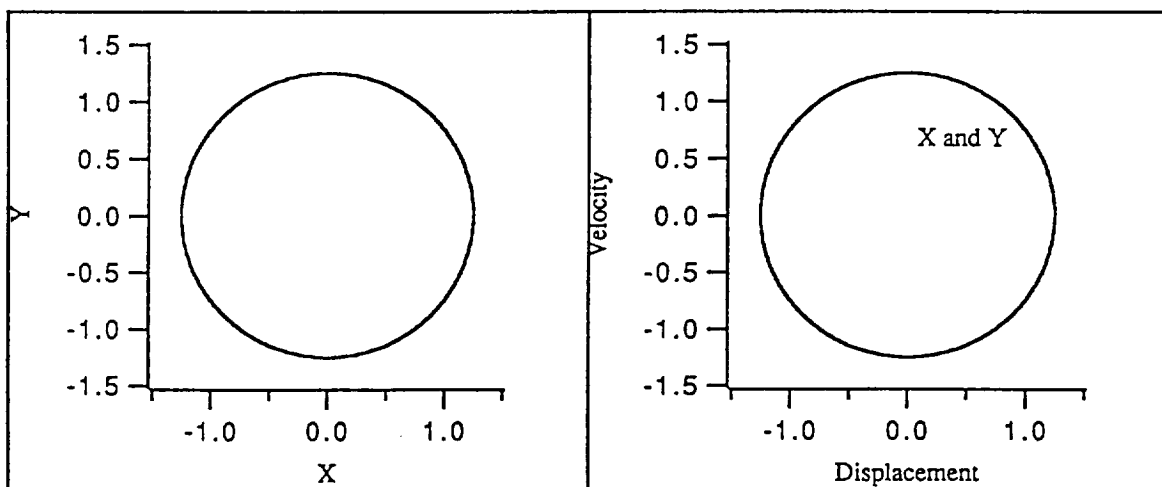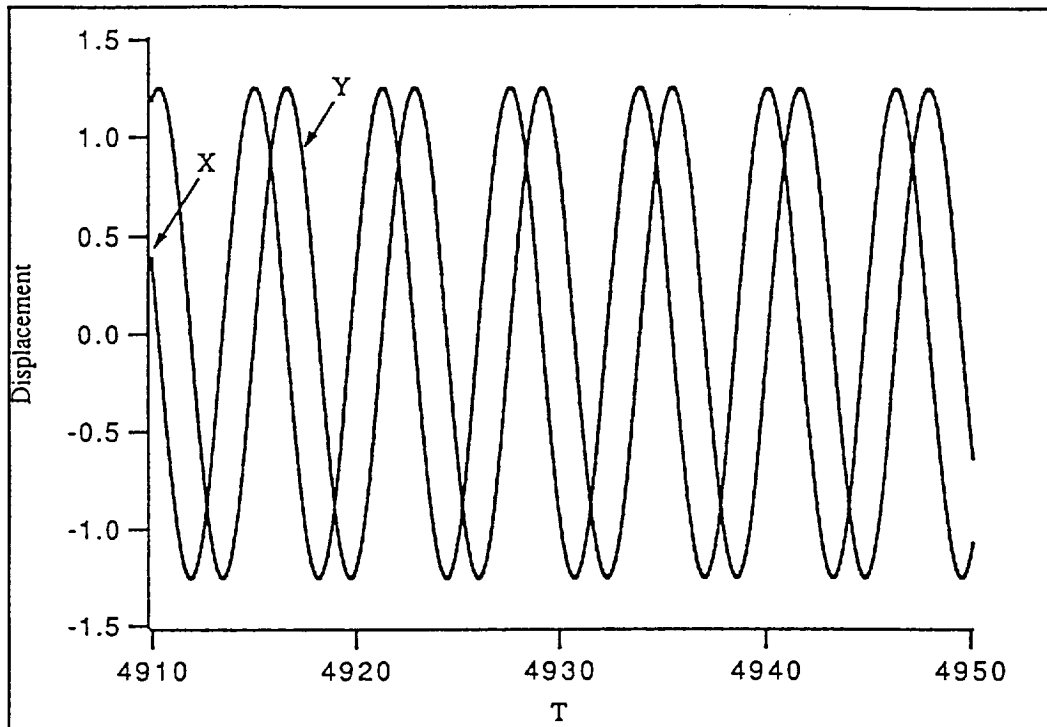
Figure 3.10: Numerical uncoupled steady-state a. Time series b. Trajectory c. Phase portrait where K=5, A=0, Γ=0.4, E=0.1 and Ω=1.

some further interesting behavior. (Note that Figures 3.9 and 3.10 are at different values of Ω, this is necessary because α was not included in the selection of ω_n.) As expected, in the linear time series, Figure 3.10a, the maximum amplitudes are $\pi/2$ out of phase. This however is not true in the nonlinear case, Figure 3.9a.; therefore, when one component of displacement is at its maximum the other has a nonzero value and the path resembles an angled ellipse. In addition, the maximum radial amplitude in the nonlinear case, Figure 3.9b, is larger thus increasing the likelihood of the rotor striking the magnetic actuator. It should be noted that, although the actual maximum amplitudes and the transient motion in Figures 3.7 to 3.10 and some of the subsequent graphs are well outside the physical limitations of the bearing, it is beneficial to examine these cases because they provide a better dynamic understanding of the system and may prove even more useful if the amplitude restriction is somehow changed.

In Figures 3.11a to 3.11c, every variable except the normal force proportionality constant is fixed. In each of the three graphs the amplitudes tend to decrease only slightly and the peaks and the entire plots tend to be slightly shifted to the left for increasing A. Once again this shift in amplitude is purely a function of what natural frequency is used in the nondimensionalization of the equations of motion. If $\kappa - \dfrac{\alpha}{2}$ replaced κ in equation (2.19) then no shifts would occur in Figures 3.11a to 3.11c. The major difference between the three graphs is, in the third graph, Figure 3.11c, another amplitude split occurs. However, unlike the two distinct maximum amplitudes in Figure 3.7c, these different amplitudes result because for greater values of A the system will deviate more from the linear case, recall Figures 3.1a to 3.1c.

Unlike K and A, Γ must be decreased for the maximum X and Y displacements to split. Actually, the effect of the dimensionless derivative control coefficient on the amplitude response curves, Figure 3.12a to 3.12c, is extremely similar to the
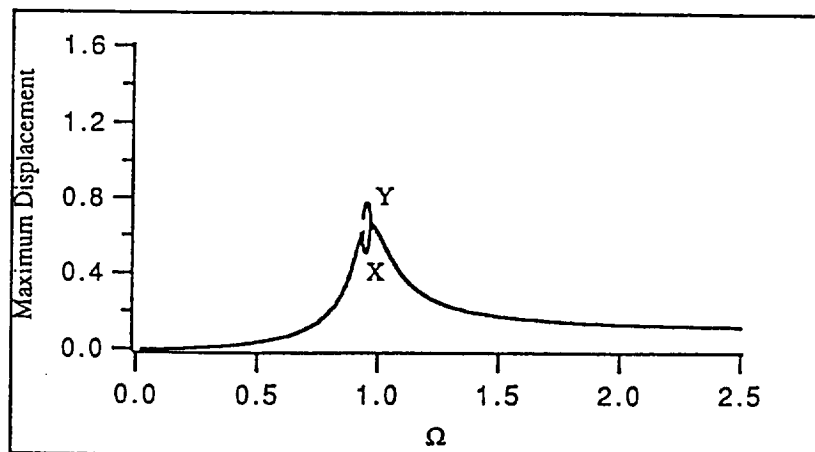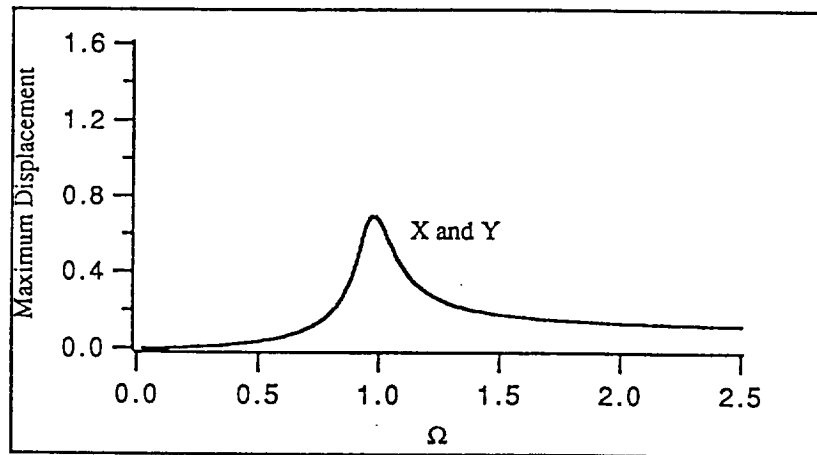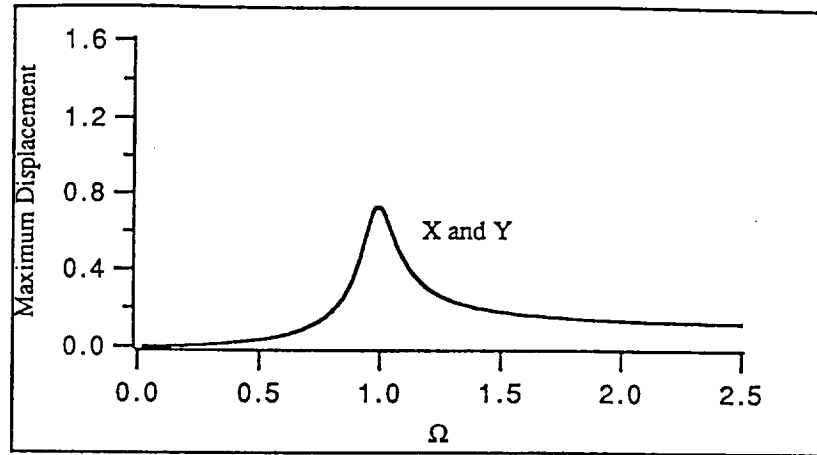
Figure 3.11: Numerical amplitude response curves where K=3, Γ=0.4, E=0.1 and a. A=0.05 b. A=0.15 c. A=0.25.
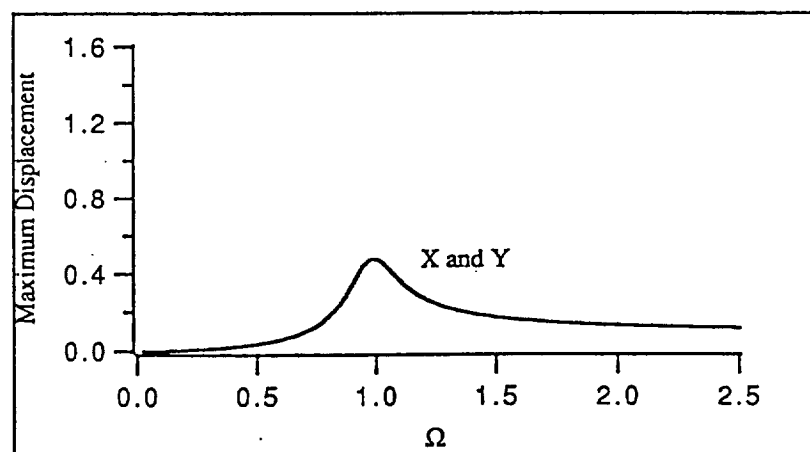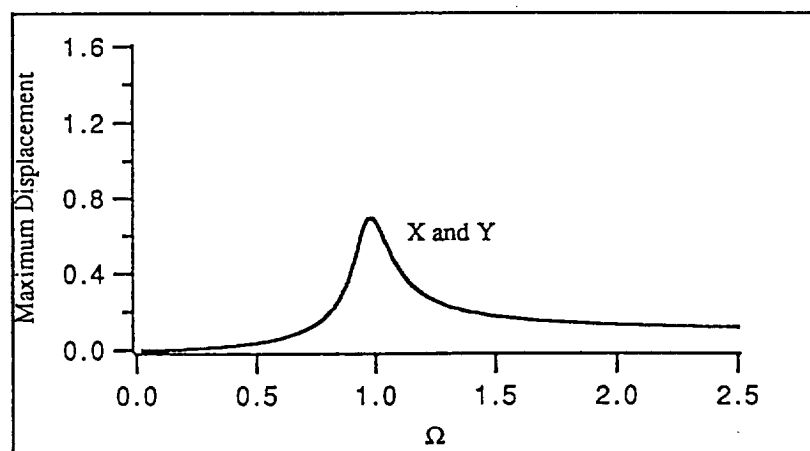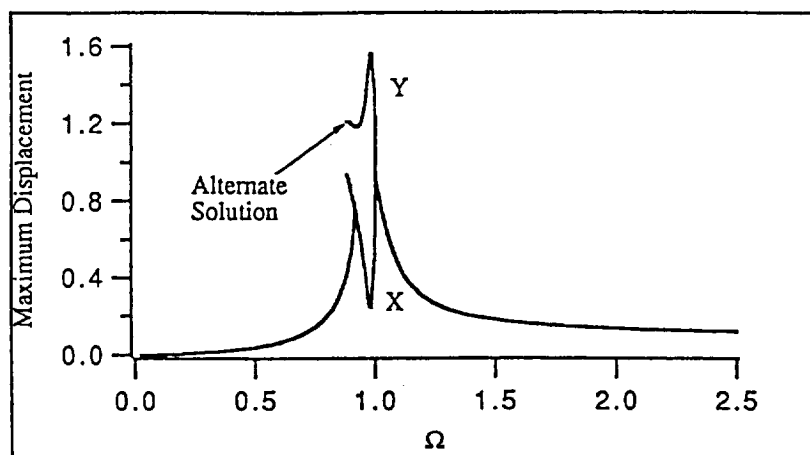
Figure 3.12: Numerical amplitude response curves where K=3, A=0.15, E=0.1 and a. Γ=0.2 b. Γ=0.4 c. Γ=0.6.

influence of $1/K$ on Figures 3.7a to 3.7c; in that any increase in Γ results in smaller maximum amplitudes especially near resonance. This relationship between the two variables is not surprising because the uncoupled damping ratios in the equations of motion are equal to $\Gamma/2K$. In Figure 3.12a, unlike any other plot up until this point, an additional solution occurs directly to the left of the amplitude split. This tiny branch of solutions was found using different initial conditions from the traditional all zeros. Instead, the frequency ratio was slowly decreased from 2.5 and the starting values for each decrease in Ω were obtained using steady-state data from the preceding frequency ratio. Using this method, the alternate solution was tracked until approximately $\Omega \cong 0.8875$. At that point, the only solution that could be located was the one where the two maximum amplitudes agree. It is also likely that an unstable curve exists from the lowest frequency ratio of the alternate solution to the initial point of the amplitude split, $\Omega \cong 0.9125$. Tracking this unstable motion using present path-following algorithms is however beyond the scope of the current work. Also, because of the high complexity of investigating every initial condition, no specialized attempt will be made to locate other possible stable solutions.

A more complete picture of how A, Γ and K, because of its close inverse relationship to Γ, change the amplitude response curves and thus the dynamic motion of the rotor, is shown in Figure 3.13. The results confirm the previous analysis. An increase in the normal force proportionality constant will cause a slight decrease in amplitude but an increased probability that the maximum amplitudes will not be identical near resonance and that an additional solution will appear before resonance. Decreasing Γ as well as increasing K mainly cause an increase in the amplitude near resonance and an increase in the likelihood of an amplitude split.

From a design standpoint it is also important to investigate how the eccentricity of the shaft affects the amplitudes at given frequency ratios, Figures 3.14a to 3.14c.

33
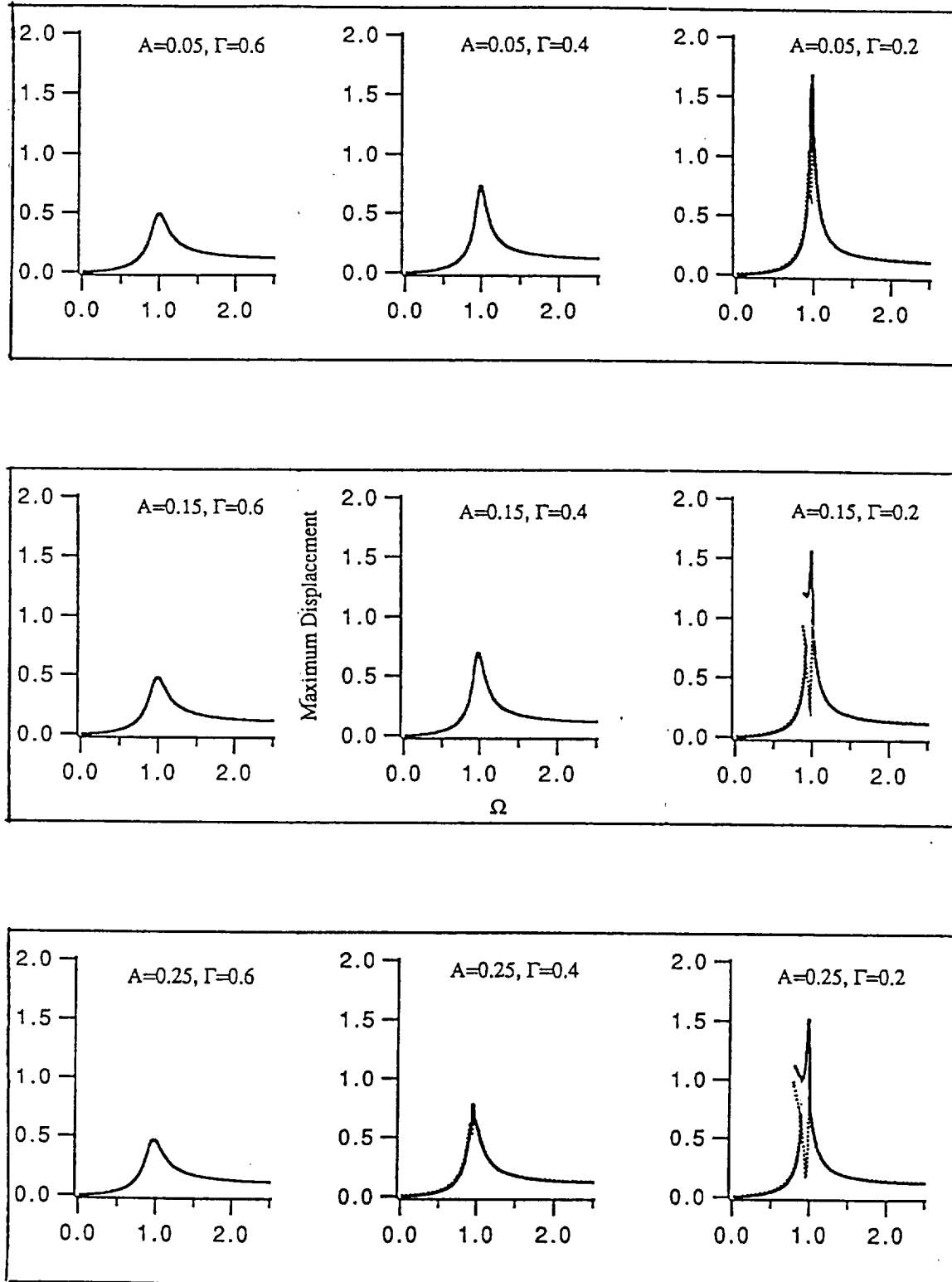
Figure 3.13: Numerical amplitude response curves for K=3, E=0.1 and varying A and Γ where a dashed line represents X, a solid line represents Y, and a single solid line represents both X and Y.
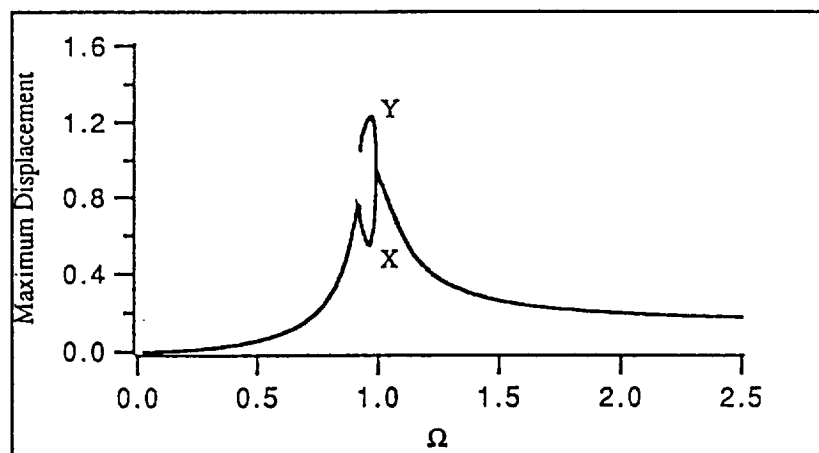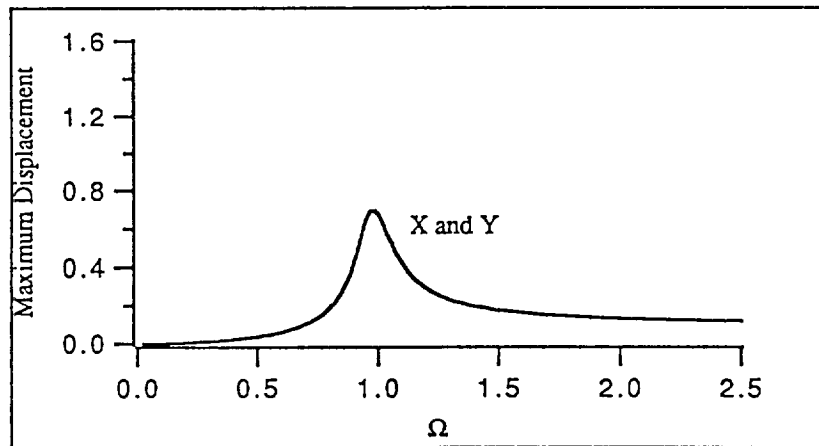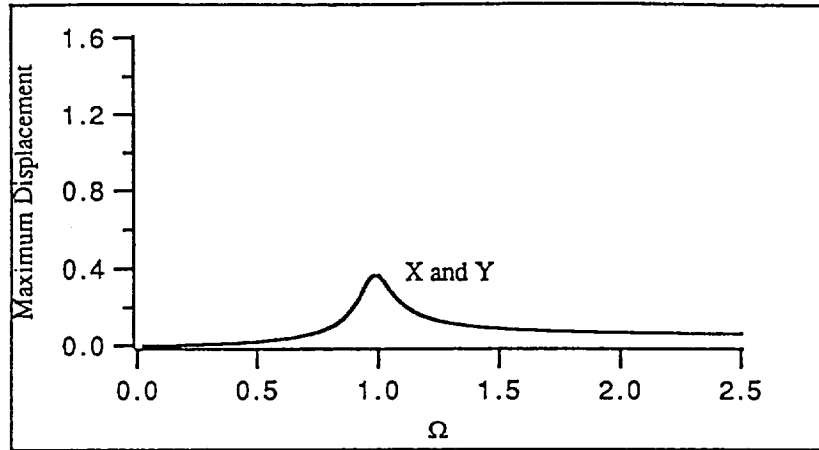
34

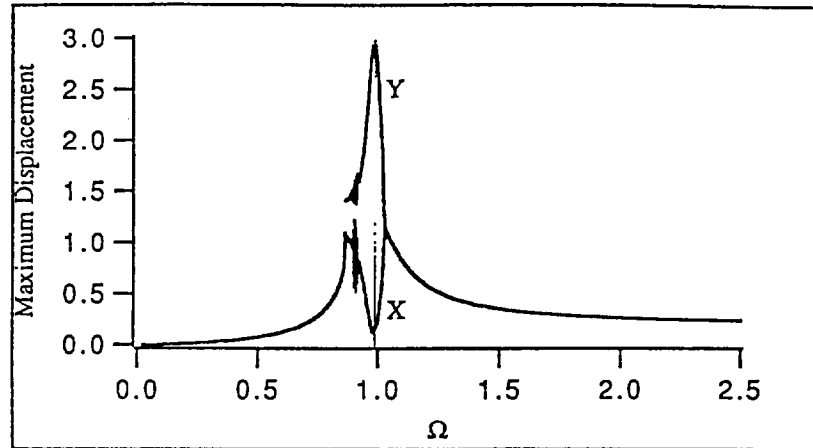Figure 3.14: Numerical amplitude response curves where K=3, A=0.15 Γ=0.4 and a. E=0.05 b. E=0.1 c. E=0.15.

Figure 3.15: Numerical amplitude response curve where K=3, A=0.175, Γ=0.2 and E=0.2.

Because E is proportional to the external rotating unbalance forcing amplitude, any increase in it results in an almost proportional increase in maximum displacement for a given Ω. Thus, as E gets larger, the displacements increase and an amplitude split becomes more likely, Figure 3.14c. If the initial forcing phase of the system is now varied, the results in Figure 3.14 and all of the other previous graphs will remain generally the same. The one exception is that for some initial forcing phases the amplitudes and phase shifts of X and Y may be interchanged.

Other interesting, nonlinear behavior besides the amplitude jump can occur with the governing equations. For instance, in Figure 3.15, an amplitude response curve where K = 3, A = 0.175, Γ = 0.2 and E = 0.2, at approximately $\Omega \cong 0.9$ and again at $\Omega \cong 0.9875$ there exists multiple maximum amplitudes for the given frequency ratios. At both frequency ratios, the maximum X and Y displacements fluctuate from period to period, Figures 3.16a and 3.17a, suggesting either chaotic or quasi-periodic motion (Thompson and Stewart (1986)). In order to correctly classify this behavior it is necessary to complete a spectral analysis of the time series data using the Fast Fourier Transform (FFT). The FFT converts 2^N, where N is any positive integer,
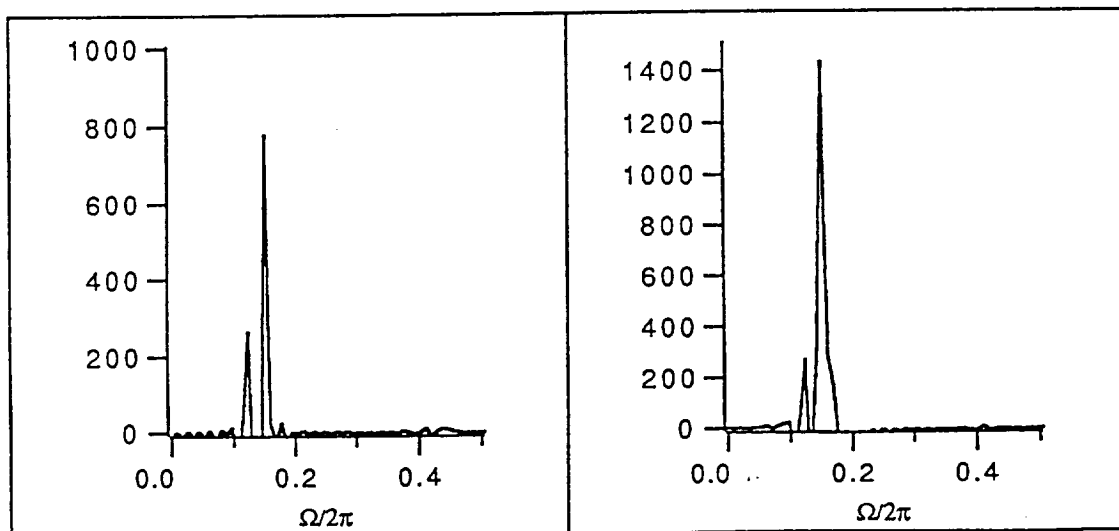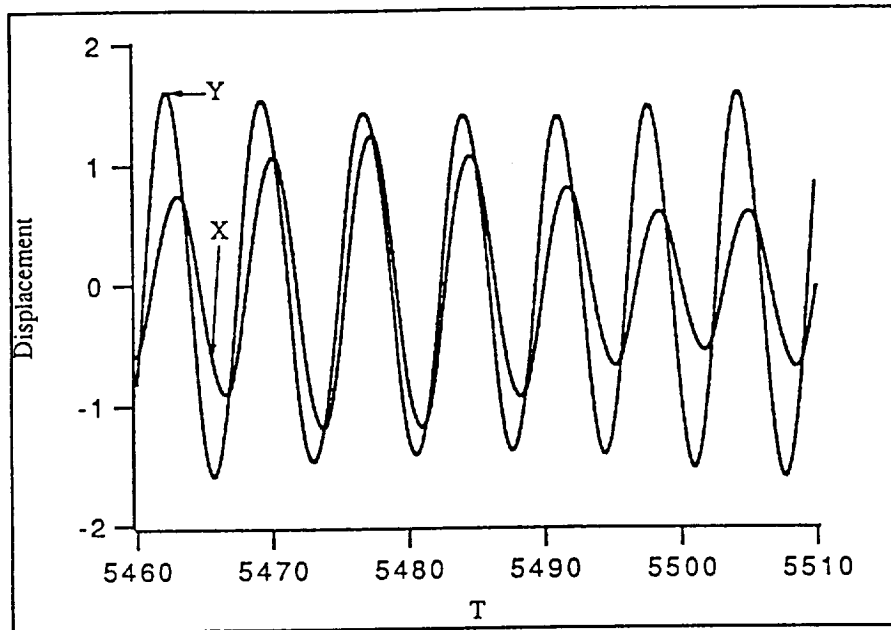
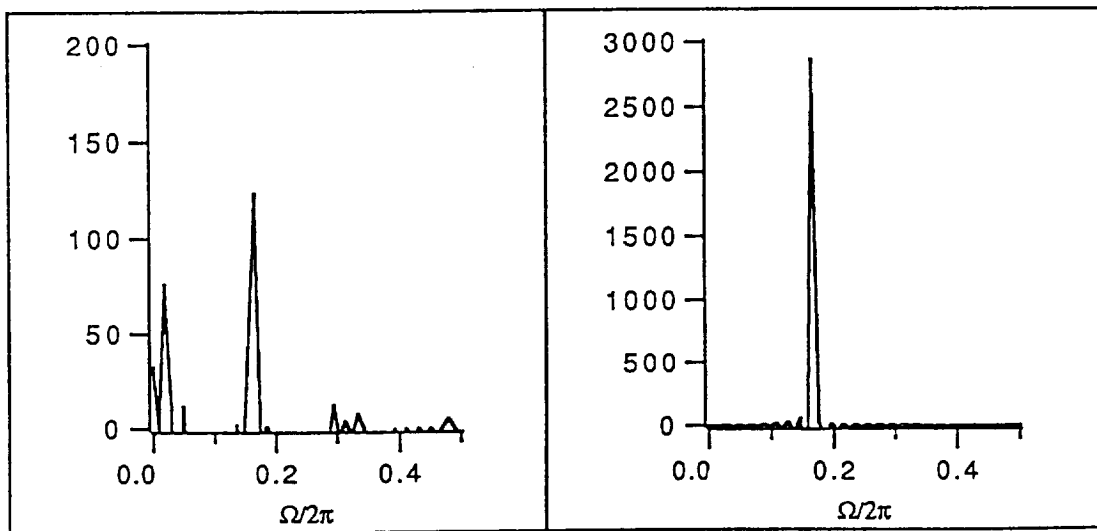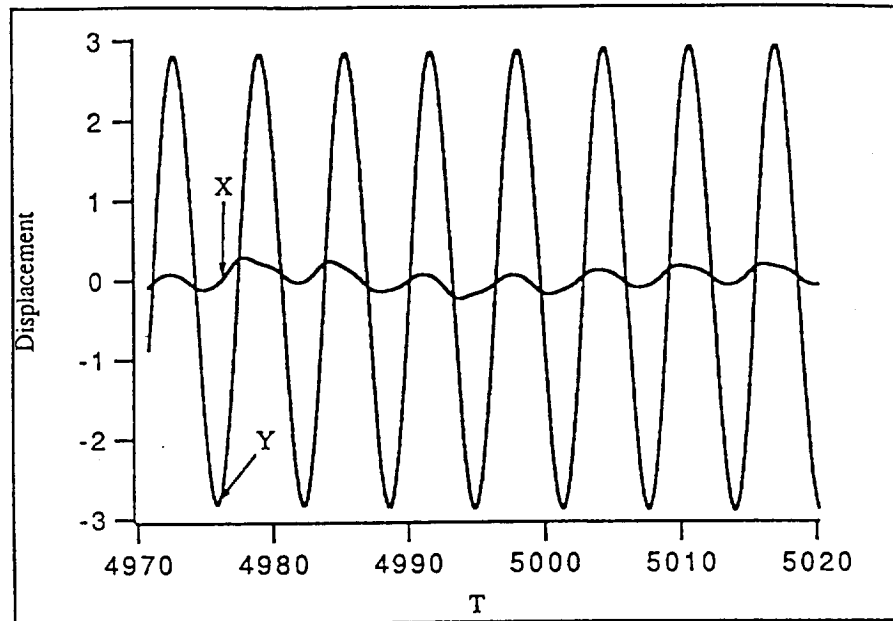Figure 3.16: a. Numerical time series b. FFT of X c. FFT of Y for K=3, A=0.175, Γ=0.2, E=0.2 and Ω=0.9.

Figure 3.17: a. Numerical time series b. FFT of X c. FFT of Y for K=3, A=0.175, Γ=0.2, E=0.2 and Ω=0.9875.

equally spaced discrete data points, making sure that there are at least two points per highest forcing period, to a frequency based domain using the Fourier Transform. After the data has been changed to its new domain, it will only have significant amplitudes at various combinations of its forcing frequencies. Thus, with the FFT, it is possible to classify any motion as periodic, one forcing frequency, chaotic, infinite forcing frequencies (also known as a broad-banded solution), or, as in the case of Figure 3.16 and 3.17, quasi-periodic, two or more driving frequencies.

3.2.3 Harmonic Balance Method Forced Vibration Results

The dynamic behavior of the circular shaft can also be analyzed using an analytical method called harmonic balance. This technique predicts the steady-state response of the system by assuming solutions of the form

$$Y = C\cos\Omega T + D\sin\Omega T \tag{3.4}$$

and

$$X = G\cos\Omega T + H\sin\Omega T \tag{3.5}$$

where C, D, G and H are unknown constants. Substituting (3.4) and (3.5) and their first and second derivatives with respect to nondimensional time, T, into (2.20) and (2.21) yields the first two equations shown in Appendix B. Both equations can be simplified by expanding, replacing the higher powered terms with their appropriate trigonometric relations,

$$\cos^3\theta = \frac{1}{4}(3\cos\theta + \cos 3\theta) \qquad\qquad \sin^3\theta = \frac{1}{4}(3\sin\theta + \sin 3\theta)$$

$$\cos^2\theta \sin\theta = \frac{1}{4}(\sin\theta - \sin 3\theta) \qquad \cos\theta \sin^2\theta = \frac{1}{4}(\cos\theta - \cos 3\theta)$$

and neglecting the higher harmonics. See Equations B.3 and B.4 in Appendix B. Next, the necessary equations needed to solve for the four unknowns, C, D, G and H, result by separately grouping all of the $\cos\Omega t$ and $\sin\Omega t$ terms in B.3 and B.4 and setting them equal to zero (balancing the harmonics).

However, due to the coupling and higher-order terms in the resulting governing equations, B.5 to B.8, the constants cannot be solved for analytically. Instead, they must be determined by using a numerical procedure called Newton's method for nonlinear systems. The method of solution for this technique is analogous to the more well known Newton-Raphson method. Both methods use an initial guess of the unknown(s), the partial derivatives of the function(s) and iteration to converge quadrically on a local solution. In cases where multiple solutions exist, however, the result can be solely dependent on the starting values of the unknowns and thus, different initial guesses may yield different results. This however makes it possible to locate a variety of approximate analytical solutions for given K, A, Γ and E by simply choosing different initial guesses for C, D, G and H.

Since the approximate analytical approach ignores all higher harmonics, it is necessary to examine if, in this case, the technique yields valid results. This can be accomplished by simply comparing graphs which are constructed using the approximate analytical approach, Figures 3.18a and 3.19a, with graphs which are obtained using numerical simulation, Figures 3.18b and 3.19b. The first two graphs plot the displacement versus the frequency ratio, Ω, at any steady-state nondimensional time $n\pi$, where n=0,2,4,..., and Figures 3.19a and 3.19b plot the velocity versus the Ω at the same time, $n\pi$. Both sets of graphs are almost identical,
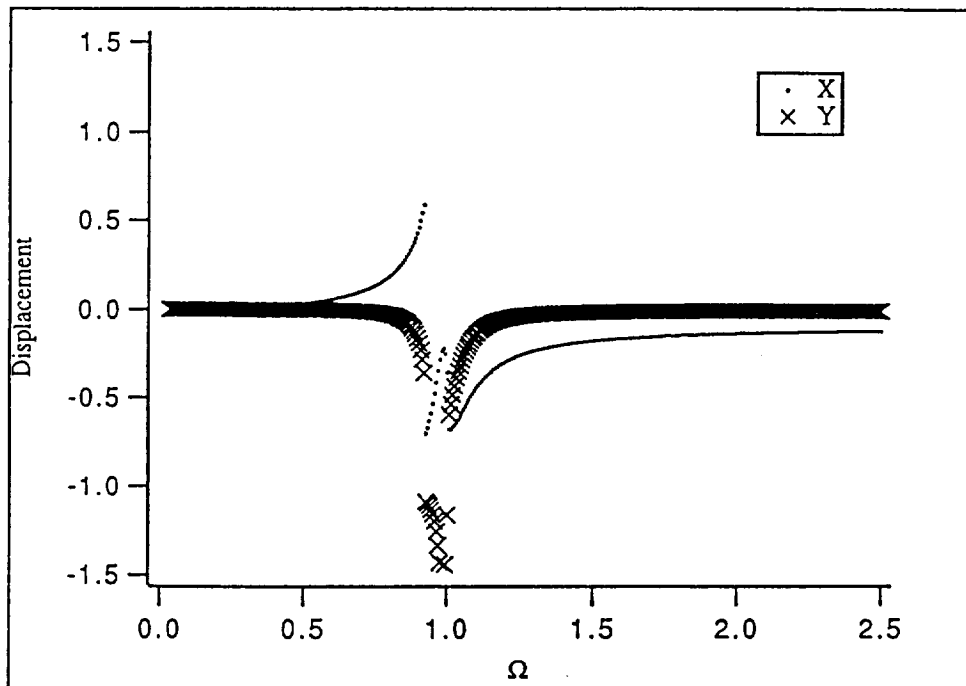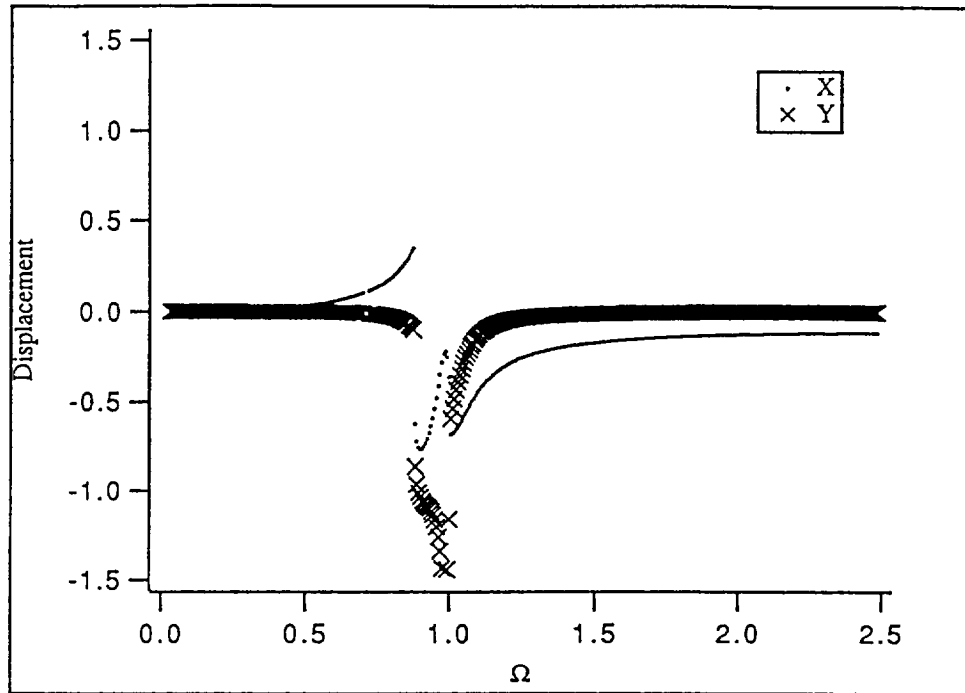
Figure 3.18: *Displacement versus frequency ratio* at $n\pi$ where n=0,2,4,...., K=3, A=0.15, Γ=0.2 and E=0.1 a. Harmonic balance b. Numerical.
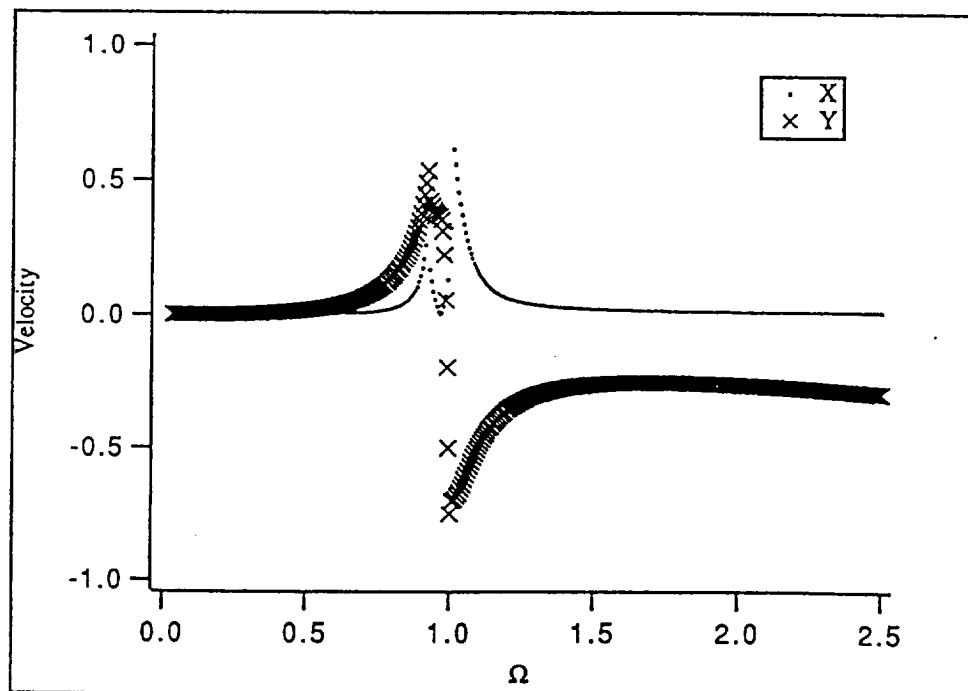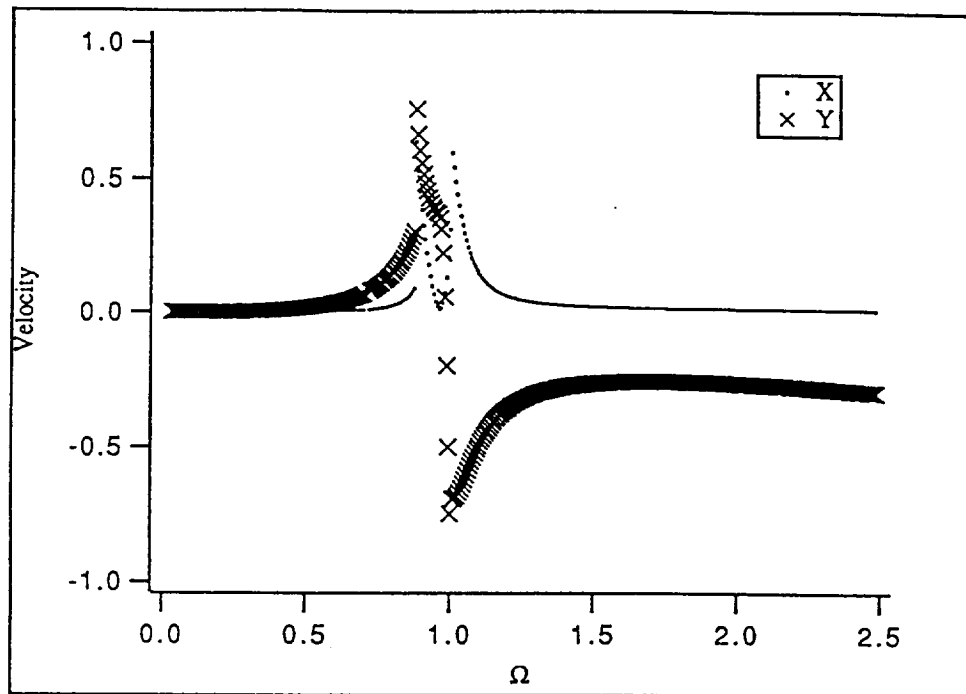
Figure 3.19: Velocity versus frequency ratio at $n\pi$ where $n=0,2,4,...$, K=3, A=0.15, Γ=0.2 and E=0.1 a.Harmonic balance b. Numerical.
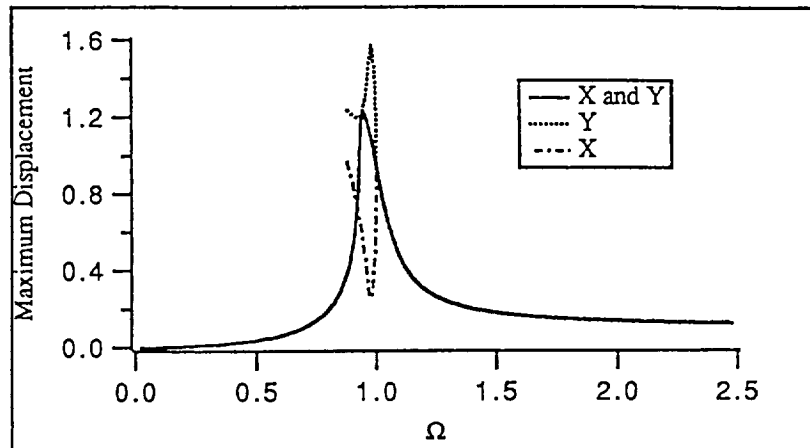
42

Figure 3.20: Harmonic balance amplitude response curve where K=3, A=0.15, Γ=0.2 and E=0.1.

suggesting that the approximate analytical approach does provide an accurate description of the steady-state dynamic behavior of the shaft. As an additional check, an amplitude response curve with the same parameters as Figure 3.12a can be constructed using the approximate analytical approach, Figure 3.20. A quick comparison of these graphs continues to strengthen the validity of the approximate analytical approach because the plots are almost identical with the exception of a third solution near resonance in Figure 3.20. The absence of this additional solution in Figure 3.12a can be simply attributed to the fact that it is probably unstable and numerical simulation can only be used to locate stable solutions.

3.2.4 Limiting Shaft Displacement for Varying Parameters

Ideally, the unbalanced shaft displacement should be minimal and at worst it should never come into contact with the bearing. Thus, for certain values of K, A and Γ it is beneficial to know what nondimensionalized eccentricities will cause a

specified unwanted displacement and what effect varying each parameter has on these eccentricity values. Figure 3.21a, which was constructed using the approximate analytical approach, is a plot of the lowest eccentricity value which causes the amplitude of either X or Y, X_{max}, to exceed 0.4, 0.7 and 1.0 versus the frequency ratio for $K = 3$, $A = 0.15$ and $\Gamma = 0.4$. As expected, the allowable nondimensional eccentricity for each specified amplitude is smallest near resonance and largest as $\Omega = 0$ is approached. Somewhat surprising however is that below $\Omega \cong 0.75$, the curves are identical. At these small frequency ratios, the lowest eccentricity value corresponds to the smallest E which causes the amplitudes to split. In each case below $\Omega \cong 0.75$, the amplitude of X or Y for these eccentricities is always greater than one and as a result, the curves coalesce. The final noteworthy point of Figure 3.21a is the presence of a kink, which is denoted by an arrow, in the $X_{max} = 1.0$ case. This bend only occurs in large maximum amplitude cases because for large displacements, the amplitude response curves will not be smooth, as indicated by Figures 3.7c, 3.12a and 3.14c.

The next three graphs, Figures 3.21b, 3.22a and 3.22b, continue to have the lowest E and Ω as the abscissa and ordinate variables; however, the amplitude limit is no longer the third variable. Instead, either K, A or Γ, depending on the plot, becomes the last parameter. As for the maximum allowable amplitude, it has been set at 0.4 in each graph because, typically, the displacements should be kept as small as possible. In the first of the three figures, the nondimensional proportional control coefficient has been increased from one to five. As anticipated, when $\Omega \approx 1$, the smaller the K, the larger the eccentricity needs to be for either of the displacements to become 0.4, recall Figures 3.7a to 3.7c. It also makes sense that at high values of Ω there is very little difference in the required E; however, according to the amplitude response curves this same behavior is also expected at low frequency
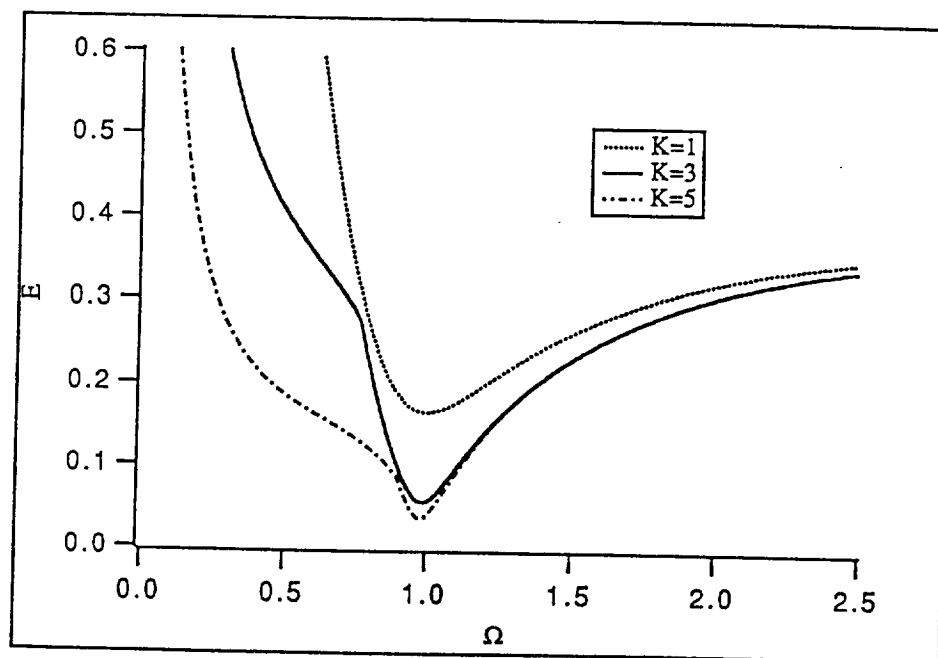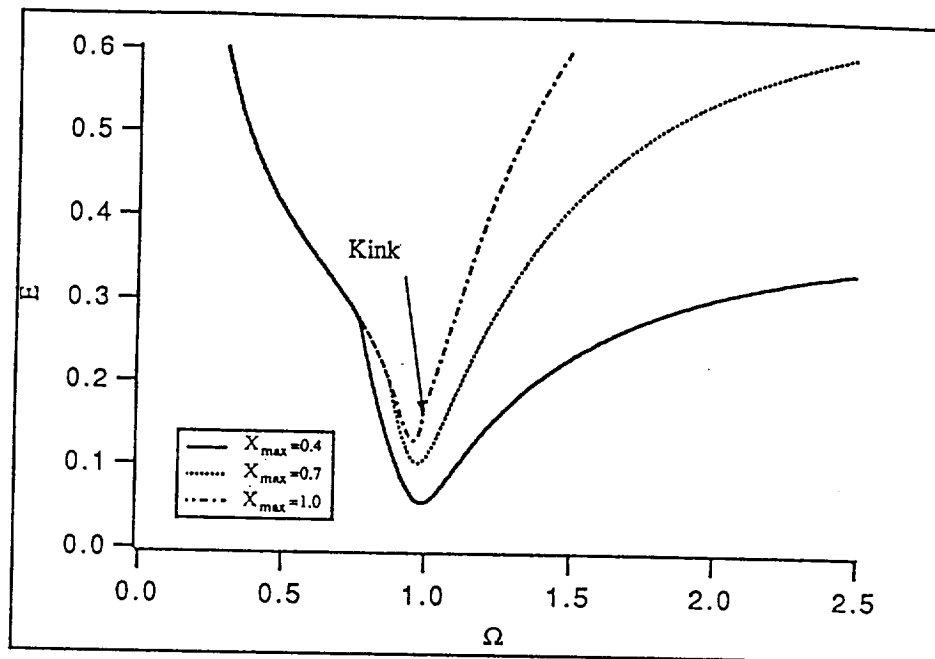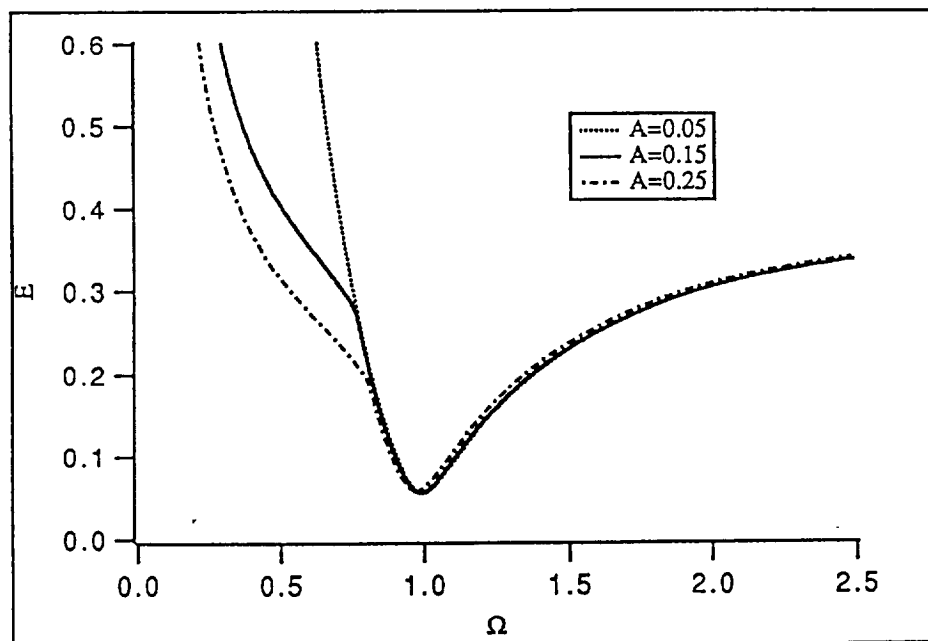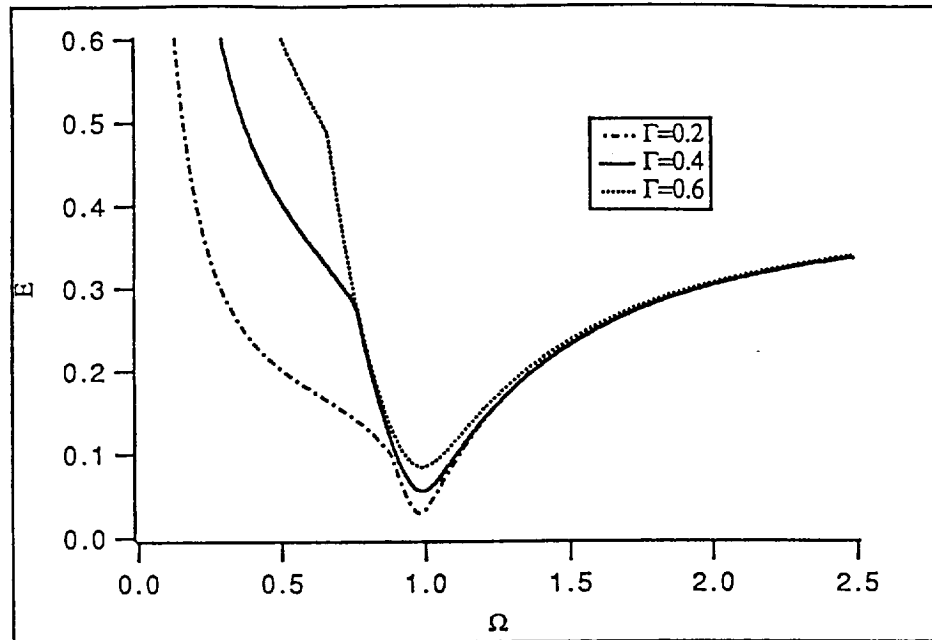
Figure 3.21: Harmonic balance results which show the lowest eccentricity value which causes a specified displacement at a given frequency ratio for A=0.15, Γ=0.4, a. K=3 and varying X_{max} b. X_{max} and varying K.

Figure 3.22: Harmonic balance results which show the lowest eccentricity value which causes a specified displacement at a given frequency ratio for K=3, X_{max}=0.4, a. A=0.15 and varying Γ b. Γ=0.4 and varying A.

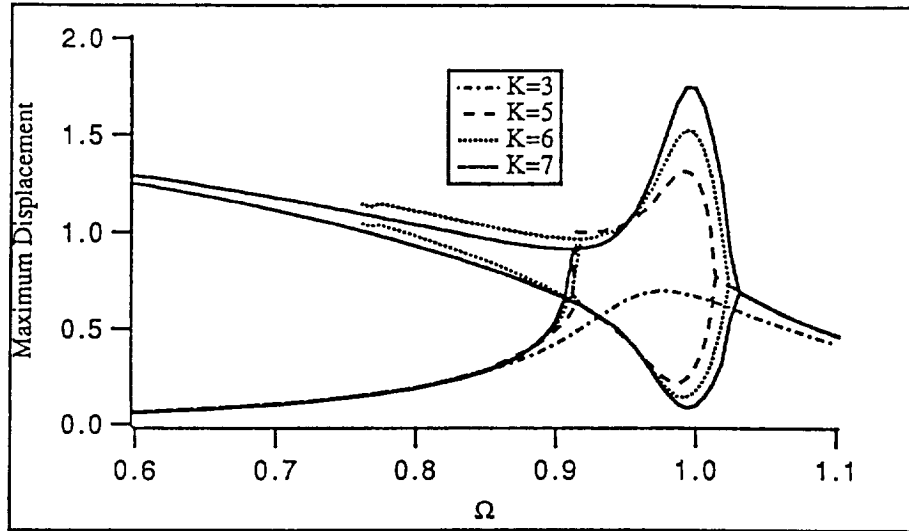Figure 3.23: Harmonic balance amplitude response curves where A=0.15, Γ=0.4, E=0.1 and K is varying.

ratios. But as stated in the previous paragraph, at small frequency ratios the lowest value of the nondimensional eccentricity is dependent on the lowest E at which the amplitude split occurs. And for varying K, these values are different, Figure 3.23. In examining Figure 3.23, it is also important to recognize that for increasing values of K greater than five, there exists a range of frequency ratios where the amplitudes decrease and a larger E would be required to cause a specified displacement. Although this only occurs for values of K which induce a split, the entire behavior is completely contrary to any other previous results and would actually mean that if K = 6 and K = 7 were included in Figure 3.21b their solutions would cross. In Figure 3.22a, the derivative control coefficient has replaced K as the third parameter. Because the effect of Γ on displacement is almost identical to the influence of 1 / K on the same variable, see Figures 3.7 to 3.12, Figures 3.21b and 3.22a exhibit similar results for the same reasons.

Finally, the effect of the normal force proportionality constant on the lowest

eccentricity value which causes the maximum displacement of either X or Y to exceed 0.4 is examined in Figure 3.22b. For most of the frequency ratios, any change in A results in little or no change in the lowest eccentricity value. This agrees with the results from the earlier amplitude response curves, Figures 3.11a to 3.11c, where an increase in A meant little change in amplitude. However, once again, at small frequency ratios the lowest value of eccentricity does not relate to the amplitude response curves because, as in the case of K and Γ, the value at which the split occurs varies for a changing A.

Each of the graphs, 3.21a, 3.21b, 3.22a and 3.22b, were constructed using the approximate analytical approach. Although it has been shown that this technique is sound when examining steady-state behavior, it does ignore transient motion which may be significant especially if the rotor is started from rest. Thus, if escape from the potential well, defined as the magnitude of X and Y exceeding $\dfrac{2K - A}{AK^2}$ at the same nondimensional time, T, occurs before the onset of steady-state behavior, then Figures 3.21 to 3.22 are rendered inappropriate. It should be noted that the transient behavior will actually cause the shaft to strike the bearing before escape can occur, unless K is unreasonably high, thus changing the equations of motion of the shaft, see Figures 3.2 to 3.3. This modification of the equations has been ignored in the upcoming graphical analysis; however, for a system with larger physical bounds the forthcoming figures are appropriate.

Figures 3.24 and 3.25 display the nondimensional eccentricities, for a range of frequency ratios, which cause escape during the first one hundred dynamic cycles, after which transient motion has been assumed to have died out. (This is usually but not necessarily the case.) Comparing the results obtained in Figure 3.22a with Figures 3.24a and 3.25, it is evident that the lowest eccentricity values which cause escape during transient motion are always larger than the values which cause the steady-state
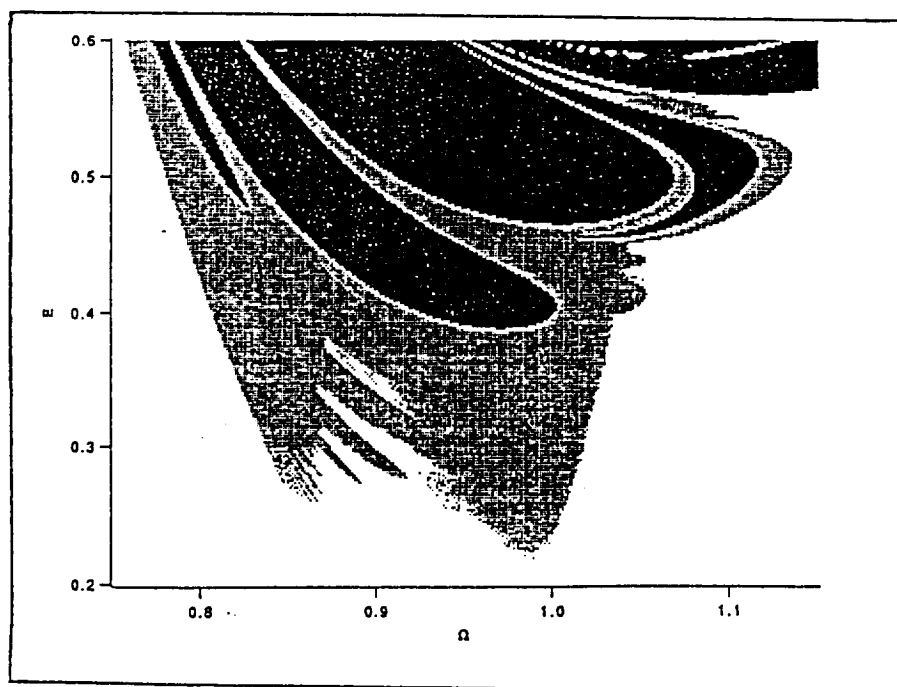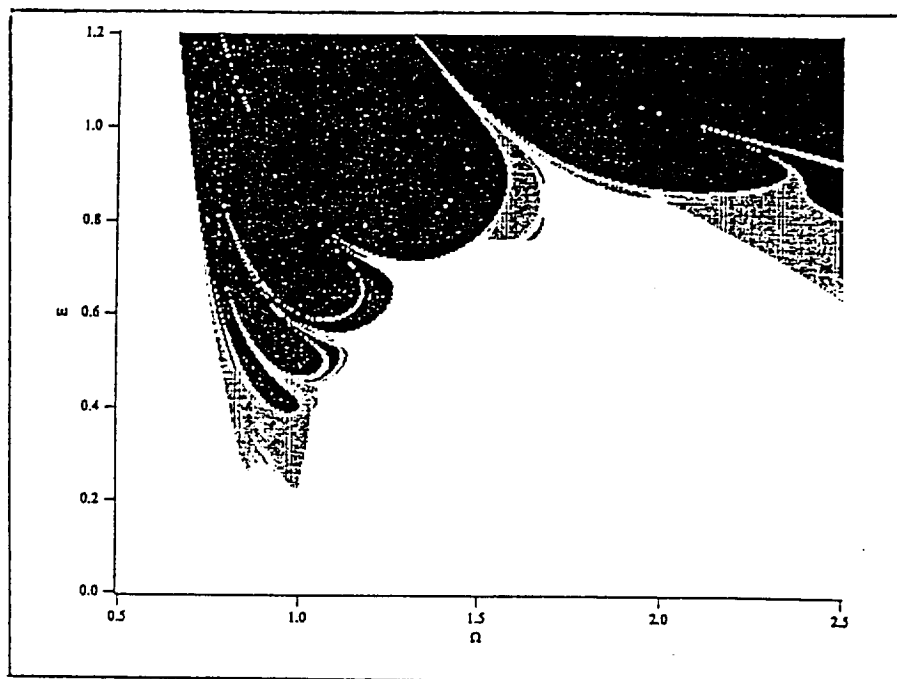
Figure 3.24: Numerically obtained escape eccentricity versus frequency ratio for K=3, A=0.15, Γ=0.2 and E=0.1 a. Full graph b. Blow up.
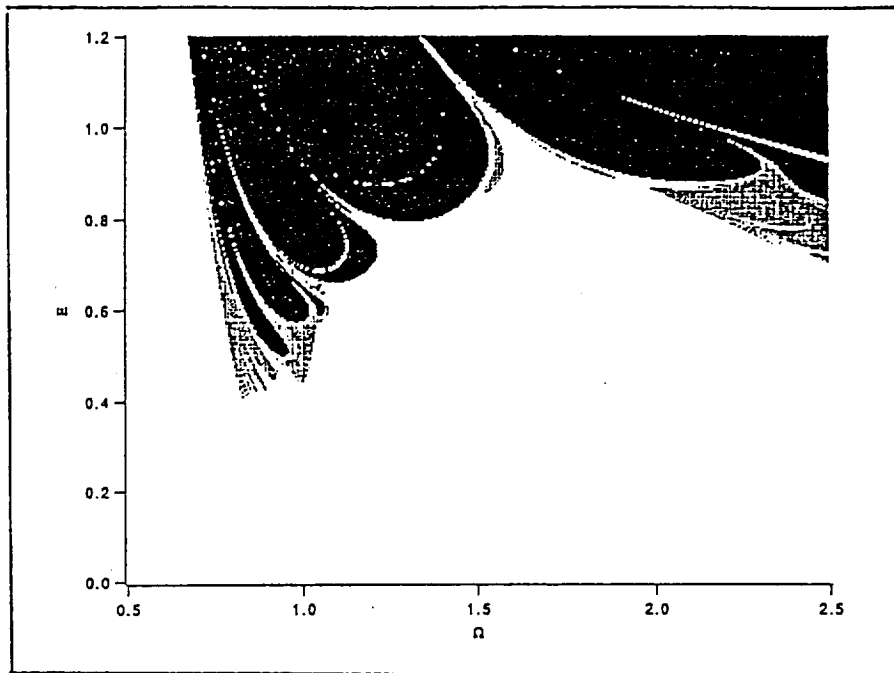
49

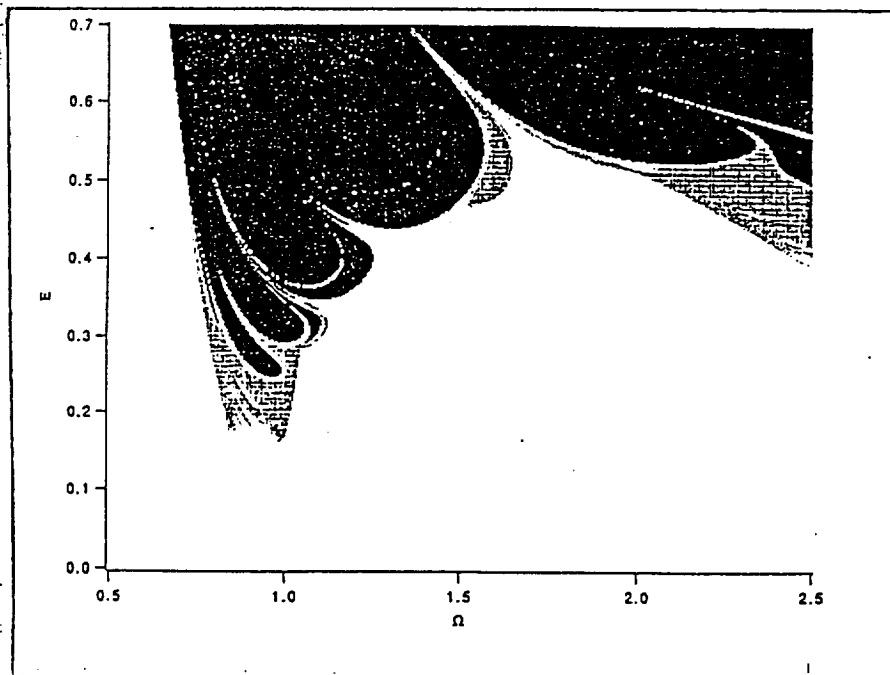Figure 3.25: Numerically obtained escape eccentricity versus frequency ratio for K=3, A=0.15, Γ=0.4 and E=0.1.

Figure 3.26: Numerically obtained escape eccentricity versus frequency ratio for K=5, A=0.25, Γ=0.4 and E=0.1.

amplitude to exceed 0.4. Thus, Figures 3.21 to 3.22 are valid.

The Figures 3.24a and 3.25 are themselves noteworthy. First, in both graphs there is not a solid line which separates escape eccentricities from nonescape eccentricities and the boundaries which do exist are fractal (Crilly et al. (1991) and Feder (1988)). For instance, in Figure 3.24 as the resolution of the graph increases the boundaries change and if these escape boundaries are zoomed in upon further and further then the fractal behavior of the plot will continue infinitely. (It is possible to calculate the noninteger dimension of these boundaries, however, due to the time constraints of this thesis it was not attempted.) The actual shape of either graph is extremely complex as well, with gray areas, denoting escape between four cycles and one hundred cycles, often occupying regions which are completely surrounded by black sections, escape within the first three cycles, see Figure 3.24b. Yet each plot tends to exhibit expected behavior. For example, when the derivative control coefficient is increased the shape of either graph generally remains the same except the escape eccentricity decreases for all frequency ratios. Also, the minimum value of E in both graphs occurs near resonance, and at low frequency ratios, extremely high eccentricities are necessary for escape. Varying K and A does not produce any unexpected results either, Figure 3.26. Once again, the graph tends mainly to shift downward. The one unexpected and definitely nonlinear quality of Figures 3.24 to 3.26, is the fact that for increasing Γ, thus damping, the minimum E tends to move towards a lower frequency ratio. This agrees with the nonlinear large amplitude motion of Figure 3.23; however, in linear rotating unbalance and even in the magnetically controlled shaft where the damping ratio is sufficiently high enough that the system is close to being linear, Figure 3.27, the maximum steady-state amplitude tends to move to the right for increasing Γ.
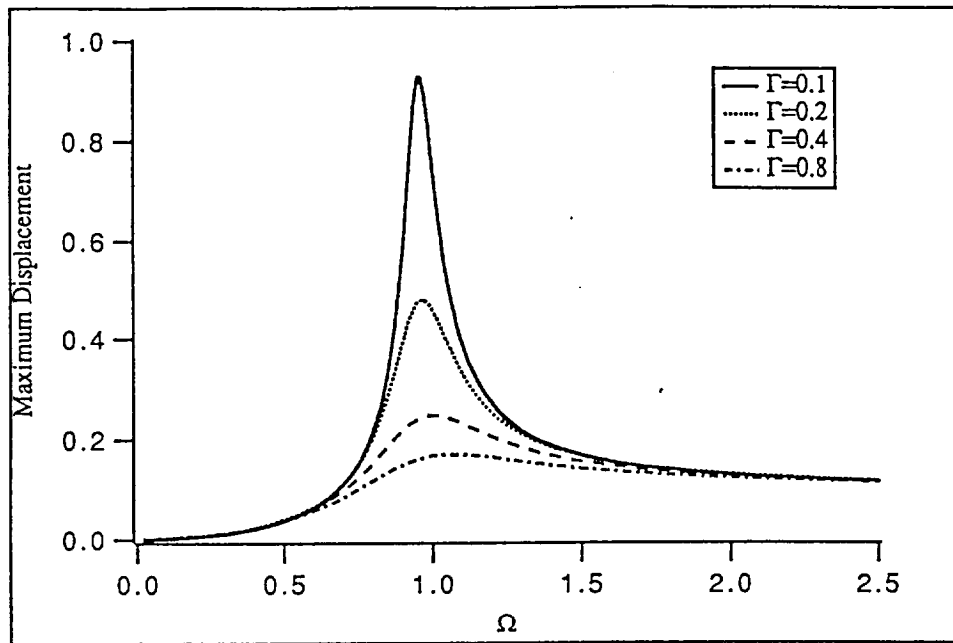
Figure 3.27: Numerical amplitude response curves for K=1, A=0.15, E=0.1 and varying Γ.

Chapter 4

Conclusions and Further Work

Recent active magnetic bearing research determined that curved magnets produce forces which are two-dimensional. Using this conclusion, this dissertation has accurately modelled the proportional-derivative flux controlled forces of the magnetic bearings and the motion of an unbalanced rotating shaft which is being minimized by these magnetic forces. The resulting governing equations are coupled and nonlinear and exhibit important atypical dynamic behavior such as quasi-periodic motion and hysteresis. In addition, the nonlinear terms also introduce the possibility of having unstable motion within the actuator and it is also possible that near resonance and with either large displacements or a large normal force proportionality constant, that the steady-state maximum amplitudes may not be identical and multiple different larger amplitude solutions may exist for a given set of parameters. Variations in any one of these parameters tends to affect the dynamic motion differently; however, generally, any increase in the nondimensional proportional control coefficient, K, or the nondimensional rotating unbalance, E, or decrease in the nondimensional derivative control coefficient, Γ, will cause an increase in amplitude and thus, increase the possibility of introducing the unwanted nonlinear behavior. An increase in A, the dimensionless normal force proportionality constant, will not increase the

amplitude; however, it will make the nonlinear larger amplitude motion more probable.

Further magnetic bearing research still needs to be completed in two areas. First, because an increased nondimensional normal force proportionality constant can introduce unwanted nonlinear behavior without any change in amplitude, it is necessary to further examine its specific value in opposed pairs of magnets. In addition, the previously presented results need to be experimentally verified.

Appendix A

Runge Kutta Method

The fourth-order Runge-Kutta method is the most popular numerical technique that is used to solve nonlinear ordinary differential equations because it strikes a balance between the computational complexity and accuracy of the solution. The derivation of this method can be found in any numerical analysis text and yields the following formulas for two coupled, first-order differential equations, $\dot{v} = f(t, v, x)$ and $\dot{x} = g(t, v, x)$,

$$v_{n+1} = v_n + \frac{h}{6}(K_1 + 2K_2 + 2K_3 + K_4) \tag{A.1}$$

$$x_{n+1} = x_n + \frac{h}{6}(L_1 + 2L_2 + 2L_3 + L_4) \tag{A.2}$$

where h is the time step, n is any integer, v_0 and x_0 are known and

$$K_1 = f(t_n, v_n, x_n)$$
$$K_2 = f\left(t_n + \frac{h}{2}, v_n + \frac{K_1}{2}, x_n + \frac{L_1}{2}\right)$$
$$K_3 = f\left(t_n + \frac{h}{2}, v_n + \frac{K_2}{2}, x_n + \frac{L_2}{2}\right)$$

$$K_4 = f\left(t_n + h, v_n + K_3, x_n + L_3\right)$$

$$L_1 = g\left(t_n, v_n, x_n\right)$$

$$L_2 = g\left(t_n + \frac{h}{2}, v_n + \frac{K_1}{2}, x_n + \frac{L_1}{2}\right)$$

$$L_3 = g\left(t_n + \frac{h}{2}, v_n + \frac{K_2}{2}, x_n + \frac{L_2}{2}\right)$$

$$L_4 = g\left(t_n + h, v_n + K_3, x_n + L_3\right)$$

When the two coupled equations of motion are second-order, it is necessary to put each into state space form,

$$\dot{v} = w \qquad\qquad \dot{x} = y$$

$$\dot{w} = f(t, v, w, x, y) \qquad\qquad \dot{y} = g(t, v, w, x, y)$$

The same general theory can now be used to solve these four coupled first-order equations,

$$v_{n+1} = v_n + \frac{h}{6}\left(W_1 + 2W_2 + 2W_3 + W_4\right) \tag{A.3}$$

$$w_{n+1} = w_n + \frac{h}{6}\left(K_1 + 2K_2 + 2K_3 + K_4\right) \tag{A.4}$$

$$x_{n+1} = x_n + \frac{h}{6}\left(Y_1 + 2Y_2 + 2Y_3 + Y_4\right) \tag{A.5}$$

$$y_{n+1} = y_n + \frac{h}{6}\left(L_1 + 2L_2 + 2L_3 + L_4\right) \tag{A.6}$$

except in this case w_0 and y_0 are also known and

56

$$W_1 = w_n$$

$$K_1 = f(t_n, v_n, W_1, x_n, Y_1)$$

$$Y_1 = y_n$$

$$L_1 = g(t_n, v_n, W_1, x_n, Y_1)$$

$$W_2 = w_n + \frac{h}{2}K_1$$

$$L_2 = g\left(t_n + \frac{h}{2}, v_n + \frac{h}{2}W_1, W_2, x_n + \frac{h}{2}Y_1, Y_2\right)$$

$$Y_2 = y_n + \frac{h}{2}L_1$$

$$K_2 = f\left(t_n + \frac{h}{2}, v_n + \frac{h}{2}W_1, W_2, x_n + \frac{h}{2}Y_1, Y_2\right)$$

$$W_3 = w_n + \frac{h}{2}K_2$$

$$K_3 = f\left(t_n + \frac{h}{2}, v_n + \frac{h}{2}W_2, W_3, x_n + \frac{h}{2}Y_2, Y_3\right)$$

$$Y_3 = y_n + \frac{h}{2}L_2$$

$$W_4 = w_n + hK_3$$

$$K_4 = f(t_n + h, v_n + hW_3, W_4, x_n + hY_3, Y_4)$$

$$Y_4 = y_n + hL_3$$

$$L_4 = g(t_n + h, v_n + hW_3, W_4, x_n + hY_3, Y_4)$$

Appendix B

Harmonic Balance Method Equations

$$-C\Omega^2\cos\Omega T - D\Omega^2\sin\Omega T + \Gamma(-C\Omega\sin\Omega T + D\Omega\cos\Omega T) + K(C\cos\Omega T + D\sin\Omega T)$$
$$-\frac{A}{2}(C\cos\Omega T + D\sin\Omega T)(1 + K^2(G\cos\Omega T + H\sin\Omega T)^2$$
$$+2K\Gamma(G\cos\Omega T + H\sin\Omega T)(-G\Omega\sin\Omega T + H\Omega\cos\Omega T) + \Gamma^2(-G\Omega\sin\Omega T + H\Omega\cos\Omega T)^2)$$
$$= E\Omega^2\sin\Omega T \tag{B.1}$$

$$-G\Omega^2\cos\Omega T - H\Omega^2\sin\Omega T + \Gamma(-G\Omega\sin\Omega T + H\Omega\cos\Omega T) + K(G\cos\Omega T + H\sin\Omega T)$$
$$-\frac{A}{2}(G\cos\Omega T + H\sin\Omega T)(1 + K^2(C\cos\Omega T + D\sin\Omega T)^2$$
$$+2K\Gamma(C\cos\Omega T + D\sin\Omega T)(-C\Omega\sin\Omega T + D\Omega\cos\Omega T) + \Gamma^2(-C\Omega\sin\Omega T + D\Omega\cos\Omega T)^2)$$
$$= E\Omega^2\cos\Omega T \tag{B.2}$$

$$-C\Omega^2\cos\Omega T - D\Omega^2\sin\Omega T + \Gamma(-C\Omega\sin\Omega T + D\Omega\cos\Omega T) + K(C\cos\Omega T + D\sin\Omega T)$$
$$-\frac{A}{2}((C\cos\Omega T + D\sin\Omega T) + K^2(\left(\frac{3}{4}CG^2 + \frac{1}{4}CH^2 + \frac{1}{2}DGH\right)\cos\Omega T$$
$$+\left(\frac{1}{4}DG^2 + \frac{3}{4}DH^2 + \frac{1}{2}CGH\right)\sin\Omega T) + 2K\Gamma\Omega(\left(-\frac{1}{4}DG^2 + \frac{1}{4}DH^2 + \frac{1}{2}CGH\right)\cos\Omega T$$
$$+\left(-\frac{1}{4}CG^2 + \frac{1}{4}CH^2 - \frac{1}{2}DGH\right)\sin\Omega T) - \Gamma^2\Omega^2(\left(\frac{1}{4}CG^2 + \frac{3}{4}DG^2 - \frac{1}{2}DGH\right)\sin\Omega T$$
$$+\left(\frac{1}{4}CH^2 + \frac{3}{4}DH^2 - \frac{1}{2}CGH\right))) = E\Omega^2\sin\Omega T \tag{B.3}$$

58

$$-G\Omega^2\cos\Omega T - H\Omega^2\sin\Omega T + \Gamma(-G\Omega\sin\Omega T + H\Omega\cos\Omega T) + K(G\cos\Omega T + H\sin\Omega T)$$

$$-\frac{A}{2}\left((G\cos\Omega T + H\sin\Omega T) + K^2\left(\left(\frac{3}{4}C^2G + \frac{1}{4}D^2G + \frac{1}{2}CDH\right)\cos\Omega T\right.\right.$$

$$+\left(\frac{1}{4}C^2H + \frac{3}{4}D^2H + \frac{1}{2}CDG\right)\sin\Omega T\right) + 2K\Gamma\Omega\left(\left(-\frac{1}{4}C^2H + \frac{1}{4}D^2H + \frac{1}{2}CDG\right)\cos\Omega T$$

$$+\left(-\frac{1}{4}C^2G + \frac{1}{4}D^2G - \frac{1}{2}CDH\right)\sin\Omega T\right) - \Gamma^2\Omega^2\left(\left(\frac{1}{4}C^2G + \frac{3}{4}C^2H - \frac{1}{2}CDH\right)\sin\Omega T$$

$$\left.\left.+\left(\frac{1}{4}D^2G + \frac{3}{4}D^2H - \frac{1}{2}CDG\right)\right)\right) = E\Omega^2\cos\Omega T \qquad\text{(B.4)}$$

(B.5)

$$-CK\Omega^2 + CK + D\Gamma\Omega - \frac{A}{2}C - \frac{A}{4}DGHK^2 - \frac{3A}{8}CG^2K^2 - \frac{A}{8}CH^2K^2 - \frac{A}{2}CGHK\Gamma\Omega$$

$$+\frac{A}{4}DG^2K\Gamma\Omega - \frac{A}{4}DH^2K\Gamma\Omega + \frac{A}{4}DGH\Gamma^2\Omega^2 - \frac{A}{8}CG^2\Gamma^2\Omega^2 - \frac{3A}{8}CH^2\Gamma^2\Omega^2 = 0$$

(B.6)

$$-DK\Omega^2 + DK - C\Gamma\Omega - \frac{A}{2}D - \frac{A}{4}CGHK^2 - \frac{A}{8}DG^2K^2 - \frac{3A}{8}DH^2K^2 + \frac{A}{2}DGHK\Gamma\Omega$$

$$+\frac{A}{4}CG^2K\Gamma\Omega - \frac{A}{4}CH^2K\Gamma\Omega + \frac{A}{4}CGH\Gamma^2\Omega^2 - \frac{3A}{8}DG^2\Gamma^2\Omega^2 - \frac{A}{8}DH^2\Gamma^2\Omega^2 = EK\Omega^2$$

(B.7)

$$-GK\Omega^2 + GK + H\Gamma\Omega - \frac{A}{2}G - \frac{A}{4}CDHK^2 - \frac{3A}{8}C^2GK^2 - \frac{A}{8}D^2GK^2 - \frac{A}{2}CDGK\Gamma\Omega$$

$$+\frac{A}{4}C^2HK\Gamma\Omega - \frac{A}{4}D^2HK\Gamma\Omega + \frac{A}{4}CDH\Gamma^2\Omega^2 - \frac{A}{8}C^2G\Gamma^2\Omega^2 - \frac{3A}{8}D^2G\Gamma^2\Omega^2 = EK\Omega^2$$

(B.8)

$$-HK\Omega^2 + HK - G\Gamma\Omega - \frac{A}{2}H - \frac{A}{4}CDGK^2 - \frac{A}{8}C^2HK^2 - \frac{3A}{8}D^2HK^2 + \frac{A}{2}CDHK\Gamma\Omega$$

$$+\frac{A}{4}C^2GK\Gamma\Omega - \frac{A}{4}D^2GK\Gamma\Omega + \frac{A}{4}CDG\Gamma^2\Omega^2 - \frac{3A}{8}C^2H\Gamma^2\Omega^2 - \frac{A}{8}D^2H\Gamma^2\Omega^2 = 0$$

Bibliography

Bornstein, K. R., "Dynamic load capabilities of active electromagnetic bearings," *Journal of Tribology*, July 1991, Vol. 113, No. 3, pp. 598-603.

Burden, R. L. and Faires, J. D., *Numerical Analysis* (PWS Publishers, Boston), 1985.

Chen, H. M., and Darlow, M. S., "Magnetic bearings with rotating force control," *Journal of Tribology*, January 1988, Vol. 110, No. 1, pp. 100-105.

Chen, H. M., "Magnetic bearings and flexible rotor dynamics," *Tribology Transactions*, January 1989, Vol. 32, No. 1, pp. 9-15.

Crilly, A. J., Earnshaw, R. A., and Jones, H., *Fractals and Chaos* (Springer-Verlag, New York), 1991.

Etter, D. M., *Structured FORTRAN for Engineers and Scientists* (Benjamin/Cummings, New York), 1990.

Feder, J., *Fractals* (Plenum Press, New York), 1988.

Humphris, R. R., Kelm, R. D., and Lewis, D. W., " Effect of control algorithms on magnetic journal bearing properties," *Journal of Engineering for Gas Turbines and Power*, October 1986, Vol. 108, No. 4, pp. 624-632.

Imlach, J., Blair, B. J., and Allaire, P. E., "Measured and predicted force and stiffness characteristics of industrial magnetic bearings," *Journal of Tribology*, October 1991, Vol. 113, No. 4, pp. 784-788.

Jordan, D. W., and Smith, P., *Nonlinear Ordinary Differential Equations* (Clarendon Press, Oxford), 1977.

Kasarda, M. E. F., Allaire, P. E., and Humphris, R. R., "A magnetic damper for first-mode vibration reduction in multimass flexible rotors," *Journal of Engineering for Gas Turbines and Power*, October, 1990, Vol. 112, No. 4, pp. 463-469.

Keith, F. J., Williams, R. D., and Allaire, P. E., "Digital control of magnetic bearings supporting a multimass flexible rotor," *Tribology Transactions*, July 1990, Vol. 33, No. 3, pp. 307-314.

Knight, J. D., Xia, Z., and McCaul, E. B., "Determination of forces in a magnetic bearing actuator: numerical computation with comparison to experiment," *Journal of Tribology*, October 1992, Vol. 114, No. 4, pp. 796-801.

Lee, C-W, and Kim J-S, "Modal testing and suboptimal vibration control of flexible rotor bearing system by using a magnetic bearing," *Journal of Dynamic*

Systems, Measurement , and Control, June 1992, Vol. 114, No. 2, pp. 244-252.

Lewis, D. W., Allaire, P. E., and Thomas, P. W., "Active magnetic control of oscillatory axial shaft vibrations in ship shaft transmission systems," *Tribology Transactions*, April 1989, Vol. 32, No. 2, pp. 170-188.

Maslen, E. H., Hermann, P., and Allaire, P. E., "Practical Limits to the performance of magnetic bearings: peak force, slew rate, and displacement sensitivity," *Journal of Tribology*, April 1989, Vol. 111, No. 2, pp. 331-336.

Maslen, E. H., and Bielk, J. R., "A stability model for flexible rotors with magnetic bearings," *Journal of Dynamic Systems, Measurement , and Control*, March 1992, Vol. 114, No. 1, pp. 172-175.

Maslen, E. H., and Allaire, P. E., "Magnetic bearing sizing for flexible rotors," *Journal of Tribology*, April 1992, Vol. 114, No. 2, pp. 223-239.

Nagaraj, H. S., "Investigation of magnetic fields and forces arising in open-circuit-type magnetic bearings," *Tribology Transactions*, April 1988, Vol. 31, No. 2, pp. 192-201.

Nonami, K., Yamanaka, T., and Tominaga, M., "Vibration and control of a flexible rotor supported by magnetic bearings," *JSME International Journal*, December 1990, Series III, Vol. 33, No. 4, pp. 475-482.

O'Connor, L., "Active magnetic bearing give systems a lift," *Mechanical*

Engineering, July 1992, Vol. 114, No. 7, pp. 52-57.

Pinckney, F. D., Frank, D., and Keesee, J. M., "Magnetic bearing design and control optimization for a four-stage centrifugal compressor," *Tribology Transactions*, July 1992, Vol. 35, No. 3, pp. 561-565.

Rao, D. K., Brown, G. V., and Lewis, P., "Stiffness of magnetic bearings subjected to combined static and dynamic loads," *Journal of Tribology*, October 1992, Vol. 114, No. 4, pp. 785-789.

Reinig, K. D., and Desrochers, A. A., "Disturbance accommodating controllers for rotating mechanical systems," *Journal of Dynamic Systems, Measurement, and Control*, March 1986, Vol. 108, No. 1, pp. 24-31.

Scudiere, M. B., Willems, R. A., and Gilles, G. T., "Digital controller for a magnetic suspension system," *Review of Scientific Instrumentation*, August 1986, Vol. 57, No. 8, pp. 1616-1626.

Thompson, J. M. T., and Stewart, H. B., *Nonlinear Dynamics and Chaos* (John Wiley and Sons, New York), 1986.

Tsuchiya, K., Inoue, M., and Akishita, S., "Anisotropic stiffness effect on stability of a magnetically suspended momentum wheel," *Journal of Guidance, Control, and Dynamics*, March/April 1991, Vol. 14, No. 2, pp. 300-336.

Vierck, R. K., *Vibration Analysis* (Harper and Row, New York), 1979.

Virgin, L. N., "On the harmonic response of an oscillator with unsymmetric restoring force," *Journal of Sound and Vibration*, October 1988, Vol. 126, No. 1, pp. 157-165.

Virgin, L. N., "Approximate criterion for capsize based on deterministic dynamics," *Dynamics and Stability of Systems*, Vol. 4, No. 1, 1989, pp. 55-70.

Virgin, L. N., Plaut, R. H., and Cheng, C. C., "Prediction of escape from a potential well under harmonic excitation," *International Journal Of Nonlinear Mechanics*, May 1992, Vol. 27, No. 3, pp. 357 365.

Williams, R. D., Keith, F. J., and Allaire, P. E., "A comparison of analog and digital controls for rotor dynamic vibration reduction through active magnetic bearings," *Journal of Engineering for Gas Turbines and Power*, October 1991, Vol. 113, No. 4, pp. 535-543.

Yates, S. W., and Williams, R. D., "A fault-tolerant multiprocessor controller for magnetic bearings," *IEEE Micro*, August 1988, Vol. 8, No. 4, pp. 6-17.